Modelling nanoscale fields in microelectronics components studied by operando electron holography

Kilian Gruel

Université Fédérale
Toulouse Midi-Pyrénées

THÈSE

En vue de l'obtention du
DOCTORAT DE L'UNIVERSITÉ DE TOULOUSE
Délivré par l'Université Toulouse 3 - Paul Sabatier

Présentée et soutenue par

Kilian GRUEL

Le 14 avril 2023

Modélisation des phénomènes physiques à l'échelle nanométrique dans les composants de la microélectronique étudiés par holographie électronique operando.

Ecole doctorale : **SDM - SCIENCES DE LA MATIERE - Toulouse**

Spécialité : **Nanophysique**

Unité de recherche :
CEMES - Centre d'Elaboration de Matériaux et d'Etudes Structurales

Thèse dirigée par
Martin HYTCH et Christophe GATEL

Jury

Mme Catherine DUBOURDIEU, Rapporteure
M. Williams LEFEBVRE, Rapporteur
M. Christian RICOLLEAU, Examinateur
M. Martin HYTCH, Directeur de thèse
M. Christophe GATEL, Co-directeur de thèse
M. Jérémie GRISOLIA, Président

Table of contents:

Remerciements:

Je tiens à exprimer ma profonde gratitude et ma reconnaissance envers toutes les personnes qui ont contribué à l'achèvement de cette thèse en nanophysique. Sans leur soutien, leur encouragement et leur assistance inestimable, cette entreprise n'aurait pas été possible.

Tout d'abord, je tiens à adresser mes sincères remerciements à mes directeurs de thèse, dont l'expertise, les conseils et l'engagement indéfectible envers l'excellence ont façonné mon parcours de recherche. Je leur suis vraiment reconnaissant pour leur encadrement et pour les opportunités qu'ils m'ont offertes au cours de mes études doctorales. Merci Martin, pour ces discussions scientifiques au calme et pour ta sérénité devant l'adversité. Merci Christophe, pour ces discussions scientifiques autant énergiques qu'intéressantes et pour avoir toujours été là.

Merci à STMicroelectronics d'avoir rendu ma thèse possible, notamment à Frederic ainsi qu'aux collaborations avec Maria.

Merci à l'équipe I3EM, pour avoir toujours été présent pour mes présentations et d'avoir toujours eu autant de discussions passionnantes à cette issue. Merci Etienne pour m'avoir largement aidé pour mes conférences. Florant, pour sa passion tant pour la science que la musique. Pier pour m'avoir guidé dans l'enseignement des TP à L'INSA. Sophie, de te battre pour qu'il existe un partage scientifique entre les membres du groupe et d'avoir été bienveillante. Bénédicte, sans qui de nombreux évènements scientifiques n'existeraient pas et de prendre du temps pour l'équipe malgré ton emploi du temps surchargé. Mia, pour ta bonne humeur légendaire et pour les moments passés lors de la conférence à Portland. Aurélien, merci d'avoir initié les travaux qui ont permis ma thèse et d'organiser autant de supers évènements.

Merci Julien, pour avoir partagé le bureau durant la plus grande partie de ma thèse me permettant non seulement d'obtenir d'excellents conseils en programmation, mais aussi nous permettant d'échanger de longues heures sur des sujets autant fascinants que personnels. Merci Leifeng pour nos discussions animées sur la science et la politique. Anaïs, merci d'avoir toujours été là tant au labo qu'à l'extérieur ! Et bien sûr merci pour ces partages de BD. Loïc, merci de toujours être là, que ce soit entre quatre murs au bureau, sous le soleil éclatant à la mer ou même tout en haut d'une montagne

! Marine, merci pour ta joie de vivre et les super moments déjà passés ensemble. Elio merci de m'avoir fait confiance pour garder au frais tes petits (bactériophages). Merci Lucas, pour m'avoir fait découvrir la montagne noire et les tips sur Python. Merci à Mireille, merci pour ta disponibilité et pour m'avoir toujours accueilli avec sourire dans ton bureau. Merci également à mon stagiaire Marc, pour avoir rendu possible une étude en intelligence artificielle durant ma thèse.

Merci aux membres du CEMES. Merci aux doctorants tant à ceux qui sont là depuis le début qu'à ceux qui sont arrivés par vagues successives. Merci Cécile, pour ta bonne humeur et bien sûr pour tes supers « carto ». Merci à mes amis de PPM, notamment à Joël qui non seulement m'a sauvé un nombre incalculable de fois administrativement, mais avec qui j'ai aussi pu avoir de longues discussions notamment sur la technologie et les Mac ! Merci, à Nicolas qui m'a soutenu émotionnellement durant cette épreuve et avec qui j'ai toujours pu avoir de bonnes discussions. Merci Marc, pour ta bonne humeur et tes mails, qui m'ont réconforté et diverti avant et après ma soutenance.

Merci à Lionel d'avoir été un de mes premiers encadrants me donnant envie de continuer en recherche et d'avoir été un excellent professeur. Merci à Elodie, qui m'a toujours accueillie avec le sourire et qui finalement permet de se motiver le matin.

Merci à tous ceux que j'ai pu rencontrer et qui m'ont aidé pour accomplir cette thèse.

Merci à mes amis toulousains qui m'ont soutenu durant ma thèse, mais aussi avec qui je me suis bien amusé. Et bien sûr merci à tous mes amis de Bretagne qui, par leur ouverture d'esprit et nos discussions, m'ont construit.

Merci, Louis et Vincent, d'avoir toujours été présents pour nos réunions hebdomadaires éclairées par de la mousse. Je vous remercie aussi pour nos discussions passionnantes tant scientifiques que philosophiques. Merci, Louis d'avoir toujours été là, ce qui me permet de souligner ta motivation sans défaut ! Merci, Vincent de vouloir toujours pousser les questions et la compréhension que l'on a sur certains sujets.

Merci à mon Mac sans lequel je n'aurais pas pu analyser ces belles images de couleur et qui, entre nous, a travaillé jour et nuit et qui par certains égards a plus longtemps travaillé que moi sur cette thèse.

Je tiens à exprimer ma profonde gratitude envers ma famille pour leur soutien inébranlable tout au long de mon parcours, malgré les moments d'absence que cela a pu engendrer. Merci Loïc, d'avoir toujours été à l'écoute et de m'avoir aidé socialement. Merci Lana, d'être toujours aussi combattante, ça donne de la force aux personnes qui sont autour de toi ! Merci à mon père, Fabrice, je souhaite exprimer ma gratitude pour ta constante présence, même lors des moments les plus ardus, merci pour toutes les opportunités que tu m'as offertes et la curiosité que tu m'as poussé à développer, me guidant du monde de l'aviation vers celui des sciences. Merci à ma mère, Anouck pour m'avoir accordé la liberté nécessaire à accomplir mes rêves et pour avoir été un soutien inconditionnel dans mes choix passés. Merci à mon parrain Didier pour nos discussions sur les sciences depuis mon plus jeune âge, ce qui, je sais, a fait partie de ce qui m'a donné le goût des sciences. Merci également d'être toujours présent et d'avoir assisté à ma soutenance. Merci, Cécile et Lou, pour m'avoir accueilli durant ces super étés et périodes de Noël, vous êtes supers !

Merci, Océane d'avoir été là depuis le début de mes études en oubliant la fuite d'une année en Écosse (qui a été loin d'être inutile). Nous avons quitté la Bretagne pour Toulouse avec détermination, et bien que les premières années aient présenté leur lot de défis, nous les avons surmontés avec résilience. Merci d'avoir été présente non seulement durant ces moments difficiles, mais aussi pendant les plus joyeux et les plus mémorables. Nous avons surpassé toutes les limites, soutenant maintenant la même année, témoignant du succès de notre union, et je suis certain qu'elle continuera à prospérer. Merci aussi pour tous ces moments à deux.

"To succeed, planning alone is insufficient. One must improvise as well."
— Isaac Asimov, Foundation

This manuscript encompasses the processing, physical, and statistical analysis of electron holography microscopy data, obtained through collaboration with my I3EM and STMicroelectronics teams.

Chapter 1 — Introduction and Motivation

General Context of the Microelectronics Industry

Microelectronics has become an indispensable part of our daily life and the global economy. As proof, I can refer to the chip shortage that occurred during my PhD thesis, which had a huge impact on many sectors of production. Not only the internet of things (IoT), for example, for smart homes and connected cities, but also artificial intelligence (AI) applications, for autonomous cars and smart robots, have grown in importance in recent years, creating a strong demand for silicon-based microelectronics. Because these two types of applications do not have the same requirements for computing power and energy consumption, they are based on different technologies and different fabrication techniques.

Computing power is less important than autonomy for applications in the internet of things, so the length scale of components (called "nodes" in the microelectronics industry) can be less aggressive and the deep ultraviolet (DUV) machines that are already in place are sufficient. Indeed, this type of lithography currently accounts for 80% of demand, implying that we can produce more machines of the same type to meet demand.

However, to power the next generation of autonomous vehicles as well as the microelectronics of tomorrow, we need chips with both extreme computational capability and low power consumption. To accomplish this, each electronic component must be reduced in size, new concepts and materials developed, and new machines conceived to pattern them.

These machines while there are very expensive to develop and build, create components always thinner. There are only a few enterprises, such as TSMC, Intel, and Samsung, that can afford them, coupled with increased demand from fabless

companies such as Apple, Qualcomm, Nvidia, and others. As a result, our supply chain for the next information revolution will be based solely on a few companies with localised fabs in the world, making the system vulnerable to natural disasters such as earthquakes and pandemics... Many political reactions are underway to diversify and expand production, with the EU chips act, the US chips act, the Japanese chips act, and so on... The investment in new technology to build and characterise the components of tomorrow is significant.

Current Challenges

There are numerous challenges to maintaining growth in the microelectronics sector, the first and foremost being the development of current and future technologies such as Magnetic Random Access Memories (MRAM) (Moodera et al., 1995; Sbiaa et al., 2011; Slonczewski, 1996), memristors (Chua, 1971; Di Ventra and Pershin, 2013; Strukov et al., 2008), phase-change memory (PCM) (Burr et al., 2010; Jung et al., 2011; Krebs et al., 2009; Simone Raoux et al., 2008; S. Raoux et al., 2008), spintronic (Hirohata et al., 2015), or, in the distant future, skyrmionic (Ma and Li, 2022), optoelectronic (Yu et al., 2016), or molecular (Wang and Nijhuis, 2016). For instance, ferroelectric materials which have a spontaneous polarisation even in the absence of an applied field, have excited tremendous interest to produce devices exploiting negative capacitance (Khan et al., 2015; Robertson and Wallace, 2015; Hoffmann et al., 2019; Íñiguez et al., 2019) and to offer a solution to power dissipation and overheating occurring in transistor miniaturisation (Theis and Solomon, 2010). The amplification of low gate voltage using the negative capacitance would enable low-power operation (Zhirnov and Cavin, 2008).

All of these devices are driven by electrical currents and depend on the manipulation and control of electric or magnetic fields at very small length scales. The possibility to measure electrical signals locally and electric charge distributions of the working chip is critical to support these developments and improve existing technologies as well as developing a new generation of devices. Correlating local electric fields, mapped across a chosen device while it is in operation, to its structural and chemical properties would greatly help research laboratories and the microelectronics industry. Furthermore, the local studies of the electric fields could also provide methods to

determine the root causes of electrical failure (Engelmann et al., 2000) to improve the devices in terms of reliability, speed, and power consumption.

Electrical characterisation can now be carried out directly on single nanodevices by contacting with nanotips, currently named as nanoprobing (Toh et al., 2007, 2008). This technology has the benefit of allowing electronic chips to be studied in their natural environment and at a microscopic scale by measuring their global response to excitation. However, due to chip shrinkage, the elementary blocks that make up the component have to be studied at a higher resolution, *i.e.* the nanometric scale, in order to progress. More importantly perhaps, such electrical characterisation techniques measure the global response of a system or device: they cannot supply information on the localisation of the electric fields or charge distributions inside a device.

Transmission electron microscopy (TEM) is a powerful technique for studying the properties of individual nanosystems with very high spatial resolution. There is much current excitement surrounding attempts to map local electric fields using four-dimensional scanning transmission electron microscopy (4D-STEM) (Ophus, 2019). These techniques base their measurements on the deviation of the electron beam caused by the Lorentz force of a local electric field. In principle, the local field within a component could be determined in such a way, as opposed to microtips, which measure the overall response.

4D-STEM techniques can even have atomic resolution (Jiang et al., 2018) and are capable of reconstructing three-dimensional information (Jarausch et al., 2009). However, they do not measure the electric potential. Furthermore, because they are based on scanning, they are extremely difficult to implement for *in situ* experiments. For example, scanning-based techniques can be very sensitive to sample drift (Yang et al., 2016). They are also highly demanding in terms of data collection and storage. For example, each image is about four megapixels, resulting in a total dataset size of 420 GB with an average of 49 adjacent probe image (in a 7×7 grid) (Ophus, 2019).

An older though less widespread technique is off-axis electron holography (EH), an interferometric method that allows quantitative mapping of electrical distributions. The response of a component after an electric (Rau et al., 1999; Twitchett et al., 2002), magnetic (Gatel et al., 2015; Dunin-Borkowski et al., 2019), or strain (Hÿtch et al.,

2008) excitation can now be measured. The measurement of charge distributions have also been reported (Midgley and Dunin-Borkowski, 2009; McCartney et al., 2010; Beleggia et al., 2011, 2014; McCartney et al., 2019), this measurement can even achieve precision down to the elementary charge level (Gatel et al., 2013).

Electron holography retrieves these interactions through the mapping of the phase difference between the part of the electron wave passing through the active area of the specimen and a reference wave in the vacuum. The phase shift is directly related to the electromagnetic potentials encountered along the trajectory of the electron beam, both within the sample and in the surrounding stray field.

However, despite these encouraging prospects, electron holography has rarely been used to investigate the local electrical properties of nanosystems. A few model systems, including nanotips (Cumings et al., 2002; de Knoop et al., 2015, 2014; He and Cumings, 2013; Migunov et al., 2017), quantum wells (Liu et al., 2012), nano-wires (den Hertog et al., 2013, 2009), p–n junctions (Beleggia et al., 2003; He et al., 2013; Twitchett et al., 2002; Twitchett-Harrison et al., 2008; Yazdi et al., 2015), oxide layers (Yao et al., 2013), transistor (Rau et al., 1999), have been studied. However, the experimental data interpretation can be influenced by many factors, such as specimen preparation, surface damage layers, stray field, and electron radiation (Park et al., 2014; Wolf et al., 2013; Yazdi et al., 2015). Besides, the investigation of real magnetic devices (Einsle et al., 2015; Goto et al., 2013) as well as electrical (Ikarashi et al., 2012), has been reported but more research is still required.

An important demand from the industry has been to develop methods to analyse dopant distribution inside components (Diebold, 1996). Many research has thus been dedicated to the characterisation of p-n junctions, a large part using TEM and among them including pioneering *in situ* study in electron holography (Frabboni et al., 1985). However, electron holography of p-n junctions encountered several difficulties, notably sample preparation, which changed the doping inside the junction. The implantation of Ga atoms into the surface of the sample during focused ion beam (FIB) milling results in so-called dead layers (Cooper et al., 2010; Twitchett et al., 2002) and amorphous conductive layers (Han et al., 2008). Moreover, it is difficult to generate quantitative data because the measured phase shift corresponds to the integration of the electrical potentials along the electron beam path.

During my PhD thesis, I have attempted to address some of these issues by combining the latest experimental data from *operando* electron holography experiments with modelling performed with the finite element method (FEM). This work was supported by the recent developments in the group on the experimental methodology, in terms of sample preparation, *in situ* biasing, microscope control, and data acquisition and processing.

We deliberately chose to study a different fundamental microelectronics component than the p-n junction: the nanocapacitor. This component is both widely used in the microelectronic industry and exhibits rich and varied physical phenomena.

More specifically, I developed a FEM-based methodology for modelling the electrostatic potential in and around electrically polarised nanodevices using commercial software (COMSOL Multiphysics). I will show how the problems related to the stray fields generated by the biased nanocapacitor can be resolved through numerical simulations, and similarly for other artefacts such as surface damage introduced during FIB sample preparation or beam-induced charging (beam-induced charge and sample preparation artefacts). More importantly, the numerical modelling will allow the experimental data to be satisfactorily interpreted leading to a better understanding of the underlying physics, uncovering of unexpected phenomena and measurement of electrical characteristics of the devices studied.

Chapter Description

The structure of the rest of the manuscript is as follows.

Chapter 2 presents the methods developed and used in my thesis along with the theoretical background. I begin with a definition of the charged particle and present the theory behind the capacitor using the equations of Maxwell. As a result, the capacitor will be completely described from nanoscopic to macroscopic dimensions.

I will introduce the holography technique, the theory and the methodology behind the data analysis. The finite element method (FEM) will be introduced, its formalism and some practical aspects. Finally, I will present some numerical tools that I developed during my thesis concerning the fitting of experimental data, processes that allow a maximum of human bias to be removed while also speeding up the study, such as fitting algorithms and AI.

Chapter 3 examines the theories that link the FEM model and the phase images extracted from the holograms. We first start with the evaluation of numerical artefacts by examining the nonphysical parameters such as the finite simulation size and FEM mesh geometry. After determining the conditions for which the model is free of non-physical parameters, I will examine what we can learn from simulations. In this regard, I will demonstrate that we can gain a better understanding of the effect of certain phenomena by investigating the relationship between the physical model and the phase image as a result of adjusting the model parameters.

Chapter 4 presents the first analysis of experimental data. Given the immense complexity and diversity of the study, we began with a model capacitor created in laboratory specifically for the experiment, allowing us to test several techniques developed for the occasion. We wanted to see if our expectations of capacitor behaviour at this scale were met first and foremost. Whilst some expectations were confirmed, the analysis also led to some surprising results. For example, we highlight the presence of volume charged regions that alter the expected electrical characteristics of model metal-oxide-semiconductor (MOS) nanocapacitors, despite the fact that this type of nanodevice was considered to be completely understood. At last, even though we can retrieve the sample *in operando*, the sample is thinned to achieve electron transparency, so there may be some disparity between the sample measurement and its true macro behaviour.

Chapter 5 presents a study of the uncertainties on the retrieved parameters and methods to minimise human bias in the fitting process. I will present the accepted method from metrology to quantify uncertainty and the links between parameters. We discovered that some measurement parameters are correlated during the theoretical study, so the main question is whether we can measure them if they are correlated. As a result, we use statistical tools to solve this problem, specifically the correlation matrix, which allows us to compute the uncertainty propagation across the measured standard deviation.

Furthermore, developing numerical simulations has the advantage of allowing us to build a complex data analysis while also developing tools for analysing experimental data such as scripting, autofitting, or developing IA.

Chapter 6 presents the application of these techniques to real-world devices which present more complex geometries. The results on nanodevices from STMicroelectronics production lines are presented and analysed, and errors investigated. Before concluding the studies of two capacitors working together, I show a study of a capacitor in operation as well as a study failure, demonstrating that even when we make mistakes, the final result is always interesting.

Chapter 2 — Method

The work in this thesis required the combination of several existing techniques as well as the development of new ones. However, before delving into these techniques, I will begin the chapter by discussing some basic theoretical aspects.

Because we want to measure charges inside operating nanodevices, it seemed pertinent to start with how charges are defined in physics and how this leads to the theoretical description of a capacitor. I will then discuss how capacitors behave within electrical circuits. As a result, the capacitor will be completely described from nanoscopic to macroscopic dimensions. Finally, I will also develop aspects of the equations of Maxwell and the continuity conditions at interfaces, which will give us a good idea of what to expect from the behaviour of the system under consideration.

The first technique I will describe is electron holography and the way we can attempt to map an electromagnetic potential at a nanometric scale with the interaction between the electron beam and the various electromagnetic potentials encountered during their journey through the microscope. Beginning with a description of fast electrons using special relativity and quantum mechanics, I will present the main equations required for understanding the theoretical background and the interaction between the electron and the electrostatic potential.

A fundamental issue with electron holography is that interaction comes from the integral of the potential along the electron trajectory, which means the information parallel to the dimension along the electron path is very difficult to interpret: the well-known projection problem. This is a major justification for using numerical simulations. We can use the finite element method to extract quantitative data and reconstruct the history of the beam path to respond to this lost dimension. With an example, I will explain the basic theory and show how the method works in practice.

The last part of the chapter is devoted to an automated fitting routine I developed to remove as much human bias as possible in the data analysis. I will go over the two methods I used to automate the calculation, as well as an artificial intelligence-based method that, while much faster than finite elements, raises new questions about the definition of uncertainties associated with these methods.

1. The Capacitor

1.I. Electrostatics

1.I.A. Equation of Maxwell in Vacuum

First and foremost, to describe potential maps within electronic devices such as the capacitor, we need to begin with the definition of positive and negative charges (Figure 2.1).

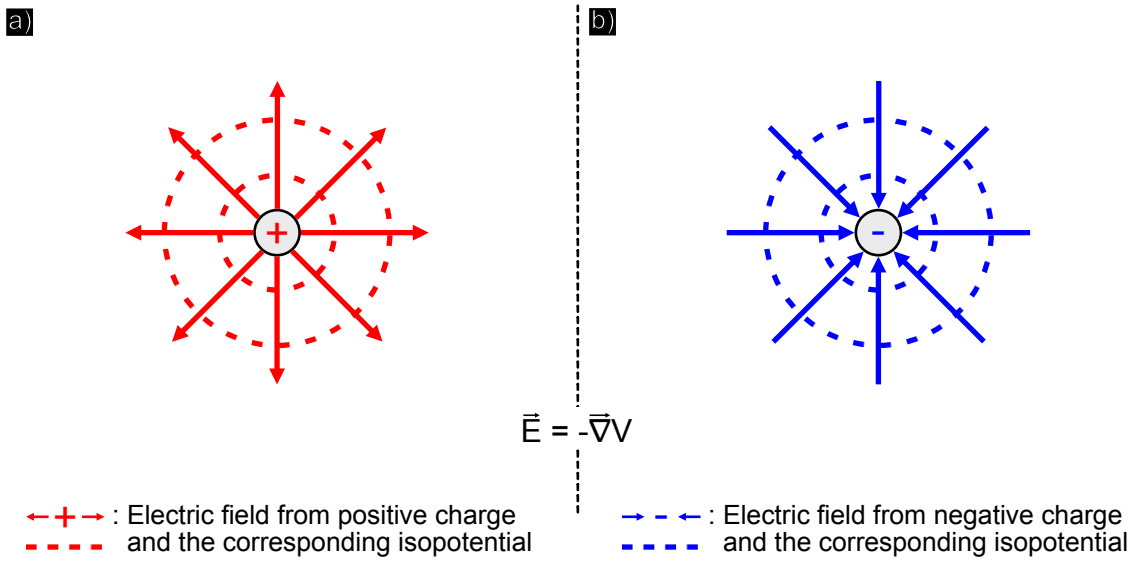

Figure 2.1 : The electric field produced by a positive charge a) or a negative charge b) and its iso-potential are depicted in the diagram.

Charges are an intrinsic property of matter that cannot be split, and present a quantum equal to $e = 1.60217733 \times 10^{-19}\, C$ that can be positive or negative. The field from a positive charge projects outwards with central symmetry, whereas the field from a

negative charge points inwards. The relationship between electrostatic potential, *V*, and the electric field, $\overrightarrow{E}$ is given by (2.1):

$$\vec{E} = -\vec{\nabla}V \qquad (2.1)$$

We see that the electric fields are always perpendicular to iso-potential lines. If a particle of charge, q , passes through an electric or magnetic field, $\vec{B}$, with velocity $\vec{v}$, it will be subjected to the Coulomb-Lorentz force, $\vec{F}$:

$$\vec{F} = q(\vec{E} + \vec{v} \wedge \vec{B}) \qquad (2.2)$$

Based on this assumption, the primary goal of electromagnetism is to calculate the fields $\vec{E}$ and $\vec{B}$ in order to describe the force. The devices studied in this thesis are primarily electrostatic, so we will not consider the magnetic fields in the following developments.

When we move away from the atomistic description, we define the charge by a continuous charge per unit volume or charge density ρ, regardless of the fundamental quantification of the charges.

By analogy with fluid flow, we can also define an electric current I and the current density $\vec{J}$ which corresponds to a collective motion of charges by time unit and through a finite surface $d\vec{S}$ (2.3):

$$I = \frac{dQ}{dt} = \int_s \vec{J}\, d\vec{S} \; ; \; \vec{J} = \rho\vec{v} \qquad (2.3)$$

Depending on the geometry, crystal structure, and chemical components of the materials involved, the current will flow more or less with the same force applied to them. So, this physics is captured on a large scale by the conductivity σ and the form factor $\frac{l}{S}$, with S the cross section and l the length of the medium, meaning that the important parameter is the resistivity R:

$$R = \frac{1}{\sigma}\,\frac{l}{S} \qquad (2.4)$$

Electrons find it more difficult to flow as the resistivity increases.

Inside semiconductors, such as silicon, the current is described in a quantum manner with two types of carriers, which means that there are also hole currents that flow in the opposite direction of the electrons. It is also necessary to introduce the effective mass of an electron ${m_e}^*$ and a hole ${m_h}^*$ in silicon respectively equal to ${m_e}^* = 0.9\, m_e$

and $m_h{}^* = 0.5\, m_e$ with m_e and m_h the mass at the rest of electron and hole respectively. These expressions are based on a quantum calculation and interpretation of the curvature of the band structure. We must thus use the appropriate tools depending on the phenomenon and materials to be studied.

If the collective movement of electrons produces a current, it is equally important to describe the field that these particles produce. To be more specific, in the case of point charges, the forces on a charge q at a point $\vec{r}$ that is made by N charges q_k at point $\overrightarrow{r_k}$ are given by the law of Coulomb:

$$\vec{F} = \frac{1}{4\pi\varepsilon_0}\sum_{k=1}^{N} q q_k \frac{\vec{r} - \overrightarrow{r_k}}{|\vec{r} - \overrightarrow{r_k}|^3} \; ; \; \vec{F} = q\vec{E} \qquad (2.5)$$

The definition of $\vec{E}$ explicitly states the principle of superposition, *i.e.* an arbitrary charge distribution is the vector sum of the electric field produced by each individual charge. The principle of superposition will be crucial in understanding the field recorded by electron holography.

Two of the equations of Maxwell are of particular importance:

$$\nabla.\overrightarrow{E} = \frac{\rho}{\varepsilon_0} \; ; \; \nabla \wedge \vec{E} = 0 \qquad (2.6)$$

The first equation is law of Gauss, which defines the produced field source, and the second is the structure equation, which defines the potential V via vector analysis. While the first can work on dynamic, the second is only applicable to electrostatic problems.

Despite the fact that the equations of Maxwell were developed to analyse macroscopic phenomena, they can also be applied at the microscopic scale. Lorentz averaging can be used to create this link. As a result, I can introduce the concept of mean inner potential (MIP), which is an intrinsic parameter of matter. MIP is the volume average of the total electrostatic potential within a crystal in relation to vacuum.

$$V_0 = \frac{1}{\Omega}\int_{\Omega} V(\vec{r}) d^3r \qquad (2.7)$$

where Ω is the crystal volume and $V(\vec{r})$ the potential at the position $\vec{r}$.

We see how to calculate a field from charges, and it is also interesting to see how charges at surfaces influence an external field. When an electric field penetrates a charged surface defined by a normal vector $\vec{n}$, its normal component changes while

there is a continuity of the tangential component. The interface condition describes this discontinuity, which is dependent on the magnitude of the charge density at the interface:

$$\vec{n} \cdot \left[\overrightarrow{E_2} - \overrightarrow{E_1}\right] = \frac{\rho_s}{\varepsilon_0} \quad (2.8)$$

where charged surface ρ_s modifies the relation between the incident normal component $E_{1\perp}$ and the incident normal component $E_{2\perp}$. However, because these equations do not account for the true nature of matter, I will provide a brief introduction to the modifications we must make to these equations in order to treat this topic. While acknowledging that this is a vast subject that will require extensive research, I will not be able to cover it entirely.

1.I.B. Equation of Maxwell in Matter

By stating that the charge density is zero at all points within an isolated sample of neutral matter, and by including free volume charge density ρ_f that is only extrinsic to the dielectric, the external charge field will cause charge reorganisation and current flow in dielectric matter. And we can describe this charge reorganisation by introducing a vector field $\vec{P}$ that describes dielectric polarisation and it is incorporated into the theory of Maxwell as follows:

$$\rho = \rho_f - \nabla\vec{P} \quad (2.9)$$

The macroscopic auxiliary field or electric displacement $\vec{D}$ is then used to describe the entire charge reorganisation:

$$\vec{D} = \varepsilon_0\vec{E} + \vec{P}\ ;\ \nabla\overrightarrow{D} = \rho_f \quad (2.10)$$

Like the electric field, this auxiliary field has an interface condition depending on the free surface charge σ_f:

$$\hat{n} \cdot \left[\overrightarrow{D_2} - \overrightarrow{D_1}\right] = \rho_s \quad (2.11)$$

Nonetheless, the inclusion of the constitutive relation is imperative to finalise the set of equations:

$$\vec{D} = \varepsilon\vec{E} = \varepsilon_0\varepsilon_r\vec{E} = \varepsilon_0(1+\chi)\vec{E}\varepsilon_0 = \vec{E} + \vec{P} \quad (2.12)$$

ε_r is the relative permittivity (no unit or dimension is associated).

Alternatively, we can then use the electric susceptibility χ:

$$\vec{P} = \varepsilon_0 \chi \vec{E} \quad (2.13)$$

To develop on the interface condition, if we consider the superposition of two materials with different permittivity, we can calculate the angle formed by the difference in permittivity at an interface (Figure 2.2).

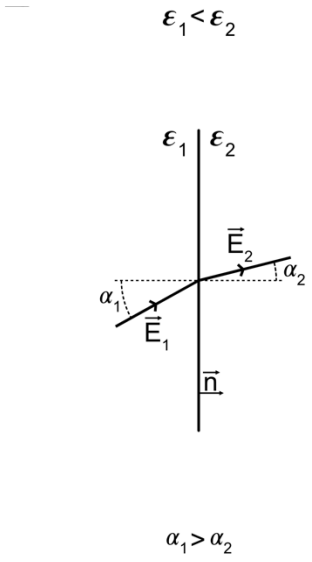

Figure 2.2 : An interface between two areas with different permittivity is depicted in this diagram.

We can write these two equations in the absence of free charge:

$$\nabla \wedge \vec{E} = 0 \ \& \ \nabla \cdot \vec{D} = 0 \quad (2.14)$$

And by projecting it:

$$E_1 \sin(\alpha_1) = E_2 \sin(\alpha_2) \ \& \ \varepsilon_1 E_1 \cos(\alpha_1) = \varepsilon_2 E_2 \cos(\alpha_2) \quad (2.15)$$

If we combine these equations by divide one by the other, we find:

$$\alpha_2 = tan^{-1}\left(\frac{\varepsilon_1}{\varepsilon_2} tan\, \alpha_1\right) \quad (2.16)$$

This equation can be computed for multiple parameters of α_1 and ε_1 while $\varepsilon_2 = 1$ as in the vacuum (Figure 2.3).

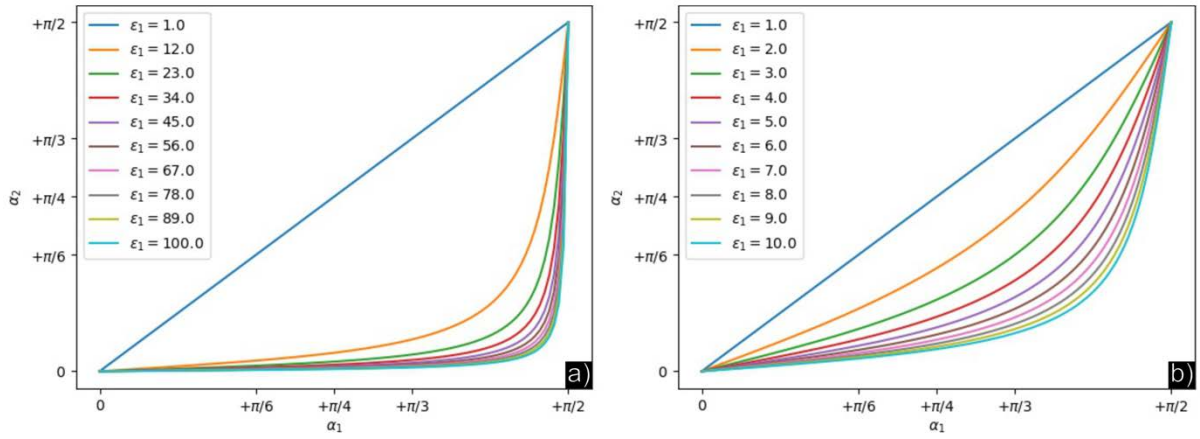

Figure 2.3 : Relationship between the two angles for different permittivity on the left a) and with lower permittivity on the right b).

These figures show that as the dielectric value exceeds 10, the effect stabilises, indicating that we consider to have reached saturation. We can also see that when the angle α_1 is close to $\frac{\pi}{2}$, the exit angle α_2 is also close to $\frac{\pi}{2}$, because the field perpendicular to the surface is not modified, as shown in the equation (2.14).
Another intriguing aspect could be choosing an angle that is close to the reality of an electric field inside the dielectric. It is near the interface between the dielectric and the vacuum, implying α_1 is very low (Figure 2.2). And then we observe how the exit angle changes as the dielectric permittivity in relation to the vacuum varied (Figure 2.4).

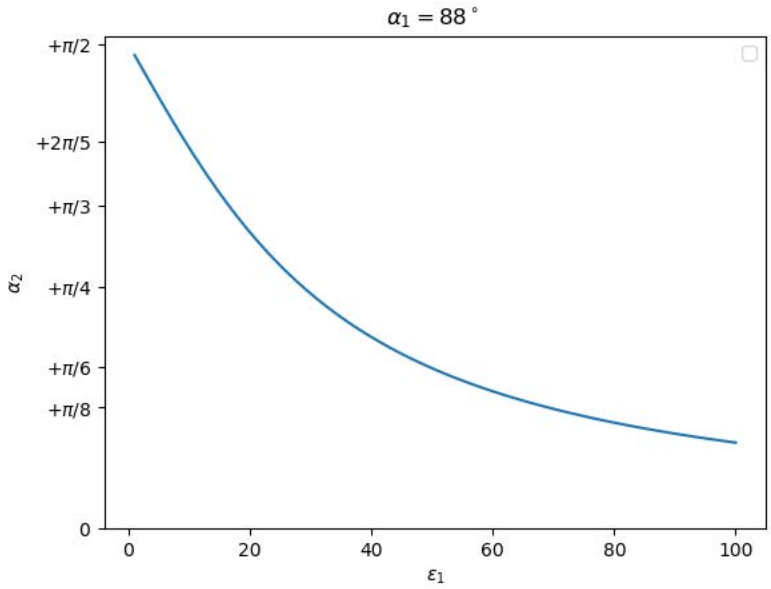

Figure 2.4 : variation of α_2 with α_1 at 88 deg when ε_1 varies between 1 to 100.

We can clearly see that, as the dielectric permittivity increases, the exit angle decrease. Meaning, as permittivity increases, more charges accumulate on the surfaces, resulting in a larger secondary field – *i.e.*, stray field.

1.I.C. Capacitors

Capacitors are essential and the most fundamental components of all electronic devices. In the case of nanocapacitors, they are made up of two conductive layers separated by an insulating layer of a nanometric thickness. They are widely used in memory devices such as flash memories and random access memory (DRAM, SDRAM,...), as well as processors whose performance is dependent on miniaturisation and operation or to improve the efficiency of photovoltaic cells and to build ultrafast diodes. Despite the very interesting effect of tunnel junctions that occur when the thickness of the insulator is less than 10 nm, which means that electrons can easily pass through an insulating layer due to the tunnelling quantum, we will not address this phenomenon in this thesis with samples larger than 10 nm. Regardless, other phenomena such as charge injection will be of interest.

We will begin with what happens inside the capacitor. At first approximation, the internal electric field of the capacitor initially made up of two infinity charged planes separated by a dielectric create straight field, as shown in Figure 2.5.

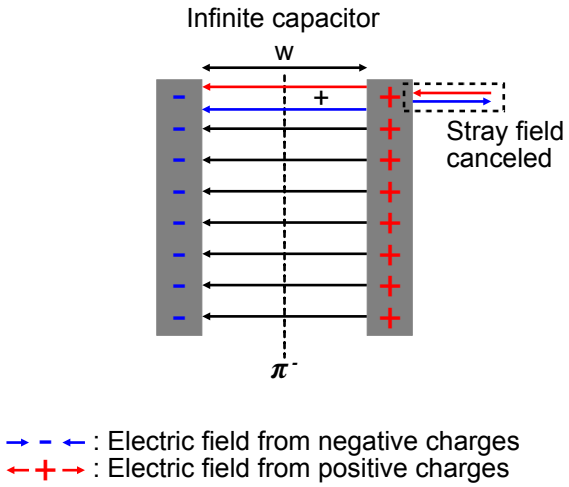

Figure 2.5 : Picture of a charged plan with positive and negative charge that combined creates a capacitor.

Despite the fact that capacitors can have a variety of geometries, such as imbricated fins or wrap capacitors, we will focus on planar capacitors because they are closest to those used in the silicon-based devices from microelectronic industries.

To begin, an infinite capacitor is composed of two opposite charged plates that allow the addition of the electric field inside the capacitor while cancelling the external field and maintaining overall charge neutrality. In this way, the electric field is confined only between the charged plates. The charge arrangement corresponds to a symmetry π^-, allowing us to study only the component of the field perpendicular to the plate constituting the capacitor $\vec{E}.\vec{n} = E_x$. Law of Gauss can be used to calculate the field produced by a single charged plate (with a surface-free charged density $\rho_{s,f}$):

$$\oiint_s \vec{E}\overrightarrow{ds} = \frac{1}{\varepsilon_0}\iiint_v \rho_{s,f}\, dv \qquad (2.17)$$

By integrating the field produced by an infinitely charged plate with the total number of charges Q, we find:

$$\int_0^{-x} -E_x\, ds + \int_0^{x} E_x ds = \frac{Q}{\varepsilon_0}\,; Q = \rho_{s,f}\, S \qquad (2.18)$$

$$E_x = \frac{\rho_{s,f}}{2\,\varepsilon_0} \qquad (2.19)$$

By design and by the principle of superposition, we can add the field created by the two plates:

$$E = \frac{\rho_{s,f}}{\varepsilon_0} \quad (2.20)$$

The potential associated with a capacitor can then be calculated using the electric field. It is made up of two charged plates of opposite sign separated by a dielectric of thickness w:

$$\int_{V_1}^{V_2} dV = -\int_0^w \vec{E}\,\overrightarrow{dl} \quad (2.21)$$

$$V_c = \frac{\rho_{s,f} w}{\varepsilon_0} = \frac{Q}{C}\ ;\ C = \frac{\varepsilon_0 S}{w} \quad (2.22)$$

These equations depict the basic behaviour of a capacitor, indicating that as the distance between the plates w decreases, the capacity C increases while the capacitor bias V_c decreases for the same amount of accumulated charged (*i.e.* these equations describe a capacitor with a set number of charge densities (without generators). Similarly, as the section increases S, the capacity increases while the bias decreases.

In reality, a capacitor is not infinite, especially when studied using TEM techniques, because the sample must be extremely thin to allow the electron to pass through. We previously assumed that the electric field was straight all the way along the capacitor, but in reality, the electric fields become curved when they are close to the interfaces between the dielectric and the vacuum (Figure 2.6). Furthermore, stray fields appear around the capacitor in this configuration, which, as we will see later, must be accounted for in the simulations. In a sense, each plane of the capacitor is charged with electrons of opposite sign. Each charge generates a field, which, when combined with the fields of the other charges, produces the final electric field between the plates using the principle of superposition.

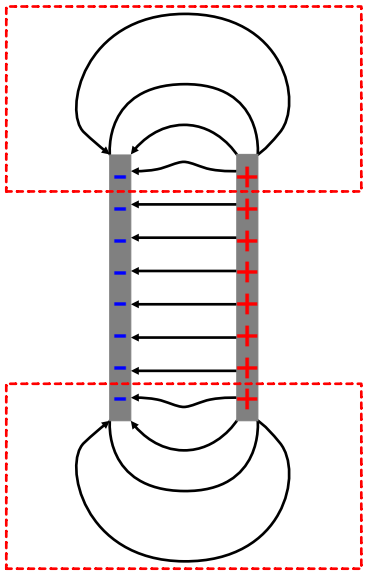

Figure 2.6 : Scheme of a real capacitor with the stray field around it.

Let us reformulate this by going from an infinite capacitor to a finite capacitor. We have a naturally curved electric field distribution when only two charges are placed on each plate as shown Figure 2.7(a). When the capacitor is energised, millions of charges accumulate on each plate, and the electric field from each plate adds up to a straight electric field perpendicular to each plate, as shown in Figure 2.7(b) in green lines.

If considering a non-infinite capacitor, the electric field bends near the edge. Figure 2.6 also depicts this inside the red dotted area. In the previous example, the sum of each electric field of each charge of each plate compensated for each part of the electric field parallel to the π^- axis. As we approach the edge, there is less and less charge to compensate for this component of the field, causing the electric field to bend. In other words, if we start in the centre of the capacitor and work our way out, there is a compensation of the electric field parallel to the π^- plane that is created in a chain until the edge where there is no more charges, in which the field bends and is no longer completely compensated. The stray fields of the capacitor look like the field produced by two opposite charges partially compensated by the field produced by two rows of opposite charges just above two charges.

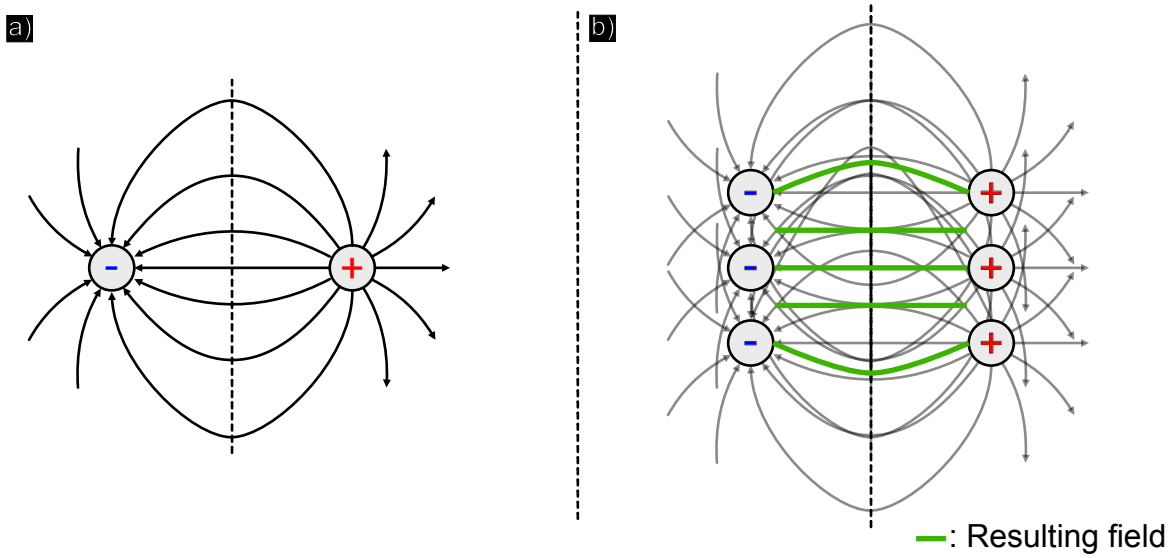

Figure 2.7 : Electric Field made by two opposite charges a) and the resulting field made by multiple opposite charges arranged like a capacitor b)

Based on the aspect ratio between the length of the dielectric and the thickness of the sample, the sample studied here is much closer to a real capacitor than an infinite capacitor. We must consider this parameter to understand its effect. The importance of the stray field will be discussed in detail in the following sections and chapter. But first, I would like to discuss a capacitor modification that increases its energy without changing its geometry: the physics behind dielectrics.

1.II. Dielectric Capacitors

Because a dielectric allows for more charges storage on the capacitor plate than the vacuum, several efforts have been made in recent years to incorporate dielectric with increasing relative permittivity inside nanocapacitors: with the same geometry and bias, these materials allow the capacitor to store significantly more charges and thus significantly more energy.

Indeed, the first reaction of a dielectric to an external electric field is to counteract the field by rearranging its internal charges until it reaches a limit defined by its permittivity (Figure 2.8). The capacitor will now be connected to a generator to better describe the capacitor used in real life. At first, we could say that the potential will

drop but this is without taking into account that the capacitor is connected to a generator. The main effect of which is to impose a bias on the device, bringing the number of charges required to maintain the initial bias increasing its energy.

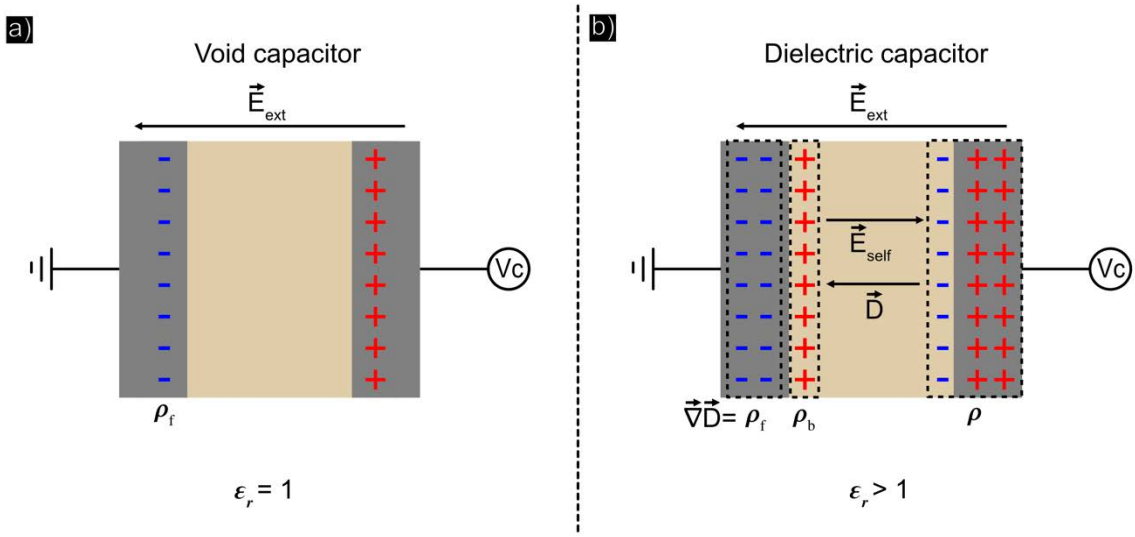

Figure 2.8 : Scheme of bias capacitor with a void spacer a) and the induction of new charges by inserting a ferroelectric or dielectric.

In other words, the dielectric will generate bound charges in response to the electrode field. As a result, the bound charges will screen the electron on the plate of the capacitor, and the generator will react by injecting more charges inside the electrodes to conserve the designated potential drop.

We can take this phenomenon into account by replacing ε_0 by $\varepsilon = \varepsilon_0 \varepsilon_r$ with ε_r the relative permittivity of the dielectric in the above equations:

$$E = \frac{\rho_{s,f}}{\varepsilon} \qquad (2.23)$$

The relative permittivity is directly related to the susceptibility as shown by the equation (2.22).The equation (2.22) are then modified as follows:

$$V_c = \frac{\rho_{s,f} w}{\varepsilon} = \frac{Q}{C} \; ; \; C = \frac{\varepsilon S}{w} \qquad (2.24)$$

These equations depict the behaviour of a capacitor with a dielectric. To illustrate, when we add a permittivity ε element between the two plates, the capacity increases whilst the bias should decrease. But with the fixed bias brings by the generator, the charges on the plate will grow. Overall, the potential drop across the capacitor will be the same with or without a dielectric, but with a dielectric, many more charges will be stored. This is well described by the equation (2.9), where the resulting charge is equal to the generator charge minus the polarisation charges.
Because a capacitor is not perfect and its connection to the circuit can cause contact resistance, we always describe a capacitor in series with a resistor.

1.III. Circuit Point of View

Despite the fact that we want to measure phenomena at the nanometric scale, it is useful to review the operating parameters of a capacitor at a more macroscopic level (Figure 2.9).

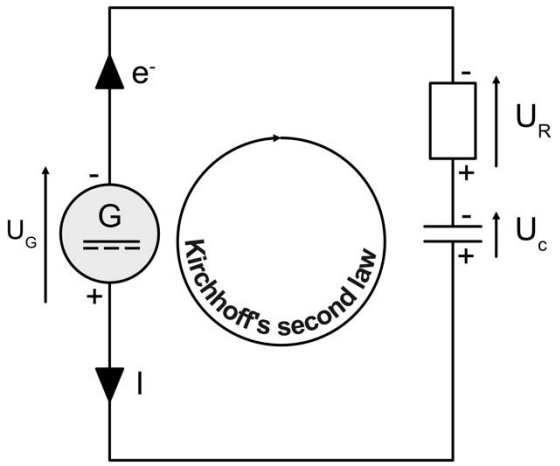

Figure 2.9 : A capacitor is powered by a dc current in this simple electric scheme.

A capacitor is always coupled with a resistance *R* to simulate the resistivity of a real capacitor while also accounting for the resistivity of the circuit. The basic equations related to a capacitor can be defined in the quasistatic approximation:

$$c = \frac{Q(t)}{U_c} \; ; I = \frac{dQ(t)}{dt} \qquad (2.25)$$

Where c capacity, U_c the bias of the capacitor and I the intensity of the circuit.
Using the second law of Kirchhoff that is derived from the law of Maxwell, we can write this relation:

$$U_G - U_R - U_c = 0 \quad (2.26)$$

Where U_R, the bias of the resistance and U_G, the applied bias by the generator.
By combining the fact that the circuit is in series and by combining the equation (2.25) and (2.26) we fund the Differential equation of the system:

$$\frac{dU_c}{dt} + \frac{U_c}{RC} = \frac{U_G}{RC} \quad (2.27)$$

Then by resolving the homogenous differential equation and the particular solution we can write this equation:

$$U_c = U_0 e^{-\frac{t}{RC}} + U_G \quad (2.28)$$

This equation describes two transitory steps: charging, which occurs while the energy is stored, and discharging, which occurs when the capacitor delivers its energy to the circuit. Each transitory step begging with an initial capacitor bias U_0. To begin, we must use the initial conditions $t = 0$ and $U_c = 0$ to find the equation that describes the charging process:

$$U_c = U_G \left(1 - e^{\frac{t}{RC}}\right) \quad (2.29)$$

The charging of a capacitor will follow an exponential form that is parametrically defined by the initial generator bias U_G and the combination of the resistivity and capacity. As a result, we can introduce $\tau = RC$ as the characteristic time of the system. This means that at τ, the capacitor is charged with 63% of its maximum capacity, and it is generally accepted that it will be at its maximum capacity after 5τ has elapsed from the time the discharged capacitor was switched on, corresponding to a charge of 99.3%.
When the generator bias is reduced, the capacitor discharges. To find the linked equation, we typically calculate for a generator with bias $U_G = 0$, but in practice, any bias can be used. To simplify the calculation, we can set the initial time to the beginning of the potential drop at $t = t_0 = 0$:

$$U_c = U_c(t_0) e^{-\frac{t}{\tau}} \quad (2.30)$$

We want to look into the distribution of the field and charges produced by a capacitor or other electronic component that is as of now in a static state, and one method for gathering qualitative data is electron holography.

2. Electron Holography

2.I. TEM

Transmission electron microscopy, rather than light microscopy, is now required to study microelectronic components because of their miniaturisation. The first transistor, which had a channel length of approximately 40 µm and was fully observable through an optical microscope with a resolution of 0.2 µm, was developed in 1948. A worldwide race toward the miniaturisation of electronic components has been set up in order to save energy while also accelerating the computing speed of electronic chips. The channel size of a transistor today is around 5 nm to 10 nm, so these components are no longer observable by optical microscope due to a lack of resolution. Fortunately, some years before the first transistor, Ernst Ruska and Max Knoll developed the first prototype electron microscope in 1931, capable of producing images magnified up to 400 times, which was followed in 1933 by the development of a second prototype capable of exceeding the maximum resolution achievable by a photonic microscope.
The exceeding of the optical resolution limit using electrons is caused by a property of matter described by a wave-like photon and characterised by the de Broglie wavelength λ_B (2.31):

$$\lambda_B = \frac{h}{p} \qquad (2.31)$$

which includes, h the Planck constant and p the momentum (2.32).
Electrons are accelerated at such a rate that the relativistic aspect of their mass must be considered. Naturally, the acceleration voltage V_0 experienced inside the gun determines the wavelength of the electron inside an electron microscope (this acceleration voltage will always be 300 kV during the subsequent studies).

$$p = mv \qquad (2.32)$$

We use relativistic corrected mass m when m_0 is the invariant mass as follows:

$$m = \gamma m_0 = \frac{m_0}{\left(1 - \frac{v^2}{c^2}\right)^{1/2}} \quad (2.33)$$

With c the speed of light and v the velocity of the electrons, we also define γ the relativistic Lorentz factor. Then, we calculate the difference in relativistic energy corresponding to an acceleration voltage V_0 (*i.e.* kinetic energy) with e the charge of an electron:

$$eV_0 = (m - m_0)c^2 \quad (2.34)$$

We can then re-express γ (2.35) and V (2.36) in terms of V_0 by coupling the upper equations ((2.33);(2.34)):

$$\gamma = \frac{eV_0}{m_0 c^2} + 1 \quad (2.35)$$

$$V^2 = \left(1 - \frac{1}{\left(\frac{eV_0}{m_0 c^2} + 1\right)^2}\right) c^2 = 2.28 \times 10^8 \, m/s \quad (2.36)$$

This velocity corresponds to 76% or ¾ of the speed of light at 300 kV, which is a massive acceleration even compared with a million-volt microscope, as is originally housed inside the "Boule" at the CEMES-CNRS.

Then by injecting these equations into the momentum, we find the relativist momentum (2.37):

$$p = \left\{2m_0 e\left(\frac{eV_0^2}{2m_0 c^2} + V_0\right)\right\}^{\frac{1}{2}} \quad (2.37)$$

We finish with the de Broglie relation, which allows us to calculate the wavelength of electrons (2.38) accelerated by potential V_0:

$$\lambda_B = \frac{h}{\sqrt{2m_0 e V_r}} \; ; V_r = V_0 + \left(\frac{e}{2m_0 c^2}\right) V_0^2 \quad (2.38)$$

In the following section, we define V_r as the relativistic corrected accelerating potential. Because the acceleration voltage is around 300 kV, the wavelength of the electrons is about 2 pm using the equation (2.38).

The Rayleigh criterion states that two airy patches on a screen can be distinguished if the first minimum of one airy spot is greater than or equal to the position of the maximum of the second.

$$R = 0.61\frac{\lambda_B}{\alpha} \quad (2.39)$$

The wavelength of an electron indicates that the resolution is also less than 2 pm. In practice, however, this resolution is never achieved due to a variety of factors such as electromagnetic lens aberration, mechanical and electronic instabilities of the electron microscope and acquisition system. Despite the fact that we are usually focused on the resolution of the microscope, in this thesis we are also concerned with the phase of the electron.

2.II. TEM Holographic Mode

2.II.A. Theoretical Background

One of the few techniques that can measure electric, magnetic, and strain fields at the nanoscale is electron holography. As a result, when combined with *in situ* biasing experiments, electron holography becomes a powerful technique for measuring electric potentials and fields in working microelectronics devices.

Gabor (1949) first described electron holography, but an electron interferometer to study the phase of an electron beam was missing. Many attempts were made to produce interference phenomena using thin single crystals as a beam splitter and two others to produce interference phenomena, but due to the complexity and short lifetime of such crystals, another pathway was taken. When working with dark field micrographs in the electrostatic electron microscope in 1950, Professor Gottfried Möllenstedt noticed that a thin tungsten wire used to intercept the primary beam in the focal plane of the electrostatic objective lens for dark fields had charged up, resulting in a double image on the screen. This observation led to a series of experiments that resulted in the invention of the Fresnel electron biprism by Professor Gottfried Möllenstedt in 1956, which served as the foundation for off-axis electron holography.

Nevertheless, the use of a biprism induces Fresnel fringes, which are the manifestation of electron diffraction onto the wire biprism, which causes an information loss into the beam. In addition, the interference area and the interfringe distance are closely linked and can not be set separately in this configuration. More recently, a double-biprism configuration has been proposed to overcome these difficulties(Harada et al., 2004): an upper filament and a lower biprism are installed in

the image plane and between the crossover point and the image plane of the magnifying lens respectively. The removing of Fresnel fringes as the lower filament remains inside the shaded area of the upper filament improves the signal-to-noise ratio (Harada et al., 2004). In addition to eliminating Fresnel fringes, the second biprism allows to control independently the interfringe by changing the potential applied to the upper biprism and the interference area with the potential of the lower biprism (Harada, 2005). We used this double-biprism configuration for all studies presented within this manuscript.

In contrast to conventional TEM, which records only the spatial distribution of intensity, we can record the phase between a portion of the beam that passes through the vacuum named “reference wave” that has in principle not undergone interaction with any field and a portion that passes through the specimen, called “object wave”, and acquires a phase shift due to its interaction with a magnetic, electric, or strain field (Gabor, 1948; Tonomura, 1987; Hÿtch et al., 2008; Pozzi et al., 2014) (Figure 2.10). We can study the local variation of these fields because this interaction can be recorded as an interference pattern. The resulting interference pattern (*i.e.* the hologram) contains all of the information on the phase shift of the electron wave experienced when interacting with the local electromagnetic fields (Tonomura, 1987; Midgley and Dunin-Borkowski, 2009). Multiple techniques, such as the off-axis technique used here, have been developed to obtain this phase, therefore up to 20 other techniques, such as in-line holography, can also be used (Cowley, 1992), which I will not go into detail about.

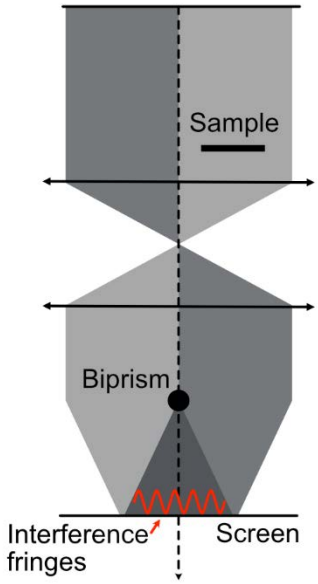

Figure 2.10 : Simple schematic of off-axis electron holography.

When an electron wave interacts with an object or with an electromagnetic field, its phase changes. We know from quantum mechanics that the electron function, which describes the behaviour of relativistic electrons in an electromagnetic field, can be deduced from the Dirac equation by ignoring the electron spin:

$$\frac{1}{2m_0}(-i\hbar\nabla + eA)^2\psi(x,y,z) = e[V_r + \gamma V_0]\psi(x,y,z) \qquad (2.40)$$

where A and V represent the magnetic and electric potentials respectively, e the electron charge, m_0 the rest mass of an electron, γ the relativistic Lorentz factor, and V_r the relativistic corrected accelerating potential. The solution to this equation corresponds to the object electron wave $\psi_i(\vec{r}) = A_i(\vec{r})\, e^{[i\phi_i(\vec{r})]}$, where the phase term is modified by the Aharonov-Bohm effect (Aharonov and Bohm, 1961, 1959; Ehrenberg and Siday, 1949):

$$\Phi(x,y) = \frac{\pi\gamma}{\lambda_B V_r}\oint V(\vec{r})dz - \frac{e}{\hbar}\oint A_z(\vec{r})dz \qquad (2.41)$$

with λ_B representing the electron relativistic wavelength and A_z the magnetic vector potential along the beam direction. Equation (2.41) is also written as describe by (Lichte and Lehmann, 2008):

$$\Phi(x,y) = C_e\oint V(\vec{r})dz - \frac{e}{\hbar}\iint B_\perp(\vec{r})drdz \qquad (2.42)$$

The aim of this work is to study the phase shift due electric potential in biased nanosystems. As a consequence, in the following, we will only use the first term of the equation (2.42).

It is also interesting to develop λ_B from (2.38) to express the coefficient C_e:

$$\lambda_B = \frac{2\pi\hbar}{\sqrt{2m_0\left(E_k + \frac{{E_k}^2}{2E_0}\right)}}\,;E_k = eV_0;E_0 = m_0c^2 \qquad (2.43)$$

Where $E_k$kinetic energy and E_0energy at rest.

By starting from:

$$C_e = \frac{2\pi e}{\lambda_B}\frac{E_k + E_0}{E_k(E_k + 2E_0)} \qquad (2.44)$$

we can rewrite the equation above without explicitly introducing the wavelength:

$$\mathrm{C}_e = \frac{e}{\hbar}\frac{\sqrt{m_0}}{\sqrt{E_kE_0}}\frac{E_k + E_0}{\sqrt{E_k + 2E_0}} \qquad (2.45)$$

As the electrons are accelerated, the constant C_e decreases, implying that the resulting phase shift decreases, whereas we gain resolution from equation (2.43). In addition, the phase shift related to the displacement of interferometric fringes, or change of their periodicity, is measured if at least two fringes are taken into account. As a consequence, the spatial resolution obtained on the phase shift measurement is equal or two times higher than the interfringe distance. The phase noise can be reduced if more fringes are considered for a local measurement of the phase. As a result, we must find a compromise between the spatial resolution and the signal-to-noise ratio of the measured phase.

This theory allows the study of samples that are charged or biased. For example, I can illustrate the effect on the phase onto electron that traverses an electrostatic potential Figure 2.11.

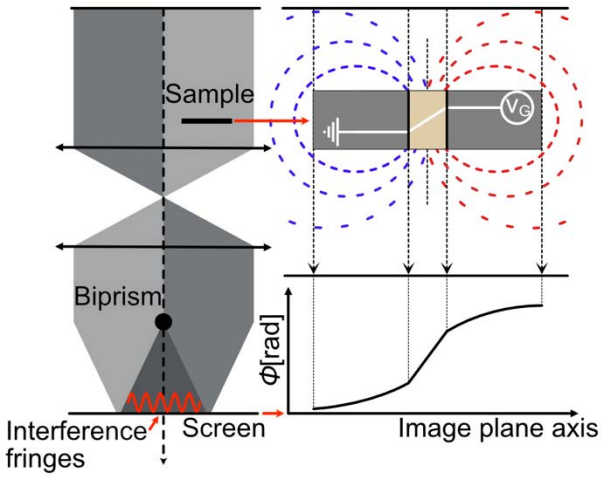

Figure 2.11 : Scheme of the holography technique on the resulting phase image of a model capacitor.

Figure 2.11 shows that we can study the drop of the potential inside a bias capacitor with electron holography because of the link between the phase and the potential encountered by the electron as it passes through the sample. The stray field has a strong influence on the phase image because the sample is not infinite. As a result, the curvature of the phase within the electrodes area is the direct consequence of the stray field. These and other effects will be discussed in the following chapters, both theoretically and experimentally.

All experimental observations were performed using the I2TEM microscope (In-situ Interferometry TEM), a Hitachi 3300-C operating at 300 kV equipped with a cold field emission gun for a very coherence and a BCOR aberration corrector from CEOS with a spatial resolution of 0.5 nm in Lorentz mode and 0.08 nm in high-resolution mode (Snoeck et al., 2014a). For electron holography experiments, elliptical illumination and two post-specimen biprisms have been used to avoid artefacts linked to Fresnel fringes and to allow adjustment of the interference area with respect to the fringe spacing (Harada et al., 2008) as explained previously. This microscope presents two goniometers with a large gap between pole pieces where the specimen holder can be introduced. One of this goniometer is dedicated to Lorentz observations, *i.e.* for a large field of view and/or magnetic studies. A 4k x 4k CMOS camera presenting a high frame rate (One View camera from Gatan) to record the holograms completes the setup. But to be able to measure the phase with an increasing sensibility while keep

a good resolution and improve the ratio signal/noise, some custom technique was developed such as the dynamic control of the microscope (Gatel et al., 2018) and smart acquisition routines (Volkov et al., 2013a).

2.II.B. Automatic Stabilisation by Dynamic Control for Electron Holography

This section was developed in the framework of the thesis of Julien Dupuy, and for more information and a bibliography, please see the related document.

The goal of dynamic control is to compensate in real time for instabilities during the acquisition process in order to increase the signal-to-noise ratio of the phase image by more electrons through longer exposure time. We describe these instabilities and their effects on the hologram, as well as how they can be compensated in real time using feedback loops, allowing us to significantly lengthen exposure times while reducing noise by an order of magnitude.

The signal-to-noise ratio is primarily determined by the contrast or visibility V and the number of electrons collected per pixel N_e/pix, which can be characterised by the phase noise σ_ϕ (2.46), that either directly contributes to the sensitivity and accuracy of the measured quantity:

$$\sigma_\phi = \frac{1}{V}\sqrt{\frac{2}{DQE \times N_e/pix}} \qquad (2.46)$$

where DQE (Detective Quantum Efficiency) is the quantitative efficiency of the detector, defined as the ratio of electrons measured inside the detector compared to electrons received by the detector while the visibility is defined by the equation (2.47).

$$Visibility = \frac{i_{max} - i_{min}}{i_{max} + i_{min}} \qquad (2.47)$$

where i_{max} the maximum measured intensity (maximum of the holographic fringes) and i_{min} the minimum intensity (minimum of the fringes) on the hologram.

The aim is to reduce σ_ϕ, which will improve phase sensitivity. We can increase the number of coherent electrons by improving the characteristics of the microscope and

acquisition conditions, which will increase visibility, or we can do so by increasing the intensity of the source, illumination conditions, and resolving more aberrations. This intensity, which corresponds to an electronic dose per second, must be modulated in relation to the sample being studied in order to avoid degradation. The most natural solution is to increase the exposure time for the same current density. However, excessive exposition times are counterproductive due to residual experimental instabilities during final image acquisition. In off-axis holography, these instabilities are primarily the result of sample drift and interference fringes (mechanical drift of the biprisms). As a result, sample drift degrades spatial resolution, whereas fringe derivation causes a loss of visibility (Figure 2.12) and thus an increase in phase noise, which will oppose and surpass the gain caused by the increase in the number of electrons. These instabilities, which are completely independent of one another in a relatively stable environment, limit exposure times from a few seconds to tens or so seconds (Lehmann and Lichte, 2005).

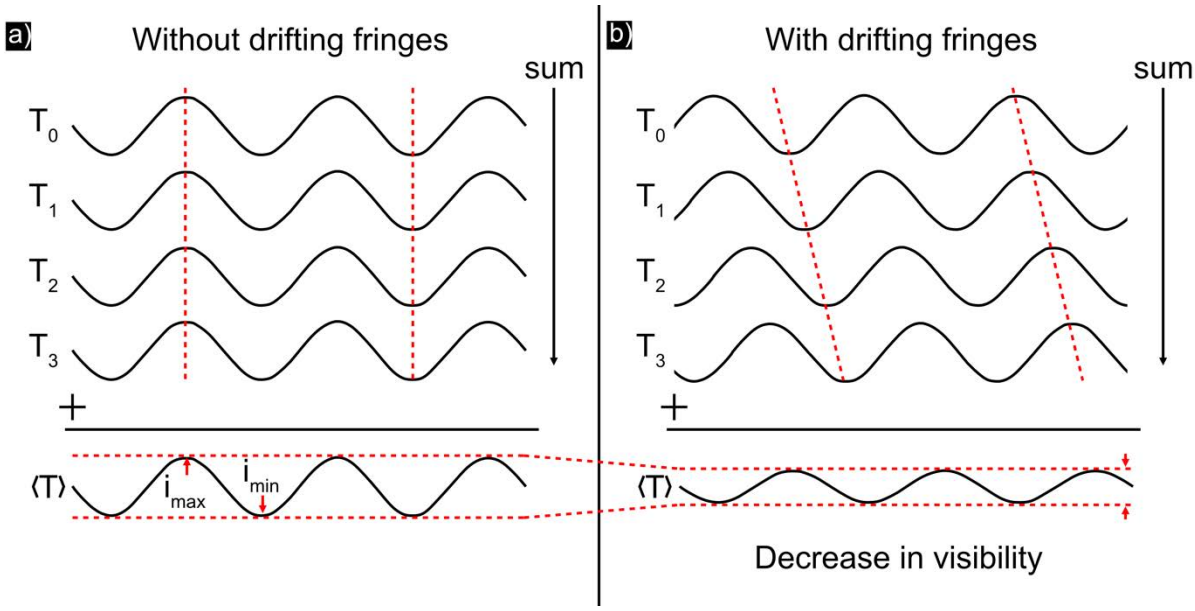

Figure 2.12 : Illustration of the effect of drifting fringes on visibility during the acquisition of a hologram. The fringes on the left do not change over time, and the total hologram has a maximum visibility a) while on the right, the derivation over time reduces the contrast during image addition over time b). Then dotted line allows you to compare the final heights of the two sinusoids.

To obtain a long exposure time or a data set with a high number of collected electrons, the most common method is to record a series of holograms, each with a short

exposure time reducing the effects of instabilities (Voelkl and Tang, 2010). Then each phase images are extracted from holograms before being realigned to overcome the drift and to be summed for a final phase image. However, there are several drawbacks to this approach. Realignment may result in a smaller field of view because only the common part of each image is useful for reconstruction. In addition, the drift associated with the interferometric fringes and the sample must be treated separately because they do not have the same drift, making alignment extremely difficult and resulting in digital artefacts. Furthermore, if we take 4s of exposure per hologram for a total time of 600s, the amount of data to record and process for a series of one hologram is about 10 Go. This approach is thus not really compatible with *in situ* studies that require the acquisition of numerous holograms for each state of the sample (Gatel et al., 2018) or tomography with a series of holograms based on the projection angle.

In order to avoid these consequences, instabilities must be corrected during the acquisition process rather than afterwards. This is accomplished by incorporating a feedback loop into the hologram acquisition process, which will measure the instabilities and will continuously change some parameters of the microscope to compensate them in real time. As previously stated, the instabilities caused by sample and holographic fringes are completely distinct, necessitating the use of multiple independent loops. So, the positions of the fringes are thus controlled by repositioning them with deflecting coils at the level of the gun or condenser lens. Independently, the specimen is mechanically stabilised by controlling the displacement of the goniometer.

The exposure time is thus no longer limited by the microscope instabilities thanks to this correction system, but by the object and its resistance to electronic radiation and contamination. Finally, a unique hologram is obtained from which the phase image can be extracted without the need for sophisticated post-processing on large amounts of data.

Furthermore, controlling the position of the fringes enables the implementation of advanced hologram acquisition or phase reconstruction methods, such as the π-shifting method (Volkov et al., 2013b), which records and subtracts a pair of holograms. This method has the advantage of eliminating the autocorrelation function

and the noise associated with a portion of the camera gain. As a result, the signal-to-noise ratio has risen yet again (Boureau et al., 2018). Then, without resorting to a Fourier reconstruction treatment, phase-shifting can also be used to reconstruct a phase image with a resolution of one pixel.

2.II.C. Extraction of a Phase Image From a Hologram

The formation of holographic interference fringes originates from the overlapping of a reference wave that travels through a reference are (in general vacuum) with an electron wave that crossed the specimen and surrounding fields. If the coherence is high enough, two overlapping of the reference and object waves will produce interference fringes.

To begin, we can express the electron wave function in the image plane as follows:

$$\psi_i(\vec{r}) = A_i(\vec{r})\, e^{[i\phi_i(\vec{r})]} \qquad (2.48)$$

with $\vec{r}$ a two-dimensional vector in the plane of the specimen, *A* and ϕ correspond to the amplitude and the phase while the subscript *i* refer to the image plane. To obtain the intensity distribution, we must square the absolute value of the equation of the amplitude (2.48):

$$I_i(\vec{r}) = |A_i(\vec{r})| \qquad (2.49)$$

The off-axis intensity of electron hologram is defined by the addition of a tilted plane reference wave to the complex specimen wave:

$$I_{hol}(\vec{r}) = \left|\psi_i(\vec{r}) + e^{[2\pi i\overrightarrow{q_c}\cdot\vec{r}]}\right|^2 \qquad (2.50)$$

$$= 1 + A_i^2(\vec{r}) + 2A_i(\vec{r})cos[2\pi i\overrightarrow{q_c}\cdot\vec{r} + \phi_i(\vec{r})] \qquad (2.51)$$

with $\overrightarrow{\boldsymbol{q_c}}$ is the tilt of the reference wave by the two-dimensional reciprocal space vector. The resulting intensity is composed of the intensity of the reference wave, the intensity of the image wave, and a set of sinusoidal fringes with local phase shifts and amplitudes that are exactly equivalent to the phase and amplitude of the electron wave function in the image plane, ϕ_i and A_i, respectively.

So, since the amplitude and phase information are recorded in the hologram, we use the Fourier transform (FT) to extract them from the equation (2.51).

$$FT[I_{hol}(\vec{r})] = \delta(\vec{q}) + FT[A_i^2(\vec{r})] + \delta(\vec{q} + \vec{q}_c) \otimes FT\left[A_i(\vec{r}) e^{i\Phi_i(\vec{r})}\right] + \delta(\vec{q} - \vec{q}_c) \otimes FT\left[A_i(\vec{r}) e^{-i\Phi_i(\vec{r})}\right] \quad (2.52)$$

The first term corresponds to the FT of the reference image, and the second to the bright field, which are centred in the reciprocal space, called the centre band. The FT of the desired image wave function and the complex conjugate of the wave function are represented by the peaks centred at $\vec{q} = -\vec{q}_c$ and $\vec{q} = \vec{q}_c$, respectively, called the side bands (last two terms). To extract the amplitude and phase image from the hologram, we use custom software implemented within the GMS software, as shown on an example in Figure 2.13.

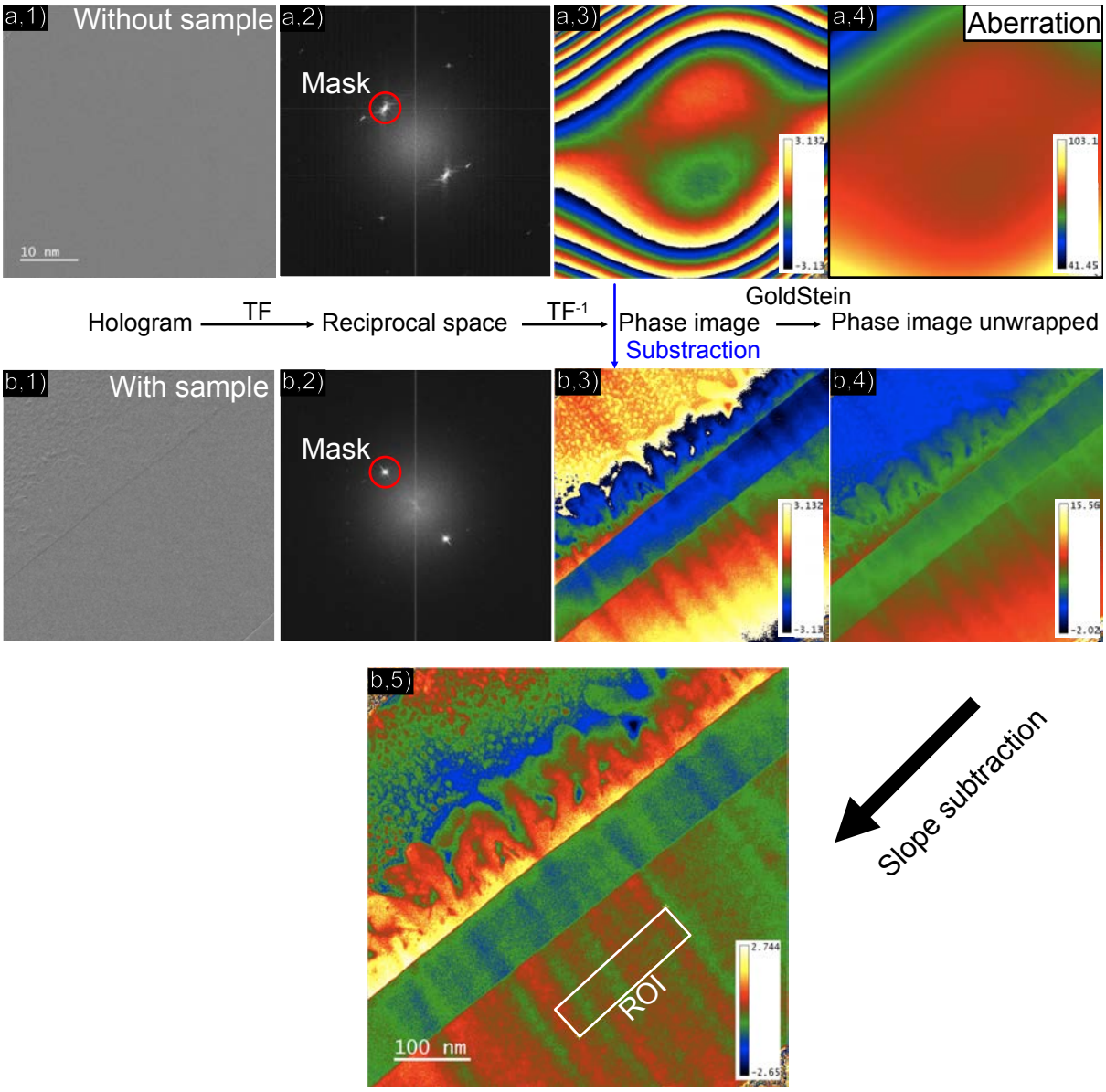

Figure 2.13 : Phase image processing with subtraction of the aberrations.

The phase of the beam electron is also affected by distortions coming from the microscope setup, mainly the distortion of the projector lenses (low-frequency distortion) and the CCD or CMOS camera (low and high frequencies). To remove them, a hologram without any sample is recorded before extracting the phase image which contains only the microscope contribution as shown Figure 2.13(a). For extracting the phase image from the hologram, a FT on the holograms is computed (Figure 2.13(a&b;2)), then a sideband corresponding to the carrier frequency of the fringes is selected by surrounding it by a numerical mask (because of the π-shifting method we

don't see the centre band). The radius of the mask defines the spatial resolution of the phase image but also the signal-to-noise ratio. It is important to note that the choice of this radius is a balance between a nice spatial resolution (larger radius for higher spatial frequencies) and the minimisation of the noise (smaller radius for less noise kept inside the surface define by the mask). The inverse Fourier transform is then calculated from the masked FT after recentring the masked area: the resulting complex image contains both the amplitude image corresponding to the amplitude of the fringes and similar to what will be obtained in conventional microscopy, and the phase image which represents the displacement and the periodicity variation of the fringes compared to a reference area. The phase image is wrapped between $-\pi$ and π by (Figure 2.13(a&b;3)). The microscope distortions are removed by subtracting the phase image in the vacuum Figure 2.13(a,3) from the phase image with the sample Figure 2.13(b,3) (de Ruijter and Weiss, 1993).

Finally, because the phase may have a slope as a result of multiple large-scale interactions that are irrelevant in our case and if the side band is not chosen exactly at the centre of the extracted subregion, a residual tilted plane can be added to the phase image (de Ruijter and Weiss, 1993). An area is chosen to subtract a slope computed by fitting the area. This procedure will not only subtract this slope across the entire image, but because the phase is defined up to a constant, the zero will be set to correspond to the minimum of this area.

This technique enables the study of real samples. In this thesis, we will divide the processing into two complementary parts, grounded study versus bias study. Because the electron beam interacts with the sample, resulting in the formation of a charge density area in the insulating material, we can investigate this extrinsic phenomenon by grounding the capacitor and observing the phase shift. Moreover, using the grounded capacitor we can study the mean inner potential MIP by observing the phase shift depending on the sample geometries. This processing not only allows the study of extrinsic phenomena as well as the MIP but can also be used to extract these effects from the biased sample. To accomplish this, subtract the biased phase image from the grounded phase image, which allows the study of the intrinsic biasing effect.

Finally, by following the procedure for each kind of study (grounded or biased), we can begin to investigate the phase image and try to extract quantitative information using numerical simulations (finite element methods).

3. Finite Element Method (FEM)

3.I. Theory of FEM

The primary aim of finite element method (FEM) nowadays is to convert continuous differential equations that describe complicated linear and nonlinear equations to discrete, finite equations that can be solved by a computer. Many methods for discretising equations were invented throughout history, beginning with the work of Fermat and Benrnoulli in the year 1700 with the calculus of variation.

Many years later, the Galerkin method was invented, the principle of which is to approach the solution with the sum of simple function and trial function. The issue is how much each function contributes to the solution. As a result, we must compute a coefficient that multiplies each function while minimising the system energy. However, because Galerkin does not have access to a computer at this time, he is forced to guess with functions that are very close to the solution.

Nowadays, the power of our computers allows us to compute thousands of thousands of trial functions, so we can use very simple functions like the top-hat function. FEM is widely used in many fields of engineering and physics, such as the strain, fluid, and electromagnetic domain calculus, to solve many complex problems that would be impossible to solve otherwise.

3.II. Equations and Meshing

The problem that will be extensively developed during this thesis is the use of the equation of Poisson to solve complex problems in order to interpret experimental data of electrostatic components studied with electron holography. We can write the equation of Poisson in a more general form (2.53), known as the strong form. In general, we can set different values on the domain boundary, but for simplicity, it will be set at zero like the potential at infinity of a general electrostatic problem.

$$-\Delta u = f \ in \ \Omega$$
$$u = 0 \ on \ \partial\Omega \qquad (2.53)$$

The function u is the one we want to solve; it can be a dependent variable such as stress, pressure, electric potential, and so on. To solve this equation in the discrete domain, we must first convert the equation (2.53) to an equivalent formulation known as the weak form or variational form.

Equation (2.53) remains valid when multiplied on the right with a test function φ from $H_0^1(\Omega)$, a Hilbert space that essentially extends linear algebra methods by generalising the concepts of Euclidean space (usual (3D) space) and Hermitian space (complex space) to any dimension (finite or infinite). To deal with any dimension, we must define how the scalar product evolves within multiple dimensions (2.54):

$$(v, w) := \int_{(0,1)} v(x)w(x)dx \qquad (2.54)$$

Where v and w are two functions define inside the function space V:

$$V := \begin{Bmatrix} v | v \in \mathbb{C}[0,1], \ v' \text{is piecewise continuous and bounded on } [0,1], \\ v(0) = v(1) = 0 \end{Bmatrix} \qquad (2.55)$$

This space contains all continuous or piecewise continuous and bounded derivative functions on the closed interval from $[0,1]$, and these functions must also satisfy the boundary conditions at the boundary of the domain. To continue, after multiplying the equation (2.53) by a test function φ, the equation remains valid when integrated over the domain.

$$-\int_\Omega u''\varphi \, dx = \int_\Omega f\varphi \, dx \ ; \ \forall \varphi \in V \qquad (2.56)$$

We can use the boundary condition and integrate by parts (2.56) to find the equation (2.57):

$$\int_\Omega u' \, \varphi' dx = \int_\Omega f\varphi \, dx \qquad (2.57)$$

And, using the notation just introduced, the equation above can be rewritten:

$$(u', \varphi') = (f, \varphi) \qquad (2.58)$$

To allow for a computable solution, the physical domain must be spatially discretised. We can define a finite element in it that is a triple (K, P_K, Σ) with K being an element, P_K being polynomials on K, and Σ is a set of degrees of freedom (DoF). We can define

a finite dimensional subspace V_h (2.59) to reduce the infinite dimension of space V. Which consists solely of polynomial functions on each mesh element K.

$$V_h = V_h^k := \{v \in \mathbb{C}[0,1] | v|_{K_i} \in P^{(k)} \text{on each } K_i\} \quad (2.59)$$

We want a unique representation and use the basic functions to build its unique representation:

$$v_h(x) = \sum_{i=0}^{h} v_j \varphi_j(x) \; ; {V_h}^{(1)} \; with \; v_j \in \mathbb{R} \quad (2.60)$$

The basis function φ_j(2.61), which is a hat function, describes the trial function v_h. However, more complicated functions, such as quadratic polynomials, can also be used as basis functions.

$$\varphi_j(x_i) = \begin{cases} 1, i = j \\ 0, i \neq j \end{cases} \quad (2.61)$$

A representation of the sum of this function is shown in Figure 2.14. The goal is to find the best coefficient for each hat function that will participate in the solution to construct a good trialfunction combination. Despite meshes usually being in two or three dimensions, the following examples will be in 1D.

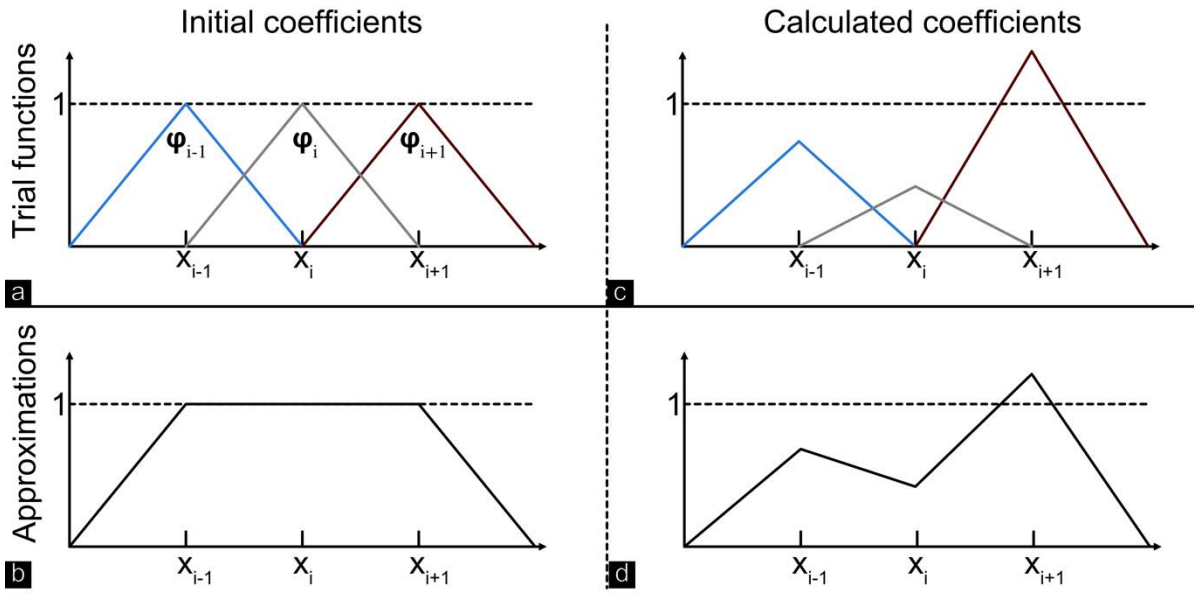

Figure 2.14 : Representation of the starting hat function (a) and the approximating function (b), followed by an adaptation of the hat function coefficients to minimise energies (c) and the resulting function (d).

Figure 2.14 depicts how the hat function is assembled and how the effect of changing the coefficient allows for the creation of an approximate solution. We begin with the coefficients all equal to one in Figure 2.14(a), followed by the sum of the trial function that results in a function that respects the boundary condition in Figure 2.14(b). The hat function coefficients are then calculated iteratively to minimise energies on Figure 2.14(c) used to fine-tune the best solution approximation Figure 2.14(d). Intuitively, we can see that as the distance between the meshes decreases, the solution will be approached more effectively.

The meshing can be complex and of various types, but there are two types that are the basis elements onto which all other finite elements are built, which are triangular or quadrilateral. The triangular one was chosen for solving the model for this thesis because it supports adaptative mesh refinement Figure 2.15, which allows us to change the size of the meshing based on the geometry and will be exploited on the next chapter. To study the electronic devices on this thesis we used Comsol Multiphysics which is a commercial software used to simulate physical phenomena using the FEM theory.

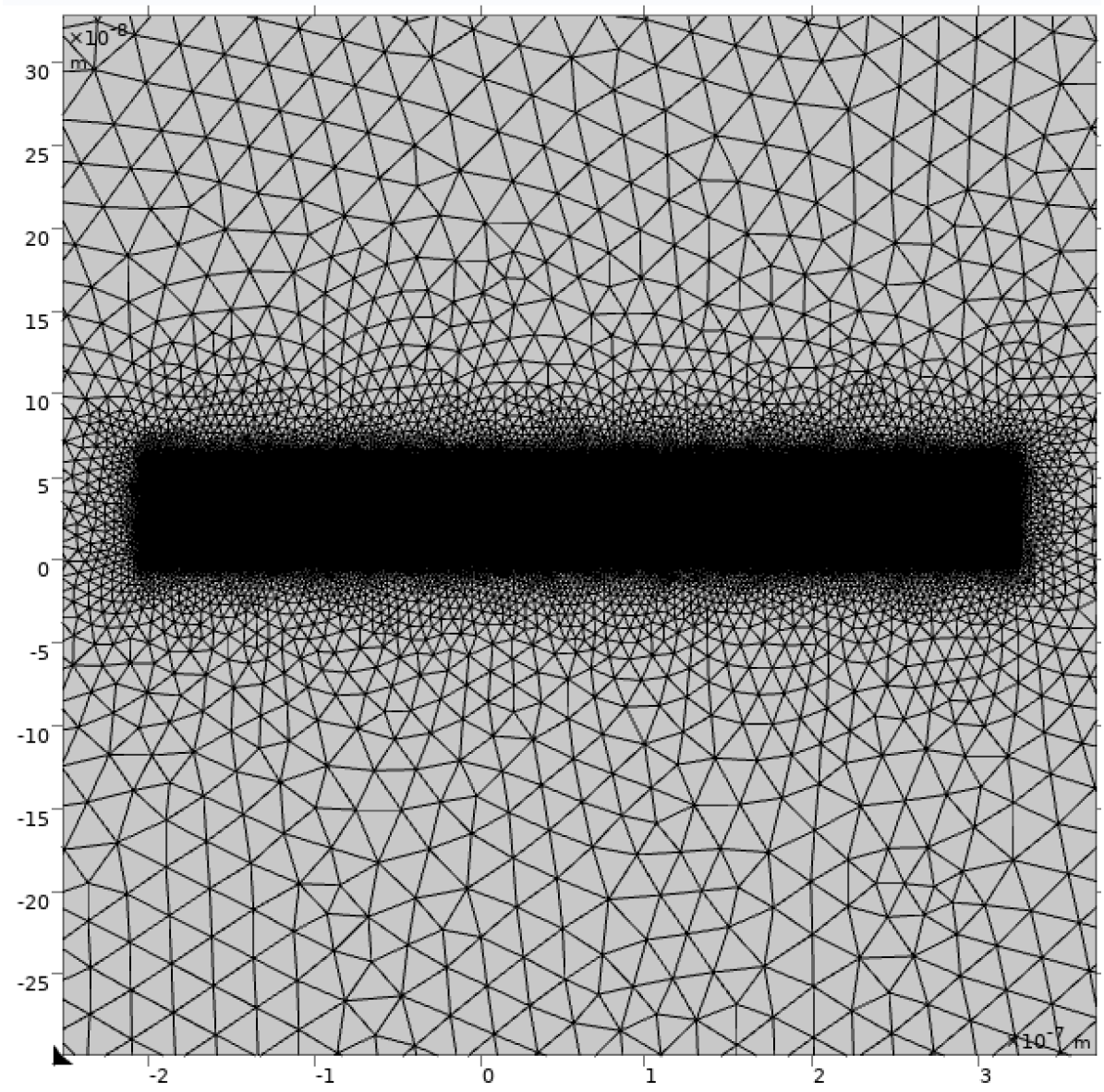

Figure 2.15 : Example of adapting triangular mesh inside the COMSOL interface

To proceed, I show a method for calculating this trial function, and each integral will be detailed step by step. Instead of the infinite dimensional space V, we want to solve the weak form with a discrete function space V_h.

$$(u_h', \varphi_h') = (f, \varphi_h)\ ;\ \forall \varphi_h \in V_h \qquad (2.62)$$

We can insert the decomposition (2.60) with the hat function into the discrete weak form equation:

$$\left(\left(\sum_{j=1}^{n} u_j \varphi_j\right)', \varphi_h'\right) = (f, \varphi_h)\ ;\ \forall \varphi_h \in V_h \qquad (2.63)$$

Because the derivative is linear, we can extract the summation from the scalar product:

$$\sum_{j=1}^{n} u_j \left({\varphi_j}', \varphi_h'\right) = (f, \varphi_h)\ ;\ \forall \varphi_h \in V_h \tag{2.64}$$

We can also decompose φ_h into its basis functions φ_i.

$$\sum_{j=1}^{n} u_j \left({\varphi_j}', \varphi_i'\right) = (f, \varphi_i)\ ;\ \forall\ 1 \leq i \leq n \tag{2.65}$$

The matrix notation can be used to better understand the upper equation:

$$\underbrace{\begin{pmatrix} ({\varphi_1}', \varphi_1') & \cdots & ({\varphi_1}', \varphi_n') \\ \vdots & \ddots & \vdots \\ ({\varphi_n}', \varphi_1') & \cdots & ({\varphi_n}', \varphi_n') \end{pmatrix}}_{=A} \underbrace{\begin{pmatrix} u_1 \\ \vdots \\ u_n \end{pmatrix}}_{=U} = \underbrace{\begin{pmatrix} (f, \varphi_1) \\ \vdots \\ (f, \varphi_n) \end{pmatrix}}_{=F} \tag{2.66}$$

To fine-tune the vector $\vec{\boldsymbol{U}}$, we must solve this linear system. However, we must first evaluate a large number of integrals. To simplify, we will resolve the 3×3 sub-matrix of $\boldsymbol{A}$ called $\tilde{\boldsymbol{A}}$:

$$\underbrace{\begin{pmatrix} ({\varphi_{i-1}}', \varphi_{i-1}') & ({\varphi_{i-1}}', \varphi_i') & ({\varphi_{i-1}}', \varphi_{i+1}') \\ ({\varphi_i}', \varphi_{i-1}') & ({\varphi_i}', \varphi_i') & ({\varphi_i}', \varphi_{i+1}') \\ ({\varphi_{i+1}}', \varphi_{i-1}') & ({\varphi_{i+1}}', \varphi_i') & ({\varphi_{i+1}}', \varphi_{i+1}') \end{pmatrix}}_{=\tilde{A}} \underbrace{\begin{pmatrix} u_1 \\ \vdots \\ u_n \end{pmatrix}}_{=U} = \underbrace{\begin{pmatrix} (f, \varphi_1) \\ \vdots \\ (f, \varphi_n) \end{pmatrix}}_{=F} \tag{2.67}$$

Where the integrals can be solved on the domain $X_{i-1}\ to\ X_{i+1}$ of a length of h.

From the sub-matrix, I will describe each integral step by step:

$$\begin{aligned} &\int_{x_{i-1}}^{x_{i+1}} {\varphi_i}'(x), \varphi_i'(x) dx \\ &= \int_{x_{i-1}}^{x_{i+1}} \frac{1}{h^2}\, dx + \int_{x_i}^{x_{i+1}} \left(-\frac{1}{h}\right)^2 dx = \frac{2}{h} \end{aligned} \tag{2.68}$$

For the diagonal value of the matrix:

$$\begin{aligned} &\int_{x_{i-1}}^{x_{i+1}} {\varphi_i}'(x), \varphi_{i+1}'(x) dx \\ &= \int_{x_i}^{x_{i+1}} -\frac{1}{h}\left(\frac{1}{h}\right) dx = -\frac{1}{h} \end{aligned} \tag{2.69}$$

Then we want to compute the intermediate diagonal value of the matrix:

$$\int_{x_{i-1}}^{x_{i+1}} \varphi_{i-1}'(x), \varphi_{i+1}'(x) dx = 0 \tag{2.70}$$

Because these functions do not share any interval spatially for non-zero functions, their product is zero.

Even though the physics is $f = \frac{\rho}{\varepsilon_0}$, we choose $f = -1$ for this example because it has no effect on the mathematics behind FEM.

$$(f, \varphi_i) = -1 \int_\Omega \varphi_i \, dx = -h \tag{2.71}$$

So, at the end the sub-matrix can be written as:

$$\underbrace{\frac{1}{h}\begin{pmatrix} 2 & -1 & 0 \\ -1 & 2 & -1 \\ 0 & -1 & 2 \end{pmatrix}}_{=\tilde{A}} \tag{2.72}$$

Then we can generalise while keeping the boundary of the system in mind, and finally we can write the matrix A:

$$\underbrace{\frac{1}{h}\begin{pmatrix} 1 & -1 & 0 & & & 0 \\ -1 & 2 & -1 & & & \\ & \ddots & \ddots & \ddots & & \\ & & 2 & & & \\ & & -1 & 2 & -1 & \\ 0 & & & 0 & 1 & \end{pmatrix}}_{=A} \tag{2.73}$$

or also with the definition of the scalar product:

$$(f, \varphi_i) = h(0, 1, \dots, 1, 0)^T \tag{2.74}$$

We can manually compute the 1D solution with that, but for more complex problems or with other test functions, the integrals cannot be done by hand. To accomplish this, we employ numerical quadrature (numerical integration) in the FEM code, with a high level of integration selected to avoid as much numerical error as possible.

To compute the model, we want to study it in 3D and its equivalent from a symmetry simplification that gives the 2D model, we obviously use FEM in higher dimensions.

Each model can then be compared to the experimental data using the equation (2.42), which gives the phase representation in 2D and 1D, respectively. The equation is calculated internally by projecting the estimated potential data along the z-axis, which represents the integral component, and multiplying the result by the constant C_E, which is determined from (2.45) and depends on the electron velocity.

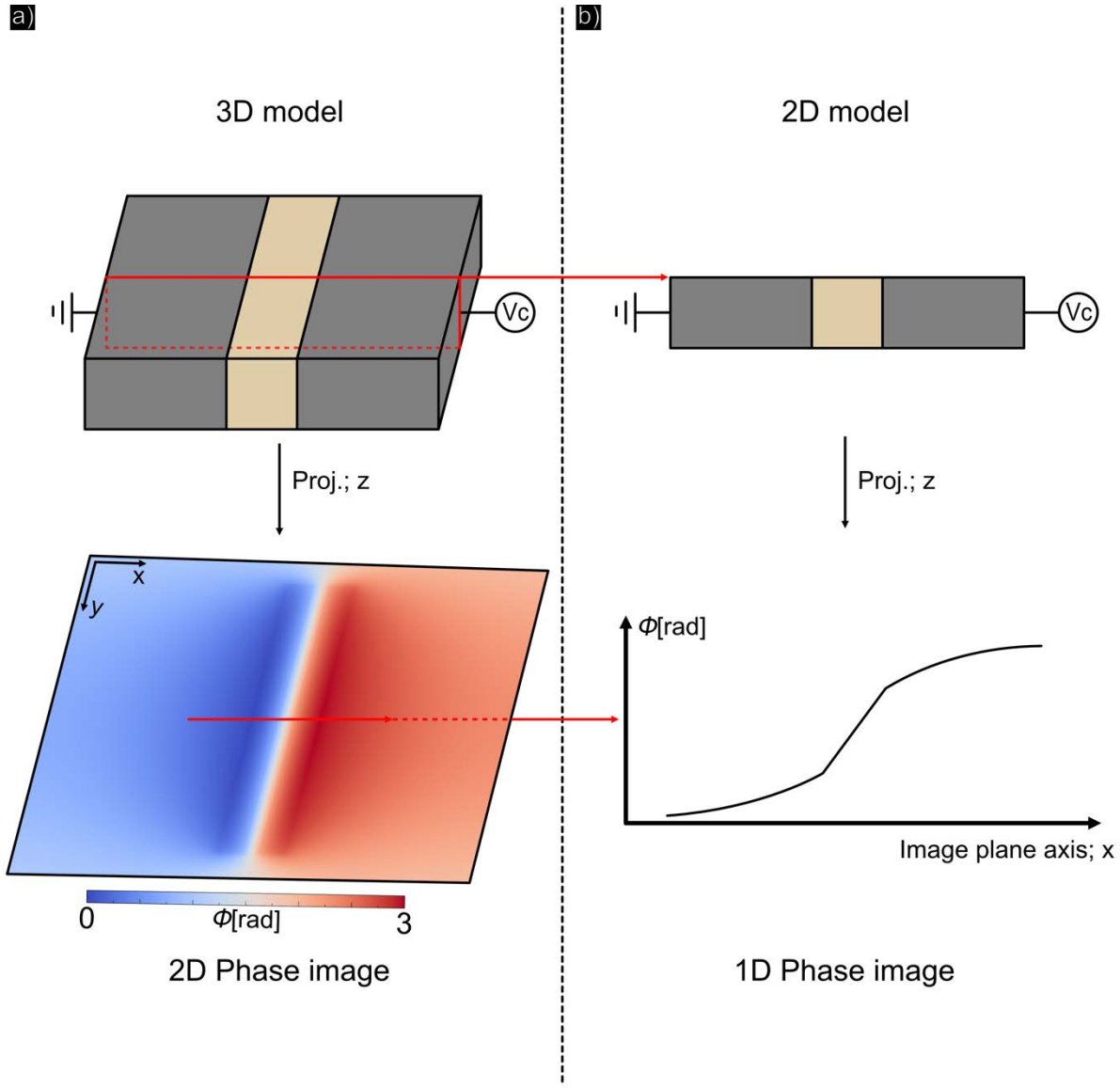

Figure 2.16 : The results of the phase projection using the 3D model (a) and its equivalent in 2D (b) are both 1 V biased.

For example, to adapt the previous calculus to higher dimensions, the simplest method is to compute the tensor product of the one-dimensional basis with itself to obtain the two-dimensional basis (2.75) and so on. In the case of a two-dimensional plan (x, y):

$$\begin{aligned} \varphi_1^{1D}(x) &= x \\ \varphi_1^{1D}(y) &= y \\ \varphi_{1,1}^{2D}(x) &= \varphi_1^{1D}(x) \cdot \varphi_1^{1D}(y) \end{aligned} \qquad (2.75)$$

However, if the system becomes too large, the matrices will be impossible to solve, so the matrix is usually solved using an iterative method and a good preconditioner.

To take it a step further, the FEM method can also be discretised in time using time-stepping schemes. The Newton method is a good method to use when the PDE also contains nonlinearity. MUMPS, which stands for **MU**ltifrontal **M**assively **P**arallel **S**pace direct solver, is the solver used in this thesis; it is a collection of multiple "attacks" designed to solve the matrix.

3.III. Boundary Conditions and Simulation Box.

To solve the potential, the shared variable *V* is calculated from a model that is divided into two main parts: the capacitor and the external medium. The first part uses two distinct solvers to simulate the conducting and insulating areas, respectively the law of Ohm (2.76) for induction (i.e. conductive areas) and the law of Gauss (2.77) for electrostatics, while the second part (the external medium) uses only electrostatics.

$$-\nabla \cdot d\left(\sigma \nabla V - \overrightarrow{J_e}\right) = dQ_j \qquad (2.76)$$

σ : conductivity S/m ; $\overrightarrow{J_e}$: external current density (injected) A/m^2 ; Q_j : current source.

$$-\nabla \cdot d\left(\varepsilon_0 \nabla V - \vec{P}\right) = \rho \qquad (2.77)$$

ε_0 : vacuum permittivity F/m ; $\vec{P}$: electrical polarisation vector; ρ : space charge density C/m^2 ; d : thickness of the plane.

To optimise and limit the box effects on FEM calculations, the conditions at the edges of the domain have been set to infinity (Figure 2.17, blue domain). The infinite domain is created by virtually enforcing a very large distance between the nodes that comprise the domain mesh, resulting in a system size that is nearly infinite. To be more specific, the domain will be enlarged by a characteristic size determined by multiplying a diagonal of an imaginary box containing the entire geometry of the model by 100.
Using such distances in the model reduces numerical errors by limiting edge effects while preserving simulation time results by limiting simulation box size, resulting in a better overall solution. The "infinite layer" is calculated on a square mesh (mapped), which is specific and optimised for this type of infinite calculation.
Because the sample will be studied *in situ* by biasing it, we must explain how we will incorporate this effect into the FEM simulation. The electrical conditions are imposed at the electrode extremities using boundary conditions, with the grounded part equalling $V = 0$ and the applied potential equalling $V_c = V$, so that the potential is

spread inside the electrodes as far as the dielectric and through the vacuum around by the shared variable V between the two solvers.

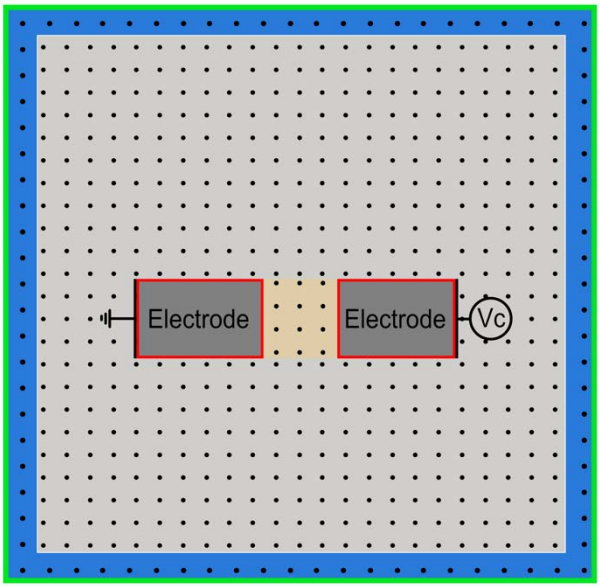

Figure 2.17 : External boundary conditions are shown in green, and the infinity domain is shown in blue; the metallic part is solved by the induction while the remainder is solved by the law of Ohm (dotted areas).

Because the two electrodes are considered to be metallic, they are relevant areas for induction physics, and the remaining area is computed using the law of Ohm, implying that we have the coexistence of two solvers to solve two distinct types of physics. This is significant because we want to be able to study conducting areas with insulating areas that can continue to charge even if we solve with the stationary solver. We accomplish this by sharing the variable V between the two solvers, but there are additional conditions between the two domains implied by the calculation in terms of the important parameters.

The boundary conditions between these two domains can be described by, on the one hand, $\vec{n} \cdot \vec{J} = 0$ for the induction and, on the other hand, $\vec{n} \cdot \vec{D} = 0$ for the law of Ohm. So, at the interface we have $\vec{n} \cdot \vec{J} = \vec{n} \cdot \vec{D}$ if projected onto the normal $J_z = D_z$ knowing that $J_z = \sigma E_{1z}$ and $D_z = \varepsilon_0 \varepsilon_r E_{2z}$ this gives the interface conditions $\frac{\sigma}{\varepsilon_0 \varepsilon_r} E_{1z} = E_{2z}$.

We can also check if the interface conditions discussed at the beginning of the chapter (2.11) are being met qualitatively by calculating the potential created by charging the dielectric and examining its derivative (Figure 2.18).

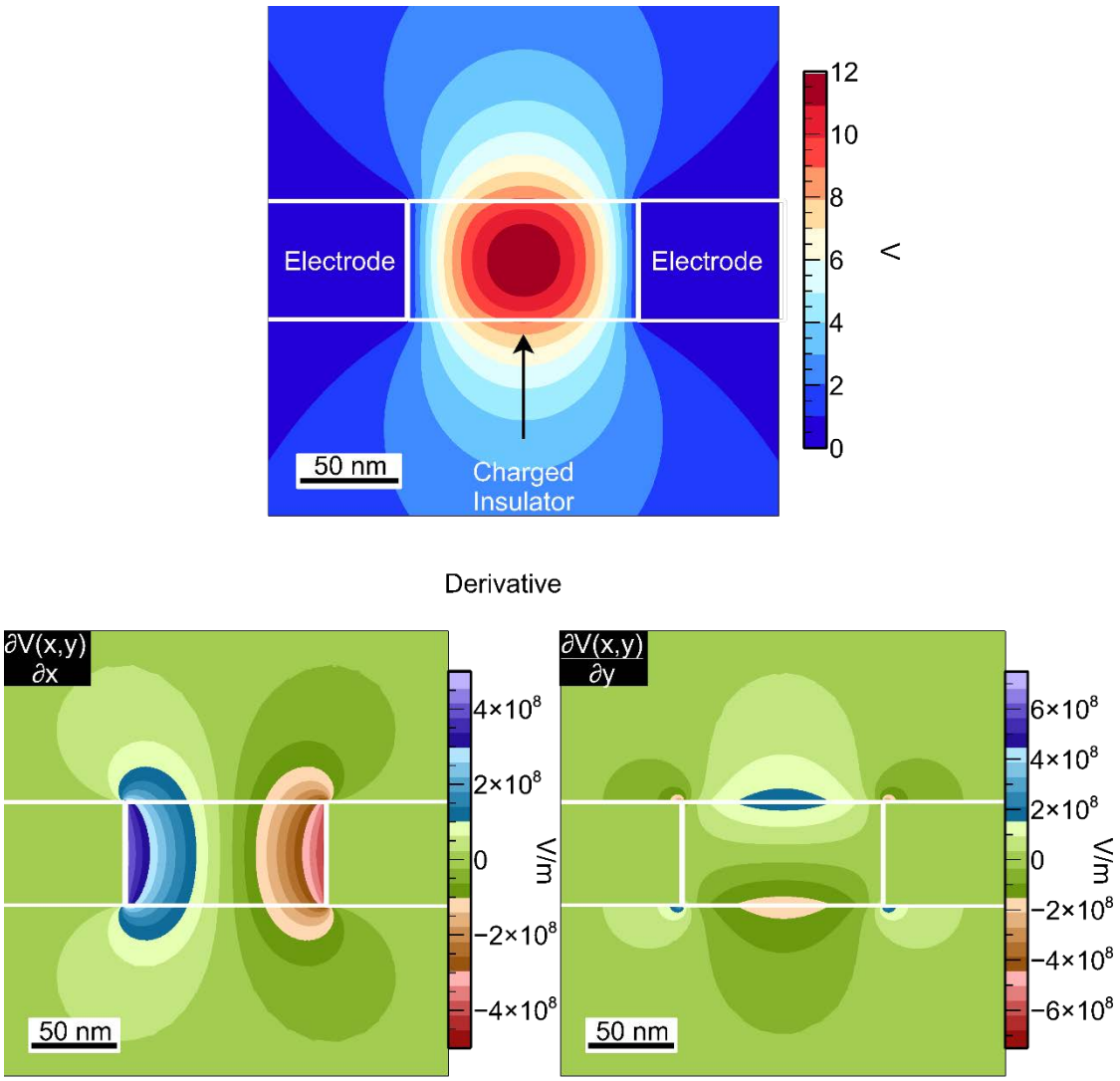

Figure 2.18 : Potential of a charged capacitor with epsilon equal to 1 and its derivation in relation to the x and y axes.

This calculation is a test model, so I chose the permittivity of the dielectric to equal that of the vacuum. The derivative with respect to the axes x and y shows that the matching condition of $\vec{D}$ is met, i.e. the field does not change at the interface between the void and the dielectric.

As a result, I confirm that, for the same permittivity, the electric field is continuous through the interface between the dielectric and the vacuum medium. However, as permittivity increases, as shown in Figure 2.19 for all dielectrics used in microelectronics, this is no longer true.

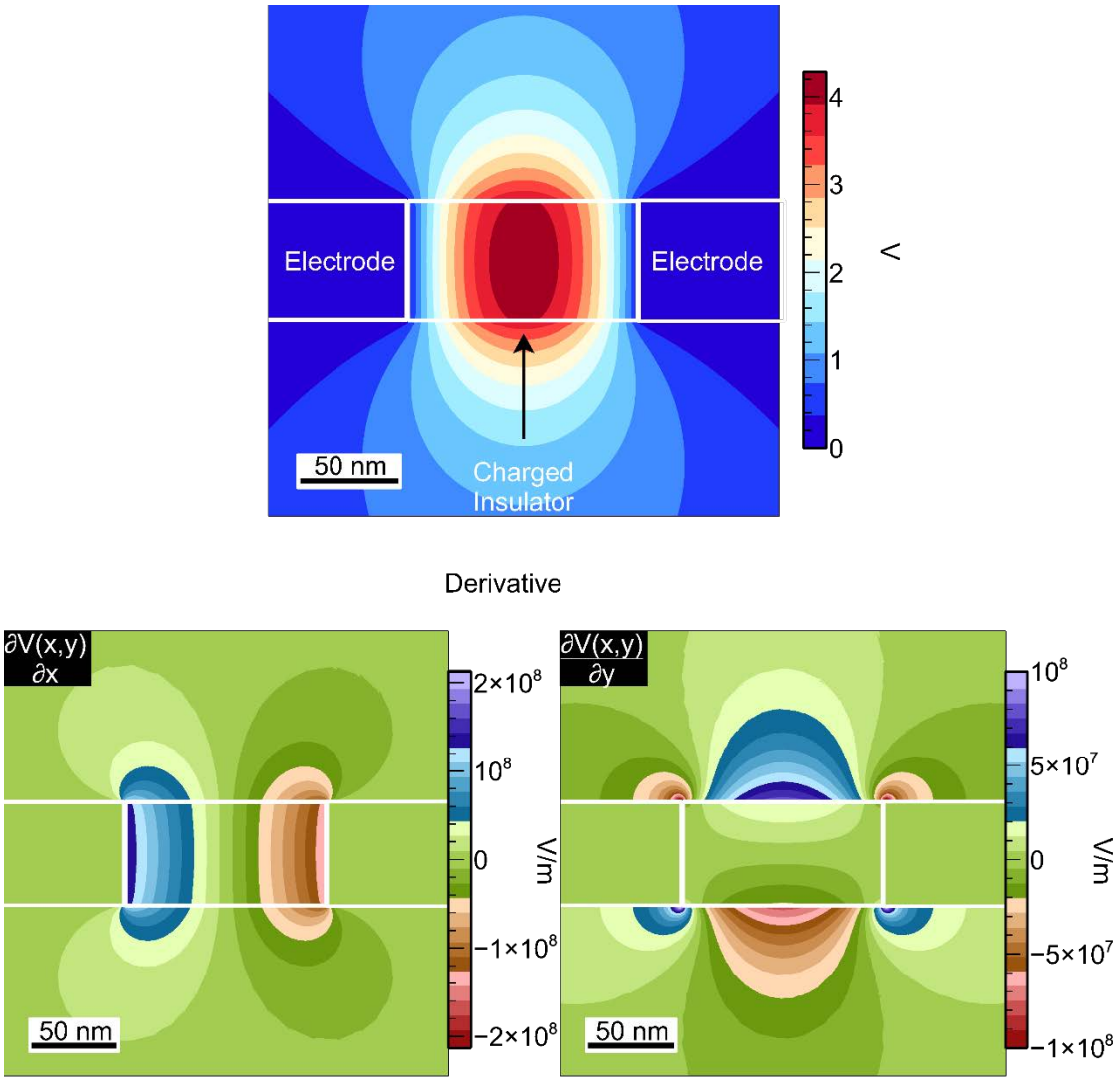

Figure 2.19 : Potential of a charged capacitor with epsilon equal to 3.9 and its derivation in relation to the x and y axes.

A difference in permittivity causes a modification of the field along the normal axis, as shown by the curvature at the interface between the dielectric and the vacuum medium on the potential image and on the different derivative images. Compared to

the Figure 2.18 with a permittivity equal to the vacuum, we clearly see the effect of the different permittivity.

I then examined the effect of conducting layers on the top and bottom of the capacitor model, which have a theoretical infinite permittivity (metallic) while the dielectric has a permittivity of about 3.9. (Figure 2.20).

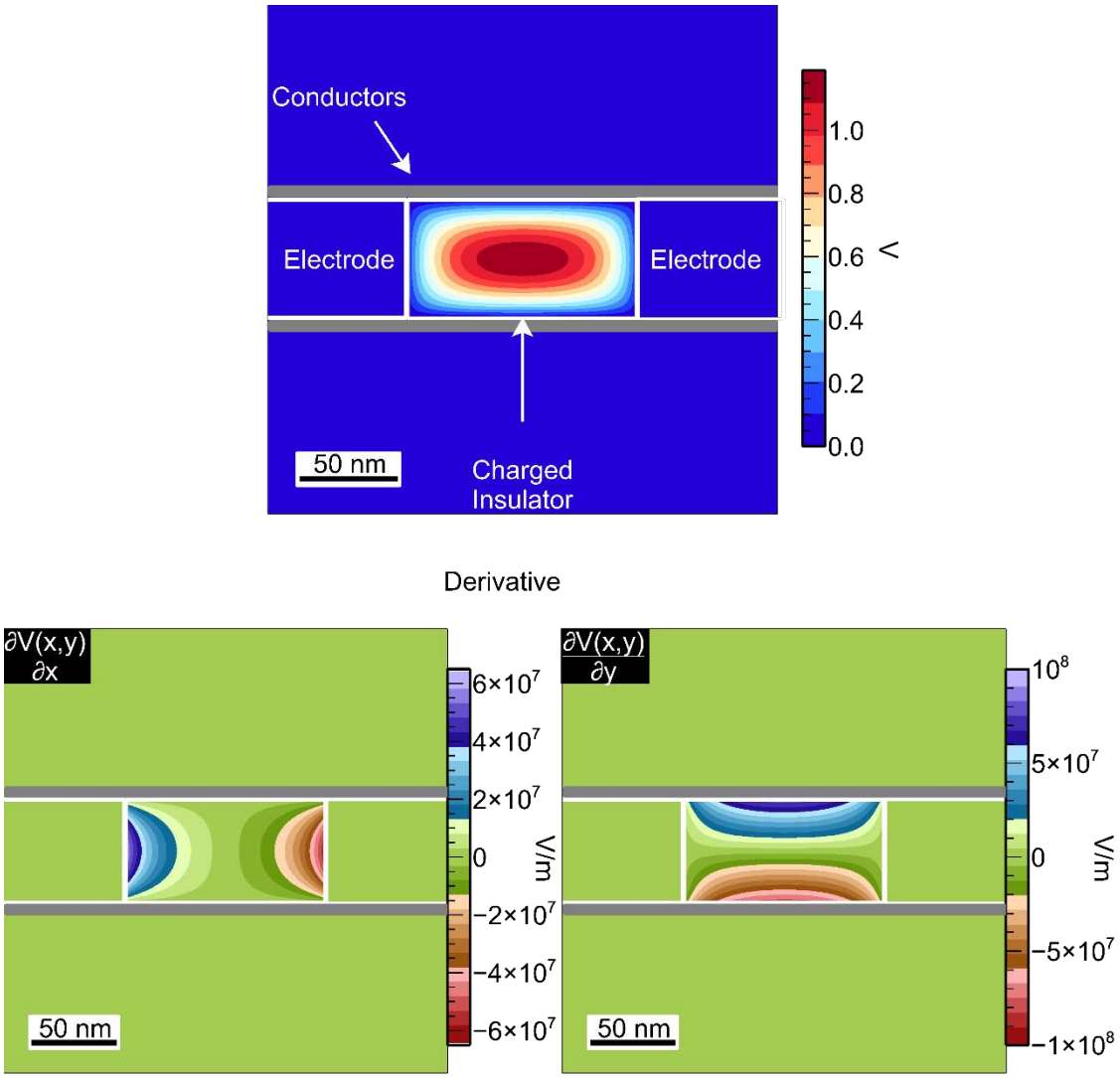

Figure 2.20 : Potential of a charged capacitor with epsilon equal to 3.9 and its derivation in relation to the x and y axes.

When a conductor is placed on top of and beneath the capacitor, the field does not penetrate the conductor and is confined. Any field produced by the conductor surrounding the capacitor in response to the charges in the dielectric is screened by

the charges brought by the electrodes connected to the ground. As a result, the conducting layers function as a Faraday cage.

4. Automatic Holographic Data Interpretation

The model initially constructed never fits the experimental data perfectly. The parameters must be adjusted until a satisfactory agreement is found between the simulations and the experiment. Indeed, this is the most time-consuming part of modelling. For the work presented here, this procedure was mostly carried out "by hand" i.e. by manually changing the parameters until a decent fit could be found. This can be extremely tedious and slow, so I also developed over the course of my thesis a more automated method. The more laudable aim is to remove as much human bias as possible from the fitting process.

To this aim, I wrote codes that allows the use of finite element software through Python and compare automatically the simulated results with the experimental. I will go over the two methods I use to automate the calculation, as well as an artificial intelligence-based method that, while much faster than finite elements, raises new questions about the definition of uncertainties associated with these methods.

4.I. Automatic Fitting Routine

4.I.A. Batch Control Software

I wanted to give us more flexibility and control over how we analyse electron holography data with COMSOL FEM simulations. The flexibility in how we can explore the space parameter in a more customised way and control for the fitting part allows us to explore the space parameter in a directed manner "on the flow" by analysing the result of the calculus in real time at each loop thus finding the next better-fitting parameters.

Python was chosen to carry out the control for a number of reasons, including the fact that it is quick to develop and create prototypes, making it ideal for research that it has a large ecosystem that includes a large number of powerful and recognised libraries for scientific computing, and that it is a popular language with a large

community. Finally, because I use macOS, I prefer multiplatform software, which allows better diffusion especially inside the Linux and Windows communities.

The connection between Python control and COMSOL is divided into two parts: sending parameters to COMSOL from Python and recovering the COMSOL solution. The first is achieved by utilising Subprocess Library of Python, which allows us to create a pipe to a shell that will send data to COMSOL via bash using the batch mode of COMSOL.

Second, I set up the COMSOL software to export the calculated solution to a Text File, which I then recovered using ReadLines() method of Python once the calculations were complete (Figure 2.21). As a result, we can use Python to create anything we want and have a calculation engine on the back end.

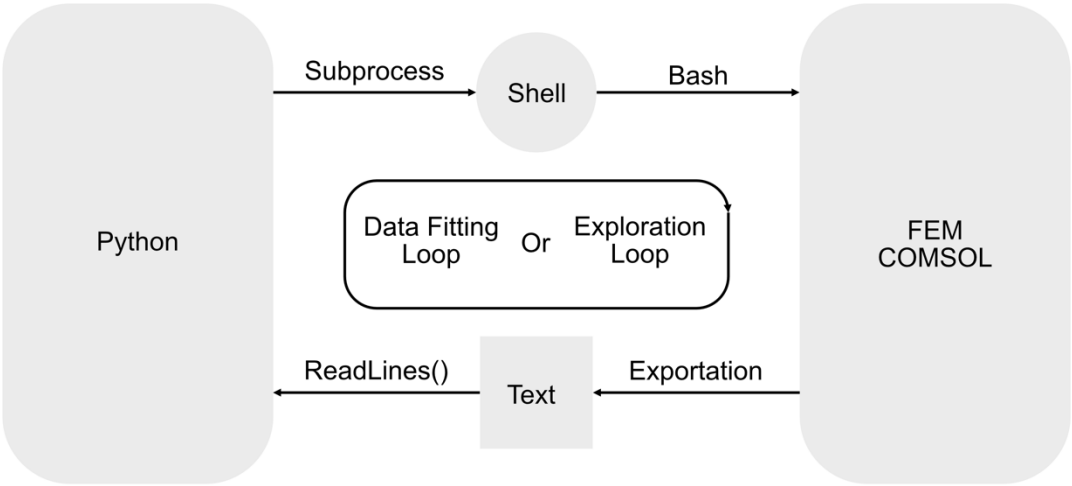

Figure 2.21 : Communication schematic between Python and COMSOL.

This development served as the foundation for many other developments, including the Data Fitting loop, in which parameters were adjusted algorithmically in an iterative manner using the Trust Region Reflective method to fit with the experimentally measured phase shift (Branch et al., 1999). Alternatively, if the space parameter has a large number of solutions, such as many local minimums, we can use Differential Evolution to solve the fitting problem (Storn, 1997). By using an exploration loop on predefined parameters, I was also able to build a database or better characterise the model with this code.

4.I.B. Trust Region Reflective Method

The automatisation of the fitting problem addresses two major issues with the fitting problem: on the one hand, we want a faster fit, and on the other, we want to be able to analyse the uncertainties. So, to accomplish this, I combine the previous developments on COMSOL control with the Trust Region Reflective method implemented within SciPy (Virtanen et al., 2020). The algorithm is an iterative process that results in successive improvements. The algorithm currently performs a shift obtained by minimising a simple model of the function (e.g., quadratic) over a confidence region usually a ball whose radius is called the confidence radius of the model. The confidence radius is adjusted so that the function decreases sufficiently at each iteration while remaining small enough to keep the simple model valid. The proposed method is an efficient method for solving large bound-constrained minimisation problems (Branch et al., 1999).

This method has the advantage of allowing the calculation of the covariance of parameter fitting. Then, using this method and others from the GUM Guide to the Expression of Uncertainty in Measurement, we can quantify the uncertainty of the measure by fitting the experimental data.

But, before testing the method of experimental data, I perform what I call a self-consistence test, in which I take a phase profile from a simulated model and modify only one parameter, the conductivity of the model, to see if the algorithm can retrieve the initial parameter. I tested it on a simple model with a conductive layer (Figure 2.22).

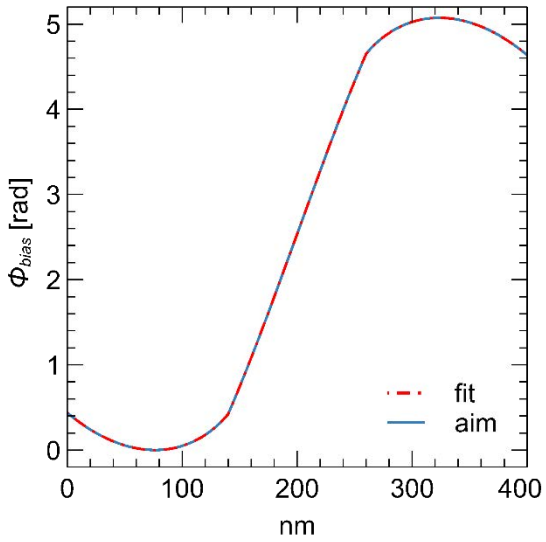

Figure 2.22 : The sigma parameter is used in a self-fitting test.

The fit is perfect and the algorithm was able to recover the exact value of the initial model, resulting in self-consistency. During the chapter on uncertainties, this algorithm will be tested on experimental data.

However, if we want to extend the fitting process with multiple parameters depending on the parameter chosen, the convergence is poor because some parameters, such as sample thickness with the bias or the layers conductivity, are highly correlated, implying that the algorithm can fit with incorrect parameters because the fitting process can become stuck inside a local minimum.

To avoid this, we can explore the parameter space with multiple start combinations at the same time. For this, I use Differential Evolution algorithm, which will explore the space parameter with multiple start points, and then combine these multiple start points with statistical rules to find the global minimum more efficiently.

4.I.C. Differential Evolution

Differential Evolution is stochastic in nature (Storn, 1997), which means it does not use gradient methods to find the minimum, and while it can search large areas of candidate space, it frequently necessitates more function evaluations than traditional gradient-based techniques.

The idea behind this algorithm is to start with a population of randomly chosen parameters, then randomly choose two members of that population, and their

difference is used to mutate the best member that is closest to the solution. This calculus is repeated at each loop named period of the calculation, and if the solution is better with the mutated one, it replaces the original member, and so on until the solution is within the defined range.

This allows for the exploration of many more parameters than the Trust Region Reflective method, which is a gradient base method, and thus allows for better parameter exploration, which is useful for scaling up the number of parameters used to fit the model at the expense of time in convergence.

Unfortunately, it does not provide access to the correlation matrix, which is critical for determining uncertainty. So, the technique is to combine these two techniques in order to explore a large space of parameters and find inconsistencies. To do so, I use the Differential Evolution solution as the initial parameter for the Trust region reflective method, thereby exploiting the incertitude associated with it.

4.II. Artificial Intelligence (Tensorflow)

There are many ways to solve a physical problem with electron holography, such as analytical or simulation for the quantification of potential or charging, but the first does not solve complex geometry and the second is very time consuming. Another way is to use AI to tackle this problem as it is a very fast solver and can have a really good sense of approximation.

There are several approaches to AI, including machine learning, which attempts to extract the rule of a problem using some algorithm, and deep learning, which is in reality a complex fit of data with a lot of parameters. We chose to develop the second method due to good results for process images and the fact that at the end we need a data fit.

To perform deep learning, we employ a neural network, which is a network of interconnected artificial neurons that allows complex problems to be solved by adjusting weighting coefficients during the learning phase. Neural networks were originally inspired by the human nervous system in the brain. The neural network can modify itself based on the outcomes of its actions, allowing for learning and problem solving without the use of algorithms rules and thus without traditional programming.

Our brains can handle vision, speech, and pattern recognition problems efficiently. All of these seemingly simple tasks for the human mind are in fact extremely complex for a computer.

Before delving into a neural network, it is critical to understand how one of these neurons, referred to as a perceptron in deep learning, works. The perceptron is analogous to a data-driven operator in that it includes an algorithm for classifying data in a linear complexity problem by using an activation function that sums all input values multiplied by their corresponding weights (Figure 2.23):

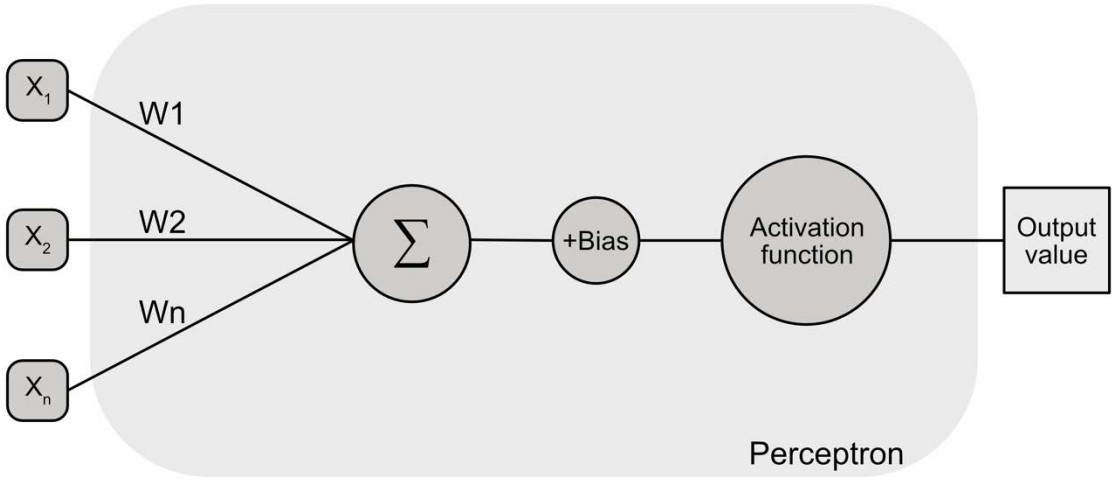

Figure 2.23 : A perceptron scheme with input values and its internal operation.

To begin, in this simplified diagram, we have inputs labelled x_1, x_2 until x_n. These inputs are multiplied by their respective "weights", W_1 and W_2, and the connections between the inputs and the weights connect the inputs to the neuron core. What happens inside the perceptron is entirely mathematical; it multiplies the inputs by the weights connected to them and then adds them all up. Then a shift is performed by adding a constant to the results known as bias; while the basic idea of the perceptron does not have a bias, it is useful for understanding the next section to introduce this notion with the perceptron.

The bias gives us control over the sensitivity of neuron excitation, which corresponds to a shift in the activation function on the x-axis. The result of summing the inputs, multiplying them by their weights, and adding the bias is an activation function.
The most common type of activation function is the sigmoid function, also known as ELU or ReLU (Figure 2.24). In contrast to the sigmoid function, the last two functions prevent gradient evanescence, allowing for a more complex perceptron assembly especially to construct deep networks –i.e. multiple layers. The activation function will convert the obtained result into an interval (for example, [0;1] in the case of the sigmoid function) and thus determine whether the neuron is "on" or "off".

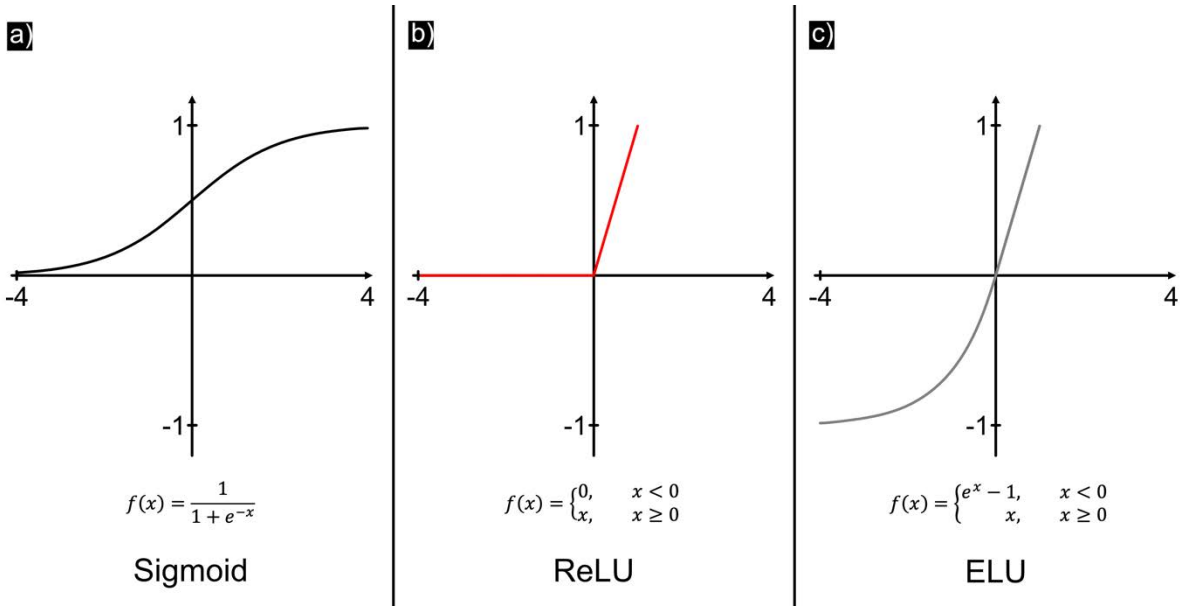

Figure 2.24 : Show some activation function such as the Sigmoid a), the Rectified Linear Unit ReLU b) and the Exponential Linear Unit ELU c).

Moving from a perceptron to a network of perceptions Figure 2.25 allows us to solve much more complex problems, such as classification of much more output or the often-better fit, because the multiplication of interconnection between the perceptron allows for more complex deduction.

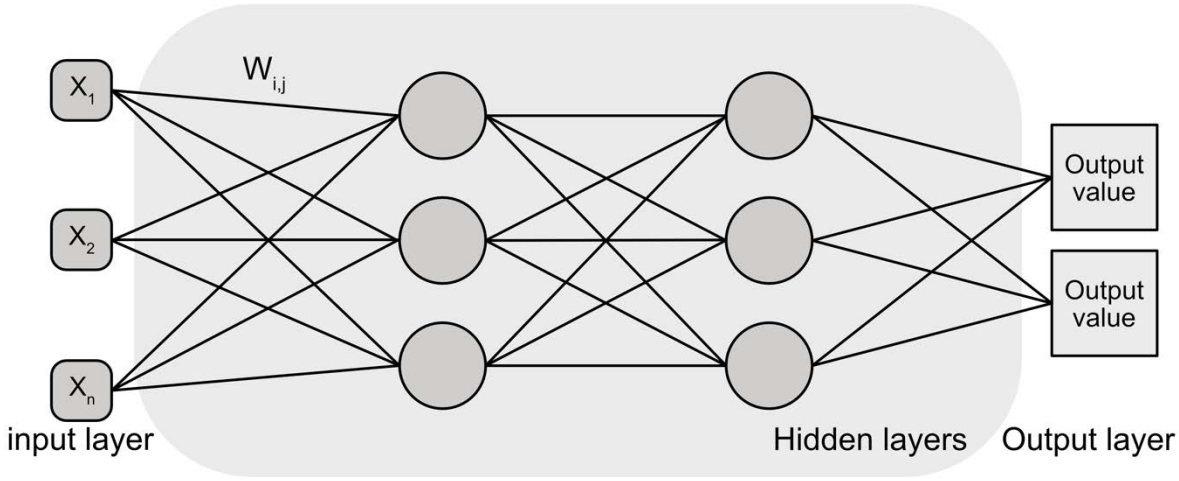

Figure 2.25 : A deep layer neural network is composed of an input layer, output layers, and hidden layers that are connected by different weights.

These neural networks are made up of multiple layers, the input layer, which takes the data to analyse and the output layer, which provides the solution, and the brain, which is called the hidden layer (middle layer).

To predict, neural networks must learn from data, which is accomplished through the use of an example database. We can build the database ourselves, and because a neural network lacks general perception, we intuitively understand that the more data in the database with a good quality and representativeness, the better the perceptron will learn. And because the neural network can learn too much by interpreting data noise as an important parameter, we also use an early stopping method to avoid overfitting.

To learn from data, this learning algorithm computes an error function at each analysis. It is generally the difference squared between the prediction and the data but we can use many different errors function. While it is not used here, to solve physical problems we can input physical equation into the error function, so ultimately the aim of the algorithm is to minimise this function over the data.

Using this neural network, we will be able to investigate how we can speed up the fitting process and measure the electron beam shape in the context of automated electron microscopy.

5. Conclusion

From the definition of a single to an assembly of charged particles using the equations of Maxwell, I discussed the physical model of a capacitor.

I described the development of continuous stabilisation for holography, without which we would not be able to obtain the results of this thesis.

Then we noted not only why we need to consider special relativity when describing the fast electron, but also that the interaction between the electron and different potentials can be described by quantum mechanics. With this description, we can create a methodology for simulating experimental data. With this, we can quickly see that the electron will be influenced not only by the potential inside the sample, but also around the sample studied (i.e. stray field). As a result, we had to simulate the stray field around the capacitor and the complex geometry of the studied sample, we needed to employ the FEM method to calculate the internal and external potential of devices.

I created Python codes that allow for a better fit with less bias from human intervention. I describe two techniques: on the one hand, I use the trust region reflective method, which is relatively fast but can get stuck inside the local minimum; on the other hand, I try to resolve this issue with Differential Evolution, which explores much more parameter space but is much more demanding in resources and calculation time. Finally, I tried a non-traditional method (AI) to find the best parameter of the model.

To summarise, the goal of this development is to conduct fundamental research on nanodevices while also developing an automatic holographic image interpreter through its flaws.

To take it a step further, even though it is not the focus of my thesis, we could have performed macroscopic measurements to fully characterise the nanodevices under consideration. Second, we could measure devices in terms of frequency, but this is still being worked on by our TEAM, so stay tuned.

Chapter 3 — Theoretical Development

Understanding experimental data necessitates theoretical development, which allows for the extraction of parameters from simulations that are not accessible experimentally. We can also go beyond experimental reality by including geometry and parameters that are not observable during an experiment. As a result, we can determine the entire set of physical laws that govern the behaviour of the investigated system.

Before all this, it is necessary to develop the FEM tools required to simulate an electron holography phase image and then test them. In this chapter, we will study a model capacitor firstly with both electrodes grounded and then, with one of the electrodes biased to different voltages. Through modelling, I will explain how the phase image is affected by the geometry of the system, the parameters of the model, the interaction with the electron beam and the artefacts from the sample preparation (amorphisation, ion implantation). To this end, we can make some connections between the model and the phase profile, allowing us to extract information from the phase profile that would not be possible without the simulation study (Yazdi et al., 2015).

Also of interest later on in this chapter will be one of the systematic sources of error, caused by the interaction between the biased sample and the specimen holder. The resulting stray field can influence the reference wave.

1. Mesh Stabilisation

To simulate phase images, we must first create a model, then discretise the space, also known as meshing, so that the algorithm can perform a finite element calculation. In other words, meshing is a discretisation step that defines a set of interconnected points for which the software computes the solutions. Because the space has been discretised, the partial differential equation will be approximated on the mesh and

solved using variational formulation. As we will see later, each component of the model solves two different types of physics, and thus two different types of differential equation.

Non-physical parameters such as the mesh, simulation box size and boundary conditions all can have an effect on the numerical calculation result. So, in order to minimise their influence, I conducted a set of preliminary studies, which are detailed below.

To ensure that the solutions are independent of the size of the simulation box (Figure 3.1(a)) and the distance between the mesh nodes, I studied the evolution of a target function that serves as an indicator. This function was the integral of the square of the potential over the surfaces denoted by *"s"* (Figure 3.1(b)). The region was chosen to include the stray field of the thinned capacitor because, as has been mentioned previously, it is critical to the solution.

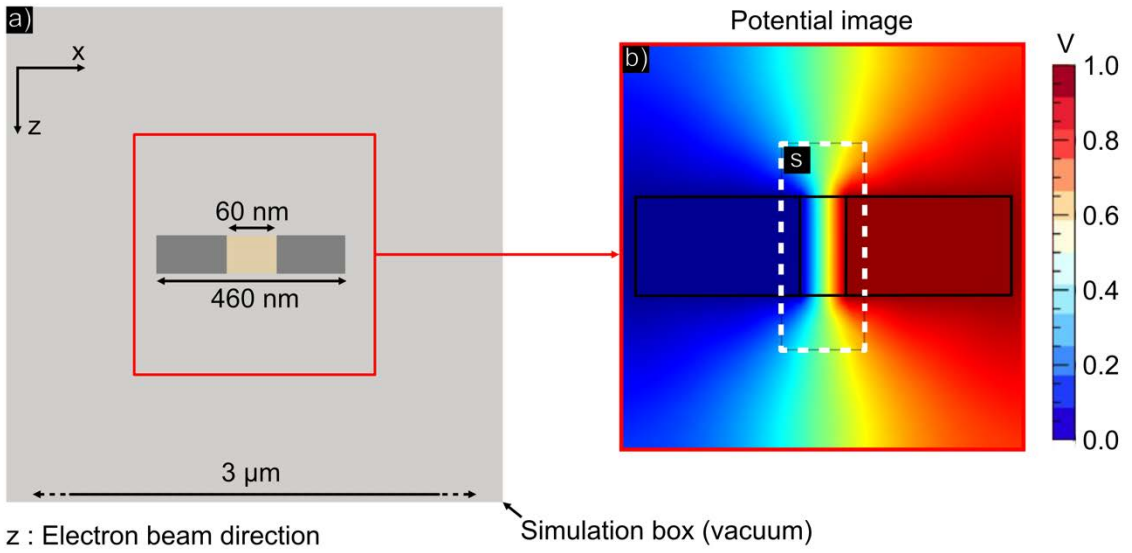

Figure 3.1. Schematic depiction of the 2D simulation geometry: (a) simulation box (in grey) with four external boundaries and a single capacitor in the centre; (b) enlargement of the capacitor showing electrical potential (in colour). Target function calculated dotted region “s”.

The mesh itself was divided into two main zones to reduce simulation execution time and computational resources: a finer mesh inside the capacitor and a coarser mesh in the vacuum surrounding the capacitor. For better continuity, the mesh also grows

gradually in size from the capacitor surface outwards into the vacuum (Figure 3.2). The software determines the exact position of the mesh points.

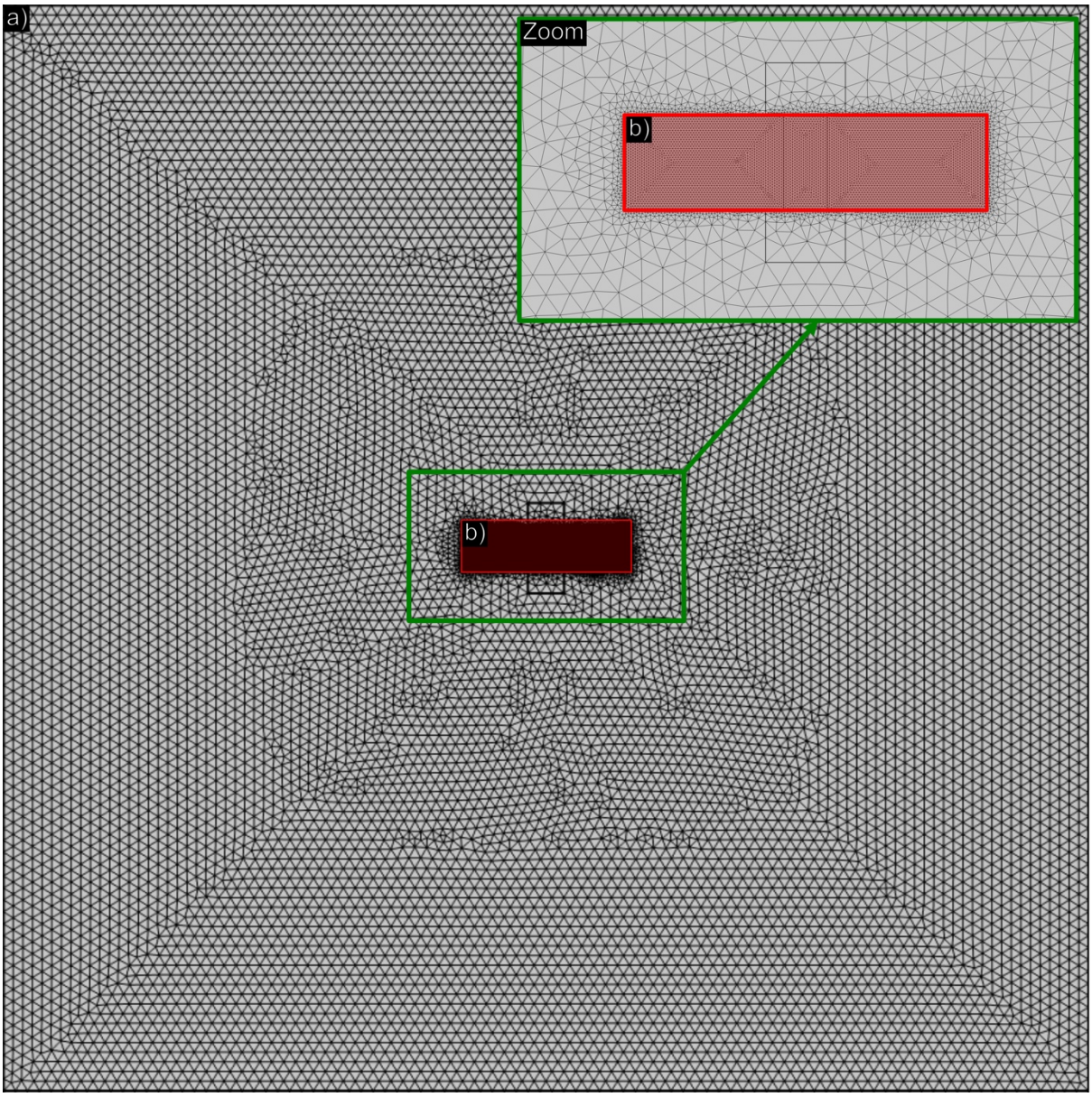

Figure 3.2 : Show two different triangular mesh sizes coarser for the vacuum area a) and finer inside the capacitor b).

A coarse mesh size, like that shown in the vacuum region of Figure 3.2(a), allowed fast computation but had a large influence on the solution whilst for a finer mesh size, near the capacitor in Figure 3.2(b), the solution was slower to converge but had a smaller influence on the outcome. The goal was to strike a balance between computation time and solution quality.

To find the optimum, I studied the target function whilst varying the box size and the average mesh spacing. A factor, which I called γ, adjusted the mesh spacing in each area: from (20 nm / γ) to (0.17 μm/ γ) in and around the capacitor to (0.2 μm/ γ) to (1.6 μm/ γ) in the vacuum. This was repeated for sizes of box, from 0.5 μm to 9.5 μm. The target function is plotted with respect to the size mesh and size box in Figure 3.3.

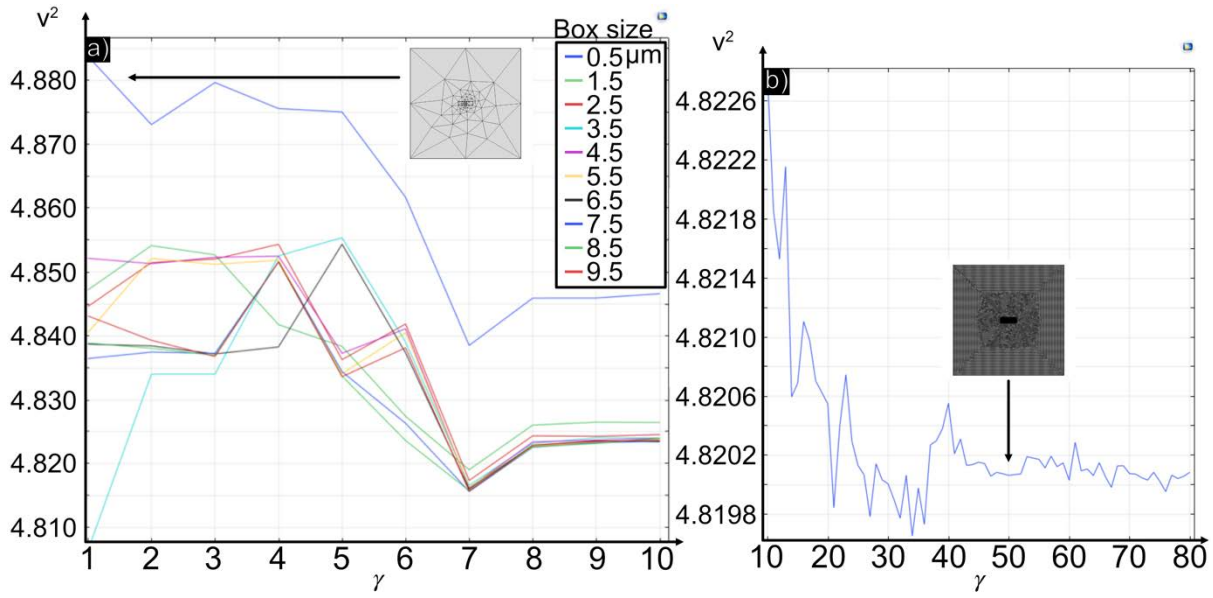

Figure 3.3 : The target function result for various box sizes depending on the level of mesh refinement a) and a study with a selected box size (3.5μm) to a finer mesh than before b).

The simulation parameters were considered to no longer affect the calculation from the moment the target function stabilises. For example, Figure 3.3(a) shows that a box size larger than 3.5 μm does not significantly improve the reliability of the calculation.

With the optimal box size determined, we can explore the effect of the mesh size (Figure 3.3(b)). As a result, we can determine the stability point of γ when the plot stabilises around 50, after which the simulation is no longer dependent on the box size and mesh. As a result, these two parameters have been determined and will be used as upper bounds in all subsequent simulations. It is worth noting that the maximum mesh size outside the capacitor with $\gamma = 50$ is 33 nm, while the minimum mesh size inside is 0.4 nm.

The outermost boundaries of the box can still cause edge effects. To reduce their influence, so-called "infinite domains" (COMSOL) can be created that simulate a box boundary that recedes to infinity. To be more specific, the infinite domain applies a very large distance between the mesh nodes of the domain. The distance between mesh nodes in the domain will be multiplied by a fixed amount determined by multiplying a diagonal of an imaginary box containing the entire geometry of the model by 100. Excessive distances to the model are avoided by using the size of the model rather than a risky and arbitrary constant, limiting numerical errors. The original box was padded with such an infinite domain (Figure 3.4(a)), subtracting 0.5 μm nominally to the initial size.

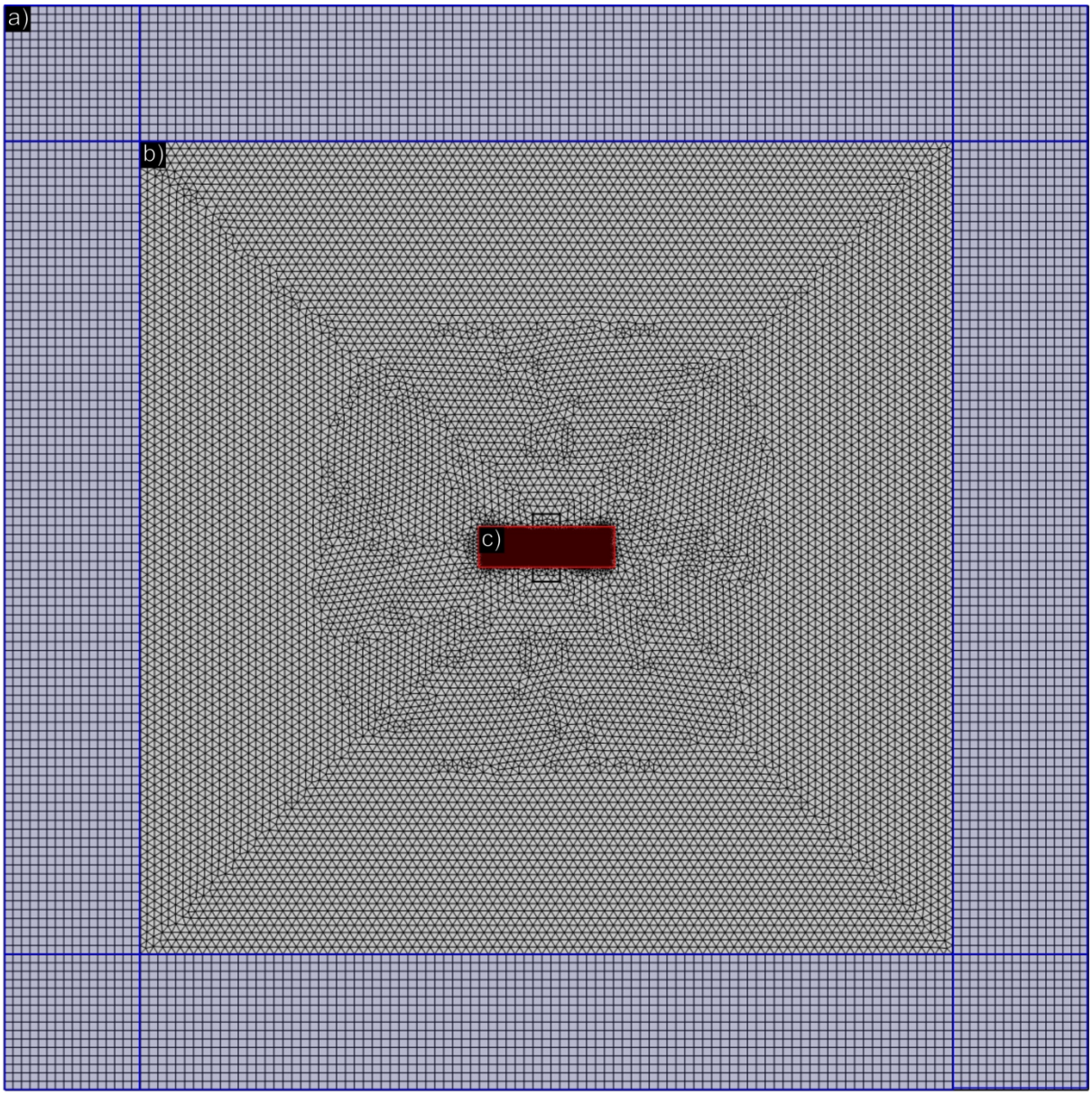

Figure 3.4 : With the new configuration, the mesh is configured as follows: the “infinity domain” with a mapped mesh around the box a) and two different triangular; a coarse mesh for the vacuum area b) and fine mesh inside the capacitor c).

The previous calculations were repeated with the infinite edge box Figure 3.5.

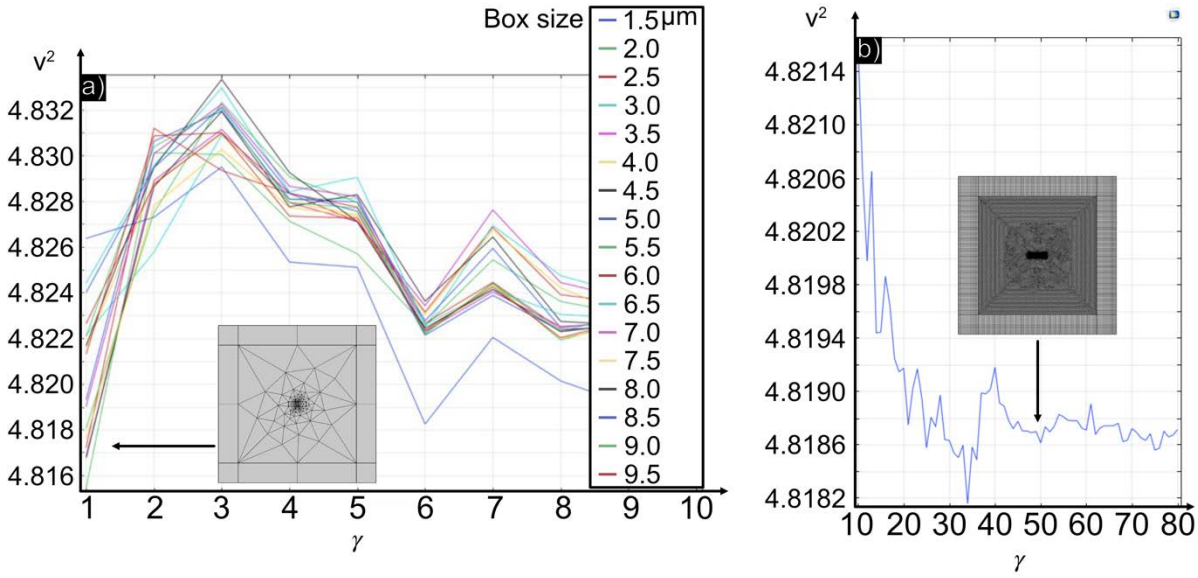

Figure 3.5 : Target function curves with varying box sizes and common divisors on the left a) and a fixed box size on the right b) with a simulation box with infinity layers.

As we can see, the infinite box reduces the expected dependence on box size, this can be seen by a smaller dispersion between the curves of the Figure 3.5(a) than on Figure 3.3(a), demonstrating the usefulness of infinite edges. We can also see that whether the box is infinite or not, the system responds to changes in mesh size in the same way as before, by decreasing and stabilising at the same γ (50) meaning that the infinity layers solve in part the box-size problem.

In the neighbouring field of research on antennas, spherical boxes are typically used (Fumeaux et al., 2007). I therefore tested the cylindrical edge conditions to study if the target function could be stabilised with even fewer computational resources. By superimposing a square simulation box Figure 3.6(a) on top of a circular one, the new conditions are illustrated in Figure 3.6(b).

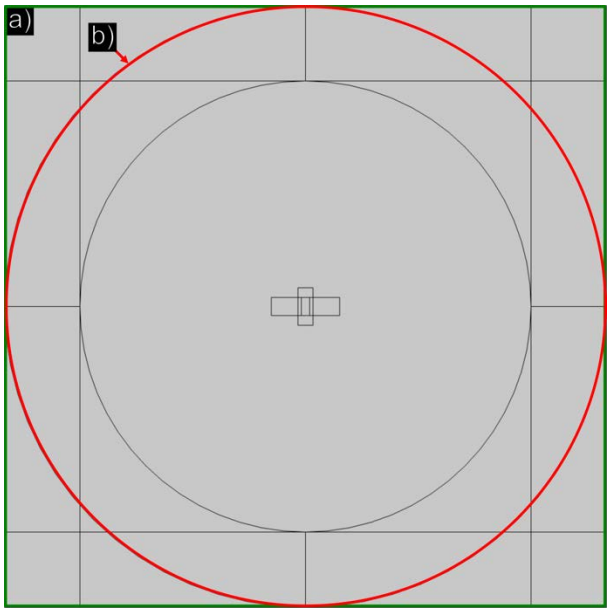

Figure 3.6 : Superposition of the square box a) and cylindrical condition b).

On the one hand, the cylindrical conditions make no discernible difference in the simulation of the smaller box sizes. On the other hand, the convergence rate for the mesh size is significantly higher because the solution stabilises for a larger mesh size than for a square condition, with a common divisor of 40 versus 50 in the previous models.

It is also worth noting that the solution with square bounds achieves the same results as the one with circular edges, despite being less time efficient. I chose therefore to continue with square boundaries due to their flexibility with the rectangular geometry and the problem simulating holograms from them because the projection along the electron path of the potential is very difficult within a circular box.

In conclusion, we were able to obtain a very good mesh that was quick to compute and had no notable influence on the calculation.

2. Electron Holography

Off-axis electron holography operates through the interference of two components of a greatly coherent electron: the object wave, which interacts with the sample and the surrounding electromagnetic fields, and the reference wave, which has not been influenced by any field (Figure 3.7).

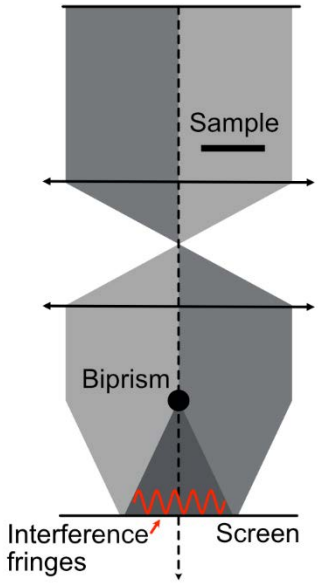

Figure 3.7 : Scheme of the holography technique recording the phase shift between the reference beam and the sample beam.

The resulting interference pattern, known as a hologram, encodes the phase shift experienced by the electron wave when it interacts with the local electromagnetic potentials, which is required for quantitative mapping of electric fields inside and outside the device.

The electrical biasing-induced phase change along the x-axis of the hologram for a 2D representation and is related to the electric potentials in the following way (3.1):

$$\phi(x) = C_e \int_{-\infty}^{+\infty} \left(V_0(x,z) + V_{SC}(x,z) + V_{bias}(x,z) + V_{IC}(x,z)\right) dz \qquad (3.1)$$

Where C_e is a constant that depends on the accelerating voltage of the fast electron and z is the direction of the electron path. V_0 relates to the mean inner potential (MIP) of the material encountered along the electron path, $V_{charges}$ the potential created by static charges, V_{bias} the electric potential caused by an applied bias, and V_{IC} potential induce by the injected charges. As a result, the measured phase shift can be divided into four contributions: ϕ^{MIP}, ϕ^{SC}, ϕ^{bias} and ϕ^{IC}. These components will be studied individually and extracted from the measured phase shift. For example, ϕ_{MIP} is biased independent and can be obtained at 0 V of applied bias in the absence of charging. Because of the integration along the path of the incident electron, the phase is sensitive to the electric potential both within and outside the specimen (i.e. which

includes the contribution from stray fields). To continue, the effect of $V_{charges}$ and V_{bias} will be investigated in the following sections.

3. Grounded Capacitors with a Uniform Charge Density in the Insulator/Dielectric

3.I. Introduction

The physics of a grounded nanocapacitor is already rich in many respects. There are two main aspects that have to be distinguished: the interaction between the electron beam and the specimen, creating positive charges in the insulator (Cazaux, 1995), and the existence of the mean inner potential (MIP), specific to each material (Beleggia et al., 2016). Furthermore, for the experimental protocol point of view, observing the grounded capacitor is the first step to understanding the effect of biasing, for many reasons that will be developed throughout this manuscript.

The experimental reality will, as usual, be simplified for the modelling. This means principally that even though the sample is a 3D volume, we can approximate it with a 2D model for symmetry reasons. Neither the variation in the width of the dielectric layer nor the thickness of the sample will be taken into account. But overall, the simplify model will allow us to understand the physics beyond the experimental sample and extract quantitative information.

The models are composed of two electrodes which are separated by a dielectric layer. An electric field is created between the electrodes when a bias is applied. When the dielectric layer is exposed to an external or internal electric field, the internal charged density reorganises so as to partial screen the applied field (Zangwill, 2012). The dielectric permittivity ε_r captures the sensitivity of the chemical bonds to an electric field. When the field is partially screened, the generator is forced to bring more charges to maintain the potential difference, allowing the capacitor to store more charges with the same bias in relation to a parallel-plate capacitor with a vacuum in between.

However, the model has to take into account other intrinsic effects such as the MIP as well as interface defects (vacancies, charge traps, stress, sample preparation

damages, and so on). Furthermore, there are also extrinsic phenomena such as preparation artefacts and charged induce by the electron beam. In fact, while FIB milling the sample for study, some gallium atoms can be implanted into the surface of the sample, forming a conductive layer (Han et al., 2008). Elsewhere, some authors refer to these artefacts as a "dead layer" or "electrically inactive layer" (Cooper et al., 2010), but this appears to refer to a lack of built-in potential (Wolf et al., 2013). Overall, we spent some time looking into the effect of conductive layers on the model. As mentioned previously, another extrinsic effect is caused by the electron beam used for the electron holography. In the following, we will study the effect of the MIP, charging of the insulating layer and a surface charge layer (Figure 1.8).

In our simplified model, the phase change of the electron beam caused by the mean-inner potential (MIP) is given by:

$$\phi^{MIP} = C_e \sum_i V_0^i \, t_i \qquad (3.2)$$

where the summation is over each material, *i*, traversed by the electron at position x, V_0 the corresponding mean-inner potential *t*, the thickness of the material. In the model, the thickness of the specimen and the conducting layer is constant, creating a series of constant phase shift between the electrodes and the insulating layer (illustrated in Figure 3.8(a)) (Beleggia et al., 2016). We calculate this independently to the finite-element model. In reality, the mean-inner potential is poorly known because its measurement is strongly difficult to measure experimentally and its calculation is also difficult influenced by size effects, bonding between the atomic constituents and valence electron densities (O'Keeffe and Spence, 1994). So, it will be put to one side for the moment.

While in our simplified model, phase change of the electron beam caused by static charges is given by:

$$\phi^{SC}(x) = C_e \int_{-\infty}^{+\infty} V_{sc}(x, z)\, dz \qquad (3.3)$$

Where the integral of V_{sc}, the static potential along the path length of the electron to take into account not only the field produce by the charges but also the stray field thus produce. The phase shift produce is a curve as shown Figure 3.8(b) and the

resulting phase shift of the effect of the MIP and the static charges is illustrated Figure 3.8(c).

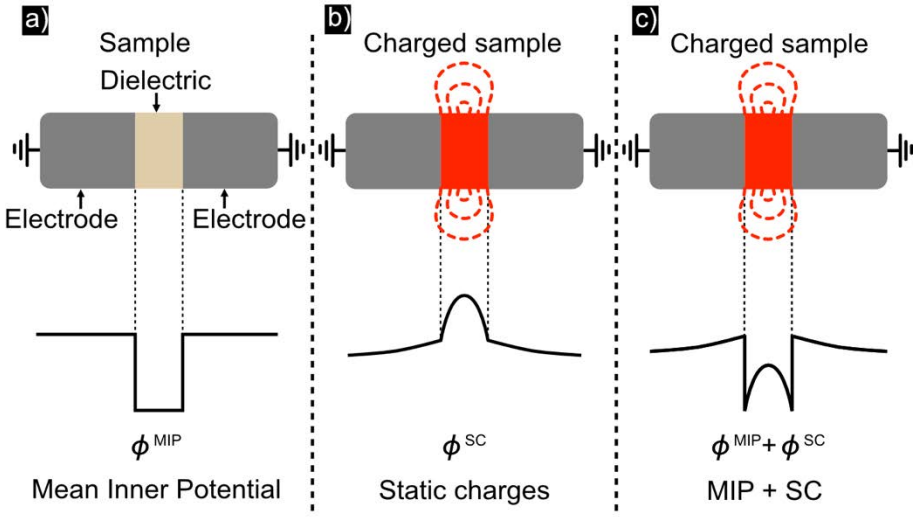

Figure 3.8 : Each model represents a specific type of interaction and the data collected by electrons passing through it. The first model includes the MIP effect a), while the second model only represents the charged potential b), and the final model is a combination of the first two models that is closest to the experiment reality c).

The other contributions to the phase images will be investigated in the following sections through multiple models with varying parameters. The Figure 3.9 shows the parameters such as the thickness t of the capacitor, the length of the electrodes L_1 and L_2, the dielectric width w and the size of the simulation box L_{box}. As a result of the damage caused by the preparation procedure by gallium-based FIB, some models include a thin surroundings conducting layers. According to the SRIM simulation and experiment from TEM (Giannuzzi et al., 2005; Huang et al., 2018), the final cleaning of the sample studied is at 2 keV and gives 2-nm amorphisation layers on silicon medium. As a result, the conducting layers will be fixed to a thickness of 2 nm, and because the conductivity of these layers is unknown, multiple conductivity $\sigma\ S/m$ will be investigated. The remaining parameters are the dielectric permittivity relative to the vacuum of the insulating layer ε_r and the charge density in the insulating layer $\rho\ C/m^3$ which we will assume is constant.

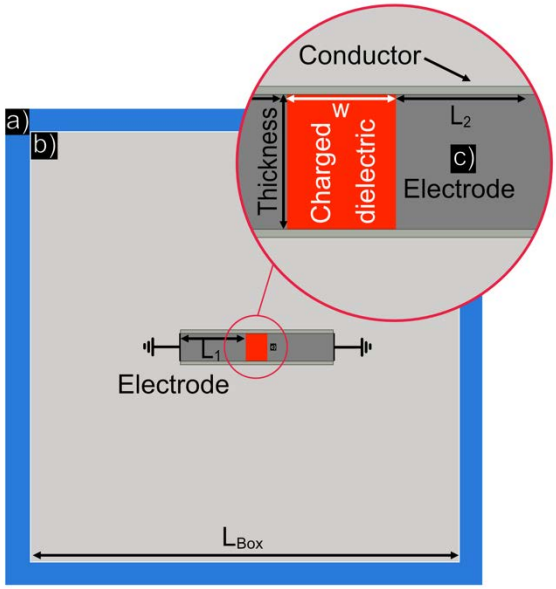

Figure 3.9 : The simulation box is surrounded by infinite boundaries a), then the meshing scales done to the capacitor b). And the model is positioned in the centre of the box c).

The model capacitor is computed by the finite element method (FEM). As described previously, multiple zones were created to balance the computer time and the quality. The conditions at the edges of the domain were placed at infinity (Figure 3.9(a)). The maximum mesh size in the vacuum is 33 nm (Figure 3.9(b)), after which the mesh dynamically scales down to the nanocapacitor (Figure 3.9(c)) with a mesh size of less than 0.1 nm to achieve a value less than the spatial resolution of the phase images. Finally, the boundary conditions are placed on each electrodes side. No MIP effects are taken into account in this calculation.

3.II. Study of the Phase Image Produced by a Charge Density

Due to the interaction between the electron beam and the capacitor, the dielectric layer can become positively charged due to emission of secondary electrons. Even though the dielectric will partially screen these charges, the charged density will give rise to a field. Indeed, in the absence of conducting layers on the surface, there will be a significant stray field in the vacuum. As a result, in order to obtain the phase profile, the stray fields as well as the internal field produced by the charge density must be considered.

Except for the parameters specifically modified during the study, the parameters will always be the same as indicated in Figure 3.10.

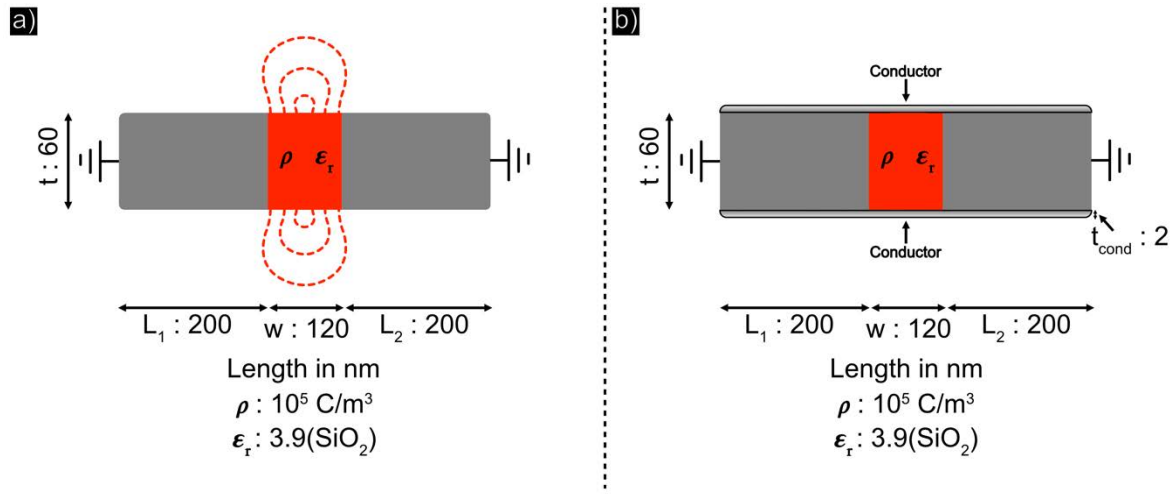

Figure 3.10 : Base models with no conducting surfaces a) and with conducting surfaces b).

Throughout the studies, we will change some parameters, sometimes several parameters at the same time, to better understand their impact on the phase profile. For example, we will investigate the effect of the conductive layers as well as the variation of the charge density, dielectric permittivity, and multiple model sizes. As the effect of the MIP is simply a constant shift upward in our case, it will not be studied here, whereas the charged density studied will be ranging from 10^5 to 3×10^5 C/m^3, corresponding to a range near the top experimentally measured values (Latychevskaia et al., 2010; Gatel et al., 2013; Beleggia et al., 2016). Finally, despite the interest in novel materials to replace SiO_2 as a dielectric, over one thousand different types of SiO_2-based transistors have been designed and manufactured to date, making this material unavoidable (Checkelsky, 2022). The models will be based on SiO_2 for the insulator with a relative permittivity of 3.9 for the simulations.

3.II.A. Variation of Charge Density and Permittivity

Charge density as well as permittivity have a direct effect on the strength of the electric field inside and outside the capacitor. Indeed, their effects are opposing: as

charged density increases, so does the strength of the field, whereas as the permittivity of the material increases, the field will decrease through screening. To begin with, we will look at charging effects. Each simulation will be performed with and without conducting surfaces in order to better understand the perturbation caused by gallium contamination during the preparation process.

Figure 3.11(a, b) depicts the simulated potentials (Figure 3.10), along with their respective phase profiles computed from the potential determined by FEM and projection along the beam path Figure 3.11(c, d) (see chapter 2).

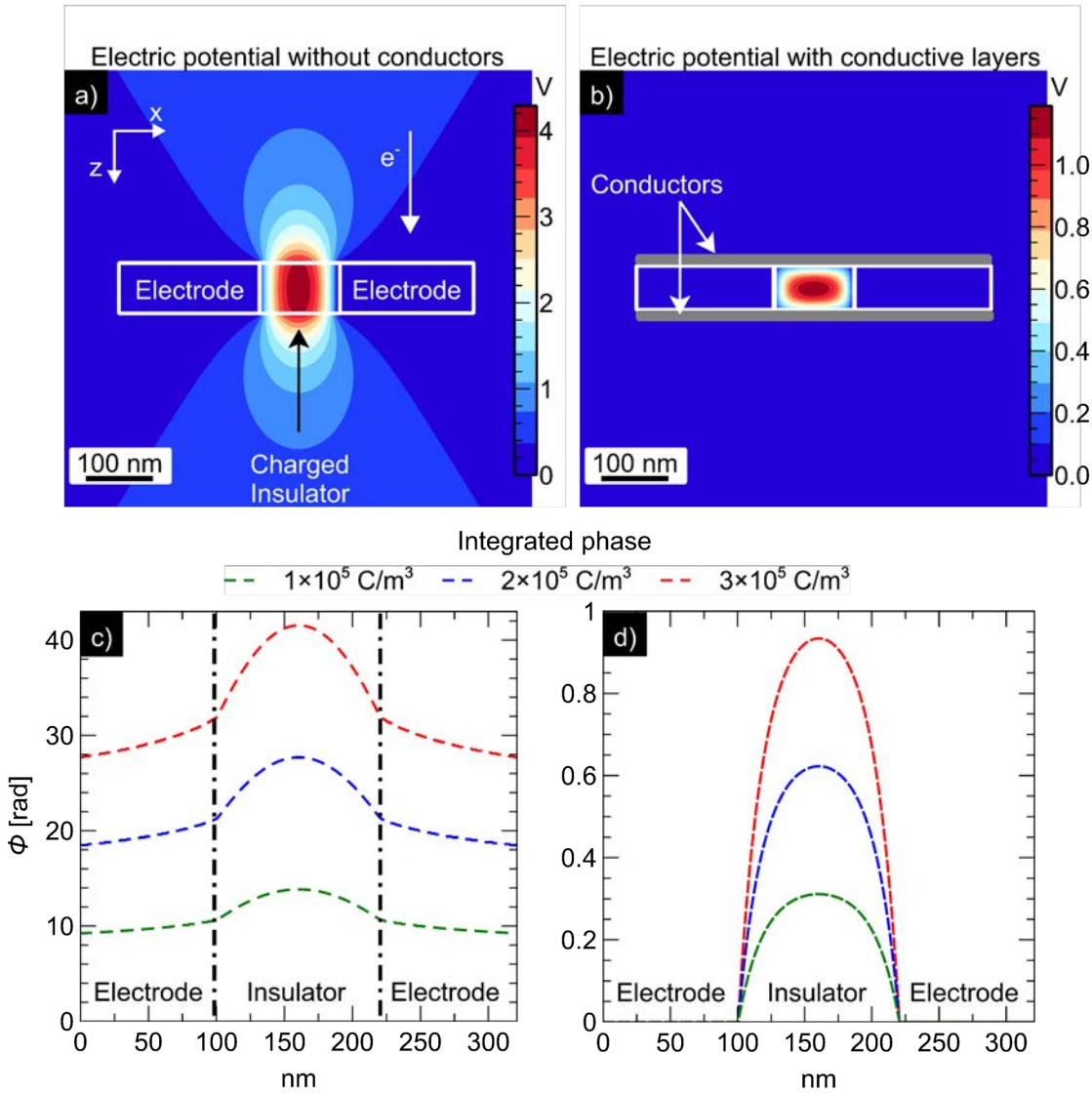

Figure 3.11 : FEM calculation of the potential produce by the models Figure 3.10 for three different charged density a), b) and their corresponding phase shift c), d).

As expected, the calculated potential on the capacitor is symmetric and the phase variation is more pronounced with increasing charge density, as seen in Figure 3.11 (a, b). More interestingly, the first model has a stray field (Figure 3.11(a)), whilst the second does not (Figure 3.11(b)). This manifests itself as a curvature of the phase in the region corresponding to the electrodes for the model without a conducting layer (Figure 3.11(c)); whilst in the model with a conducting layer, the phase is uniform and in fact zero in our case (Figure 3.11(d)). This can easily be understood from the equation of Poisson (3.4).

$$\Delta V = -\frac{\rho}{\varepsilon} \qquad (3.4)$$

The potential created by the charge density ρ inside a medium with a permittivity ε is denoted by V. The Poisson equation tells us that positives charge causes a negative curvature of the potential and in the absence of charge, the potential is uniform. Given the linear relationship between electrical potential and phase, the phase profile has the same property. In both cases, the phase is strongly (and negatively) curved in the region corresponding to the insulating layer containing the charge. For the model without a conduction layer, the stray field introduces a constant shift and creates a positive curvature in the area corresponding to the electrodes (Figure 3.11(c)). This is due to negative charge accumulation on the surfaces of the electrodes to prevent the stray field penetrating the metal.

The second model is different because conducting layer forms a Faraday cage around the whole specimen that completely screens the vacuum from the internal field. Negative free charges are generated at the top and bottom of the dielectric to perfectly compensate the field from the positive charges [see theoretical chapter 2]. Indeed, because there is no stray field and no phase variation in the electrode area, the corresponding phase profile results in a significant reduction in phase amplitude (Figure 3.11(d)).

To quantify these effects, we have studied the value of the phase at the maximum ϕ_{max} as a function of the charged density ρ. For both models, the relationship is linear, as shown in Figure 3.12.

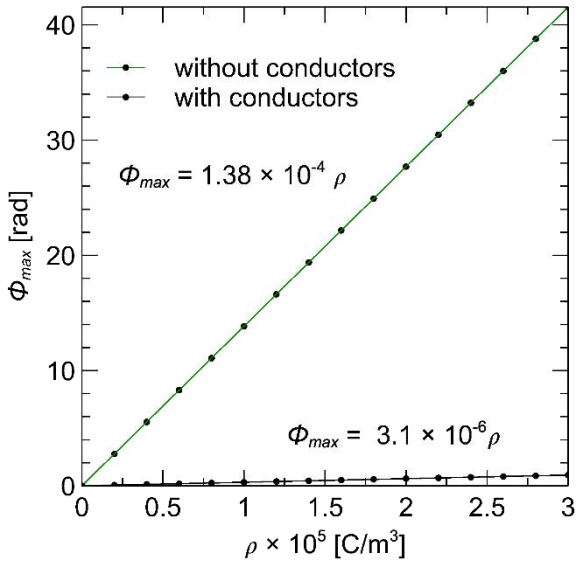

Figure 3.12 : Maximum phase versus charged density of the simple model and the model with conducting layers.

Because of the screening effect of the conducting layers, the maximum phase is lower in the second case, which reduces the slope by a factor of about 40. However, given that the MIP is not taken into account and that the phase is defined up to an arbitrary constant, a fairer comparison is obtained by removing the constant value resulting from the stray field. The value of the phase at the interface between the electrodes and the dielectric was therefore subtracted from each profile (Figure 3.13(a)).

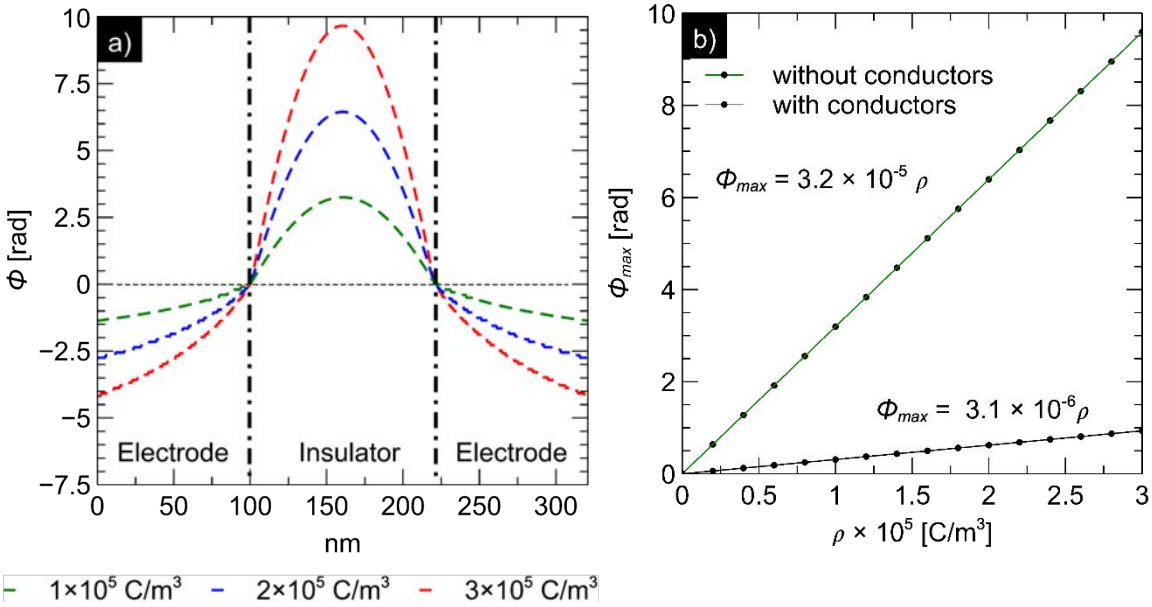

Figure 3.13 : The corrected phase profile is on the left a), and the corresponding comparison of the maximum $\boldsymbol{\phi_{max}}$ versus the charge density $\boldsymbol{\rho}$ is on the right b).

After correction, the model with a conducting layer has a slope that is 10 times lower than the model without the conducting layer (Figure 3.13(b)). This comparison makes more sense because we are only interested in the phase shift from the charge and not the MIP. In the following subsections, this procedure is applied to each phase profile. We now know that the phase profile responds linearly to variations in charge density and that a sample with a conducting layer on the surface will be 10 times less sensitive to the amount of charge present.

The next step is to study the effect of the dielectric permittivity and its relation with the screening charges in the electrodes and any conducting surfaces. The model used is the same as before, but instead of varying the charge density, the dielectric permittivity will vary from 1 (vacuum) to 30 (high-K materials)(Figure 3.14). This range contains some of the most common dielectrics used in microelectronics, such as S_iO_2, Si_3N_4, Ta_2O_5 or H_fO_2 (Robertson, 2004).

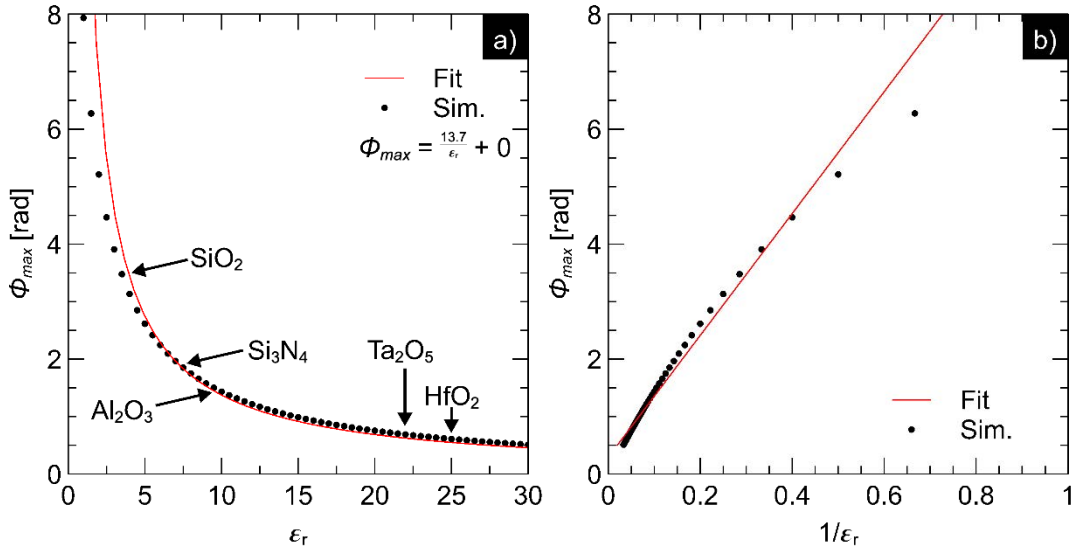

Figure 3.14 : On the left, the evolution of $\boldsymbol{\phi_{max}}$ versus $\boldsymbol{\varepsilon_r}$ From 1 to 30 for a simple capacitor a). While on the right, it is versus $1/\boldsymbol{\varepsilon_r}$ b).

The maximum phase ϕ_{max} varies approximately as $1/\varepsilon_r$ (Figure 3.14(a)). Indeed, dielectric physics predicts that the dielectric screen charges by a factor of $1/\varepsilon_r$ for an isolated material subjected to an external electric field (Figure 3.15(a)). That the relationship is not exact, can be explained by the presence of the stray field, the electrodes (Figure 3.15(b)) and conductive layers (Figure 3.15(c)).

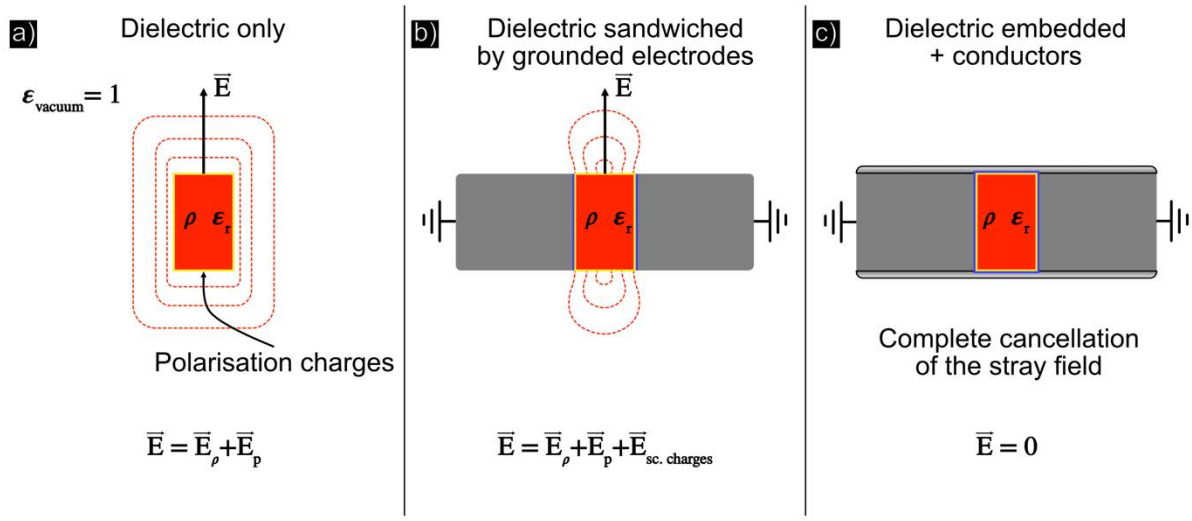

Figure 3.15 : Stray field of an charged dielectric a) followed by a compression of the stray field by the grounded electrodes b) and disappearance of the stray field by a total screening c).

As a result of the free charges introduced by the electrodes and the stray field, when we plot ϕ_{max} versus $1/\varepsilon_r$, it does not fit the linear fit. But there is a way to measure this behaviour, and the key to doing so may be to add conductive layers around the dielectric Figure 3.15(c), as explored later in this section.

Because the phase profile is affected by both the charge density and the dielectric permittivity, I plot a 3D figure of ϕ_{max} versus (ε_r, ρ) to gain a better understanding of this complex mechanism Figure 3.16.

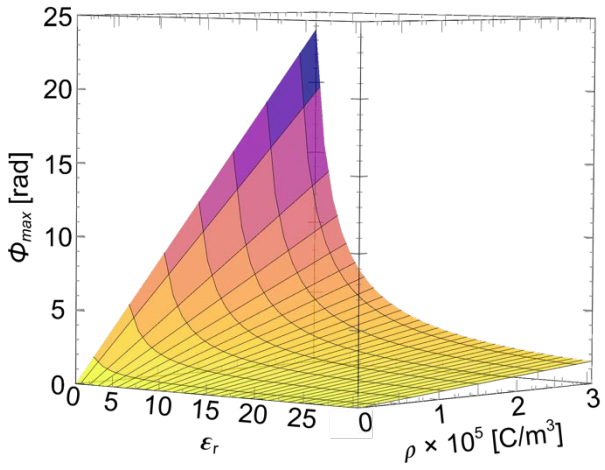

Figure 3.16 : Plot of $\boldsymbol{\phi_{max}}$ versus ($\boldsymbol{\varepsilon_r}$, $\boldsymbol{\rho}$) for a capacitor model without conductors.

The evolution of ϕ_{max} follows a linear behaviour in terms of charged density for each permittivity while being close to an inverse law in terms of medium permittivity.
To studies more in depth the charging dielectric proprieties, the same experimentation was performed with the model with conducting layers Figure 3.17.

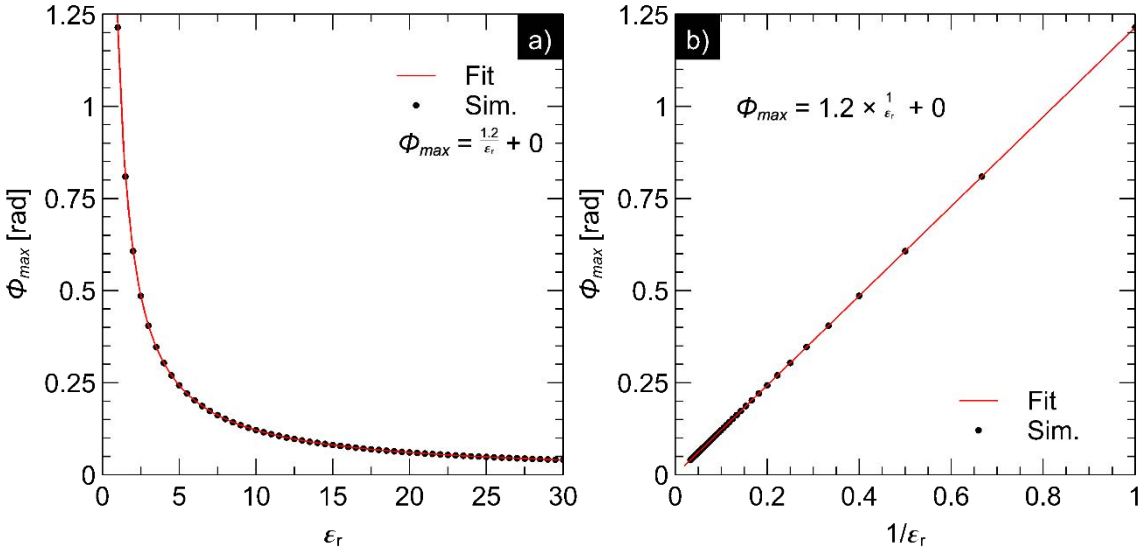

Figure 3.17 : Left: evolution of ϕ_{max} versus $\boldsymbol{\varepsilon_r}$ From 1 to 30 for a model with conductive layers in surface a). Right: evolution of ϕ_{max}as a function of $1/\varepsilon_r$ b).

This system is analogous to a dielectric embedded in a grounded metallic cage. Given that the conductors surrounding the capacitor act as a Faraday cage, there is no stray field surrounding it. In this case ϕ_{max} varies linearly with $1/\varepsilon_r$, exactly.
The plot of ϕ_{max} as a function of both parameters ε_r and ρ is presented Figure 3.18.

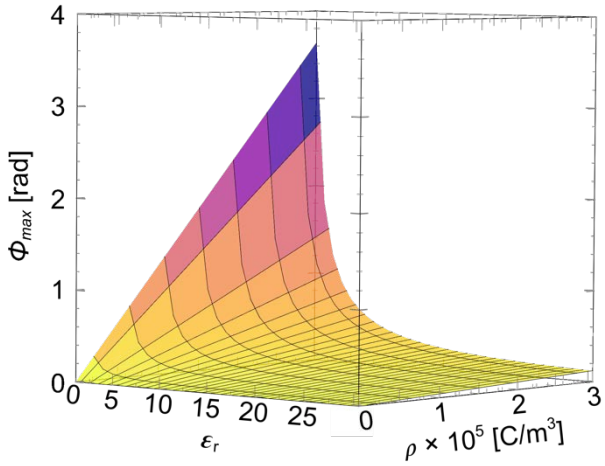

Figure 3.18 : Plot of $\boldsymbol{\phi_{max}}$ versus ($\boldsymbol{\varepsilon_r}$, $\boldsymbol{\rho}$) for a model capacitor with conductors.

Given that analytical curves fit closely the data from the simulations, we can attempt a generalisation. From each slope for ρ and $1/\varepsilon_r$ we obtained the same factor $\alpha = 1.21 * 10^{-5}$ m^3.C^{-1} which allows us to generalise:

$$\phi_{max} = \alpha \times \frac{\rho}{\varepsilon_r} \qquad (3.5)$$

This equation has an excellent accordance to the data. However, the factor itself is still dependent on the particular geometry of the model.

Using this example, we would like to investigate how much the stray field contributes to the phase profile.

3.II.B. Evolution of the Stray Field Contribution as a Function of the Dielectric Geometry (Aspect Ratio)

The purpose of the following study is to quantify the effect of the stray field on the phase profile as a function of dielectric geometry. As this effect, I investigate the contribution of the stray field to the internal field as a percentage versus the ratio of the dielectric length to the sample thickness *w/t*. In order to assess the contribution of the stray field in the final phase image, we compute separately both the internal contribution (in the capacitor) and the external contribution (in the vacuum) as presented Figure 3.19. The internal contribution to the total potential is then calculated

as a percentage *p* by taking the maximum of each curve and dividing it by the total contribution, since the total phase image is the sum of the two projections.

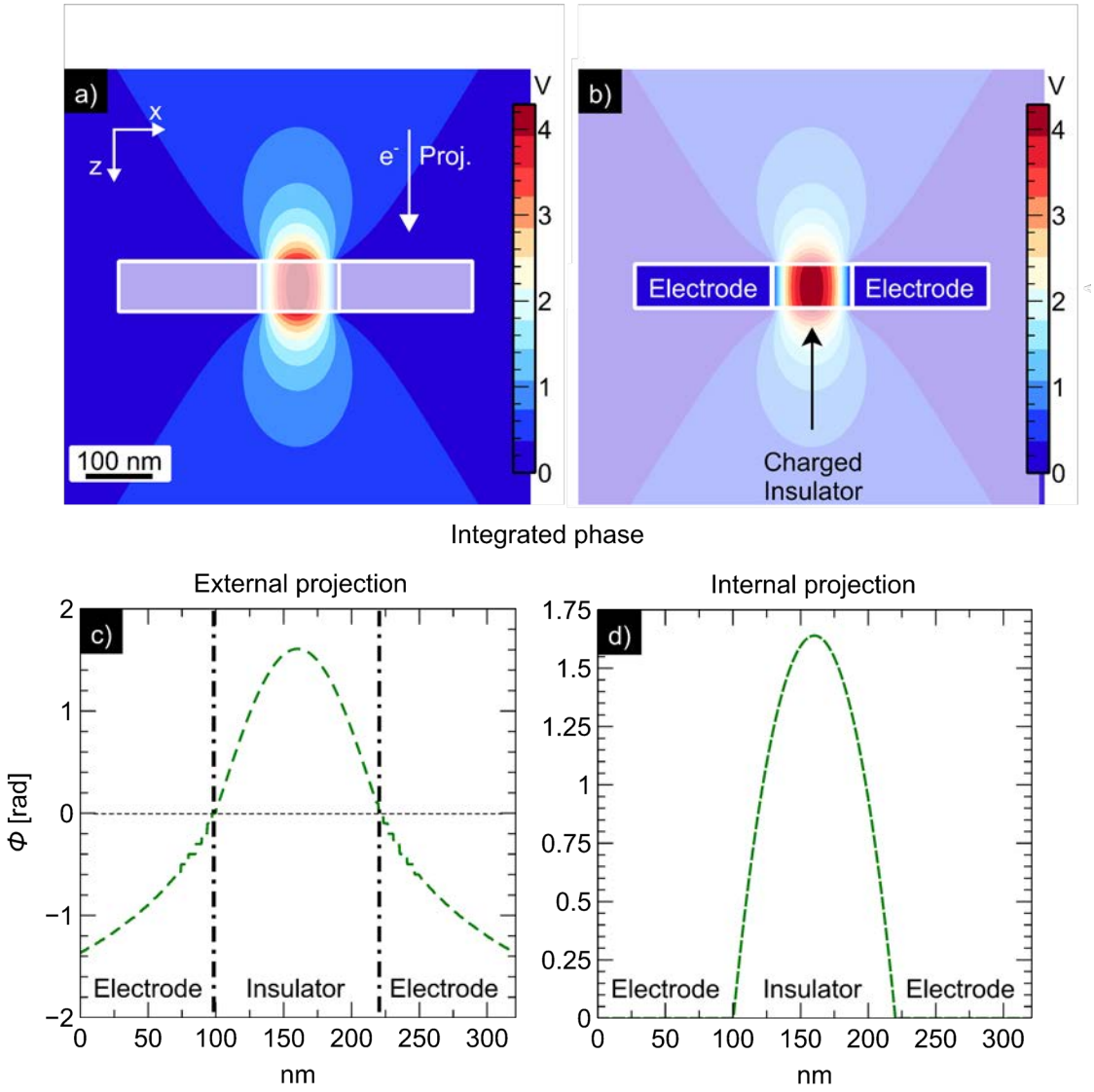

Figure 3.19 : Representation of the procedure for obtaining the external phase contribution a) and the internal phase contribution b) with the external phase profile c) and the internal phase profile d) just below.

It is worth noting that the internal potential (Figure 3.19(d)) looks similar to the phase profile of a capacitor with conductive surfaces but the magnitude is slightly larger: a grounded conductor does not only screen the stray field, but also screens the internal charges with the help of free charges.

The model was computed without the conductive layers in surfaces to determine the contribution of the internal potential to the total phase, denoted as percentage *p*. This percentage was calculated for each pair of values *w* and *t* (*w* ranging from 2 to 200 nm with a step of 10 nm, *t* ranging from 20 to 200 nm with the same step). These value ranges are framed in terms of the expected size of an electron microscopy experimental sample. The *p* versus *w*/*t* result is shown Figure 3.20.

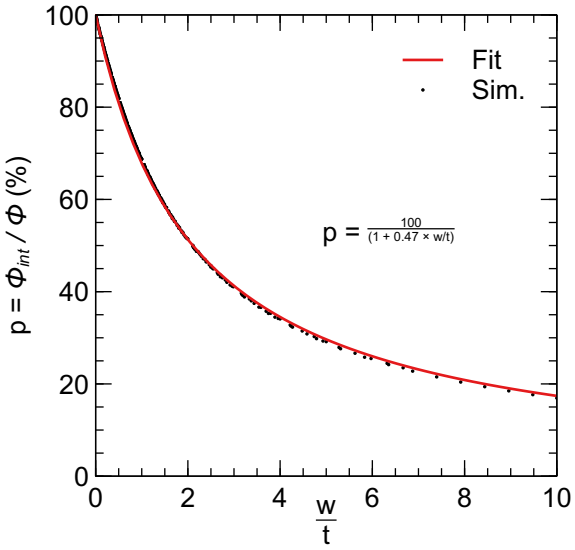

Figure 3.20 : Percentage of the internal potential versus the aspect ratio *w*/*t*.

The distribution of the points calculated from the simulations clearly highlights that the aspect ratio *w*/*t* controls the contribution of the internal potential to the total phase: *w* and *t* are not free variables as multiple combinations of produce the same results. This distribution can be fitted with the law (3.6).

$$p = \frac{100}{(1 + 0.47 \times w/t)} \qquad (3.6)$$

When *w*/*t* tends to 0, the system corresponds to a perfect capacitor (infinite sided) where no stray field is present: only the internal phase contributes to the total phase with *p* equal to 100%. The phase profile is thus easier to interpret. At the other extreme, *p* is strongly reduced as the aspect ratio decreases: the phase profile of this thinned capacitor presents a large contribution from the stray field.

The highest variation occurs up to $w/t = 2$ with a decrease of p from 100% to 50%. For larger values, p then decreases more slowly and reaches a value lower than 20% for an aspect ratio of 10, limit value in the ranges of values of w and t retained for this study.

When the aspect ratio is less than 0.5, the potential inside the sample contributes more than 90% of the signal, which appears reasonable if we only want an approximation and neglect the stray field contribution, avoiding the use of the FEM technique. To go further, the fit enables us to find a coefficient 0.47, which can represent the limit when the contributions of the internal and external phases are equal. This means that when w is twice the thicknesses crossed by the electron beam, the system reaches a tipping point. Therefore, for high values of the aspect ratio, understanding the phase profile without the stray field appears extremely difficult.

Furthermore, after attempting to change the permittivity ε_r, we find that this coefficient does not respond significantly to the permittivity of the medium. Because, despite a slight change in the stray field caused by a change in the difference in permittivity between the vacuum and the dielectric, this effect, while present, has a negligible effect on the phase shift.

3.II.C. Phase Shift Reduction Due to the Presence of a Conducting Layer of Different Aspect Ratios.

We now know that conducting layers on the surface eliminate any stray fields and partially screen the charge density within the sample. However, we previously demonstrated that the contribution of the stray field to the phase profile depends on the aspect ratio w/t. As a necessary consequence, for each aspect ratio, it is interesting to investigate the reduction caused by the conducting layers versus a simple capacitor. For each aspect ratio, two models are calculated in parallel, with and without conductive layers. The ratio of the phase maximum with and without conducting layers is then calculated (Figure 3.21).

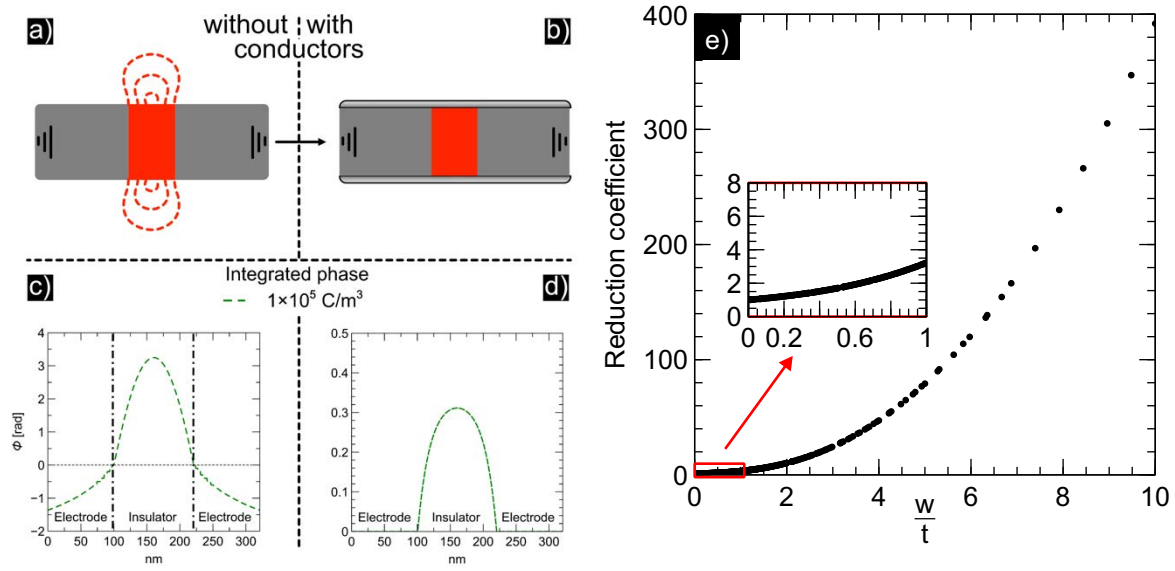

Figure 3.21 : Effect of the conductive layers in surface to a model capacitor. Left: schemes a),b) and phase profiles for each case respectively c),d). Right, the reduction coefficient as a function of the aspect ratio e).

Figure 3.21(e) shows that when the dielectric thickness is much greater than the dielectric width (*i.e. w*/*t* tends towards zero), the reduction coefficient tends to one for an infinite capacitor. This is due to the absence of stray fields when *t* is much larger than *w* the contribution of the stray field on the phase profile is thus minimal. Conversely, when the aspect ratio increases, i.e. when the stray field contributes significantly to the total phase profile, the reduction coefficient tends to infinity. In other words, when the thickness of the dielectric is much lower than the width of the dielectric, the addition of the conductor removes all of the fields that compose the phase profile.

The analysis of the phase of the grounded model shift for multiple geometries is meaningful. We can see that the stray field contributes significantly to the total phase shift. The presence of conductive layers can be determined by investigating the effect of the stray field on the phase image generated by the interaction of the insulator and the electron beam, which generates positive charges. Moreover, the phase shift due to charging is linear to the density while had an inverse relationship with the permittivity.

4. Model Biased Capacitors.

4.I. Introduction

The aim of this work is to study the potential inside a nanocapacitor when a bias is applied between its electrodes. From the experimental point of view, two holograms are recorded: with biasing and with both electrodes grounded ("hologram at 0 V") (3.7). Subtraction of the two allow the MIP and charge effects due to the electron beam to be removed, leaving only the phase change due to biasing:

$$\phi(x) = C_e \int_{-\infty}^{+\infty} V_{bias}\, dz \qquad (3.7)$$

Because the unwanted phenomena have been subtracted before the bias analysis, the modelling can ignore them.

For the following studies, the models were constructed identically to the previous cases except for the fact that the right-hand electrode is now polarised (Figure 3.22). The aspect ratio *w*/*t* was initially set to equal 2. A voltage applied to an electrode thus polarises the capacitor, resulting in phase image dissymmetry.

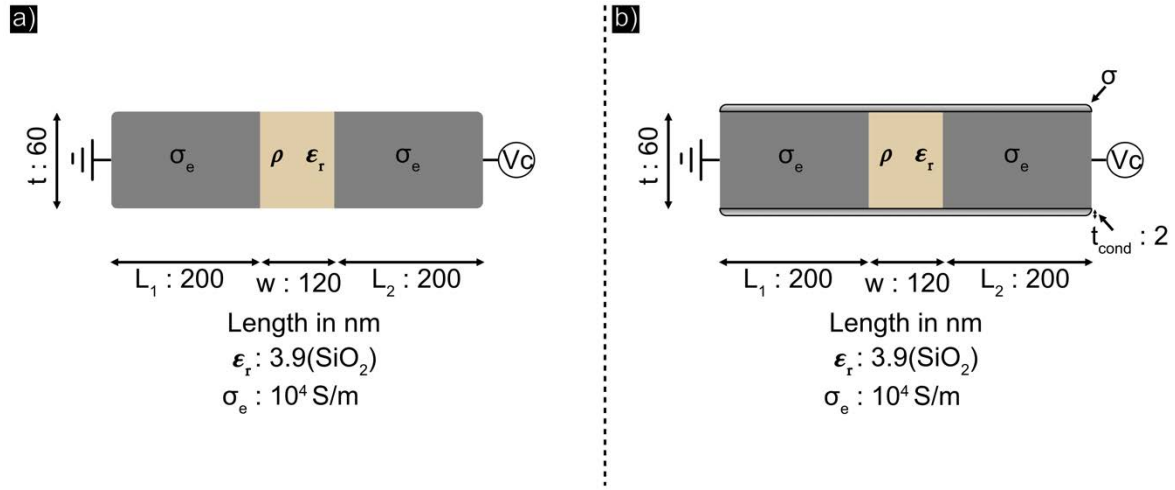

Figure 3.22 : Base model with its value parameters without conductors (1) and with conductors (2).

The conductivity of these various elements, such as the electrodes and conductors, had been purposely omitted previously because they did not previously play a role

and would only add complexity. On the contrary, the conductivity of the electrodes σ_e and conductive surfaces σ is now more important to understand what is happening in the biased model. Several parameters have been investigated, including bias V_c, sample thickness, and the presence of a conductive layer in surfaces.

4.II. Phase Image Study

4.II.A. Applied Biased Analysis

By accumulating charges on the electrode plates, a biased capacitor stores energy. These charges and the energy increase with the bias and the permittivity of the dielectric between the electrodes.

Figure 3.23 shows a comparison between biased capacitors without (a) and with (b) surface conducting layers. Biasing the two model capacitors to 1 V results in two potential distributions. The stepped colour map depicts the isopotential and its local intensity, which decreases as it moves away from the electrodes. This highlights the relationship between the stray field and the curvature inside the electrodes.

Another point to consider is that the symmetry of the models implies symmetry in the potential, which is not always the case, as will be demonstrated experimentally in the following chapter.

In marked contrast for grounded conductor capacitors, we observe that the stray field is generated for each case and contributes to the phase profile (Figure 3.23(c)). Because the stray field is imposed by the conductors. Unlike grounded capacitors with conductors acting as a Faraday cage, the biased capacitors have an imposed difference in potential between the two electrodes. The potential in the vacuum must therefore progress from one electrode to the other, creating a stray field. Whilst appearing very similar in the two cases, there are slight differences as we will see later. Furthermore, the local potential drops around the dielectric in proportion to the conductivity ratio between the electrodes and the conductors.

To follow the exact same experimental procedure for the data analysis, each simulation was subtracted from a slope calculated by fitting a straight line into a defined area of the left electrodes.

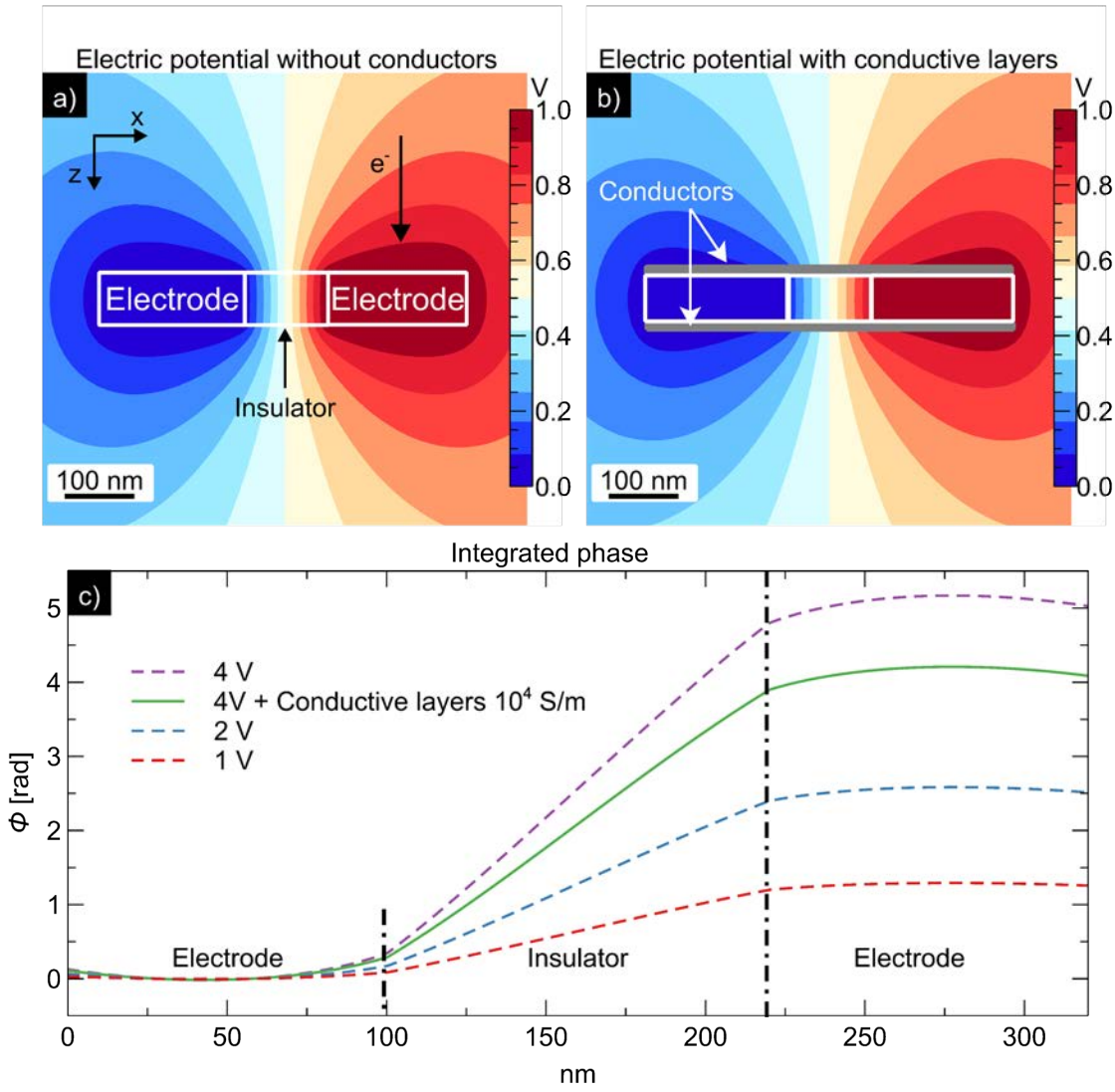

Figure 3.23 : Potential map of a biased capacitor a) without and b) with conductive layers at the surface when applying a bias of 1 V. The conductivity of these layers is of $10^4\ S/m$. c) Phase profiles calculated from a) and b) for different applied biases.

The main effect of the conducting surfaces is to reduce the local bias in the dielectric, which is visible on the potential map by a slight shift in the isopotential. This effect appears more clearly on the phase profile with a decrease of the total phase shift Figure 3.23(c).

For both cases, however, the phase shift remains linear with respect to the applied potential, as shown in Figure 3.24 by plotting and measuring the phase shift inside the dielectric area in relation to different biases.

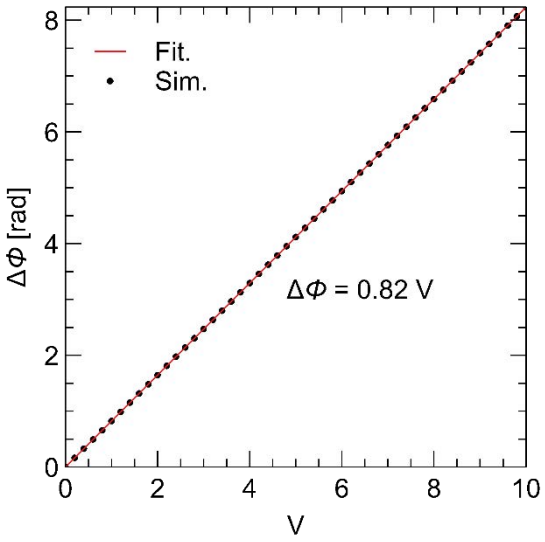

Figure 3.24 : Phase shift into the dielectric $\Delta\phi$ versus the applied bias for the model capacitor.

The phase shift $\Delta\phi$ increases linearly with the applied bias in the case of the model without conductive layers with a slop of around 0.8 related to the geometry used here (aspect ratio of 2), as we will see in the following section.

4.II.B. Evolution of the Phase Shift as a Function of the Dielectric Aspect Ratio

As previously studied for the grounded capacitor, the total phase shift results from internal and external contributions. The balance between these contributions is also extremely sensitive to the geometry of the model, and concerns here both models (with and without conductive surfaces). As a result, the phase shift between the electrodes of the simple capacitor will be affected not only by the applied bias but also by the geometry. The values of w and t are taken in the same ranges than previously. At first, we plot the phase shift as a function of dielectric thickness t and width w for a bias of 1 V (Figure 3.25).

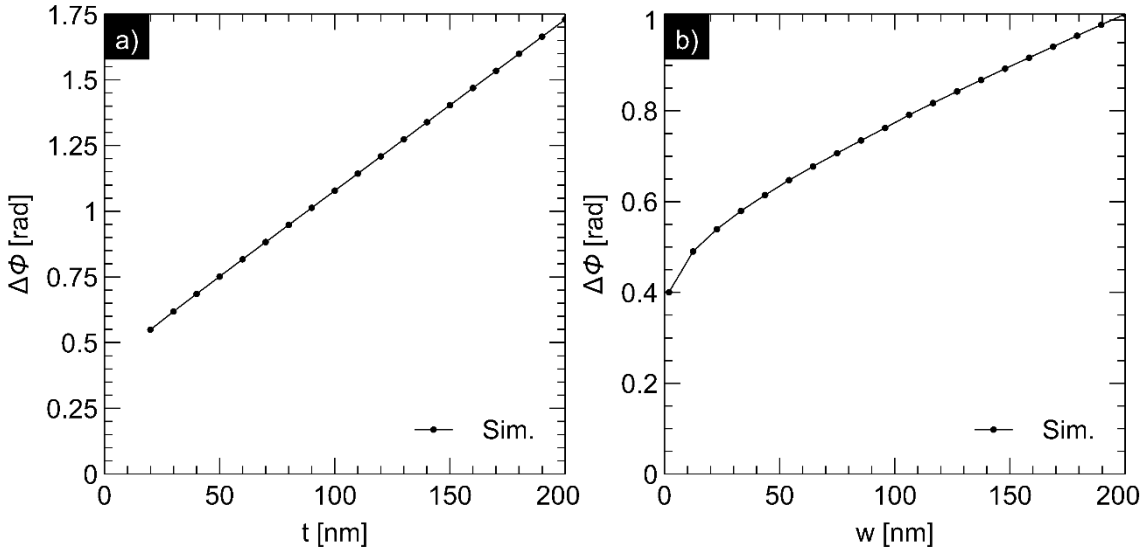

Figure 3.25 : Left: phase shift as a function of the thickness **t** crossed by the electron beam a). Right: phase shift as a function of the dielectric width **w** for the same bias b).

The phase shift in relation to *t* is linear (Figure 3.25(a)) contrary to *w* (Figure 3.25(b)). The non-linearity when varying *w* is caused by the stray field of each electrode, which compensates each other in a non-linear way as the electrodes get closer. This effect can be imagined using a simple model consisting of two charges with opposite signs that are brought together until they cancel each other out. When the two electrodes get closer together, the stray field drops very quickly, as does the phase shift. Because the geometry of the model influences the slope of the phase shift in relation to the bias, I compute the slope by varying the bias from 0 V to 10 V for each aspect ratio (Figure 3.26).

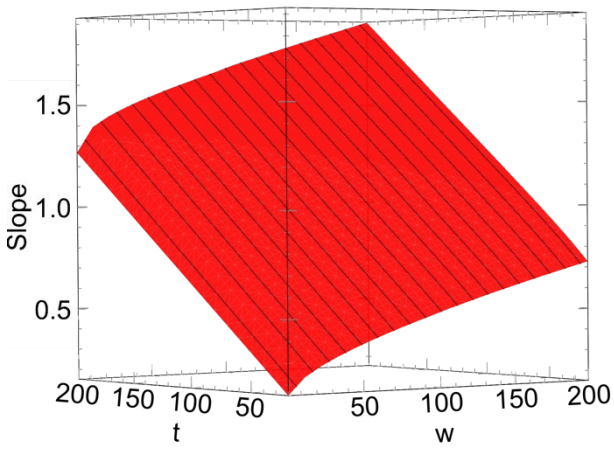

Figure 3.26 : Calculation of the phase shift slop in relation to the potential for each aspect ratio in the simple model.

The graph shows that the slope of the phase shift increases when the thickness or the length of the dielectric increase. Because the stray field is the sum of the fields produced by the negative and positive electrodes according to the principle of superposition, the increasing phase shift is caused by a weaker interaction between the stray field of each electrode as the dielectric width *w* increases. Whilst in the case of increasing thickness *t*, the increase of the phase shift is due to a greater contribution from the internal potential.

Furthermore, knowing the bias applied to the capacitor and measuring the corresponding phase shift and the dielectric width, we can use this table to calculate the thickness of the studied sample.

Other parameters, such as permittivity and electrode length, may play a role in the total phase shift. However, their contributions are much weaker as shown in Figure 3.27 for the length of the electrodes.

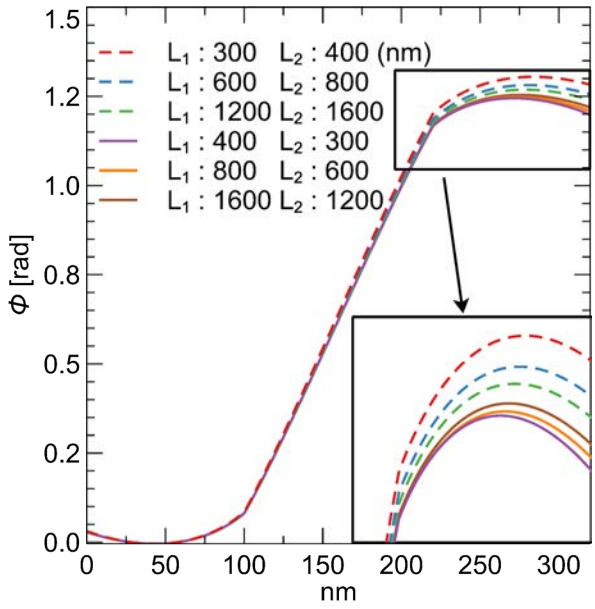

Figure 3.27 : Phase shift of a simple capacitor biased under 1 V with different lengths of the left (L_1) and right (L_2) electrodes.

When the length ratio of the left and right electrodes is equal, and the right electrode is longer than the left one, the curvature in the electrodes region appears to be highly sensitive to the length of the right electrode (represented by dotted lines). While the curvature in the electrodes region appears to be very close when the length ratio of the left and right electrodes is the same and the left electrode is larger than the right one (represented by continuous lines). This difference is caused by the realignment (slope subtraction) of the curves at the left electrode. Because the stray field around the left electrode is less sensitive to the stray field produced by the right electrode when the left electrode is larger than the right one.

On the sample we studied experimentally in the following chapter, one electrode will always be much larger than the other, so we will always take the subtraction area slope inside the left electrodes, that is, inside the silicon substrate, to be less sensitive during the measurement of the phase shift to the length of the right electrodes.

4.II.C. Evolution of the Stray Field Effect as a Function of the Dielectric Aspect Ratio

Unlike the grounded capacitor, the stray fields always exist, even in the presence of surface conductive layers. It is interesting to study the contributions of the internal

and stray fields to the total phase shift. Figure 3.28 displays the evolution of the percentage *p* of the internal contribution to the total phase for biased capacitors without (Figure 3.28(a)) and with (Figure 3.28(b)) conductive layers.

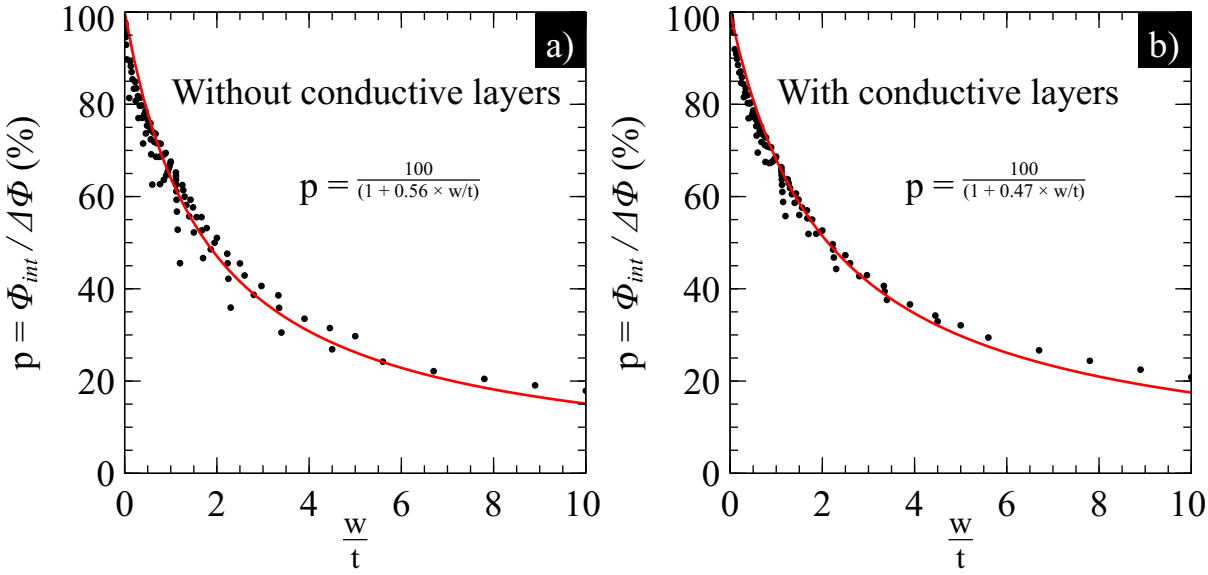

Figure 3.28 : Percentage of the contribution of the internal potential to phase shift in relation to the aspect ratio of the model with or without conductors.

The evolution of the two curves, without and with conductive layers, is very similar in terms of shape and decay, with values close to 50% for the same aspect ratio (2), indicating that the conductive layers have little influence on the contribution of the stray field to the phase shift when compared to the internal field. In fact, these coefficients are also very close to 0.47 for the grounded capacitor without conductor layers, indicating that the stray field behaves similarly to the internal field with any model.

In contrast to the grounded model, there is clear dispersion of the data points around the fit. As previously demonstrated, this dispersion is caused by the nonlinearity of the phase shift in relation to the dielectric length *w*. Furthermore, the dispersion around the curve fit differs between the models with and without conductive layers. Because the potential drop (local bias) inside the dielectric is also dependent on its geometry, the conductive layers on top of the dielectric also vary artificially as the length *w* varies. If we consider the travel of an electron from one electrode to another,

we can see that the distance travelled inside the conductive layers increases with the length of the dielectric, thereby increasing the artificial resistivity. The section that follows will go over the effects of the geometry of the model with conductive layers.

4.II.D. Effect of the Conductive Surface Layers on the Local Biased Dielectric.

The conductive layer surrounding the capacitor induces a drop in potential compared to the applied bias, which is referred to as local bias. Multiple analytical models are compared to understand the physical process induced by these layers (Figure 3.29).

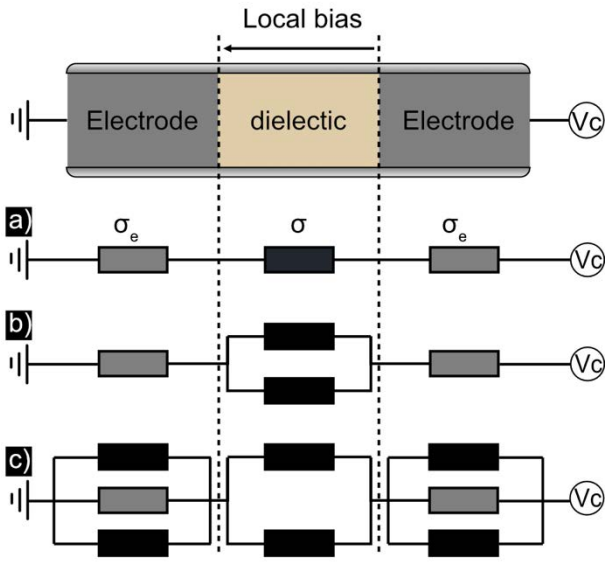

Figure 3.29 : Different analytical model tests were performed, including a series model a) and a model with only a conductive layer on the dielectric b), followed by a model with a conductive layer on the entire length of the capacitor c).

These models have been computed for a conductivity of surface layer σ from 1 to $10^6\ \mathrm{S/m}$ compared to the conductivity of the electrodes σ_e that is $10^4\ \mathrm{S/m}$. The conductivity of the surface layer is in fact rarely known. The values have been chosen between the extremes of amorphous carbon and titanium, both materials considered as possible contaminants. And because we are considering the stationary state, the capacitor is not represented. In other words, when the capacitor is fully charged, it behaves like an open circuit.

These analytical models are compared to FEM-based models in which the local bias is taken between the electrodes near the upper conductors Figure 3.30.

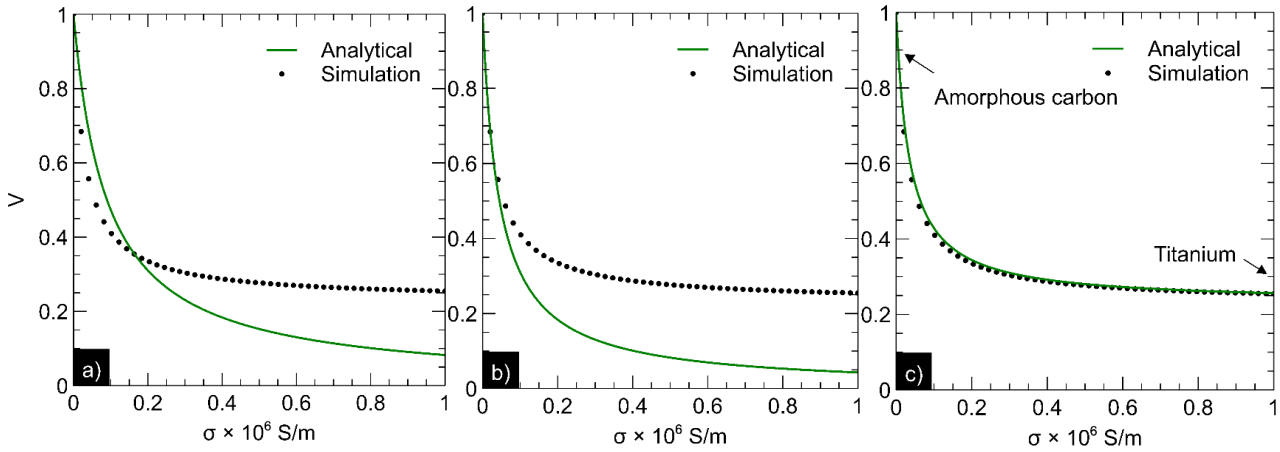

Figure 3.30 : Calculation of the local bias for the models a), b), and c) using the simulated model and the analytical model.

There is no good fit for the first two cases whereas the third captures well the variation of the local bias in respect to conductivity σ of the conductive layers. We show that the local bias is described by (3.8) by combining circuit laws of Kirchhoff and equivalent resistance.

$$\text{Local bias} = \frac{1}{\frac{2}{\left(\frac{S_e\sigma_e}{2S\sigma}+1\right)\frac{w}{L}}+1} * V_c \; ; \qquad (3.8)$$

Where V_c is the applied bias, L the length of the electrodes (same for left and right), and S_e the cross-section of the electrode in contact with the dielectric layer and the cross-section of the conductive layers S.

The conductivity ratio determines the local bias for a given geometry, and one thing to keep in mind is that when the conductivity of the conductor approaches infinity, the local bias approaches a limit and will never be 0 V as local bias even with perfectly conducting layers.

Geometry is also important. When the dielectric width w increases in relation to the electrode length, the local bias tends to V_c, whilst when the length of the electrodes approaches infinity, the local bias approaches zero because the electrodes act as two large resistors that absorb all of the potential. This is analogous to the effect of high

contact resistivity. Despite the fact that this equation was written to represent the conductivity of each element in order to create a link between the previous sections, the resistivity of each element is the parameter that really controls the local bias.

4.II.E. Charging Effect on the Biased Model

The grounded sample serves as a reference model used to subtract the charging effect and MIP for the bias capacitor. Nevertheless, whilst the MIP certainly does not change over the course of an experiment, the charging effect can change for a variety of reasons, resulting in an apparent charge density that curves the phase shift (Figure 3.31).

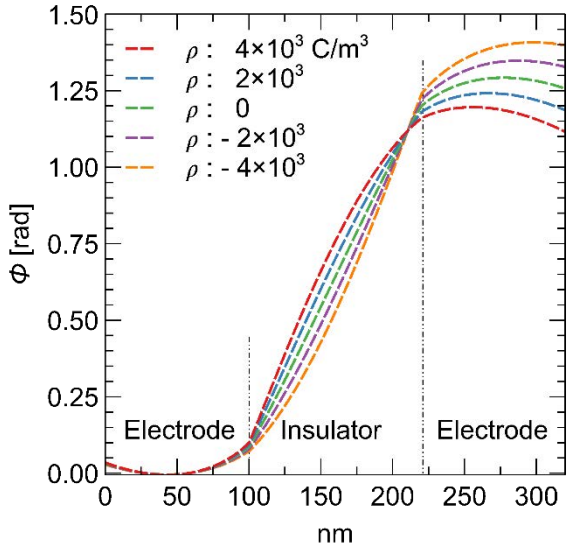

Figure 3.31 : Charging effect of the dielectric into the classical model.

These differences with the grounded state are reflected in the phase profile by a curvature into the dielectric and electrodes areas caused by the addition of the stray field from this density. The charging effect, as demonstrated previously with the grounded conductor model, has no effect on the stray field, which simply reduces the amplitude of this effect.

5. Biased Capacitors with Charge Density at the Interfaces

5.I. Introduction

Until now, we have studied perfect capacitors with charges only on the interfaces, and we have discovered (see chapter 4) that charges can be injected inside the dielectric medium. Because we work with silicon, the type of charge we inject may be electrons and holes, which means that different charge zones may form at the depth interface of the dielectric, which is to say volume. I will not go into detail on this topic because we will see this aspect of an experimental sample in the following chapter.

The injected charges will modify the phase shift by adding a component to it (3.9):

$$\phi(x) = C_e \int_{-\infty}^{+\infty} V_{bias} + V_{IC}\, dz \qquad (3.9)$$

With V_{IC} the potential of the injected charged.

This required the creation of two opposite-signed zones of charge within the dielectric. And they are predicted at the interfaces between the insulator and the electrodes (Figure 3.32).

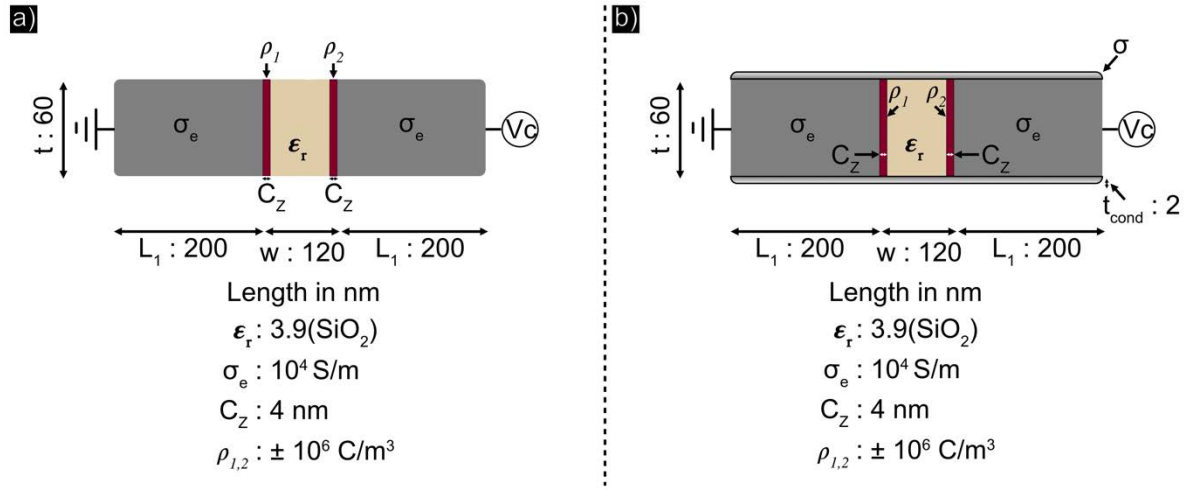

Figure 3.32 : Biased capacitors with charged density into the dielectric at these electrode interfaces without a) and with conductor layers b).

To simulate the space charge, we composed the uniform charge density on the left ρ_1 and right ρ_2 of the insulator into areas of length C_z. To be exhaustive, we will also consider charging on just one side and other configurations.

5.II. Study of Phase Profiles produced by Space Charge Density

5.II.A. Effect of Conducting Layer

The phase profiles will be similar to those of a biased capacitor, but with numerous changes caused by the space charge at the interfaces. We begin by comparing the model without and with conductors (Figure 3.33).

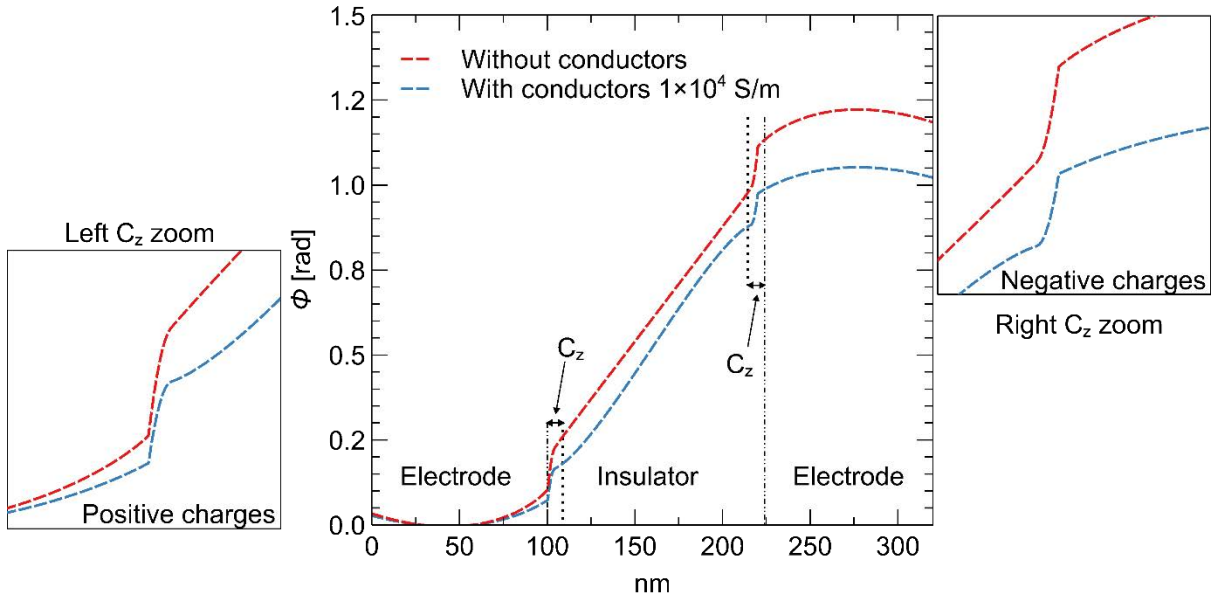

Figure 3.33 : Charging effect of two opposite charged areas inside the dielectric near the electrode interfaces.

The addition of charged areas of opposite sign on either side of the dielectric creates a negative and positive curvature within the phase image.

For the model with conductive layers, we observe a reduction of the total phase shift and of the phase shift which occurs in the charged areas. And because the conductive layers impose the stray field, we can see a slight curvature between the charged model compared to the model without conductors.

This study demonstrates the effect of conductive layer on models with charged density. Because this effect is independent of the model studied, I chose to show only

the model without conductors in the following study. However, these effects vary depending on the sign of the charge area, length, and density, as we will see in greater detail in the following sections.

5.II.B. A Single Space Charged Density Variation

To study the effect of the different parameters of the charged layers on the phase profile, we will consider in the following a single charging area as shown Figure 3.34. The applied bias is 1 V (0 V on the left electrode, +1V on the right line). The change caused by varying the width of the space charge and the sign of the charge density on the left side of the dielectric layer while leaving the right side at zero is presented on the graphs of Figure 3.34.

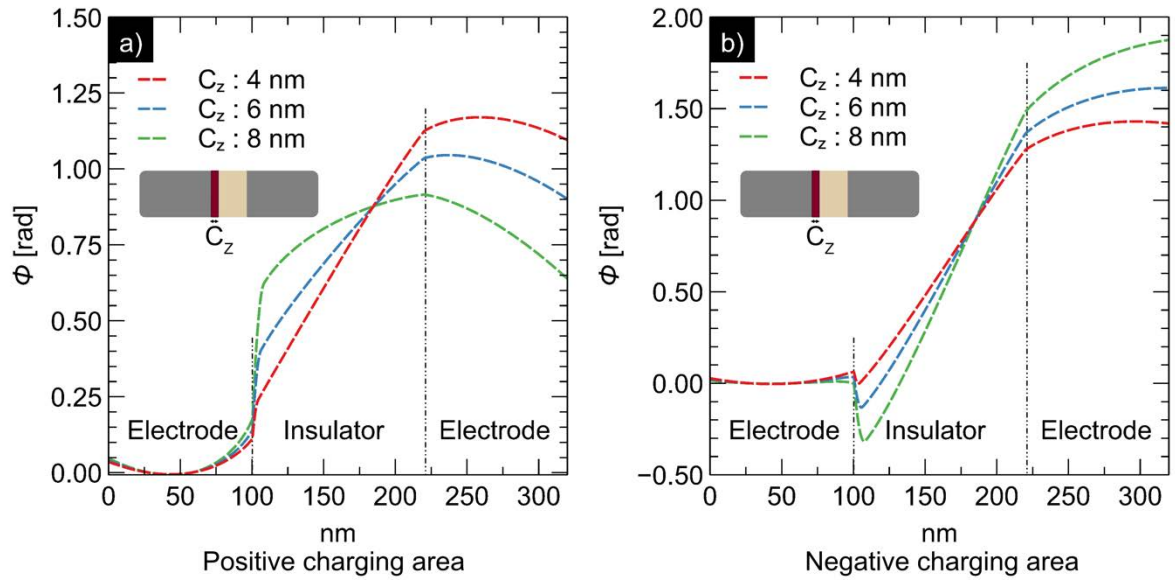

Figure 3.34 : Positive charging area on the left a) and negative charging on the right b) of the model without conductors.

In each figure, increasing the width of the charge area increases the total charge of the dielectric and consequently the curvature effect. As expected, positive charges induce a negative curvature inside the dielectric, reducing the potential drop, whereas negative charges induce a positive curvature and a larger potential drop on the right-hand figure. With this assumption, we can precisely deduce the density of charge as well as its amplitude from experimental data.

5.II.C. Two Spaces and Amplitude Charged Density Variation

In this configuration, the charge in the dielectric is of opposite sign to the charges stored by the neighbouring electrode (Figure 3.32). We compute multiple configurations of the standard model, varying the width of the space charge area and the volume charge density (Figure 3.35).

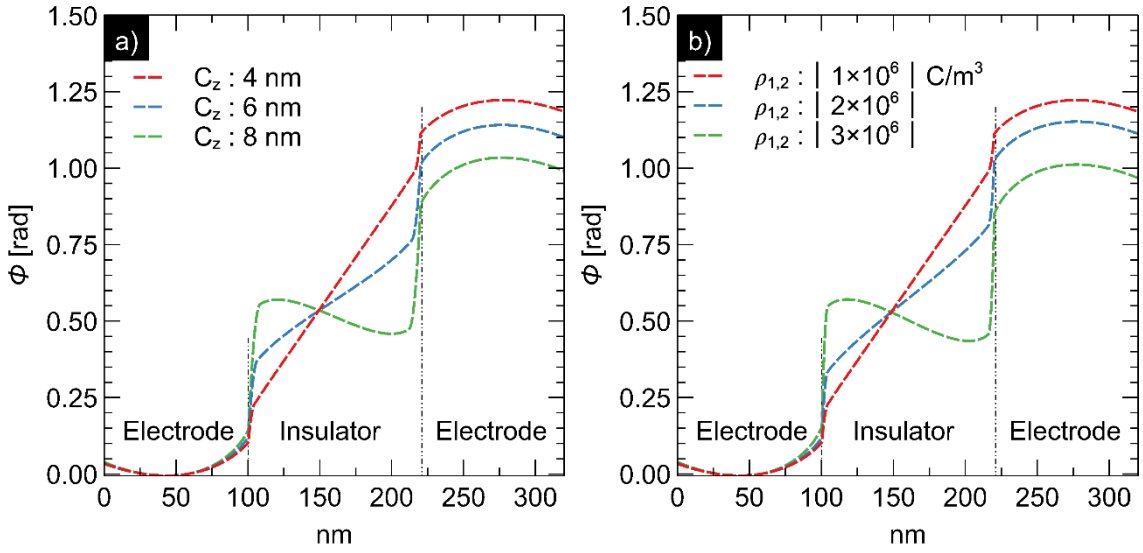

Figure 3.35 : Phase profiles of a biased capacitor (applied bias of 1 V) with charge areas of opposite sign at the interfaces. Left: Phase profiles for different area widths with $10^6 \frac{C}{m^3}$ a). Right: Phase profiles for different volume charge density with $C_z = 4\ nm$ b).

The effect of each parameter (area width and volume charge density) appears to be similar in each case, but it is not. In fact, unlike charge density, which is measured by the curvature created in the phase profile, we only measure the length of a charged density in terms of its length on the amplitude image, not its curvature strength. A comparison of these phase profiles reveals that a measurement error in the length of the charged density results in an error in the total charge. During the incertitude analysis, this effect will be more developed.

The norm of charge density can differ between charged zones; Figure 3.36 depicts this dissymmetry effect.

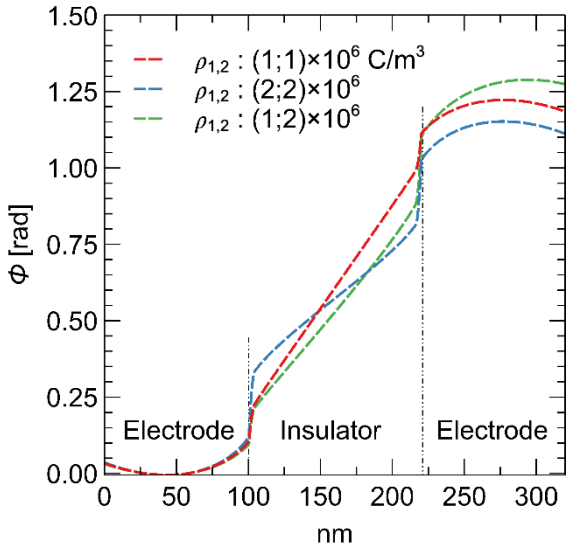

Figure 3.36 : In each charging region we modify the charged density $(\rho_1;\rho_2)$, the effect of a dissymmetry charging with a different norm is observed.

The dissymmetry effect can be seen only on the right-hand electrode, whereas a dissymmetry in the left-hand electrode would be expected. This may appear perplexing, but the dissymmetry exists in both electrodes. However we cannot see it because the profiles have been realigned to the left – i.e. the slope subtracted from each phase profile inside the left electrode area normalises this region because the phase is defined up to a constant.

5.II.D. A Space Charge Density Caused by a Change in Dielectric Permittivity.

When we combine equation (3.10) with the constitutive equation, we find that a space curvature onto the permittivity should result in a charged density, which leads to another hypothesis that could explain the density of charges in the dielectric.

$$\vec{\nabla}\vec{D} = \rho_{free} \Longrightarrow \vec{\nabla}(\varepsilon\vec{E}) = \rho_{free} \qquad (3.10)$$

$$\varepsilon\vec{\nabla}\vec{E} + \vec{E}\vec{\nabla}\varepsilon = \rho_{free} \qquad (3.11)$$

To put this hypothesis to the test, we built several models with varying permittivity within the charged area without charging them initially (Figure 3.37).

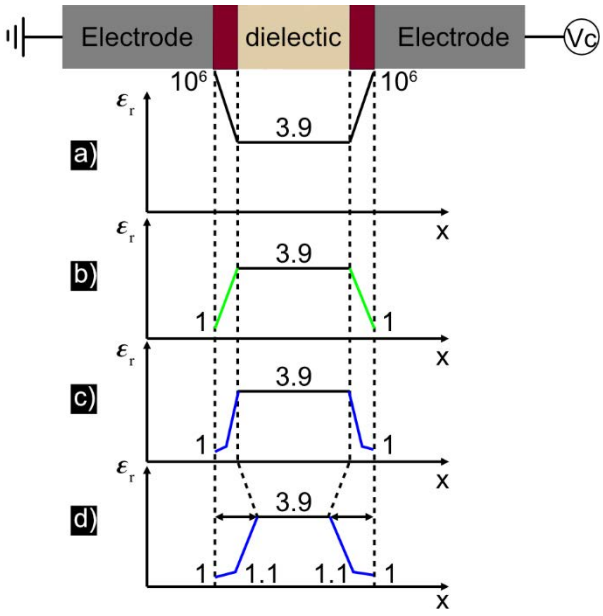

Figure 3.37 : The four models are represented as follows: With a permittivity inside the electrodes near infinity 10^6 compared to the dielectric permittivity a), and the permittivity beginning to 1 inside the electrodes b), I then broke the permittivity curve at the centre of the transition area around 1.1 c), to finish with the transition area extending from 4 nm to 10 nm d).

The first model corresponds to metallic electrodes. As a result, the relative permittivity is extremely high and a linear drop of the relative permittivity starting at the interfaces at 10^6 corresponding to near infinity in comparison to the permittivity of the dielectric that reaches 3.9 for the silicon oxide (Figure 3.37(a)). Additional models propose a relative permittivity starting at 1. We tried 3 models: they have the permittivity inside the electrode set at 1 while the permittivity of the dielectric is the same as before, the first one keeps a linear function for the evolution of the permittivity (Figure 3.37(b)), while the other two have a broken drop in the centre of the charge area (Figure 3.37(c)). Whereas the last models have a different charge area width that extends from 4 nm to 10 nm (Figure 3.37(d)). Figure 3.38 depicts the phase profiles of each model.

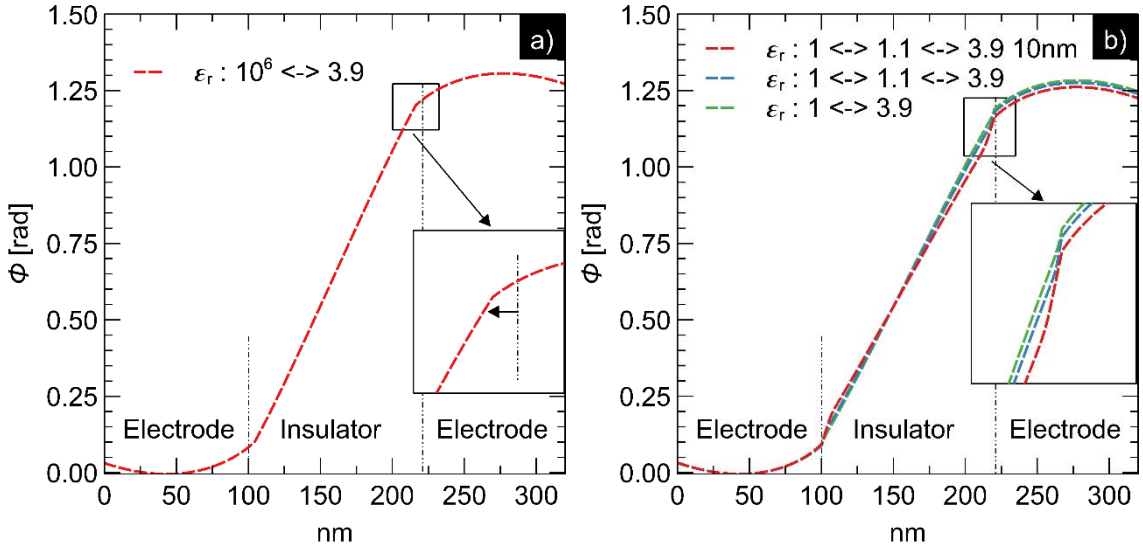

Figure 3.38 : Left: phase profile of the first model a). Right: phase profiles of three other models b).

The first model shows that curvature is absent into the space-charge area, this effect being similar to an extension of the electrode into the dielectric layer (Figure 3.38(a)). The other models work if we assume that the permittivity abruptly decreases in various atomic layers from near the infinity (electrodes) to 1 (vacuum) and then increases in the charge area until reaching the permittivity of silicon dioxide (Figure 3.38(b)). Except for the amplitude, this hypothesis produces excellent results. To magnify the effect, we have to use a broken curve, which is somewhat effective. Furthermore, we attempt to increase the length of the area from 4 nm to 10 nm in order to have a solution that is mostly comparable to the previously studied model.

However, because the effect produced by this variation never reaches the expected amplitude and is based on an improbable hypothesis, we conclude that it is not a good candidate to create curvature at the interfaces.

6. Reference Wave

To create a hologram from the studied sample, we must interfere the object wave with a reference wave where no electromagnetic field has interacted with the electron beam (in general vacuum area). In practice, this is impossible due to the geometry of the sample holder (Figure 3.39). Indeed, the sample holder is grounded and is different from the potential applied to the specimen. an electric field is therefore

created between the specimen and the holder. The reference wave is thus perturbed by this electric field, and consequently the bias measured from the phase image will be modified. We performed FEM simulations to estimate this effect.

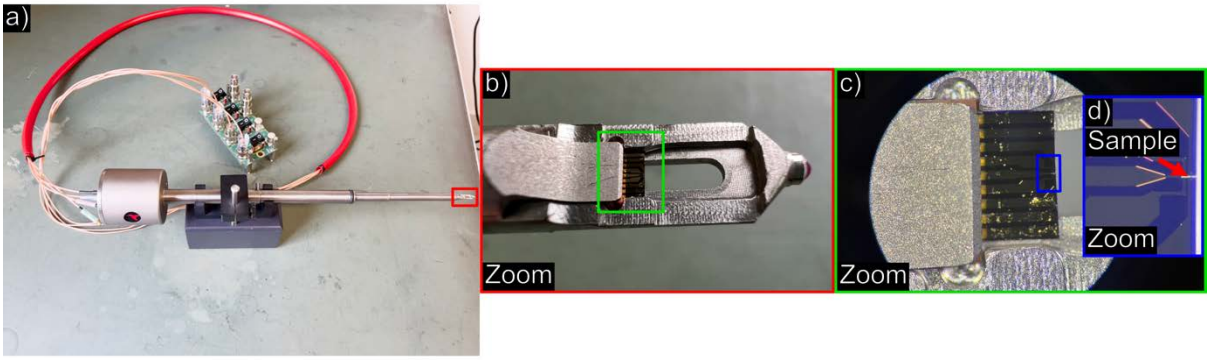

Figure 3.39 : The Hummingbird Electrical biasing holder image a), first zoom shows the tips of the holder b), then another zoom shows the Hummingbird ship c), and finally the sample contacted on the chip d).

A model of the sample holder with a 1 V biased nanocapacitor was created. To simplify, the sample holder was represented by a grounded ring with a radius of one millimetre, with the sample in the centre. The radius of the circle was chosen to be the shortest distance between the biased electrodes and the bulk of the actual sample holder. This being the worst-case scenario, if we demonstrate that the effect on the reference wave is negligible, the same will hold for the true geometry. To be consistent with the holography technique, the result of this simulation is shown as a phase image in Figure 3.40.

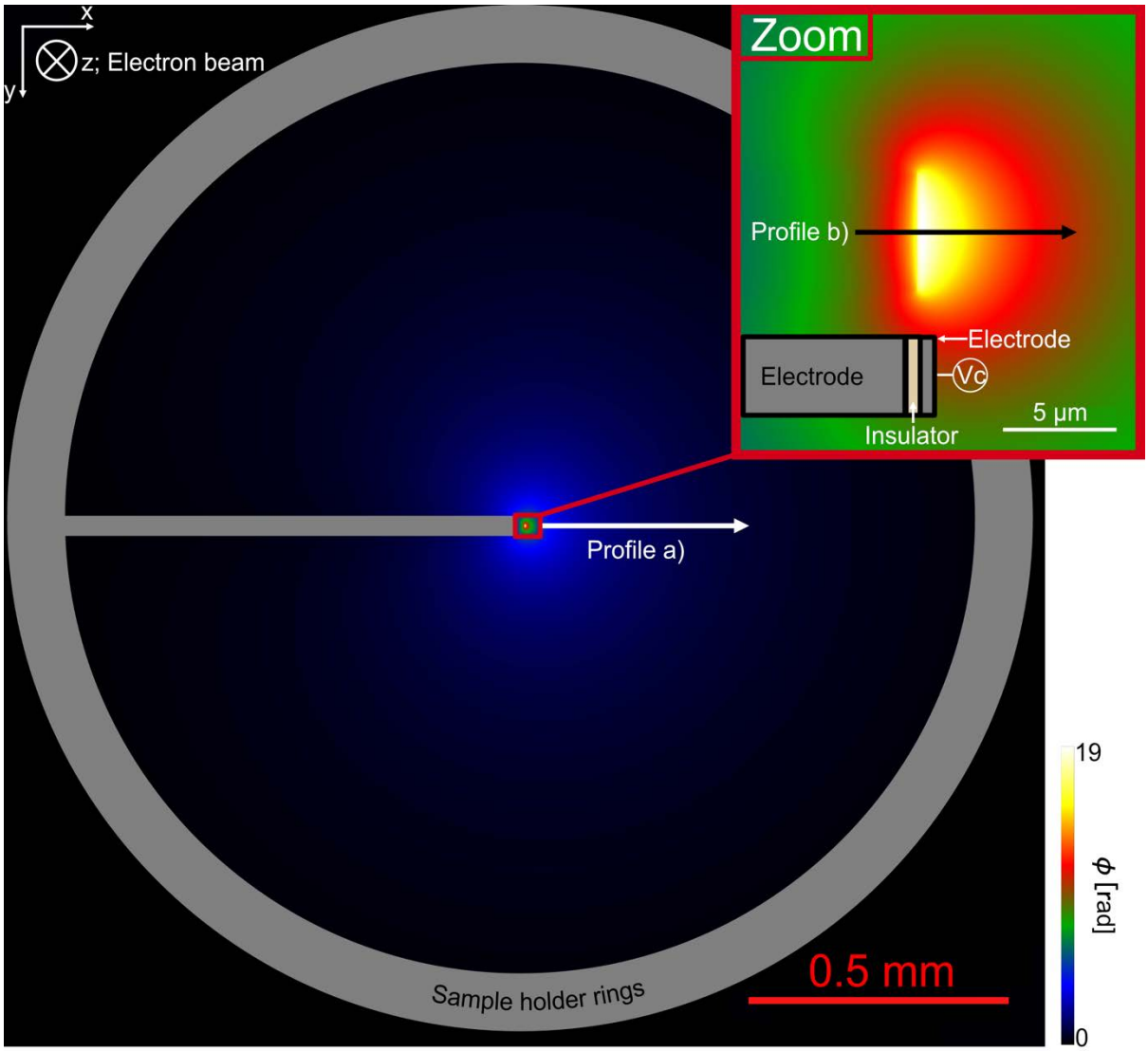

Figure 3.40 : Phase image of the whole sample holder with a capacitor biased at 1 V.

The potential distribution can be seen as a half disk centred on the specimen, and the potential decreases from the specimen to the sample holder body. Figure 3.41 presents the phase profile taken along the arrow in Figure 3.40 to compare the phase drop inside the reference area to the phase drop measured across the capacitor.

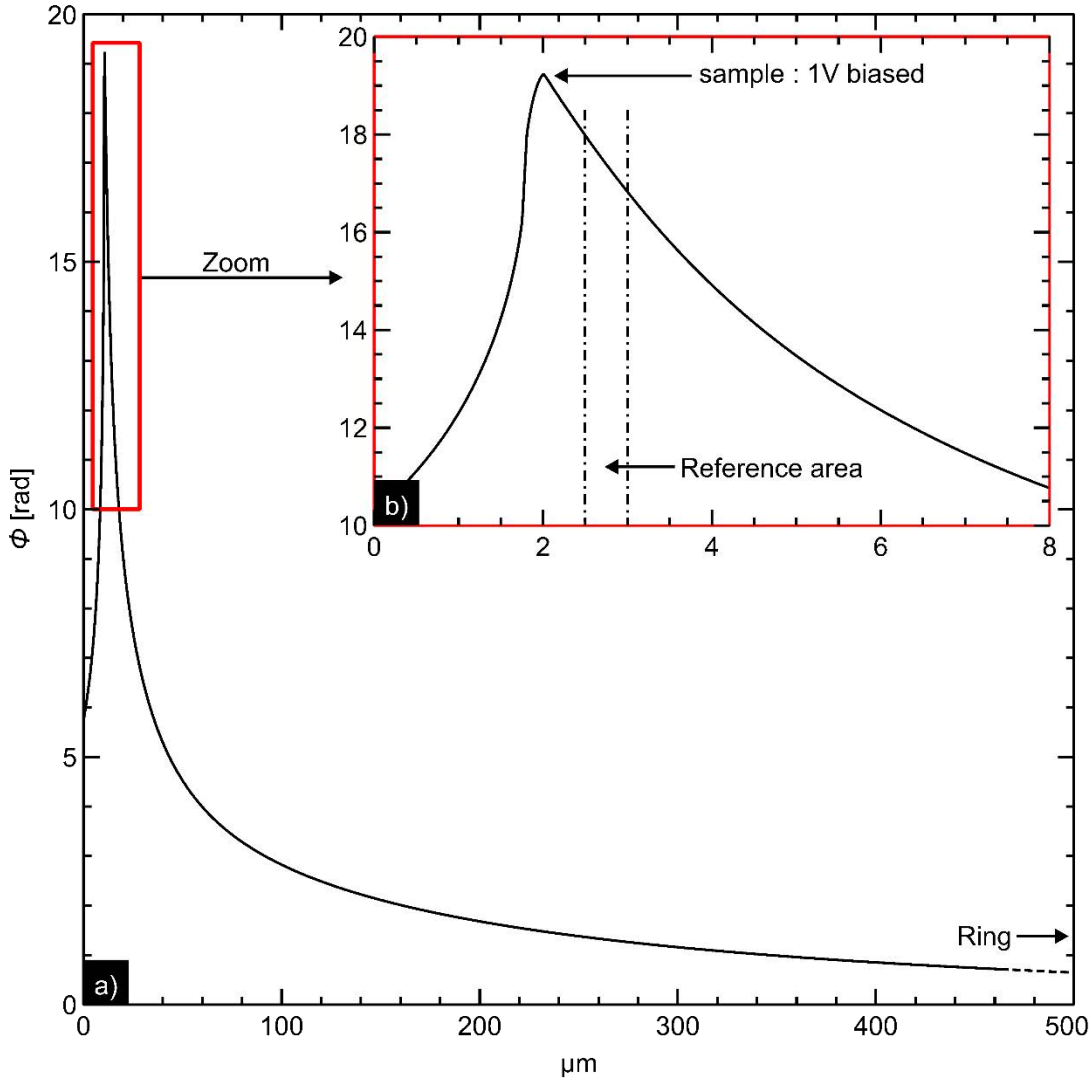

Figure 3.41 : Shows a phase profile through the sample as well as a reference area about 1μm away from the sample.

According to the profile, the phase curvature in the reference area is very small in comparison to the succession of curvatures in the working area: the associated electric field is much weaker than the one inside the capacitor. The reason is that the electric field is created on a much smaller scale in the capacitor than in the vacuum between specimen and holder. And because we subtract an average gradient during image processing, the slope into the measured phase created by the reference slope has an effect on our data only if the curvature created is of the same order of magnitude as the effects of biasing or charging.

7. Conclusion

First and foremost, we made certain that non-physical parameters did not influence the solution during our FEM analysis. To achieve this, I ran multiple studies on the simulation box size and mesh size to ensure that these parameters had no effect on the solution. We also reduced calculation time by using different mesh types and sizes in different parts of the model. In addition, a "infinity area" was added all around the simulation box allowing for more flexibility with the box size. This allowed us to change the model without having to restart the box size study for each geometry that differed from the original.

Because of the charging dielectric caused by the electron beam, phase analysis can be performed in particular when the sample is connected to the ground (0 V). If we consider a TEM sample, the stray field produced by charging is about 40% to 60% of the total measured phase, with the remainder due to internal potential. This observation contributed to the fact that we cannot extract quantitative data from experimental data without a stray field simulation.

The presence of a conductive layer around the capacitor significantly affects the phase shift. Because a conductive layer around the sample acts as a Faraday cage, eliminating the stray field outside the sample, the measured phase shift is solely due to a combination of the charges stored within the dielectric and the permittivity of the medium.

The investigation of the grounded capacitor allowed for the investigation of defects and extrinsic perturbations produced by the instrument while it also opened a way to study the biased capacitor.

First, biasing causes a phase shift inside the insulator that is proportional to the bias. The stray fields thus generated creates a phase shift curve inside the electrode area, and its contribution to the total phase is of the same order as the grounded capacitor. However, unlike the grounded capacitor, there is a stray field when conducting layers is present because it is imposed by them. Furthermore, the conducting layers produce a potential drop, which reduces local bias and can be modelled using a resistance circuit that reproduces the perfect asymptote phenomenon.

I then introduced charged density inside the biased model, which acts as a perturbation of the phase shift. These results demonstrate that not only a shift curvature is induced in each charging region that is in accordance with the Poisson law, but can also reduce the local bias and reduce the capacity.

We saw that the reference wave of the hologram can be disturbed by the stray field around the biased specimen. I showed that the perturbation is small in comparison to the phase shift caused by biasing and can be ignored in our case.

While I was only creating model capacitors to extract general system behaviour, there are numerous geometries in microelectronic devices that could also be investigated.

To take things a step further, theoretical research into ferroelectric capacitors, which have the potential to compete with SiO_2 technology, will be very interesting. I will begin to demonstrate that we can apply the theory developed in this chapter to the simulation of experimental data, which I will now present in the following chapters.

Chapter 4 — Modelling Experimental Data

Metal-oxide-semiconductor (MOS) capacitors are one of the fundamental electrical components used in integrated circuits. While much effort is currently being made to integrate new dielectric or ferroelectric materials, capacitors of silicon dioxide on silicon remain the most prevalent. It is perhaps surprising therefore that the electric field within such a capacitor has never been measured, or mapped out, at the nanoscale.

Before studying real-world microelectronic devices at the nanoscale using *operando* electron holography, we therefore chose to begin by investigating model silicon-dioxide capacitors with known and controlled materials. This allows us to test our methodology of combining electron holography and finite element method (FEM) modelling and to compare the experimental results to simulations that take into account the exact sample geometry, possible FIB damage, stray fields, and charging effects. Once a good fit for the experimental data has been established, physical parameters will be extracted from the model concerning the capacitor under observation. This chapter presents the results obtained on model silicon-dioxide nanocapacitors, including capacitors based on silicon nitride, and will reveal some unexpected physical phenomena (Gatel et al., 2022). The error analysis of this method will be detailed in an upcoming chapter.

1. Sample Preparation and TEM Experiment

Several capacitors made with different dielectrics, oxide and nitride, as well as different stacks, were specially designed for the *operando* experiments based on thin films and represented schematically Figure 4.1. They are all composed of a thin dielectric layer sandwiched between a top metal electrode and a bottom electrode of semiconductor substrate. The silicon substrates were all highly doped, either N^{++} or

P^{++} (N, P >10^{18} atoms/cm^3), to serve as a quasi-metallic bottom electrode. To ensure consistency throughout the different experiments, it is this electrode that will always be held to the ground. The dielectric layer on top of the bottom electrode will be either silicon dioxide (SiO_2), grown on the substate by dry or wet thermal oxidation with a relative permittivity of $\varepsilon_r = 3.9$, or silicon nitride (Si_3N_4 ; $\varepsilon_r = 7.5$). The top electrode will be made of titanium ($\sigma = 2.6 \times 10^6\, S/m$) or occasionally high-doped silicon ($\sigma = 2 \times 10^4\, S/m$). To be complete, a platinum protective layer was deposited during the FIB specimen preparation on top of the titanium electrode.

All of the different types of capacitors were prepared for electron microscopy analysis using a complex and lengthy procedure in the focused-ion beam (FIB) (Gatel et al., 2022). The FIB processing was performed using a FEI Helios Nanolab 600i equipped with a gallium liquid metal ion source (LMIS), an Omniprobe micromanipulator and a gas injection system (GAS). Acceleration voltages ranged from 30 kV to 5 kV for final polishing. The sample was mounted on specially designed chips for microcontacting (TEM Windows) (Figure 4.1). The Gatan *in situ* biasing sample holder and the chip are then linked together with an aluminum wireby the wedge bonding technique, which is based on a cold seal that combines pressure and ultrasonic vibration, with a Kulicke & Soffa Model 4524 Manual Ball Bonder.

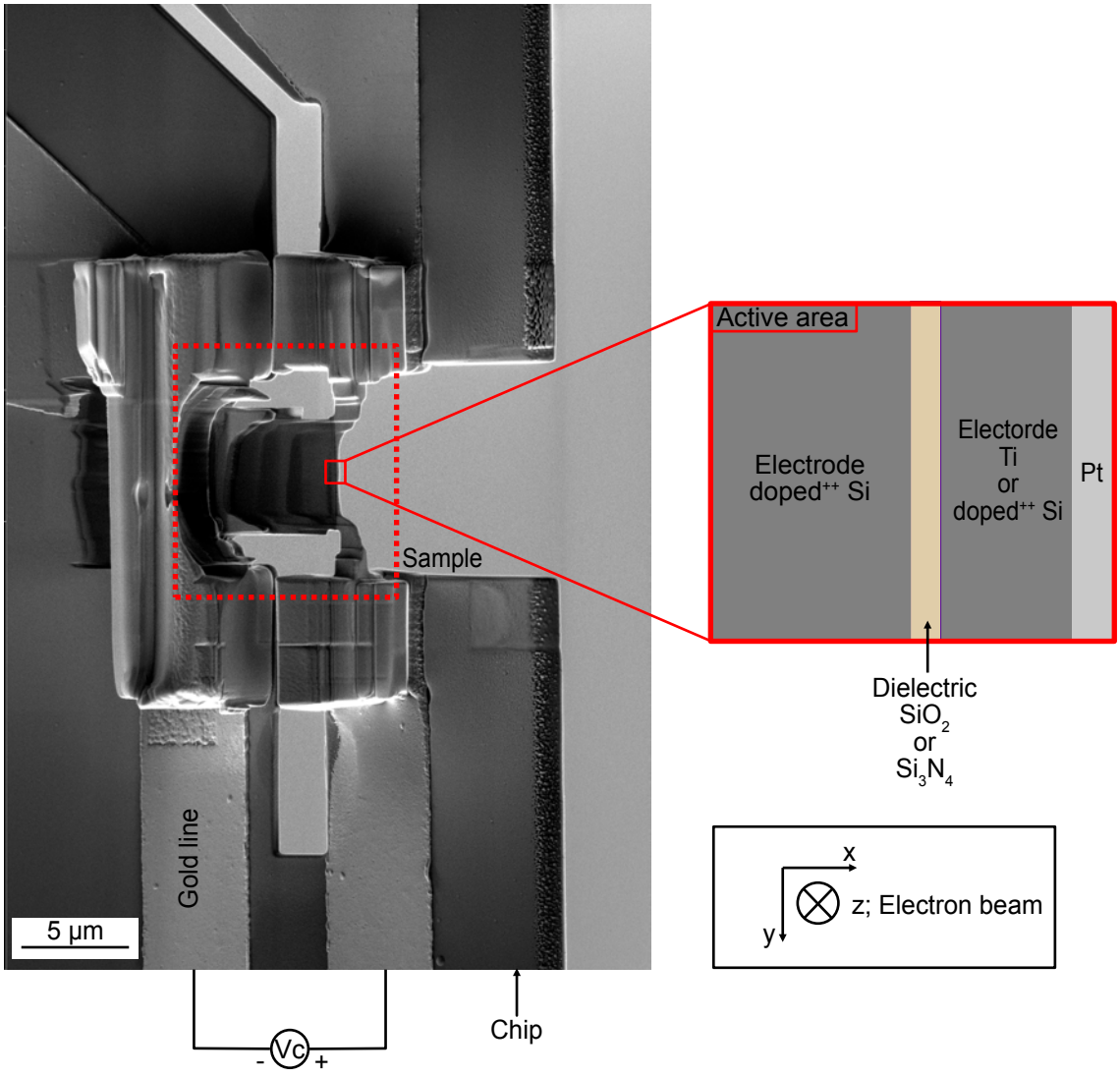

Figure 4.1 : MEB image of preparation example of a model capacitor. The gold tracks on the chip provide the potential for biasing the sample.

A dedicated setup was developed in-house using adapted switching box, cables, source meter (Keithley 2635b) and software to perform safe biasing connections and experiments while avoiding any Electrostatic Discharge (ESD) that could destroy the nanocapacitors. Indeed, these specimen devices are extremely fragile and electrically sensitive: the nanocapacitors prepared for TEM studies have a nominal capacitance of the order of 100 attofarads. Shielding and electrical protection of the connections from the sample holder to the external power supply were thus an essential part of the instrumental development.

Electron holography experiments were carried out in Lorentz mode on the I2TEM microscope (In-situ Interferometry TEM), a HF3300-C (Hitachi) equipped with a BCOR aberration corrector (Snoeck et al., 2014b) from CEOS and using 2 post-specimen biprisms to allow flexibility in the holographic configurations and to eliminate the Fresnel fringe artefacts (see Methods chapter).

2. Grounded Nanocapacitor

In a TEM, one of the advantages of using electrons rather than photons is the direct interaction between a charged particle and the electromagnetic potentials and fields in the studied system. However, other electric and inelastic interactions occur between the high-energy electron beam and the specimen, positively charging insulating components. The electrodes, on the other hand, will never be charged as they are completely compensated by currents from the ground. The process has been described in the paper (Cazaux, 1995) and I will summarise the principle as follows.
When specimen is exposed to an electron beam, the materials react by emitting secondary (SE) and Auger (AE) electrons. The emitted electrons will leave behind positives charge in the specimen. Some of the emitted electrons, however, will not have enough energy to counteract the positive potential created inside the insulator and can be reabsorbed by the dielectric. The resulting positive charge in the dielectric is an equilibrium between the emitted current and the reattracted electron current.
To investigate this phenomenon, and others not related to biasing, we studied our first model capacitor: a grounded Si-SiO_2-Si thin-layer capacitor.
Figure 4.2 shows the results of the electron holography experiment near the edge of the sample device. In particular, we analyse a profile of the phase image taken perpendicular to the interfaces, along the growth direction (x-axis) as represented by the black arrow.

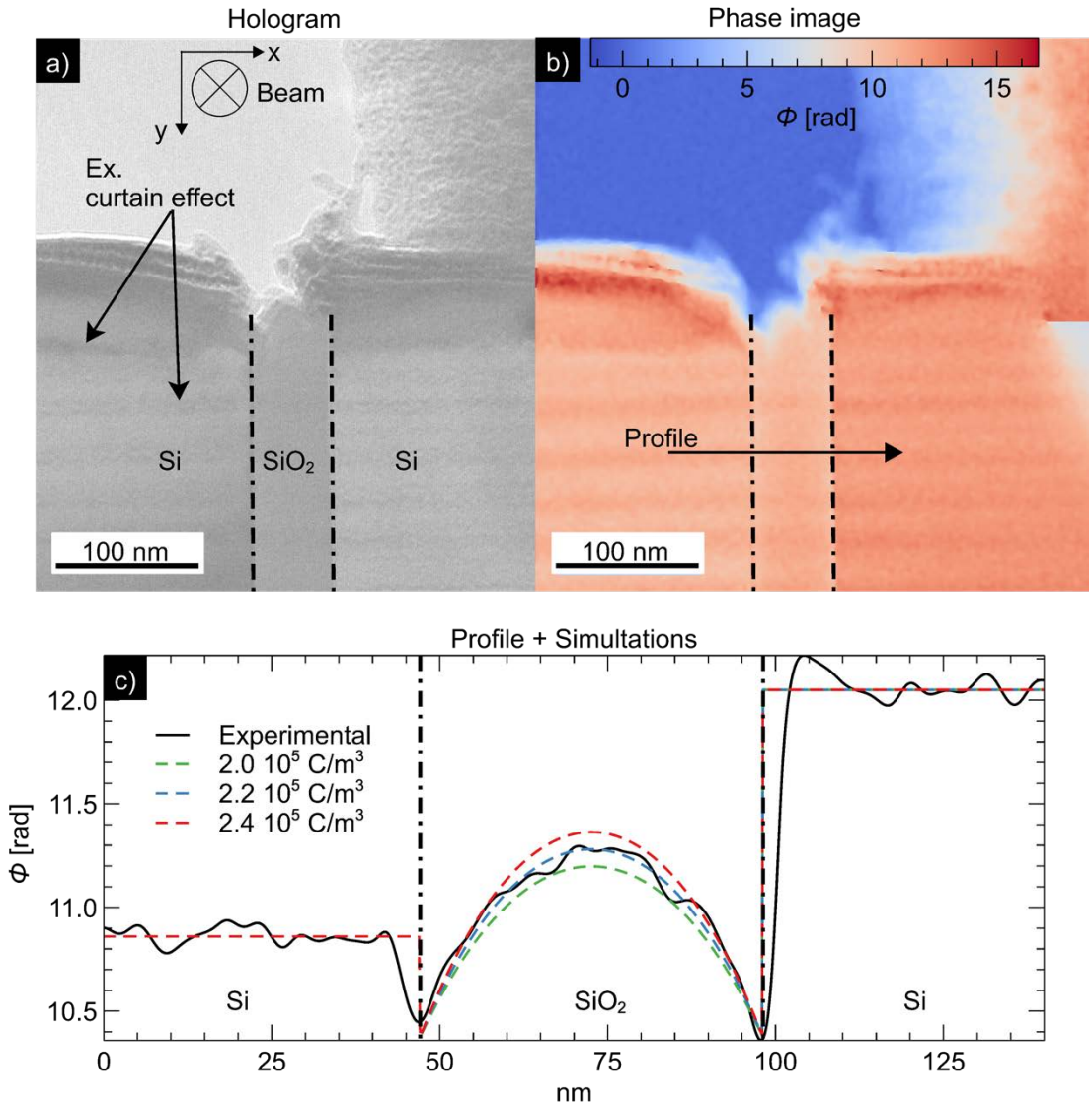

Figure 4.2 : An insulating SiO_2 layer surrounded by two Si electrodes. The corresponding hologram a) of the grounded sample, which contains amplitude and phase information, allows the extraction of a phase image b), which will be analysed further below using the simulated model c). We conclude that the capacitor has conductors surrounding it and a charge density of $(2.2 \pm 0.08) \times 10^5 C/m^3$ which fits the experimental data very well.

The different layers are directly visible in the hologram as well as the curtain effect due to the FIB preparation process. The curtain effect corresponds to slight variations of the thickness with a wave-like shape (horizontal lines in the Figure 4.2 a and b). The phase image shows the effects of both the MIP and the charging in the dielectric area from the interaction with the electron beam.

It is important to note on the Figure 4.2(c) that the value of the phase shift is constant in the electrodes. The theoretical studies from the previous chapter (3) demonstrated

that the phase should be curved in the electrodes, due to the stray field, unless there were conducting layers on the specimen surface. Therefore, we used the grounded model with conducting superficial layers, and modelled the curvature only present in the SiO_2 area with positive charge (Figure 4.3). The model has a specimen thickness, *t*, crossed by the electron beam (so parallel to the *z*-axis) of 100 nm and a dielectric width measured parallel to the *x*-axis from the experimental image of 51 nm. As no stray field is considered, the length of the electrodes does not influence the phase image: we thus set a length for the electrodes of about 200 nm even if it does not correspond to that observed.

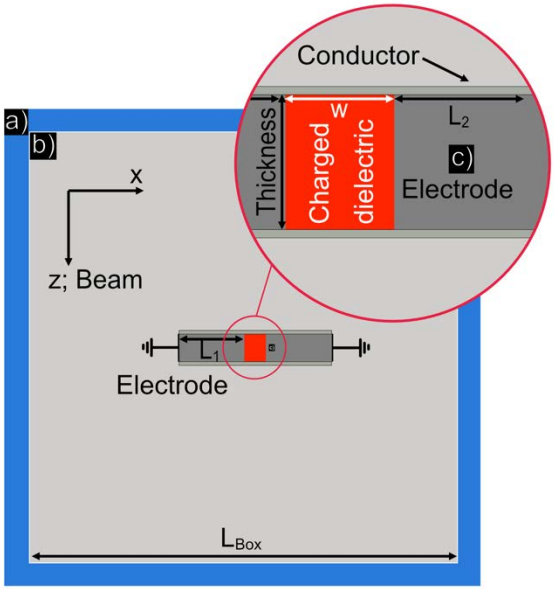

Figure 4.3 : Scheme of the grounded Si-SiO_2-Si capacitor used for the simulation.

The phase profile resulting from the FEM simulation presents a very nice agreement with the experimental one (Figure 4.2(c)). Quantitative data can then be extracted from the model and to be used to estimate the charge density of about $2.2 \pm (0.08) \times 10^5\ C/m^3$. The incertitude is calculated by considering the incertitude on the sample thickness, the dielectric width and by framing the phase noise with different charge density as shown on the phase profile (Figure 4.2(c)). The uncertainties in this example will be discussed deeply in the next chapter.

Based on the phase profile and the void area, there do not appear to be any stray fields into the vacuum. This means we could use this area to define the reference

origin, allowing the MIP contribution to the phase to be interpreted then deduce the sample thickness using the phase norm. However, because the MIP cannot be calculated and known precisely, we did not use this technique to determine sample thickness, preferring electron energy loss spectroscopy (EELS).

3. Biased Capacitor

For biasing, we studied model nanocapacitors consisting of a single layer of a dielectric, Si_3N_4 or SiO_2, and a combination of both. These two insulating materials, with different dielectric constants (ε_r = 8 for Si_3N_4 and (ε_r = 3.9 for SiO_2), are widely used in the microelectronics industry. The bottom electrode was highly-doped silicon and the top electrode titanium.

As explained previously on the method chapter, we record two holograms, with the specimen biased and with both electrodes grounded. The latter provides a reference hologram that includes the MIP contributions and all the experimental artefacts, like variable lamella thickness, damage layers, diffraction contrast, and electron beam induced charging (as seen in the previous example). The MIP and artefacts are removed by subtracting the reference signal from the holograms acquired during device operation, and the remaining phase can be attributed only to the applied electrical biasing. In the following, we will study this biasing phase.

3.I. Si_3N_4 Model Capacitor

3.I.A. First Observations of a Biased Capacitor

This nanocapacitor presents a highly-doped silicon substrate upon which was grown a 36 nm thick Si_3N_4 followed by a top electrode of Ti. The different layers can directly be seen on the amplitude image (Figure 4.4(a)) while the phase shift coming from the applied bias of -4 V appears on the phase image (Figure 4.4(b)). As explained previously, the MIP and charging effect contributions were subtracted using the phase image obtained at 0 V (grounded capacitor).

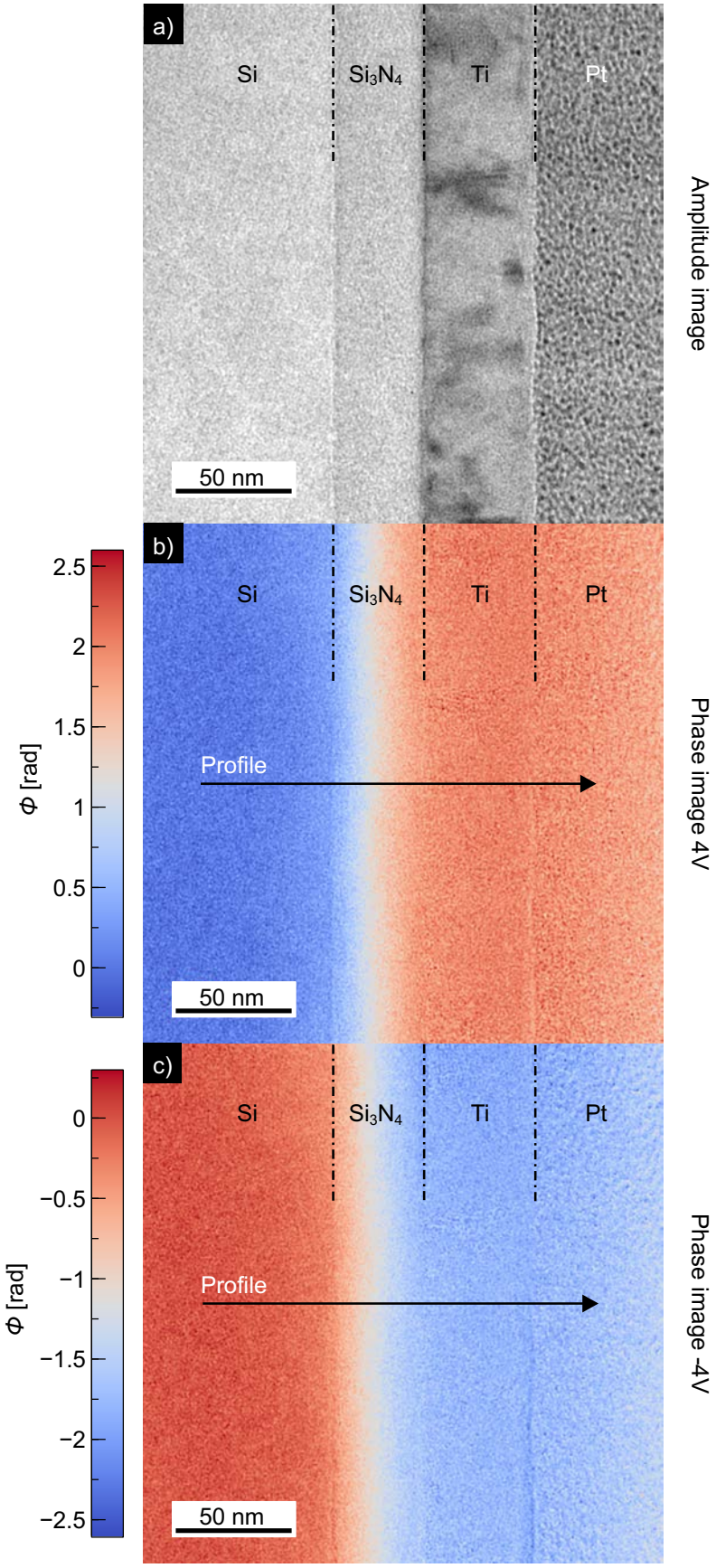

Figure 4.4 : a) Amplitude image, phase image for an applied bias of 4V b) and -4V c) after removing the phase image at 0 V.

Figure 4.4(b, c) shows a phase drop inside the Si_3N_4 dielectric meaning that the capacitor is well connected and in operation. To continue the analysis, we extracted a profile from the phase image for sample biasing of 4V and -4V, as shown Figure 4.5. The profile was integrated over 50 nm parallel to the interfaces for improving the signal-to-noise ratio. The internal reference area of the hologram was chosen, as always, in the bottom electrode.

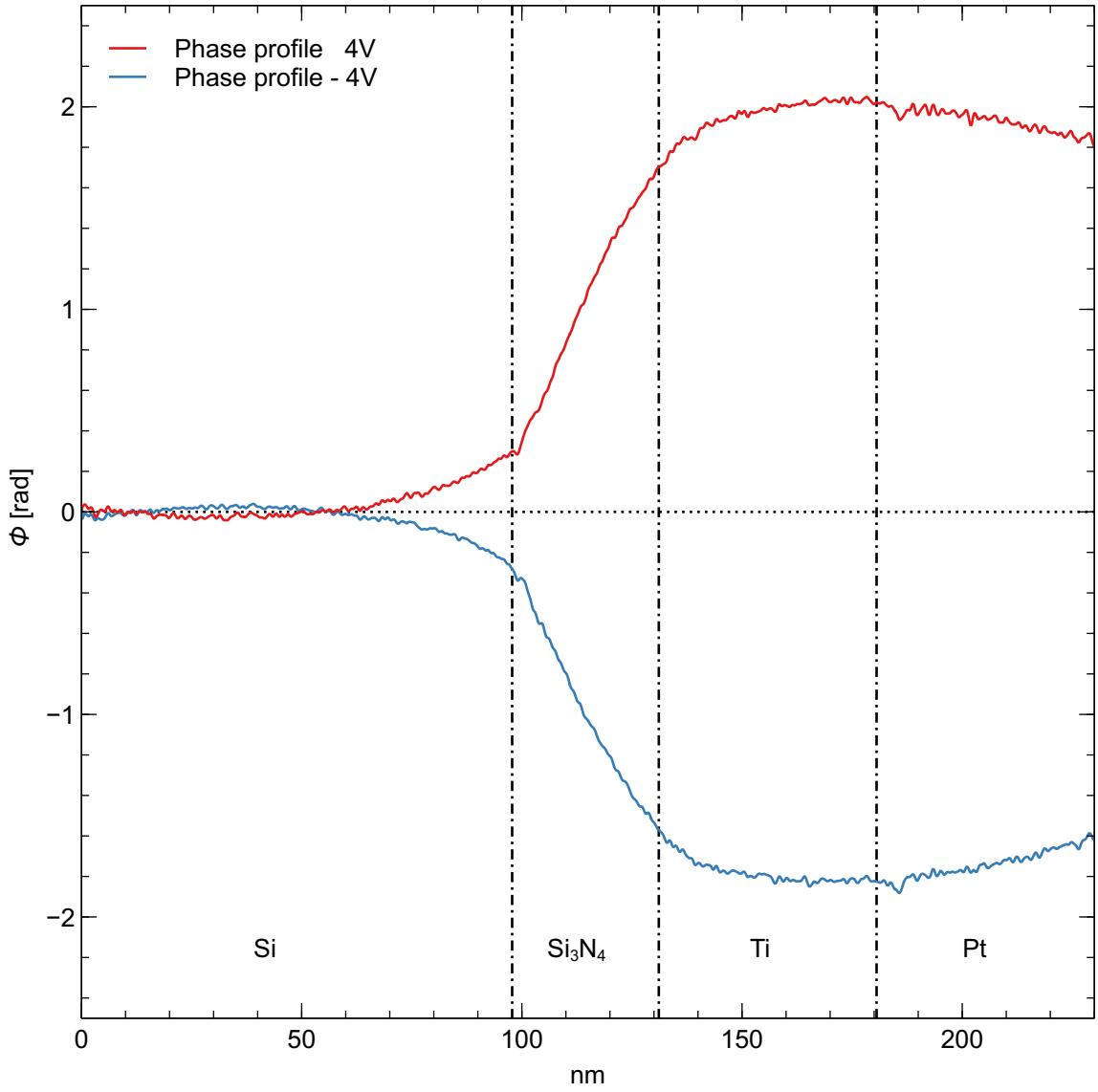

Figure 4.5 : Biased phase profile measured at 4V and -4V.

The phase profiles show a noticeable curvature in the electrodes (Figure 4.5). From the previous chapter, we can attribute this to the stray field above and below the sample. A phase change across the dielectric is significant and changes sign with the bias (as hoped). We can also note that the two curves are highly symmetric, the sum of them resulting in a curve equal to 0.

3.I.B. Fitting Method on Bias Capacitor

FEM simulations were performed using the spatial parameters measured from the amplitude image (width of the different layers) and by adjusting the specimen thickness crossed by the electron beam, measured using EELS). A phase profile was extracted from the simulated and integrated potential within COMSOL as described previously.

Figure 4.6 depicts the model used to fit the experimental data, followed by a step-by-step explanation of the method used to fit the experimental data.

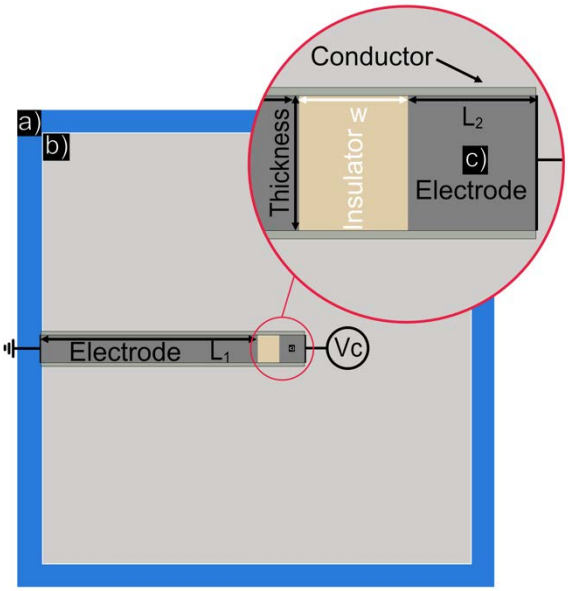

Figure 4.6 : Grounded model with conducting layers used during the simulation of the sample Si-Si_3N_4-Ti.

To simulate the experimental profile, we must proceed step by step. A simple analytical model could not be used, notably because of the stray field. Similarly, a simulation based solely on observed geometry was found to be insufficient to explain

the experimental data after much trial and error. To find a satisfactory solution, I ultimately had to introduce damage layers from the FIB preparation into the model as detailed below.

The progression from an analytical model to a finite element model is illustrated in Figure 4.7 which focuses on the sample polarised to a bias at -4 V. First, we used a purely analytical solution to calculate the potential distribution of an infinite capacitor (Figure 4.7(a)). With this knowledge, the phase profile is compared to the experimental data by calculating the phase profile from the integral potential distribution (Figure 4.7(b)). That is, we used the first part of the equation (see chapter 2 (eq. 1.42)) to integrate the potential profile across the sample thickness. We did not yet introduce the stray field, so the fit is not yet consistent with the experimental data, as expected.

To introduce the stray field, we must first produce a model capable of simulating it while accounting for the non-infinite geometry of the sample. We cannot calculate the stray fields analytically due to the relatively complex geometry of the sample, so we have to solve the problem using finite elements.

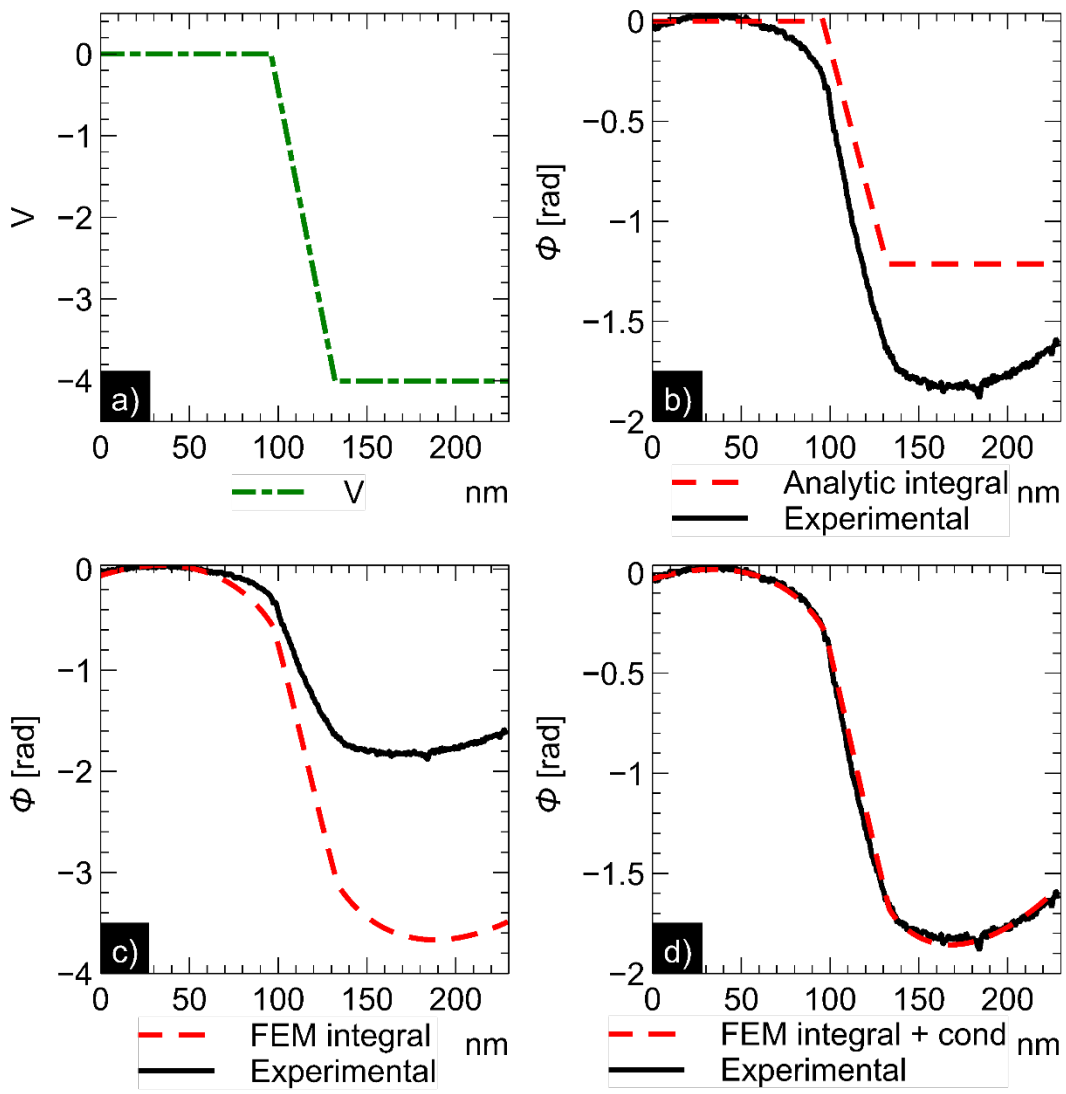

Figure 4.7 : Developing the best fit from the potential profile (a)-(d). Going through multiple steps, such as a phase profile (b) then without conductors (c).

On Figure 4.7(c), we can see the curvature inside the electrodes after performing FEM calculations, which is typical of stray fields. As a result, the simulation value is becoming increasingly consistent with the experimental data (Figure 4.7(c)).

Due to the addition of the stray field, the simulated phase shift is now larger than the experimental curve, in contrast to the previous fit. To reduce the phase shift and achieve a good fit, conducting layers were added around the sample (Figure 4.7(d)). Indeed, because the sample needed to be refined before being examined with an electron microscope, a gallium-based focused ion beam was used. As a result, a few

nanometres of slightly conductive layer could be likely deposited around the sample, causing the capacitor to be partially shorted.

3.I.C. Final result

The final comparison of simulated and experimental phase profiles is shown (Figure 4.8(c)).

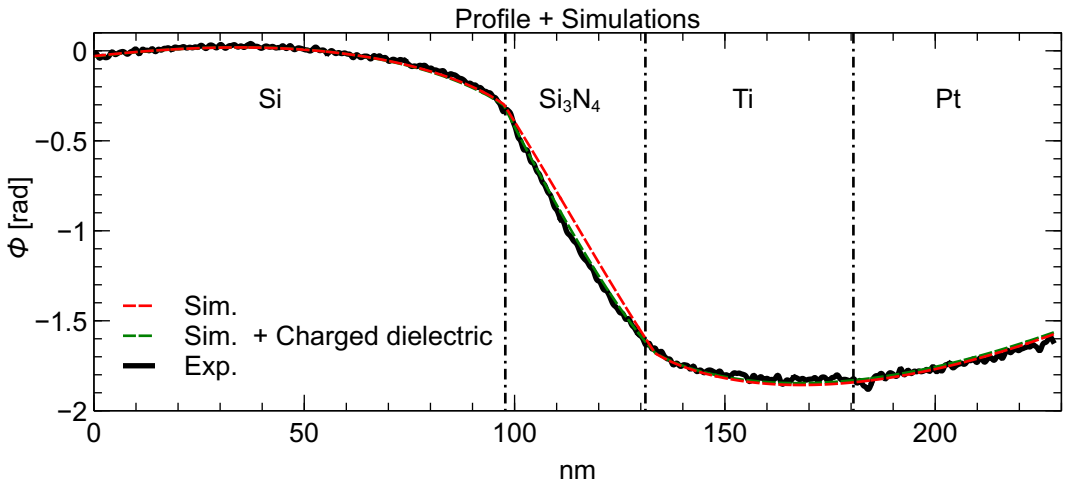

Figure 4.8 : Phase image for an applied bias of -4V after removing the phase image at 0 V, comparison between simulated (dotted red line) and simulated (dotted green line) profiles.

Except for the dielectric area, the simulated profile shows a perfect agreement with the experimental profile. The slight deviation between the simulated and experimental profiles inside the dielectric area is intriguing and might be due to an injection of electrons and hole from the electrode by Fowler-Nordheim tunnelling charge injection model (Li and Chen, 2012). For example, under a negative biasing with negative charging, there is a hole injection from the Si electrode while there is an injection of electrons from the Ti electrode. In this case there are more injected holes than electrons. This could be further explained by taking into account the energy barrier between the Si/Si_3N_4 and the Si_3N_4/Ti junctions, different for electron and hole injection. Whereas on the positive bias profile (Figure 4.5), there is a positive charging implying that these effects are reversed. To complete these proposals, an energy barrier study should be performed later with the Si doping being into consideration. We can also say that this effect was only observed in the Si_3N_4 sample and not in the

SiO_2 sample, as we will see later. As a result, charged density inside the dielectric has to be introduced to obtain a perfect fit ($2 \times 10^5 C/m^3$), which is plot in doted green line.

This study demonstrates that the applied macroscopic bias does not necessarily reach the dielectric entirely. In fact, the potential drop across the dielectric is approximately (-2.2 ± 0.2) V whereas the applied bias was approximately -4 V in this case. This potential drop between applied bias and the local bias can be attributed to the conductive layers surrounding the sample, and the simulation allows us to estimate the conductivity to be around 660 S/m with 2 nm thick layers of conductors, while the sample thickness is estimated with the simulation to be around 46 nm. This first result suggests that extreme care must be taken with the final polishing in the FIB to make the phase data more readily interpretable.

3.II. SiO_2 Model Capacitor

The next example is a sample device made from a thin film of 120 nm thick thermally grown silicon dioxide on a highly *p*-doped silicon wafer topped with a titanium electrode. The thickness of the lamella was measured to be 55±5 nm by EELS. After connecting the top electrode to the chip with locally deposited platinum and inserting it into a dedicated TEM biasing holders, positive, negative, or zero biases were applied in situ to the top electrode. This sample is the object of the study presented in (Gatel et al., 2022).

3.II.A. Comparison Between Experimental Data and Simulation

Holograms were collected in the region depicted in Figure 4.9(a) and the corresponding phase image for a positive 5 V bias is shown in Figure 4.9(b), where we can see the change in phases across the SiO_2 dielectric. The sample was also subjected to voltages ranging from -5V to 5 V with 1 V steps. The phase noise is less than 10 mrad for a spatial resolution of 0.8 nm. The phase was corrected using the hologram of the grounded sample, and an internal reference region within the silicon substrate was used. Profiles were taken in the same area of each phase image and averaged over 100 nm parallel to the interfaces to improve the signal-to-noise ratio of

the phase images. The best-fitting simulation for the experimental data at 5 V is shown Figure 4.9(c).

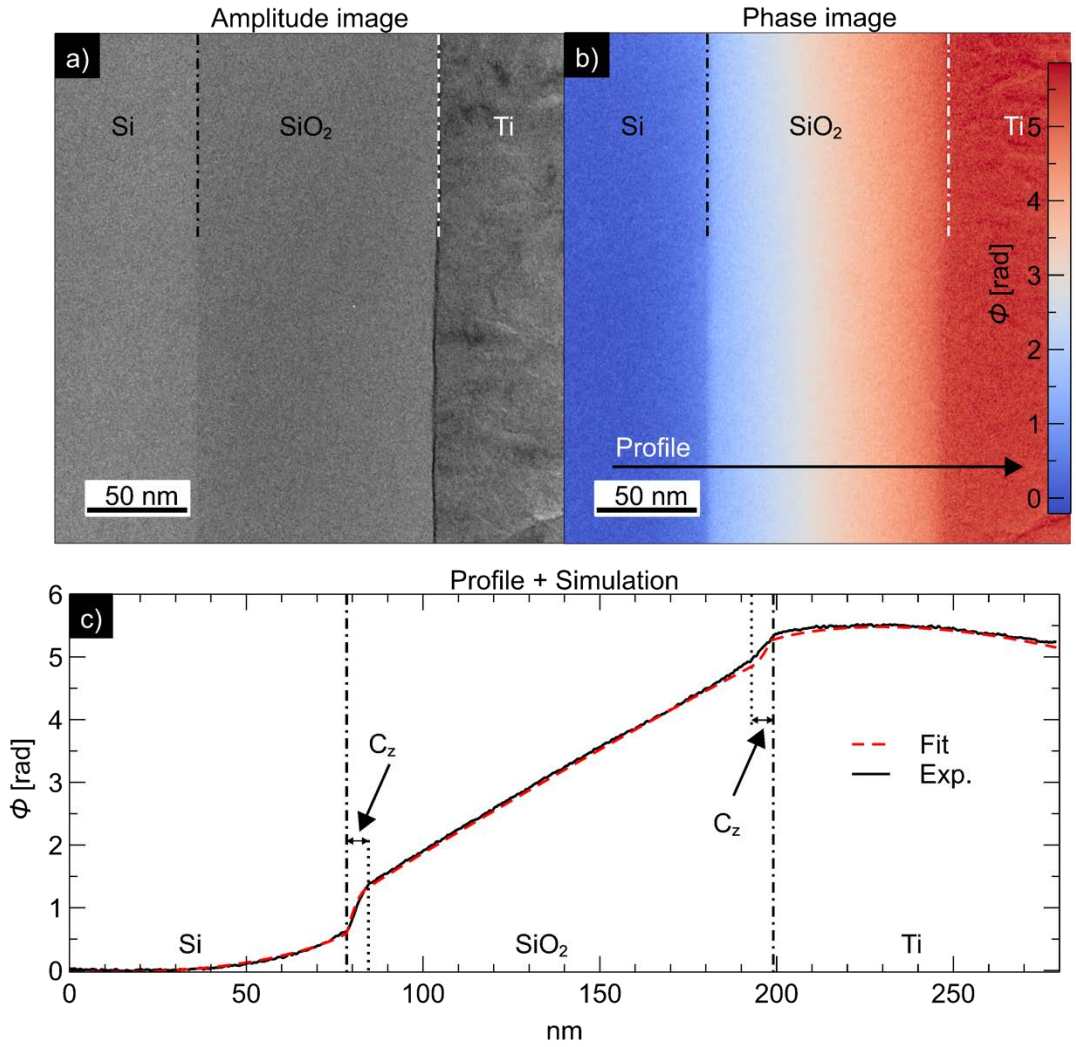

Figure 4.9 : Amplitude image a) corresponding to the area phase image b) where a profile was taken and can be seen on the plot c). The applied bias between both electrodes is equal to 5 V.

The phase change across the capacitor can be seen clearly and increases linearly with applied bias (Figure 4.10), as expected from (see chapter 2 (eq. 1.42)). However, the phase is not constant in the regions corresponding to the electrodes, whereas we would expect the electrodes to be at a uniform potential. This is due to the fact that the phase is also sensitive to the stray field above and below the sample (Aizawa et al., 2017).

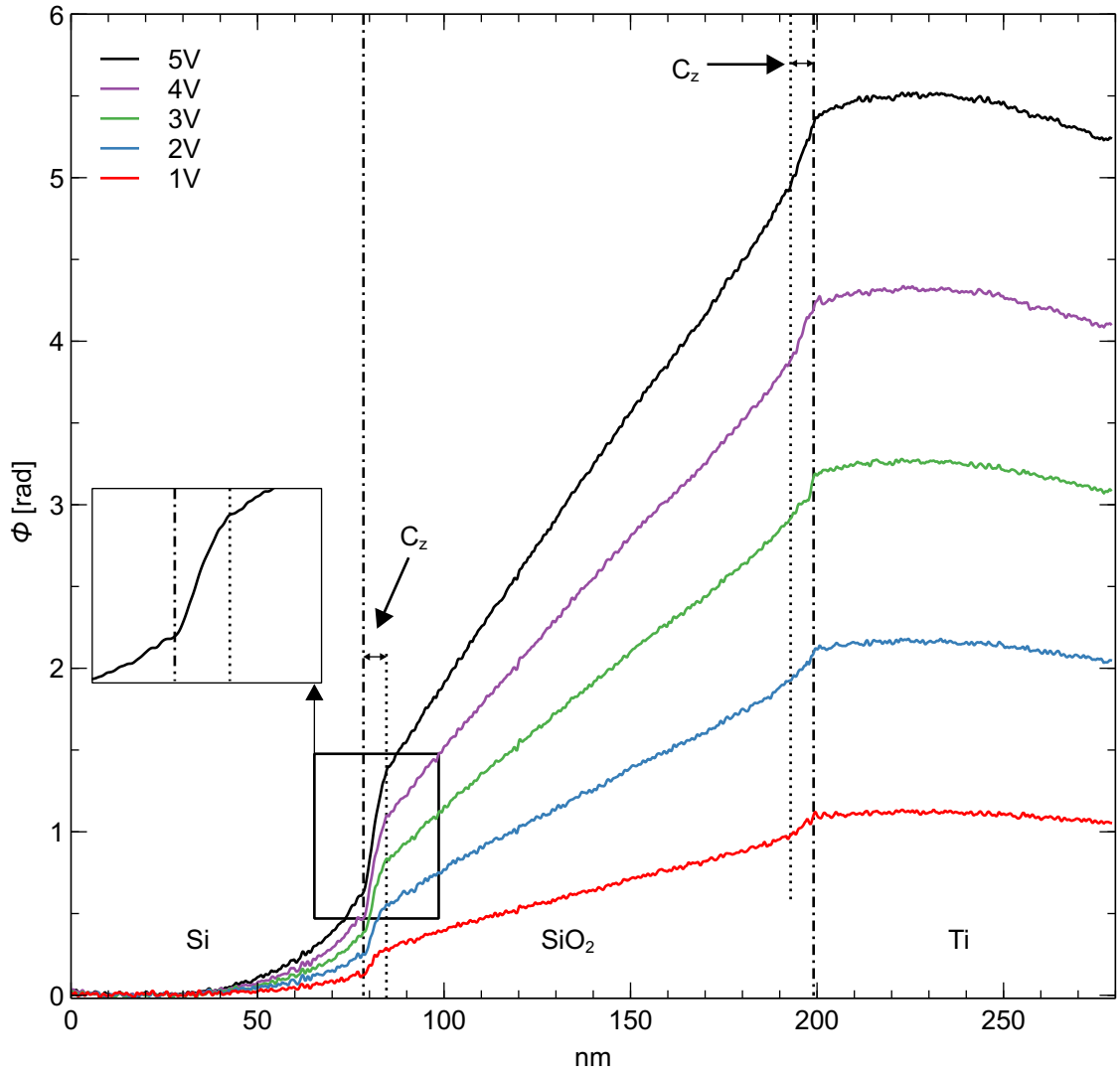

Figure 4.10: Phase profiles as a function of applied bias (1–5 V). Note the curvature of the phase within the electrodes (highly doped Si and Ti) and the phase jumps at the electrode-dielectric interfaces extending more than 5 nm inside the SiO_2 layer (see enlargement for 5 V bias).

The pronounced step in the phase occurring at both interfaces is of particular interest to the analysis and was not present in the previous example. The enlargement of Figure 4.10(c) shows that there are two points of inflection, one at the interface plane and another at least 5 nm deep into the dielectric layer. This feature was unexpected, and took much conjecture and modelling to understand where it came from.

Contrary to the previous example, simulations show that the global phase change (5.5 radians) between the two electrodes corresponds exactly to 5 V applied voltage measured on the power supply (assuming the measured sample thickness is correct).

This is highly encouraging from a methodological standpoint and it is thus possible to limit the surface damage layer during FIB milling. It also indicates the impedances of the connections are minimal. Furthermore, the phase sensitivity of 10 mrad corresponds to only 9 mV of applied bias. We see no evidence of a silicon depletion layer, which can be explained considering the high doping level. The only way to model the phase shift successfully at the interface was to include a charge layer within the dielectric layer, like the double charge layers seen in solid-state batteries (Aizawa et al., 2017). The model, which incorporates all the physics, was developed during the preceding chapter and is depicted in Figure 4.11.

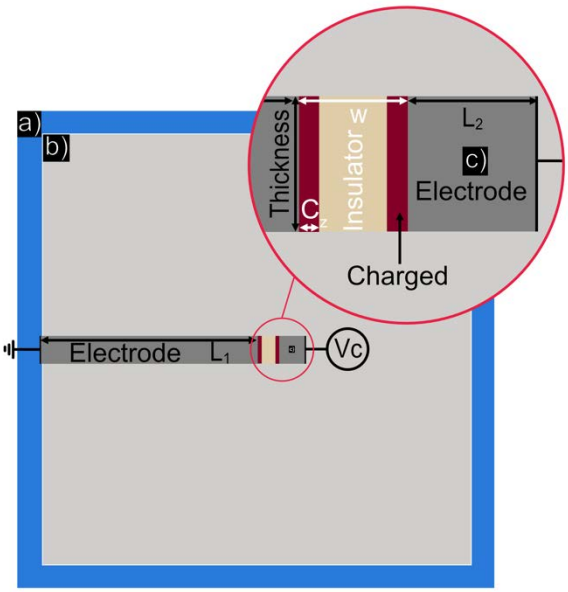

Figure 4.11 : FEM model with charged two layers inside the dielectric area of length C_z. And the various geometrical parameters that were used to model the capacitor.

I modelled this as a layer of uniform volume charge over 5.5 nm for both interfaces. Using this model, and by only changing the volume charge density, I was able to, nicely reproduce the experimental profiles for the complete biasing experiment.

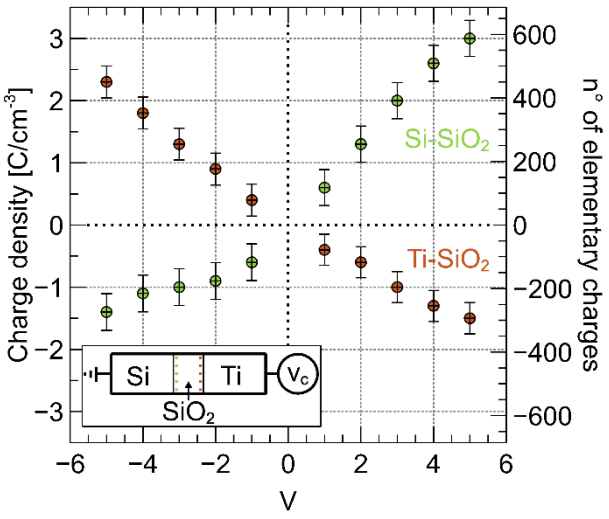

DC Bias (V_c)	ρ_1 (C/cm^3)	ρ_2 (C/cm^3)
-5	$-1.4 \pm 21,1\%$	$2.3 \pm 11,9\%$
-4	$-1.1 \pm 26,9\%$	$1.8 \pm 15,2\%$
-3	$-1.0 \pm 29,5\%$	$1.3 \pm 21,0\%$
-2	$-0.9 \pm 32,8\%$	$0.9 \pm 30,3\%$
-1	$-0.6 \pm 49,2\%$	$0.4 \pm 68,2\%$
1	$0.6 \pm 48,8\%$	$-0.4 \pm 66,7\%$
2	$1.3 \pm 22,3\%$	$-0.6 \pm 44,4\%$
3	$2.0 \pm 14,5\%$	$-1.0 \pm 26,7\%$
4	$2.6 \pm 11,1\%$	$-1.3 \pm 20,5\%$
5	$3.0 \pm 09,7\%$	$-1.5 \pm 17,8\%$

Figure 4.12 : The dielectric charge at the Si-SiO_2 (ρ_1) and SiO_2-Ti (ρ_2) interfaces as a function of applied bias. Charges per unit volume are plotted on the left axis. The number of elementary charges contained in the analysed region of the experimental specimen device is represented by the right axes. And the plotted data table is presented with the uncertainty on the right.

Each experimental phase profile was simulated in the same way as the profile shown in Figure 4.9(c). As a result, we recorded each charge density that accumulated on each interface and plotted it as a function of the bias (Figure 4.12). The volume charge densities required to fit the experimental data are displayed in Figure 4.12, including the negative biasing results. To highlight the sensitivity of the measurements, we have also indicated (right-hand scale) the number of elementary charges in the analysed area of the TEM foil.

When a negative bias is applied to the Ti electrode, the charge density on the SiO_2/Ti interface is positive and when the sign of the bias changes to positive, the charge density is negative. At the Si/SiO_2 interface, this tendency is reversed. I would like to emphasise that this was not the only sample we measured presenting charged density layers. The experiment was repeated on samples with *p-doped* and *n-doped* substrates, as well as different fabrication processes (wet and dry) and sample multiple sample thickness, where charging always occurred with even load zones up to 8 nm in width. Analysis also shows that the curvature of the phase in the region corresponding to the electrodes is indeed caused by the stray fields around the thin specimen Figure 4.13.

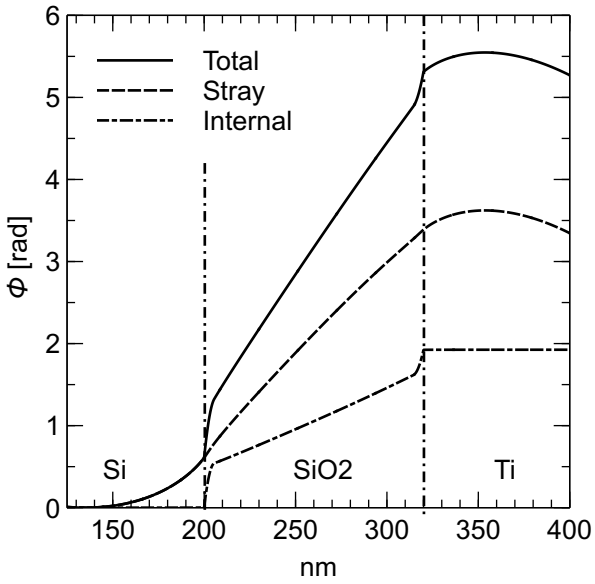

Figure 4.13: simulated phase contributions from internal potential, stray field, and total. Potential steps at interfaces caused by dielectric charge layers.

The simulated model allows for the decomposition of the internal and external phase signal. This directly shows that the contribution of the internal phase in this case corresponds to approx. 1/3 of the total signal as describes in the previous chapter.

3.II.B. Uncertainty and Induce Charge Trapping

The error bars represent the experimental uncertainties, which take into account multiple other factors such as the precise thickness of the lamella, the estimate for the width of the charge layers of 5.5(±0.5) nm. The resolution of the phase profiles is also limited to 0.8 nm, introducing a certain interplay between the width of the charge layers and the charge density therein. Nonetheless, given the detailed form of the profiles and the signal-to-noise ratio of the phase, the resulting error bars (Figure 4.12) are contained, representing to have as little as 50 elementary charges in the region analysed. The error bars for each value will be discussed in more detail in the next chapter.

Charge trapping affects the capacitance and performance of real-world devices by modifying the threshold voltage and frequency response (Deal et al., 1967) and is a major concern for dielectric breakdown (DiMaria et al., 1993). Some traps are expected to remain stable over time, while others are expected to be occupied

dynamically as a function of the applied bias. Much discussion has been made of the nature of the traps and where they occur: at the interface, in the immediate vicinity to the interface, or within the bulk of the dielectric (Deal, 1980). Others refer to border traps, being near the interface but within the dielectric layer (Fleetwood, 1992). Since interface and border traps have been linked to reliability issues, there has been renewed interest in the topic (Fleetwood, 2018; Grasser et al., 2011). The majority of characterisation techniques are based on indirect measurements, which causes uncertainty about their location. Electrical characterisation using Fermi-probe techniques, thermal activation, photoemission, X-ray photoelectron spectroscopy, and electron spin-based methods either measure a global response of the device or lack the spatial resolution to probe trap distribution at the nanometre length scale (Engström, 2014).

At first sight, we thought that the effect was caused by structural interfaces (i.e. inside the interfaces), so EELS measurements were performed (Figure 4.14).

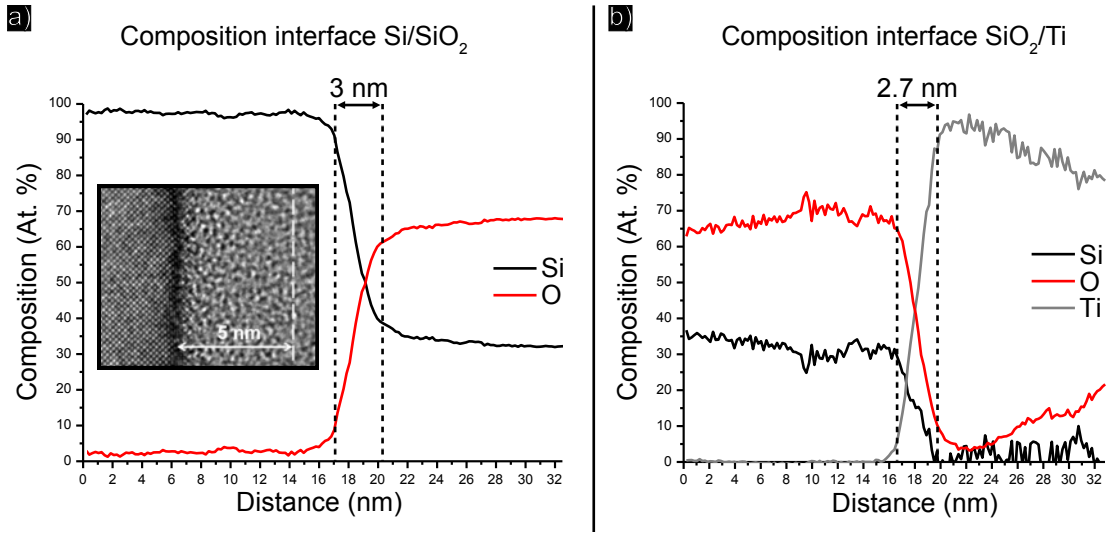

Figure 4.14 : EFTEM technology is used to measure the composition at the two interfaces on the left Si/SiO_2 a) (with a representative HRTEM image of interface region) and on the right SiO_2/Ti b).

The traps are then encountered beyond the chemical interface, which has a maximum width of 3 nm using EELS analysis (Figure 4.14) in this case, while we have measured that the traps go at least to 5.5 nm.

In contrast to the other technique, we were able to show the distribution of the traps thanks to the spatial resolution of electron holography. As a result, we investigated

the charging areas with high spatial resolution using transmission electron microscopy, specifically electron holography, which can be used to study these systems in novel ways.

Using the corresponding model for each curve, I calculated the capacitance as a function of bias (Figure 4.15).

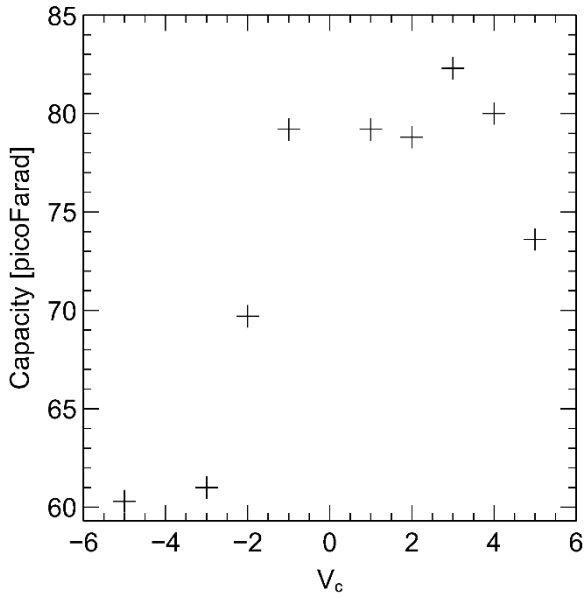

Figure 4.15 : Capacity as a result of a performance degradation caused by a defect in relation to the applied bias.

It is interesting to see how the capacity increases from the negative bias to the positive bias. Since this measurement was performed in DC mode, we were unable to compare it to frequency capacity measurements. The capacity is lower for a negative bias than for a positive bias. A difference in the balance of charges accumulated on one side versus the other could explain why the capacity is not symmetric with respect to the potential sign. The difference of charging between the areas could be due to a difference in the potential barrier between the two interfaces Si/SiO_2 and Ti/SiO_2 resulting in an unbalance injection of holes and electrons following the Fowler-Nordheim tunnelling charge injection model (Li and Chen, 2012).

3.II.C. Depletion Area

We might have expected to see a depletion layer on a biased MOS system inside the silicon substrate but as previously stated, we did not. To understand this, I tried to calculate the possible effect analytically. Based on the theory presented in (Bonnaud, 2006).

There are different types of charged areas, which are determined by the sign and magnitude of the bias. At first approximation the polarisation of the Si substrate can induce either a depletion area when the charges desert the substrate or an accumulation area when the charges are attracted within the interface.

A scheme of the potential drop caused by the depletion area, which is known as ψ_s is depict in Figure 4.16.

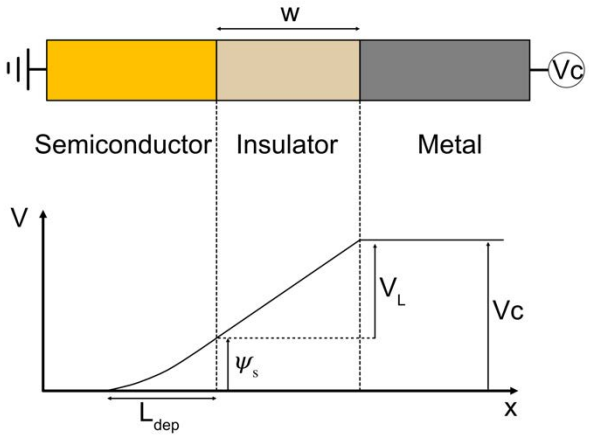

Figure 4.16 : Representation of the potential drop of the capacitor using MIS technology.

In relation to the applied bias, ψ_s in the depletion or accumulation zone can be described as follows:

$$Vc = w\frac{\varepsilon_{SC}}{\varepsilon_{ox}}\sqrt{\frac{2qN}{\varepsilon_{SC}}}\sqrt{\psi_s} + \psi_s + V_{fb} \qquad (4.1)$$

where Vc is the applied bias, w the insulator thickness, ψ_s the potential drop, ε_{SC} permittivity of the semiconductor depending on the doping, ε_{ox} permittivity of the insulator and V_{fb} flat band voltage (the potential caused by the difference in work function between the two materials).

To begin with the calculation of the equation (4.1) and find the potential drop ψ_s, we start to calculate V_{fb}. We first need to find the work function of the silicon and titanium, which is the difference between the Fermi level and the vacuum energy (Figure 4.17).

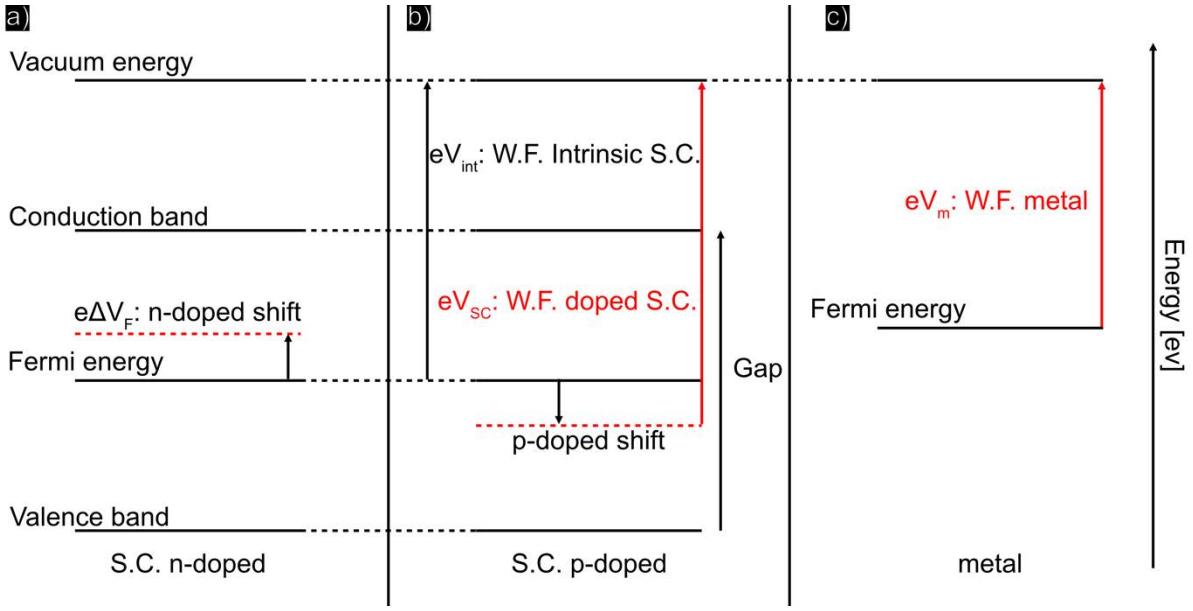

Figure 4.17 : Comparison of the band structures of *n*-doped semiconductors a) and *p*-doped semiconductors b) with metal band structures c).

Depending on the sign of the charge and the applied bias, the energy bands will move following this equation $E = qV$. Because the Fermi level is affected by doping and its type, I calculate its shift in relation to intrinsic silicon with the equation (4.2) &(4.3)), a $10^{18}\ atom \cdot cm^{-3}$ Si substrate doped and $n_i = 10^{10}$ cm^{-3} Si intrinsic density. The shift is schematically shown for each doping (Figure 4.17(a, b)).

Type n (the Fermi level approaches the BC):

$$\Delta V_F = \frac{kT}{q}\ln\left(\frac{N_d}{n_i}\right) = 0.47\ V \qquad (4.2)$$

Type p (the Fermi level approaches the BV):

$$\Delta V_F = -\frac{kT}{q}\ln\left(\frac{N_a}{n_i}\right) = -0.47\ V \qquad (4.3)$$

When a material is *p-doped*, the Fermi potential becomes negative, causing the Fermi band to move towards the valence band. While it is positive for an *n-doped* material, it causes a shift from the Fermi level to the conduction band.

The depletion state may include an inversion state which appears after a certain bias named voltage thresholds V_{th}. This state describes a configuration when the charge sign is inverted and additional applied bias is directly applied to the oxide. This corresponds to a significant system inversion and is defined by multiplying the Fermi potential by two $\psi_s = 2 * \Delta V_F$:

$$V_{th} = \alpha \sqrt{2 * \Delta V_F} + 2 * \Delta V_F + V_{fb} \sim 20V \quad (4.4)$$

For our system the voltage threshold is about 20 V. For doping of $10^{17}\ atom \cdot cm^{-3}$, the threshold bias only 5 V, implying that this assumption is highly dependent on the doping.

The weak inversion mode that is defined as $\psi_s = \Delta V_F = 14$. As a result, because we will never experimentally bias our sample higher than 10 V, the system will never be in the corresponding inversion mode and will instead develop accumulation and depletion area.

The energy difference between titanium and silicon doped *n* or *p* is then calculated while the work function of titanium is $eV_m = 4{,}3\ eV$:

Type n:

$$eV_{SC} = eV_{int} - e\Delta V_F = 5{,}13 - 0{,}47 = 4{,}66\ eV \quad (4.5)$$

Type p:

$$eV_{SC} = eV_{int} - e\Delta V_F = 5{,}13 + 0{,}47 = 5{,}6\ eV \quad (4.6)$$

With the preceding calculation, we can compute the potential flat band for each type of semiconductor:

Flat band bias n-type:

$$eV_{fb} = eV_m - eV_{SC} = 4{,}3 - 4{,}66 = -0{,}36 \quad (4.7)$$

Flat band bias p-type:

$$eV_{fb} = eV_m - eV_{SC} = 4{,}3 - 5{,}6 = -1.3 \quad (4.8)$$

We can also consider the presence of interface states because of Si-SiO_2 interface fabrication, which can result in an always positive charge at the interface with a state density almost Q_0/e 10^{10} F/cm^{-2}.

These states generate a bias that can be applied to augment the work difference V_{fb} in order to incorporate this phenomenon into the model, we use this equation:

$$V_{trap} = -\frac{Q_0}{C_o} = -0.056\ V; (Q_0/e) \text{ interface trap density and } C_0 = \frac{\varepsilon_{ox}}{w} \qquad (4.9)$$

V_{trap} is negligible in comparison to the potential of the flat band because of the higher work difference than the bias due to trap density.

Using the flat band voltage and the length of the dielectric $w = 120\ \text{nm}$, we can solve the quadratic equation to find ψ_s (4.1). We put $X = \sqrt{\psi_s}$ et $\alpha = w\frac{\varepsilon_{SC}}{\varepsilon_{ox}}\sqrt{\frac{2qN}{\varepsilon_{SC}}}$ into the quadratic formulation:

$$X^2 + \alpha\, X + \left(V_{fb} - Vc\right) = 0 \qquad (4.10)$$

$$X_{1,2} = \frac{-\alpha \mp \sqrt{\alpha^2 - 4(V_{fb} - Vc)}}{2} \qquad (4.11)$$

Only one root will have physical meaning. We will choose the lower solution compared to the applied voltage because the bias cannot exceed Vc:

$$Vc = \psi_s + V_L \qquad (4.12)$$

In our case $\alpha = 20{,}1$ So, for a bias of -5 V to 5 V, the result of each root is:

DC Bias (V_c)	ψ_sType n (V)	ψ_sType p (V)
5	0.26	0.30
1	0.07	0.14
-1	-0.03	0.01
-5	-0.20	-0.19

Figure 4.18 : Potential drop due to a type-n and type-p depletion zone with respect to the bias applied.

At room temperature, the voltage due to electron thermal energy is $\frac{kT}{e} = 25\text{mV}$, so any ψ_s value less than this one has no effect. For example, an applied bias of -1V with a *p*-type electrode has no effect, because the thermal energy of the electrons is higher

than ψ_s. The effect of ψ_s is negligible at low bias, and it remains contained representing 6% of the maximum applied bias. Moreover, after the calculation of the corresponding charge density (see annexe), we see that the charging inside the silicon is minimal compared to the density injected inside the dielectric. As a result, the effect is not accounted for in the simulation data.

3.III. SiO_2-Si_3N_4 Bilayer Capacitor

Because the electronic components become increasingly small in size, to limit the leakage currents, dielectric stacks of different materials can be employed. Here, we studied the electrical potential distribution in a model bilayer capacitor composed with 55-nm-length SiO_2 ($\varepsilon_r = 3.9$) and 40-nm-length Si_3N_4 ($\varepsilon_r = 7.2$) in series, both grown on highly *p*-doped Si substrate and topped with a Ti electrode. The TEM foil after FIB preparation was 70 nm thick.

The sample was *in situ* biased from -10 to 10 V with 1 V steps. I nevertheless decided to concentrate my analysis and discussion on the 10 V bias phase image because these conditions present the best signal-to-noise ratio. The amplitude image showing the geometry of the sample with the phase image as well as the experimental profile and corresponding simulation are depicted (Figure 4.19)

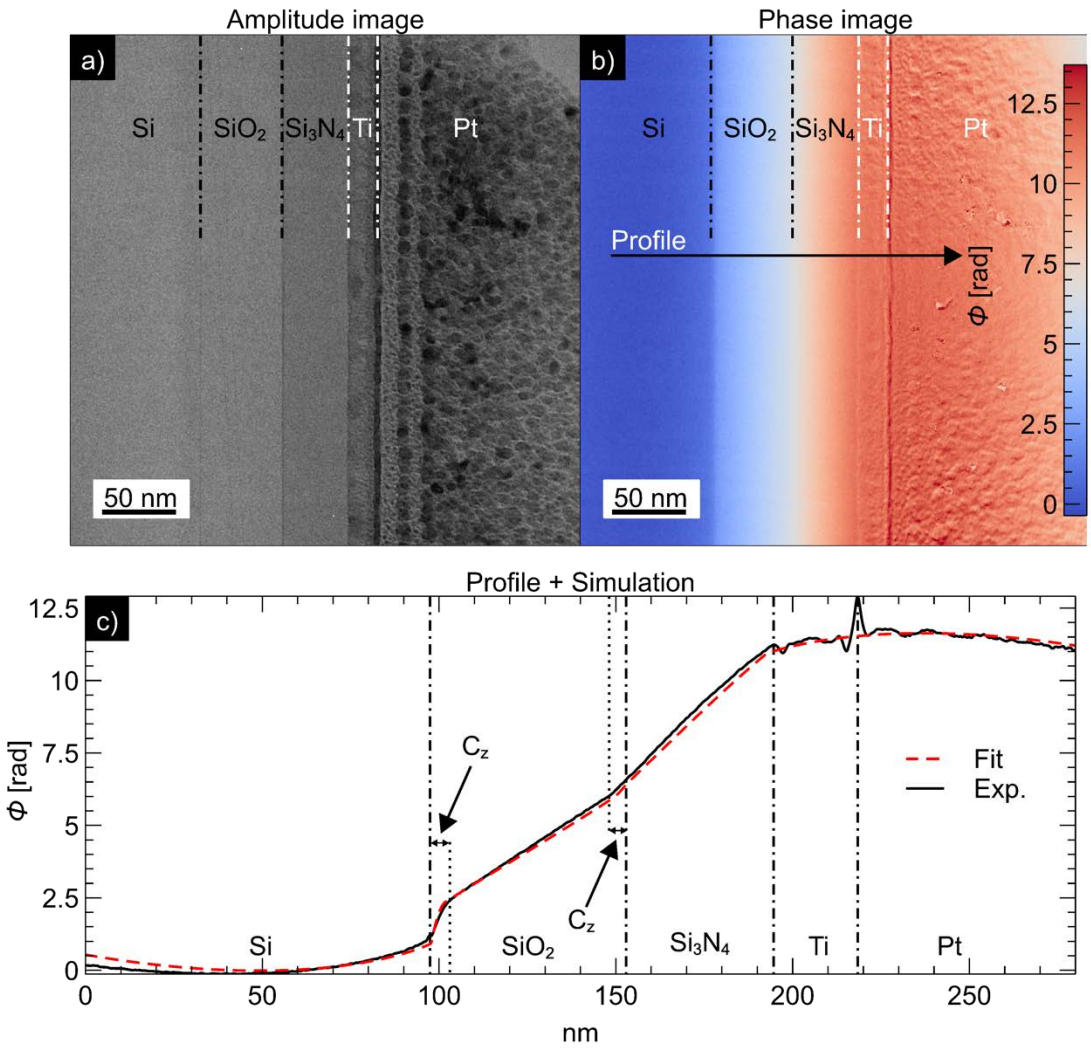

Figure 4.19 : The amplitude image depicts the structure of the sample Si-SiO_2-Si_3N_4-Ti a), whereas the phase profile in the same area depicts the phase acquired by electrons passing through the capacitor bias under 10 V b). A profile on the phase image then allows for a more in-depth analysis of the phase c).

We can clearly see a point of inflection of the phase at the interface between the two dielectrics. This is expected because the interface condition indicates that there must be a discontinuity in the electric field between two dielectrics, even when no interface free charges are present (4.13).

$$\hat{n} \cdot \left[\overrightarrow{D_2} - \overrightarrow{D_1}\right] = 0 \qquad (4.13)$$

As we previously discussed in the method chapter, there is a discontinuity in the electric field at the interface is caused by a difference in permittivity between the two materials. We can distinguish three cases: when the permittivity ratio of the two dielectrics is less than one, equal to one, or greater than one (Figure 4.20).

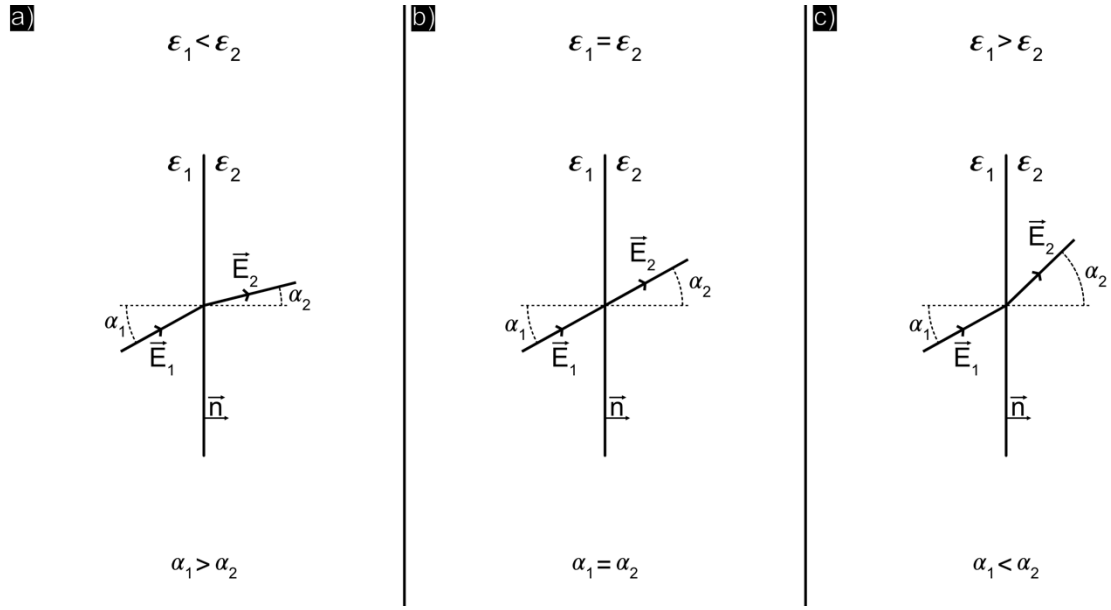

Figure 4.20 : At an interface between two media with dielectric constants varying from ε_1 to ε_2, the continuity of the normal component of the electric field is broken. When the permittivity are the same, the interface has no effect and presents a perfect continuity of the electric field; however, when ε_1 is less than ε_2, the break is negative a); otherwise, it is positive c).

When the permittivity of the second material is higher than the first, this implied negative curvature, indicating that the angle from the second field to the normal is lower than the first (Figure 4.20(a)). Then, if the dielectric constants are equal, it reacts as if the materials are the same, the angle difference does not exist (Figure 4.20(b)). And if the second material has a lower dielectric constant than the first, the curvature of the field will be the inverse (*i.e.* positive) (Figure 4.20(c)).

So, when we apply this analysis to the experimental profile Figure 4.19 , we see that it fails spectacularly. The electric field should have been smaller in the dielectric material with a higher permittivity, *i.e.* Si_3N_4 but we observe the contrary. Clearly, the curvature appears to be the exact opposite of what would be expected for a combination of an SiO_2 ($\varepsilon_r = 3.9$) dielectric and a Si_3N_4 ($\varepsilon_r = 7.2$) dielectric, with the curvature of the phase being positive rather than negative.

We saw for the model SiO_2 capacitor that this type of sample can accumulate space charge, whereas the model Si_3N_4 capacitor did not. As a result, I attempted to incorporate two charging areas within the SiO_2, into this bilayer capacitor.

By inverting the curvature inside the dielectric, this integration enables a very good fit. For instance, these areas measured on the experimental data have a length of about 4 nm, and we were able to extract the charged density from the simulation data, which was about $10 \times 10^6\ \mathrm{C/m^3}$ and $-1.5 \times 10^6\ \mathrm{C/m^3}$ on the left and right of the SiO_2 layer, respectively. It seems that SiO_2 is prone to creating border traps even at interfaces with another dielectric, and deeply modifies the expected potential distribution of such a system.

4. Analytical Calculation of Infinite Capacitor

The potential calculated by FEM will then be compared to the potential analytically calculated to see if the boundary effect created on the potential from a finite capacitor can be seen. The FEM simulation of the electric field has allowed a thorough examination of our specimen device, including the internal and external stray fields. However, our samples are thinned to electron transparency and do not necessarily represent the original device. It is therefore important to understand how the electric fields within the thinned sample compared with the internal field of an infinite-sided capacitor.

To this end we developed an analytical model for the internal potential distribution in a capacitor with infinite dimensions perpendicular to the growth direction of the dielectric layer and taken into account charged density layers at the interfaces between electrodes and insulating layer. As a result, we can compare this theoretical calculation to results from a model used to extract quantitative data from the Si-SiO_2-Ti experiment (Figure 4.21). A line section of the simulated potential by FEM was taken at the centre of the thinned sample.

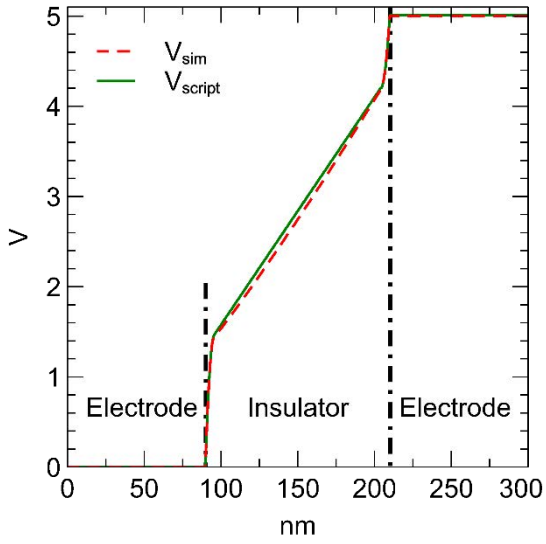

Figure 4.21 : Comparison of the internal potential determined from the analytical calculation of an infinite capacitor (solid black line) and from the thinned sample using FEM (dotted red line). Results for the Si-SiO_2-Ti sample biased to 5 V included the dielectric charge layers. Thinned sample thickness was 55 nm.

Overall, the two calculations produce the same results, notably reproducing the sharp potential change caused to the charge density at the interfaces in the dielectric layer. However, the simulated potential within the thinned sample has an additional curvature. This curvature is caused by the fact that we do not have an infinite capacitor inside the simulation, so the interfaces between the dielectric and the surrounding vacuum produces boundary effects. The experimental results are therefore very close to those of an infinite capacitor, meaning that the thinning process does not change the internal potential greatly. The good agreement also confirms that the mesh size in the FEM model was sufficiently small to avoid numerical errors, notably at the interfaces.

With the analytical solution in place, we can readily calculate internal electric fields for model capacitors including charge density layers without the need for full FEM simulations if no leak field is considered.

5. Conclusion

We demonstrated in this chapter that we have successfully simulated experimental data with the tools developed in the previous chapter. We can account for a variety of experimental anomalies such as FIB damage, stray field, and charging effect. The generality of the FIB preparation and the experimental setup are discussed, allowing us to focus directly on the charging of the grounded SiO_2 dielectric sample.

The interaction of the electron beam with the dielectric materials produces secondary electrons, which in turn produce Auger electron emission, resulting in positive charging. We have detected the presence of conductive layers all around the capacitor that screen the stray field by comparing the experimental and simulated data. Using the appropriate FEM model, we can extract quantitative information such as the real charge density inside the dielectric.

By studying the grounded capacitor, we can detect the extrinsic phenomena caused by our measurement and thus remove them from our experimental data, allowing us to open the bias capacitor study.

We began with the Si_3N_4 capacitor that we thought was a perfect model. However, we discovered FIB damage that formed a conductive layer around the sample, as well as a charged density that was injected inside the dielectric during biasing. However we noticed, as predicted during the theoretical study, that the stray field curves the phase inside the electrodes. Finally, I also show how and why we can build a good fit from the simulation to the experimental data step by step.

Then we tested a commonly used SiO_2 capacitor with a dielectric that is much more used and better known in the microelectronic industry than the Si_3N_4 capacitor. However, contrary to what was expected, we discovered induced charge in the dielectric that affects the normal operation of the device. I could quantify the charging and thus understand their impact on the capacity.

To ensure that the depletion inside the silicon has no effect on the charging area measurement, we quantify the biasing and charge generated within the substate. In this regard, we were curious if the measured charges inside the dielectric were screened by a depletion area. Even though the charging effect is not included in the

model, the mathematical demonstration shows how small this effect is compared to the applied bias.

Finally, we investigated a capacitor made up of the two layers from the previously studied dielectric. We noticed an intriguing anomaly on the field within the interfaces between the dielectrics. Therefore, we could explain and create a good fit of the experimental data by integrating the charging layers within the SiO_2 dielectrics. So, not only did we understand the flip of the field curvature, but these results also support the thesis of charging area inside the SIO_2 dielectric.

To conclude, we wanted to study the internal potential of the capacitor computed with FEM from the analytical point of view (i.e. infinite capacitor). This enabled us to see that, even if we are not interested in the stray field, the finite geometries of the capacitor create a boundary effect that will curve the internal potential inside the insulator. Despite this difference in potential drop, we confirmed that the internal field of a thin specimen corresponds closely to the infinite capacitor as well as the bulk capacitor, validating the TEM methodology to study the electric field of bulk capacitors.

To go further, the FIB preparation needs to be studied more thoroughly. We should try milling other samples with other sources, such as helium or xenon, although it may take a much longer preparation time.

Finally, these studies pave the way for further research into other microelectronic devices such as ferroelectric capacitors, transistors, and GST.

Chapter 5 — Measurement Uncertainty

I never really explained in the previous chapters why it was so difficult to create a model that fits the experimental data sufficiently to extract quantitative parameters. The main issue is that everything is linked: every parameter is correlated in some way. I have attempted to create a figure that explains the relationship between the parameters of the model and their influence on the fit by qualitatively classifying the parameters that have a strong influence and the parameters that have a weak influence in my experience (Figure 5.1).

The apparent complexity of the diagram can be frustrating, but this is a deliberate choice of representation that shows the problem as we saw it at the start of my thesis. The case of the conducting layers has even been left out for clarity. However, I can say a few words on the latter problem: the main difference between models with and without conductive layers is that local charge density no longer influences other parts of the model. Because of the conductive layer, each charged area does not produce a stray field and thus cannot influence the phase acquired by the electrons in other areas. Another distinction is that the conductor layers, rather than the bias parameters, will directly influence the net drop in phases between the electrodes.

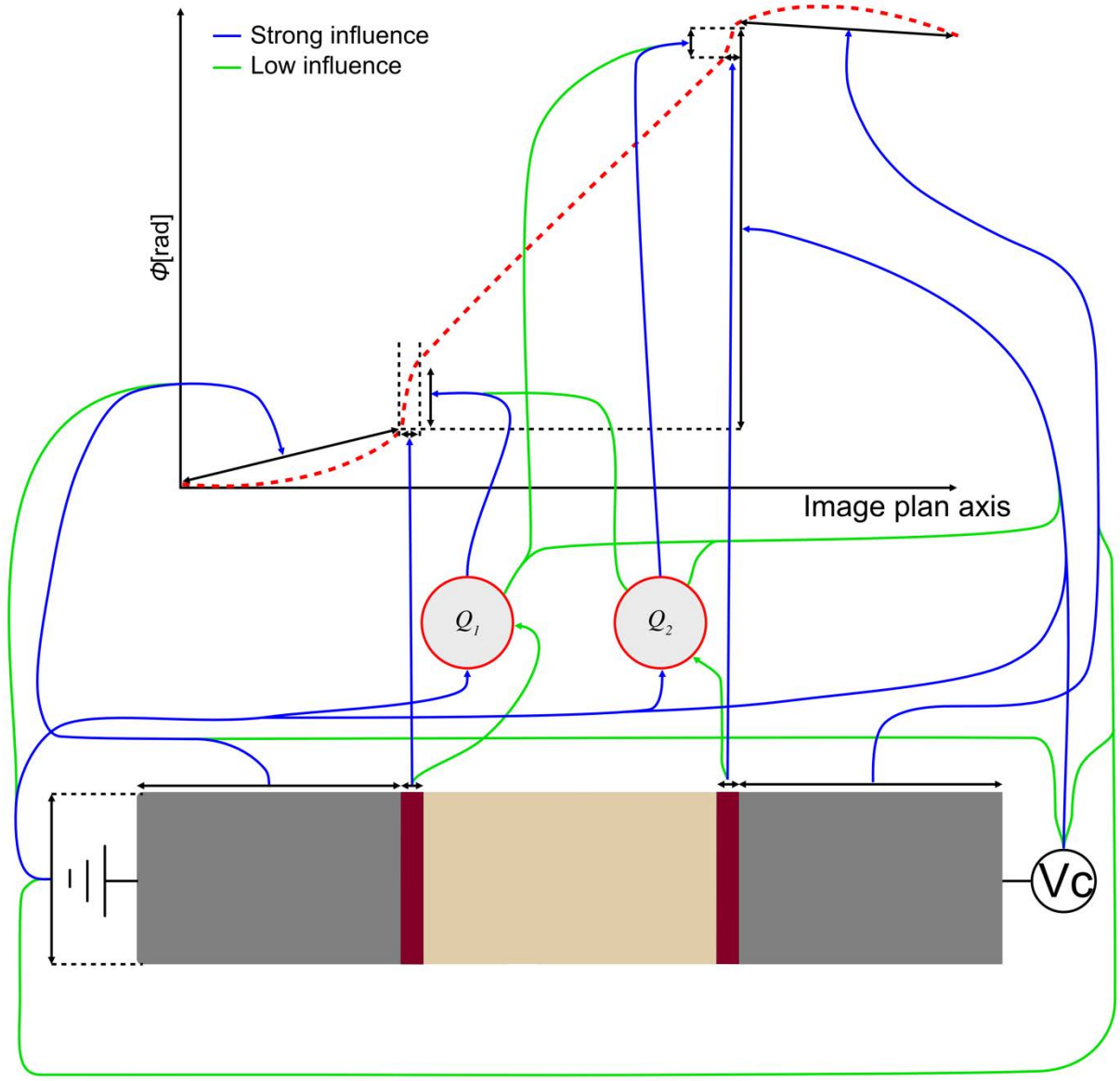

Figure 5.1 : The relationship between the model variable and its effect on the phase profile.

This diagram depicts the challenges I encountered when thinking about how we can be certain of what we are measuring and, if we measure a parameter, in what window of confidence can we be certain of our value residing. Throughout this chapter, I will untangle this *mélimélo* (i.e. pell-mell) by analysing the measurement of each parameter and applying statistical methods that will allow us to see more clearly. To calculate the uncertainties, I will follow the Guide to the expression of Uncertainty in Measurement (GUM)(International Bureau of Weights and Measures and International Organization for Standardization, 2008), a metrology guide.

This study well represents what I was doing "by hand" before I recently developed a Python code that will allow us to study the theoretical model as well as the study of algorithms to fit experimental data. Finally, I will describe an early development of a neural network during my supervision of an INSA internship. This advancement addressed two themes: the first was the development of AI capable of predicting simulation parameters from experimental data, and the second on how to extract parameters from images from the electron microscope. Whilst incomplete, this work is of interest for future developments.

1. Uncertainties in the Si-SiO_2-Ti Model

1.I. Introduction

The study of the Si-SiO_2-Ti capacitor in the previous chapter revealed that there are two charged areas with opposite signs inside the dielectric, near the electrode interfaces. This is a very interesting result, so I chose to demonstrate how I attempted to determine the uncertainty with the measurement of charged density.

To begin with, the fact that the obtained phase shift is linked to the measurand (i.e. charge density) via finite element method implies that there is no analytical link between these two variables. Indeed, the calculated charge density cannot be deduced via a simple equation due to the complexity of the system. Despite this, the GUM (Guide to the Expression of Uncertainty in Measurement) backpropagation of uncertainty equation is still valid under the assumption that each parameter has a linear influence on the phase image.

To propagate the uncertainties, we must evaluate the uncertainty of each parameter, and because they are B-type, each measure must be associated with a probability distribution. Because we do not have access to multiple repeat measurements, we have to choose carefully the probability distribution with respect to each measurand.

Furthermore, we can divide the measurand into two families: length measurements (i.e on x,y axes) and phase uncertainties which is the phase variance due to noise. The following sections describe how each parameter was measured, along with the associated uncertainty.

1.II. Length Measurement

Because the width measurements are unaffected by the projection assuming that the specimen has been well aligned, we can directly measure the width of the dielectric and charge zones from the hologram. The width of the space charge area (C_z) is 5.5 nm, along with the dielectric thickness *w*, which is about 120 nm (Figure 5.2).

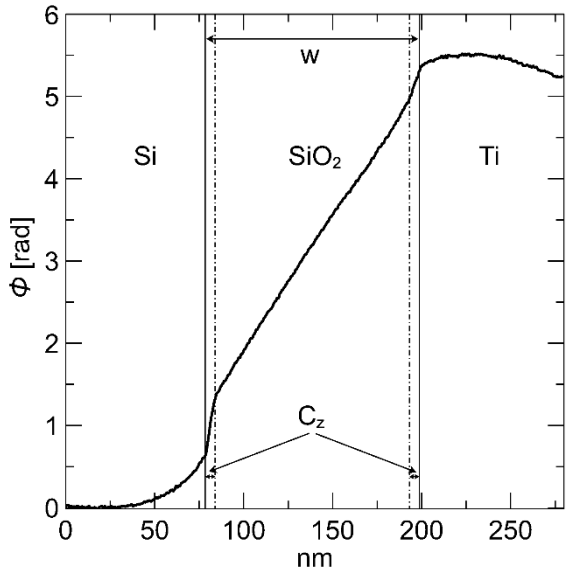

Figure 5.2 : The length of the dielectric w and the charged density area C_z are shown as parameters directly measured on the phase image.

The phase image resolution determines the uncertainty of the measurement. According to the GUM, the standard deviation u of this type of measurement can be defined by knowing that it follows a uniform distribution and is produced by a *double reading* $= \sqrt{\frac{2}{3}} \times \frac{\Delta d}{2}$. On this type of measurement, Δd can be the image resolution, which in this case is 0.8 nm. The multiplication by the square root of two corresponds to the double measurement (i.e., double reading), and the remainder of the equation is derived from the uncertainty calculated from the law for a rectangular distribution. With this equation we can estimate the standard deviation from spatial phase image measure directly but for an indirect measurement from the amplitude of the phase shift, we need other techniques.

1.III. Phase Shift Measurement

The measurement of uncertainties related to the phase is totally different from those of the width. Indeed, as we cannot measure some parameters of the model directly, we must measure them indirectly through their effects on the phase image. This is why we must measure the sensitivity of each parameter from the amplitude of phase variations.

One method is to estimate the extent to which we can discern the effect of a parameter change in the fit (i.e. sensitivity) and the range in which changing a parameter causes a significantly large change in the phase image to distinguish the fit from the image noise (i.e. technique named as framing). This is governed by two phenomena: the first is related to the sensitivity to the model parameters, and the second is related to the experimental level of noise present in the measurements. To access the phase sensitivity to each parameter, it is necessary to frame or delimit the measurement taking into account these two principles. An example of how this technique, defined as framing, can be used is shown Figure 5.3.

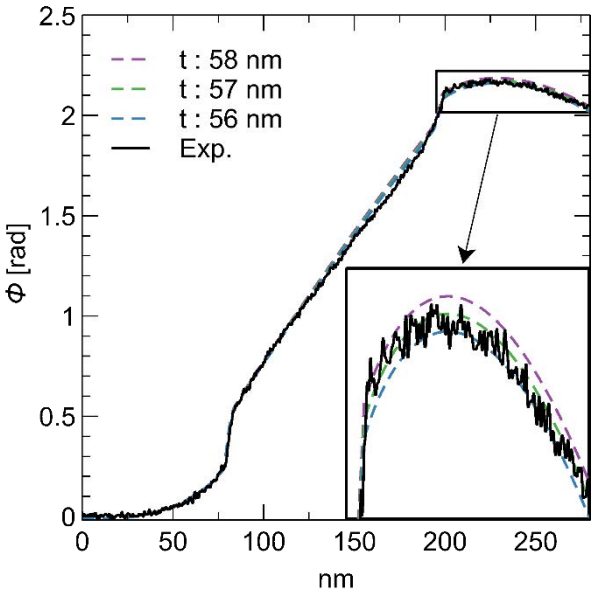

Figure 5.3 : By framing the uncertainty of the noise and the sensibility, the thickness (noise) of the sample can be directly translated.

The resulting specimen thickness measurement is approximately 57 nm, with a sensitivity of approximately ± 1 nm. Because the distribution identified will be similar to the following parameters, we will go over them after.

The sensitivity of the anode width L_2 (i.e. Ti electrodes) (Figure 5.4) was then determined with the same technique. Because of the influence of the electrodes on the stray field, geometrical considerations must also be addressed. As seen in Chapter 3, we vary the length of the smallest electrode L_2 to frame the curve because it has the most direct influence on the shape of the stray field.

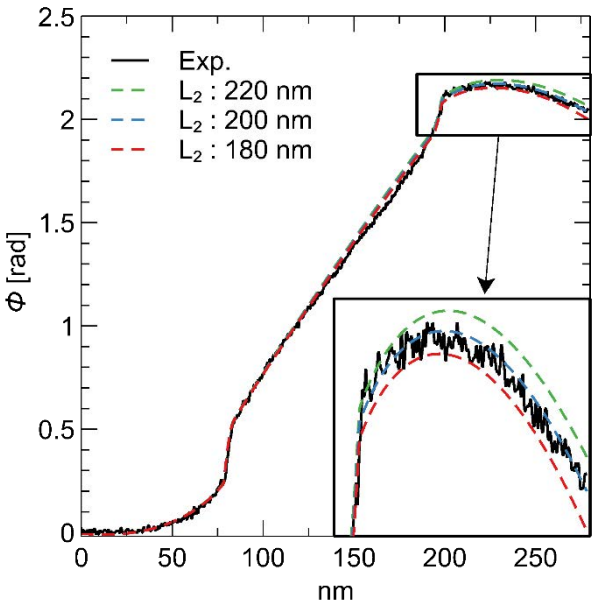

Figure 5.4 : The sensitivity of the parameter is determined by framing the anode width L2 with the phase image noise.

In this model, we can see that the sensitivity of the phase profile to the width of the anode is much smaller than that of the specimen thickness. Indeed, the fit indicates that the expected anode width is about 200 nm with a sensitivity of ± 20 nm.

The same method was used to calculate the charge density that accumulates inside the dielectric at the electrode interfaces when the capacitor is biased Figure 5.5.

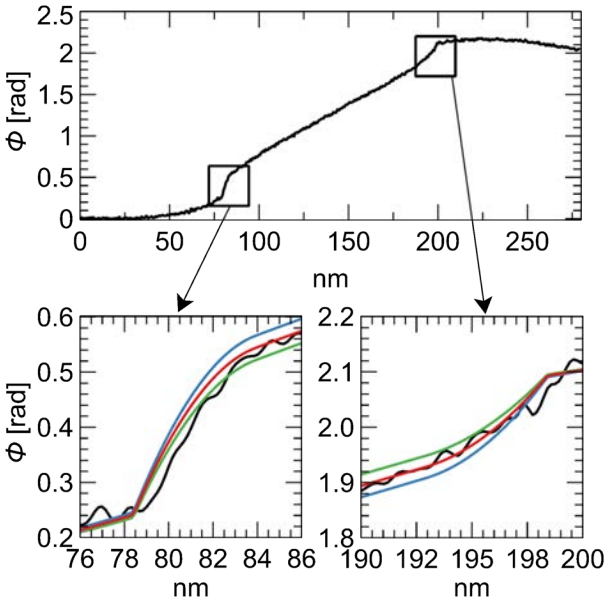

Figure 5.5 : The charged density is framed on the left and right sides to emphasise the uncertainty of charged density values.

In contrast to the previous two examples, we see a different choice of framing here. Because the fit is sensitive to the number of points used to create it, instead of aiming to fit exactly the charge density at risk of having a bad fit in the dielectric area, I fit the dielectric phase. So, the fit on this part of the model is now a function of the slope between the two electrodes to achieve a better fit.

Because Gaussian noise is considered, the distribution of these standard uncertainties will follow a normal distribution. Under these conditions, the GUM advises us to compute the standard uncertainty using the formula $u = \frac{\Delta L}{3}$. With ΔL the parameter framing corresponding to the framing of the phase image $\Delta\phi$. This law defines the uncertainty associated with a normal distribution with u^2 the variance.

Finally, measuring the uncertainty of the bias is difficult because it is directly related to the sample thickness. That is, it is extremely difficult to distinguish between the effects of a variation in sample thickness and a variation of bias. To calculate the uncertainty associated with the bias, we tried to define the maximum thickness of the sample from EELS, which in this case gave 60.5 nm. Given that, we will attempt to fit the experimental data with a model based on the maximum thickness measured with EELS, and we know that there can only be a potential drop across the capacitor

because we cannot have a bias greater than the applied bias. To do so, we must determine how much we have to reduce the bias to obtain a satisfactory fit (Figure 5.6). The reduced bias drop induces to retrieve a good fit is named delta δ and represents the uncertainty made on the bias.

To conclude, if we correlate the measurements made with EELS with those made with FEM simulations, we can exclude a bias drop greater than 0.1 V. Indeed, a drop greater than 0.1 V in the bias would imply that the thickness of the capacitor is greater than 60.5 nm, which is ruled out by the EELS measurements made.

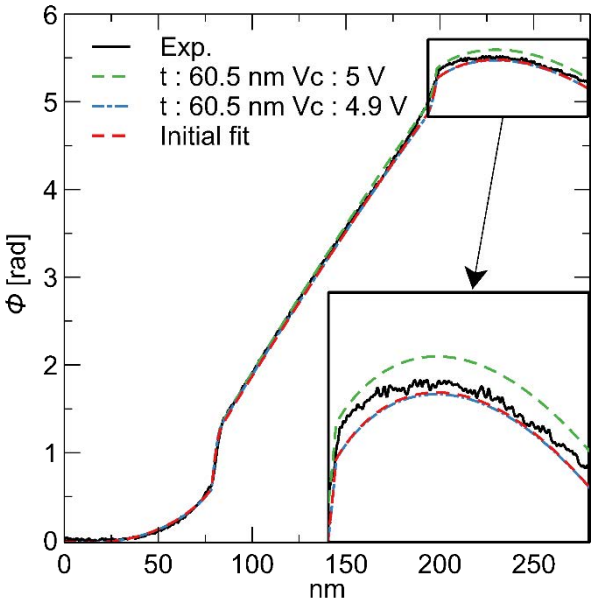

Figure 5.6 : Fit using the model with the maximum thickness measured with EELS technique by decreasing the voltage until we find the fit made with the thickness measured via the phase shift.

I have chosen to consider the probability distribution to be a right-handed triangle because the value of the voltage is more likely to be close to 5 V than to 4.9 V but cannot be greater than 5 V. The corresponding standard deviation, $\sigma = \frac{\Delta Vc}{\sqrt{18}}$. We can deduce that there is a maximum standard uncertainty of 0.01 V between what is applied to the generator and what is actually applied to the sample, which appears extraordinarily precise. However it is a measure that is only induced by the uncertainty of the sample thickness and because the sensitivity of the phase profile at variation of the thickness is lower than a variation of potential, the effect is small.

1.IV. Propagation of Uncertainties

Each one of the previous uncertainties influences the uncertainty in the charge density. We have to link each uncertainty to the parameters that we want to measure (i.e. charged density) and we know that some parameters are interdependent (correlated). To account for these phenomena, and calculate the combined variance u_c^2, we must propagate the variance of each parameter through equation (5.1).

$$u_c^2(y) = \sum_{i=1}^{N} c_i^2\, u^2(x_i) + 2\sum_{i=1}^{N-1}\sum_{j=i+1}^{N} c_i c_j u(x_i) u(x_j) r(x_i, x_j) \qquad (5.1)$$

Where:

$$c_i = \frac{\partial f}{\partial x_i}\ ;\ r(x_i, x_j) \approx \frac{u(x_i)\delta_j}{u(x_j)\delta_i} \qquad (5.2)$$

The factor of 2 is due to the fact that the matrix r is symmetric. The function "$\boldsymbol{f}$" linking the charge density to the different parameters does not exist, so we cannot calculate the C_i coefficients directly. However, C_i represents the extent to which the sensitivity of each parameter can affect the measurement of the charge density. Thus, if we measure the impact of the variation of the parameters x_i to the parameter measured for each parameter of the model, we can estimate the coefficients C_i. In practice, this consists in replacing C_i in equation (5.2) by $C_i = \frac{\partial f}{\partial x_i} \approx \frac{\Delta D}{\Delta x_i}$; Δx_i being a small variation of a parameter of the model and ΔD the correction made on the charge density D to find a correct fit after variation of a small amount Δx_i. In other words, we construct the correlation coefficient matrix (Table 5.1) that take the correlation coefficient $r(x_i, x_j)$ calculated from how much a perturbation δ_i from the parameter x_i can create a shift δ_j to the measurement of x_j.

correlation matrix	t	L_2	C_z	V_c
t	1	0.20	0	0.21
L_2	0.20	1	0	0
C_z	0	0	1	0
V_c	0.21	0	0	1

Table 5.1 : correlation matrix taking into account the dependencies between the parameters.

The correlation matrix coefficients represent the influence of each parameter on each other for the fit. Moreover, each zero represents a null correlation of the parameters for this purpose I show the parameter C_z (i.e. width charge area) that do not have any correlation with any parameters. To go further, and to refine our confidence in the measurement, it would be interesting to use a propagation of the distributions (Monte-Carlo method (Shimaoka et al., 2008)) rather than propagating the uncertainties through the standard deviations/variance. Finally, the relative incertitude is presented below (Table 5.2).

DC Bias (V_c)	ρ_1 (C/cm^3)	ρ_2 (C/cm^3)
-5	$-1.4 \pm 21,1\%$	$2.3 \pm 11,9\%$
-4	$-1.1 \pm 26,9\%$	$1.8 \pm 15,2\%$
-3	$-1.0 \pm 29,5\%$	$1.3 \pm 21,0\%$
-2	$-0.9 \pm 32,8\%$	$0.9 \pm 30,3\%$
-1	$-0.6 \pm 49,2\%$	$0.4 \pm 68,2\%$
1	$0.6 \pm 48,8\%$	$-0.4 \pm 66,7\%$
2	$1.3 \pm 22,3\%$	$-0.6 \pm 44,4\%$
3	$2.0 \pm 14,5\%$	$-1.0 \pm 26,7\%$
4	$2.6 \pm 11,1\%$	$-1.3 \pm 20,5\%$
5	$3.0 \pm 09,7\%$	$-1.5 \pm 17,8\%$

Table 5.2: Table summarising the measured charge density as a function of the voltage applied to the real capacitor with the associated relative errors.

The error is highest for the weakest bias while it is relatively small in the strongest bias. Similarly, we notice an asymmetry in the errors due to the uncertainties of the bias, thickness and size of the right electrode which acted mainly in the charge area on the right.

2. Automated Fitting Process

The above analysis was carried out "by hand", that is I adjusted the parameters manually until the experimental curves were framed by two delimiting profiles. This process was both time consuming and implied numerous human inputs (mine) whereas ideally we would like to introduce as little bias as possible. Consequently, I created an auto-fitting algorithm that also calculated the uncertainty of each fitting parameter as described in Chapter 2.

2.I. Fit Model or Self-Consistency

Before attempting to fit experimental data, I first wanted to test the algorithm on simulated data with known parameters. A variety of situations, such as grounded capacitors with charge density, bias capacitors, were chosen for this purpose based on the models already presented in Chapter 3. There were two things I wanted to test: could a perfect fit be found and would be the parameters correspond to those of the simulation. Because an automated procedure has very low bias, I also hoped to be able to study the correlation between the parameters with greater accuracy than before.

2.I.A. Grounded capacitors with a uniform charge density in the insulator/dielectric

As is customary in this thesis, we will begin with the model without bias to investigate the intrinsic parameters of the grounded capacitor. I will use the grounded model, developed in Chapter 3, without and with conductive layers. The corresponding phase profiles are shown in Figure 5.7(a, b). We can now test whether we can retrieve the simulation parameters directly from the phase profile with automated fitting.

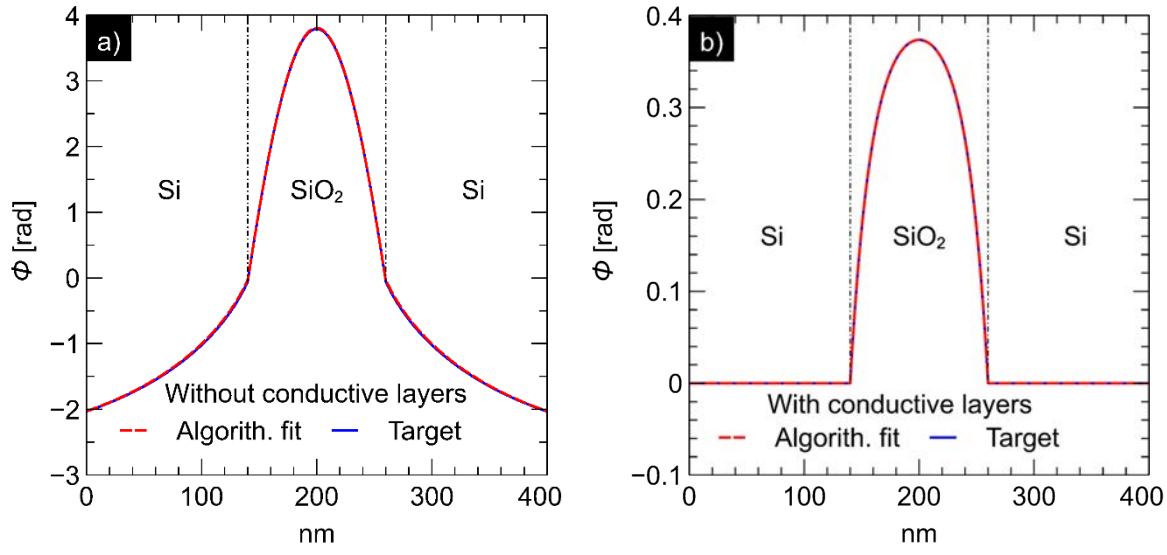

Figure 5.7 : Plots of the auto-fit on the grounded model with and without conductive layers a) and b).

In both cases, the algorithm finds almost a perfect fit, as also shown on Figure 5.7. The parameters that were fitted were the thickness of the sample, the density inside the dielectric, and the length of the dielectric layer. The parameters were retrieved with astonishing precision in this example (Table 5.3).

Fitting	Thickness (nm)	$\rho(C/cm^3)$	W (nm)
Initial	a) 60.0	0.120 000	120.0
Fitted	57.2	0.124 831	119.3
Error	4.7 %	4.0 %	0.6 %

Fitting	Thickness (nm)	$\rho(C/cm^3)$	W (nm)
Initial	b) 60	0.1	120
Fitted	60	0.1	120
Error	0 %	0 %	0 %

Table 5.3: Fitting parameters for the model without a) and with b) conductive layers for the parameters: Thickness, charged density ρ, and dielectric width W and the error associated.

The algorithm based on a gradient descent, called the trust region reflective method (Branch et al., 1999), also allows for the direct calculation of the correlation matrix, which I show just below for the two models without conductive layers Table 5.4(a) and with conductive layers Table 5.4(b).

correlation matrix	Thickness	ρ	W
a) Thickness	1	1	−0.91
ρ	1	1	−0.90
W	−0.91	−0.90	1

correlation matrix	Thickness	ρ	W
b) Thickness	1	0.79	−0.48
ρ	0.79	1	0.17
W	−0.48	0.17	1

Table 5.4 : Auto-fit correlation matrix for the model without a) and with b) conductive layers for the parameters: Thickness, charged density ρ, and dielectric width W.

The correlation matrix shows the relationship between the parameters and can be used to propagate the standard deviation to the parameters that we want to measure. I would like to point out that a correlation between two parameters may have meant in certain cases, for example the total charge with the width of the dielectric and the sample thickness. Correlation is defined as a value between -1 and 1 for maximum correlation and 0 for no correlation. A positive correlation indicates that a change in estimation on one parameter implies a predictable change in other parameters in the same direction, implying that if one parameter increases, the other will also increase. Whereas a negative correlation predicts that increasing one parameter leads to a decrease in the other one.

So, in the case of a grounded capacitor with no conductive layers, a positive variation in thickness predicts a strong variation in density and an inverse variation in dielectric length. Whereas the model with the conductive layers Table 5.4(b) exhibits the same behaviour, it has less impact, which I believe is due to the absence of any stray fields that may disturb the fitting process, to be checked in the future.

2.I.B. Biased Capacitor

The biased capacitor necessitates the inclusion of extra parameters such as the bias and the conductivity of any surface layers. The first example is a model capacitor without any charge layers in the dielectric. On both Figure 5.8, we retrieve the symmetry break caused by polarisation.

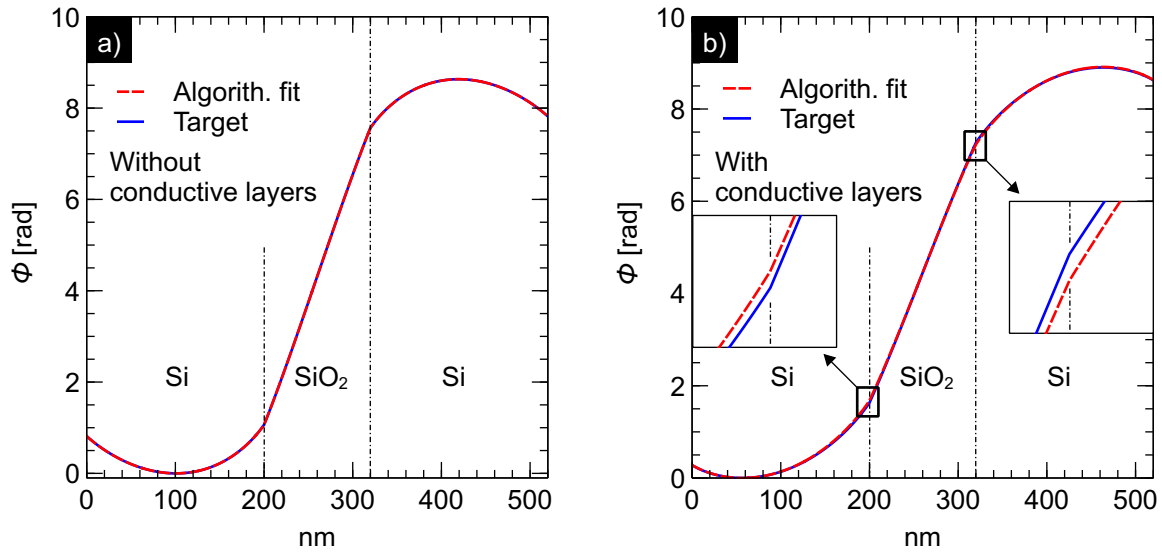

Figure 5.8 : Plots of the auto-fit on a biased model without and with conductive layers a) and b).

Regardless of the fact that there is some variation at the interface in Figure 5.8(b), the fits on the bias model are very good. The variation in the interface area is due to a lack of thickness making smother curvature, because the stray field is more important to the total phase in that case as describes in chapter 3. I chose to test only the parameters difficult to distinguish on the model that is the Thickness versus the bias and the conductivity of the conductive layers (Table 5.5).

Fitting	V_c	Thickness (nm)
Initial	a) 5	60
Fitted	5	60
Error	0 %	0 %

Fitting	Thickness (nm)	$\sigma(S/m)$
Initial	b) 60.0	30 000
Fitted	42.6	16 240
Error	29 %	46 %

Table 5.5: Fitting parameters for the model without a) and with b) conductive layers for the parameters: bias V_c, Thickness and Thickness, conductivity σ, respectively.

In most cases, the first model without conductive layers Table 5.5(a) retrieves good parameters, whereas the model with conductive layers Table 5.5(b) is inconsistent. The use of differential evolution produced better results, but is time-consuming (several hours without the proper optimisation i.e. parallelisation). The best is, I think, to reduce as much as possible the prediction window for the sample thickness using other independent measurement techniques, such as EELS thickness measurement, at the risk of obtaining incorrect predictions for the other parameters used. Table 5.6 depicts the correlation matrix of these parameters.

correlation matrix	V_c	Thickness
a) V_c	1	-0.997
Thickness	-0.997	1

correlation matrix	Thickness	σ
b) Thickness	1	-1
σ	-1	1

Table 5.6 : Correlation matrix for auto-fitting the model without a) and with b) conductive layers for the parameters: bias V_c, Thickness and Thickness, conductivity σ, respectively.

A stray field is always present in the case of the biased capacitor, which means that the correlation matrix between the models with and without conductive layers is very close, in contrast to the grounded model. The correlation matrix demonstrates that the thickness of the capacitor is inversely related to the applied bias Table 5.6(a) and the conductivity of the conductive Table 5.6(b). That is, an increase in thickness predicts a decrease in potential and conductivity.

2.I.C. Biased Capacitor with Charge Area

In the previous chapter, we showed a very captivating SiO_2 sample with charge density at the interface inside the dielectric near the electrode interfaces. Because this is a model with many parameters, automatic fitting makes perfect sense, as illustrated in Figure 5.9.

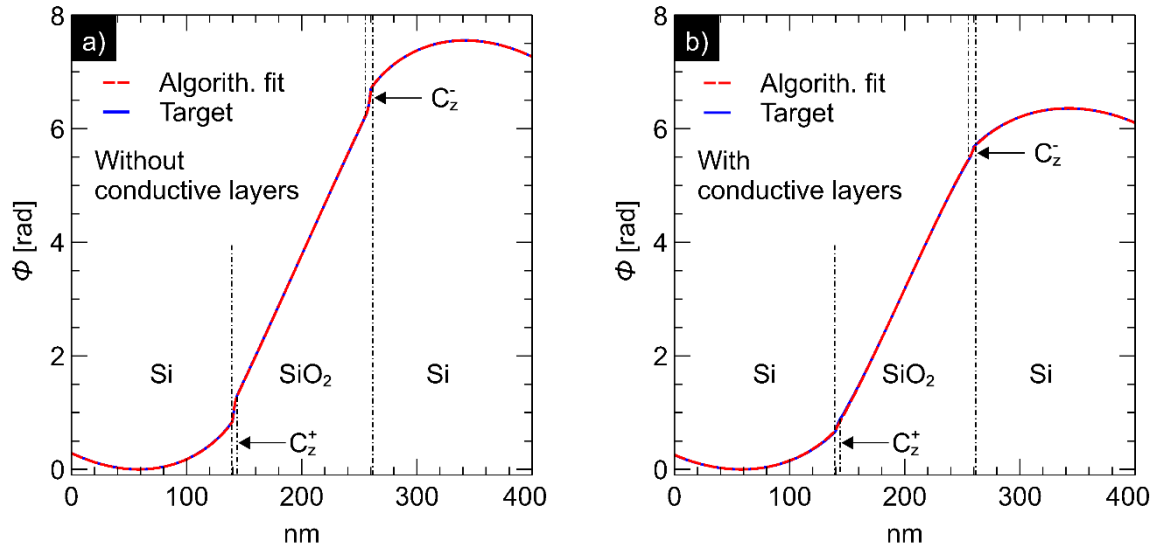

Figure 5.9 : Plot of the auto-fit on a charged biased model with and without conductive layers a) and b).

The fit is very good in both cases. It is interesting to see that the charge density is much less prominent with the second model because the conducting surface layer confines the field from the dielectric charge within the specimen, effectively shielding the stray field from its influence and had fewer charges from the beginning represented here because this is coherent with the charge density injection theory. These fits nevertheless suffer from the same fault identified previously: without better knowledge of the thickness, we cannot properly evaluate the other parameters (Table 5.7).

Fitting		V_c	Thickness (nm)	$\rho_1(C/cm^3)$	$\rho_2(C/cm^3)$	W (nm)
Initial	a)	5.0	60.0	3.000 00	−3.000 00	120.0
Fitted		4.9	62.2	2.847 79	−2.842 81	120.5
Error		2.0 %	3.7 %	5.1 %	5.2 %	0.4 %

Fitting		Thickness (nm)	$\sigma(S/m)$	$\rho_1(C/cm^3)$	$\rho_2(C/cm^3)$	W (nm)
Initial	b)	60.0	10 000	1.000 00	−1.000 00	120.0
Fitted		52.9	7446	0.077 89	−0.532 22	121.0
Error		11.8 %	25.5 %	92.2 %	46.7 %	0.8 %

Table 5.7: Fitting parameters for the model without a) conductive layers and with b) conductive layers for the parameters: bias V_c, Thickness, first ρ_1 and second ρ_2 charged density, dielectric length W and Thickness, conductivity σ, first ρ_1 and second ρ_2 charged density, dielectric length W, respectively.

Table 5.8 shows the corresponding correlation matrix.

correlation matrix		V_c	Thickness	ρ_1	ρ_2	W
a)	V_c	1	−1	1	1	0.30
	Thickness	−1	1	−1	−1	−0.24
	ρ_1	1	−1	1	1	0.30
	ρ_2	1	−1	1	1	0.30
	W	0.30	−0.24	0.30	0.30	1

correlation matrix		Thickness	σ	ρ_1	ρ_2	W
b)	Thickness	1	0.99	0.99	0.99	−0.50
	σ	0.99	1	1	1	−0.56
	ρ_1	0.99	1	1	1	−0.56
	ρ_2	0.99	1	1	1	−0.56
	W	−0.50	−0.56	−0.56	−0.56	1

Table 5.8: Correlation matrix for the auto-fit for the model without a) conductive layers and with b) conductive layers for the parameters: bias V_c, Thickness, first ρ_1 and second ρ_2 charged density, dielectric length W and Thickness, conductivity σ, first ρ_1 and second ρ_2 charged density, dielectric length W, respectively.

We can see several contradictory elements on these correlation matrices. For example, the inverse correlation of charge versus thickness and density versus width of the dielectric W, between the two models Table 5.8 (a) and (b) that cannot be explained for the moment. This suggests that the investigation of the fitting process should be continued.

2.II. Uncertainties for the Laboratory Sample

2.II.A. Uncertainties in the SiO_2 Model

In this section I will present some very preliminary results on applying the automatic fitting procedure to the experimental data.

i. Grounded capacitor

The phase profile across the SiO_2 layer in the grounded capacitor with a conducting surface layer from the previous chapter (4) is shown in Figure 5.10. The automatic fit procedure was used to determine the density of the uniform space charge in the dielectric.

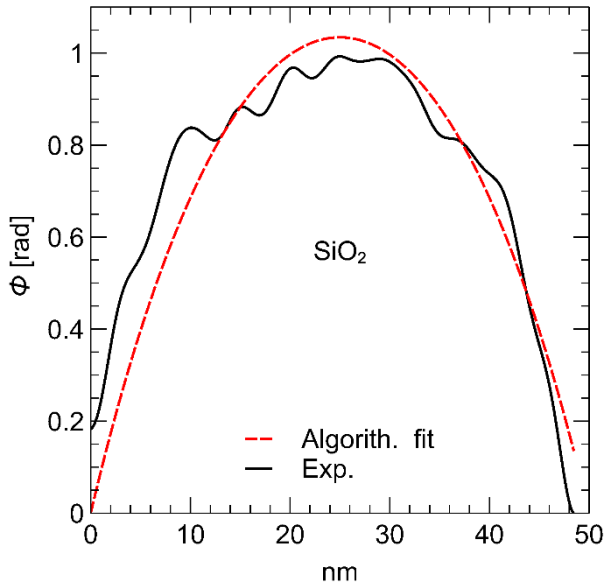

Figure 5.10 : Fit on the grounded SiO_2 sample.

On this fit we can see that, the trust region reflective method allows for a good fit, despite the fact that the experimental curve is quite noisy. The data retrieved by automatic fitting is compared to the data fit manually (Table 5.9).

Fitting	Thickness (nm)	$\rho(C/cm^3)$	W (nm)
Manually	100	0.220 000	51.0
Fitted	80	0.365 294	52.5
Error	20 %	66.0 %	2.9 %

Table 5.9: Parameters of the grounded SiO_2 sample.

In contrast to the experiment of self-consistency on the grounded model with conducting layers, the introduction of noise and the reduction in fitting area resulted in parameters that could not be retrieved without knowledge of the thickness. This reminds us of the importance of having an independent measurement of the thickness of the samples.

Table 5.10 shows the correlation matrix obtained using the experimental phase profile. We can see that it is similar but not identical to the correlation matrix obtained from the simulated data shown previously (Table 5.4), notably in the correlation with the dielectric layer width, w.

correlation matrix	Thickness	ρ	W
Thickness	1	1	-0.73
ρ	1	1	-0.73
W	-0.73	-0.73	1

Table 5.10: Correlation matrix of the grounded SiO_2 sample.

So, we can see that the correlation between the self-consistency and the real case decreases in an experimental case, which I believe is due to a reduction in the frame parameters to fit the length of the dielectric *w* because it is measured on the amplitude experimental image, and we can reduce the frame to $\pm 1\, nm$ around the value measured experimentally.

ii. Biased capacitor

I also performed a test on the SiO_2 5V biased models (Figure 5.11) from the experimental data previously studied in Chapter 3.

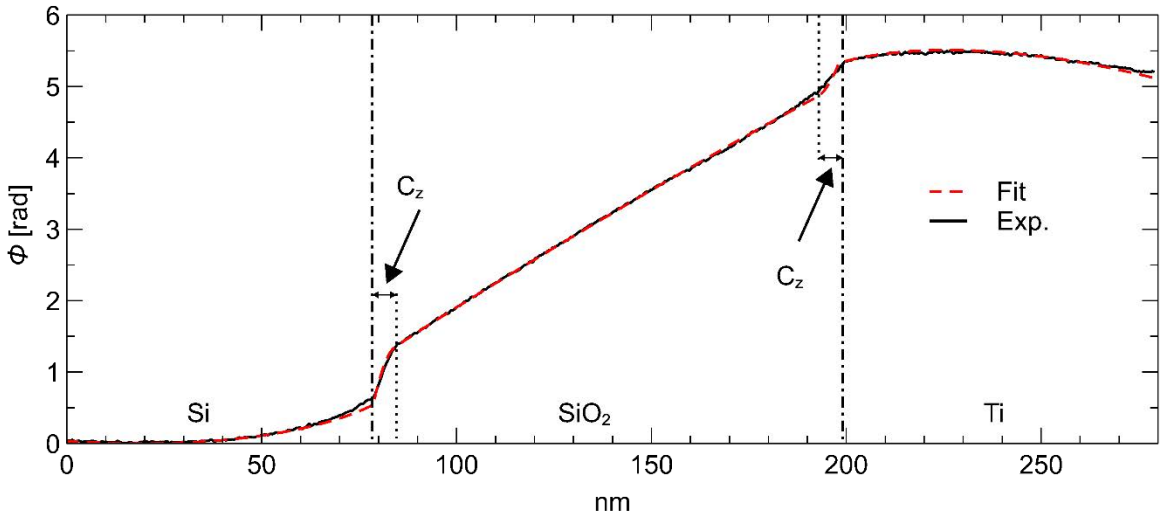

Figure 5.11 : Fit on the biased SiO_2 sample.

I let four parameters vary, the specimen thickness, the charge density in the two interface regions and the dielectric width (Table 5.11) and we obtained a good fit (Figure 5.11).

Fitting	Thickness (nm)	$\rho_1(C/cm^3)$	$\rho_2(C/cm^3)$	W (nm)
Manually	55.0	3.000 000	−1.500 000	120.0
Fitted	65.4	3.083 243	−1.585 727	119.4
Error	18.9 %	2.8 %	5.7 %	0.5 %

Table 5.11: Parameters of the biased SiO_2 sample.

The trust reflective method finds an excellent fit and good values for the parameters, with the exception of the well-known issue of sample thickness and a good quantity of charges. As we can see, the error on the thickness has a different effect on charging than the experimental grounded capacitor. Because the length of the charge area in the induce charge model is much finer, so variations in thickness imply fewer charges with a smaller charged density area.

The same phenomenon observed on the correlation matrix for the grounded sample is observed on the correlation matrix analysis of the biased sample (Table 5.12).

correlation matrix	Thickness	ρ_1	ρ_2	W
Thickness	1	−0.73	−0.23	0.24
ρ_1	−0.73	1	0.83	−0.84
ρ_2	−0.23	0.83	1	−1
W	0.24	−0.84	−1	1

Table 5.12: Correlation matrix the biased SiO_2 sample.

When we compare the results to the self-consistency study, we see that the correlation between the parameters is lower, particularly for the charged density parameters, which can be explained by the reduced the parameters ranging for each charging area in terms of norm as well as signs.

2.II.B. Uncertainties in the Si_3N_4 Model

The last sample I tried to fit was the Si_3N_4-based capacitor shown previously in chapter 4, which is relatively simple if we ignore the curvature of the phase inside the dielectric (Figure 5.12).

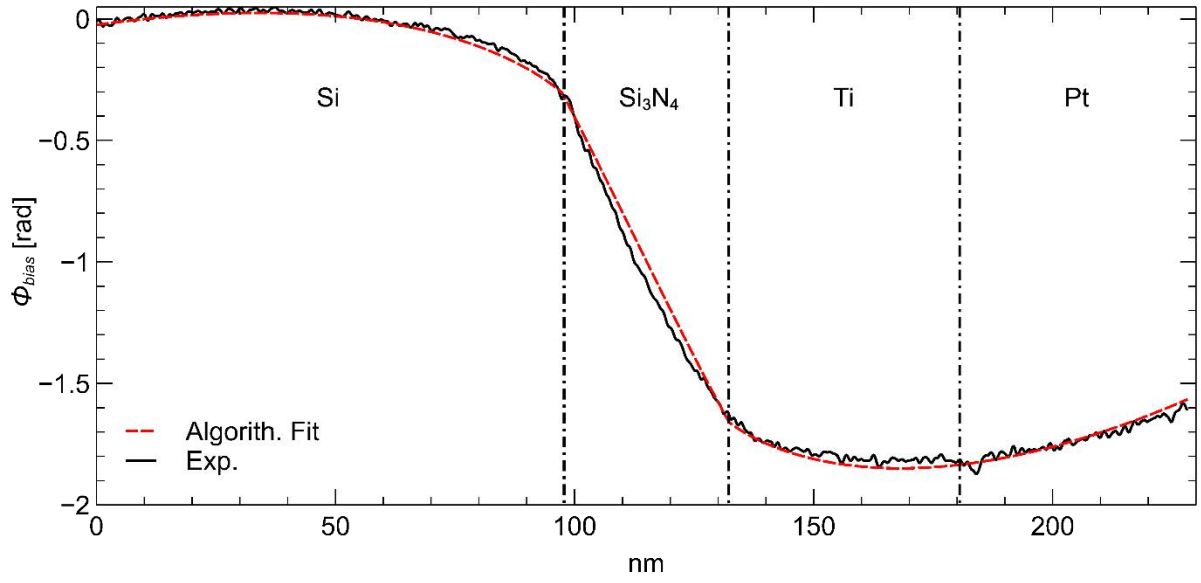

Figure 5.12 : Fit on the biased Si_3N_4 sample.

By reducing the thickness range to be between 40 nm and 50 nm as indicated by EELS measurements, the fit is very good, as are the predict parameters (Table 5.13), which are the conductivity and, indirectly, the bias.

Fitting	Thickness (nm)	$\sigma(S/m)$	W (nm)
Manually	46	660	36
Fitted	42.7	566	35
Error	7.2 %	14.2 %	2.8 %

Table 5.13: Parameters of the biased Si_3N_4 sample.

We can also compute the correlation matrix using this model (Table 5.14).

correlation matrix	Thickness	σ	W
Thickness	1	0.99	0.63
σ	0.99	1	0.68
W	0.63	0.68	1

Table 5.14: Correlation matrix of the biased Si_3N_4 sample.

Taking the analysis, a step further, we can calculate the uncertainty in the applied bias. I computed the coefficient c_i From the propagation equation (5.1) by modifying one component by 5% and determining its impact on the interesting parameter (here the bias) by refitting while blocking the other parameters. We can use these coefficients with the correlation matrix and the covariance matrix to compute the uncertainty in the bias. With a bias of - 4V applied, the algorithm predicts a local bias of $-2.2 \pm 0.2V$. Despite the incompleteness of this study, I believe this automatic technique will be very useful in the future. The code simplifies this type of analysis while removing as much human bias as possible. In a similar vein, I wish to present another promising development in the following section.

3. Machine learning

3.I. Simplified Predictions of the Internal Potential of the Capacitor

These sections were accomplished during a 4th year student project of Marc Gueissaz (INSA Toulouse) that I supervised.

Despite the accuracy of the finite element method calculations, they are slow, particularly for 3D model calculus and fitting, which can take hours or days to complete manually or via algorithm loops. Although training a neural network takes a significant

amount of time and effort, after the learning phase has been passed, a neural network execution is much faster than conventional numerical simulations. It was therefore interesting to explore whether the efficiency of the fitting process could by improved by using Machine Learning.

Rather than beginning with phase images, I chose the simpler case of the potential profile inside a capacitor, which is much easier to control because there are fewer variables that can influence the prediction. We wanted to detect several parameters, including the dielectric length *w*, the length of the space charged density C_z and its charged norm, as well as the applied bias (Figure 5.13).

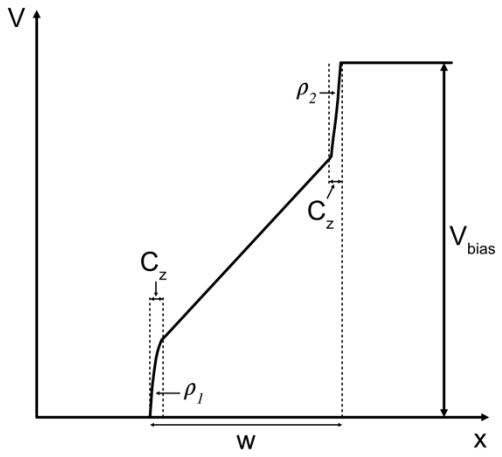

Figure 5.13 : Potential profile inside a capacitor with two charged areas.

For the learning, I created a database with 100,000 examples based on the analytical model developed with GMS script which I translated into Python code. The parameters were randomly generated by a PCG-64 pseudo-random number generator (O'Neill, 2014) with a uniform distribution, which has been chosen for its very good statistical test performance and its extreme rapidity.

The database is divided into two sections. 80% of the data set is used to train the neural network, with the remaining 20% saved for testing. The neural network is thus tested on data that it has never seen before to ensure its efficiency.

The neural networks were composed of three hidden layers with one ELU activation function framed by Two ReLU activation function [see chapter method (2)]. This

combination prevents gradient evanescence and dying (progressive decay of negative gradients).

The quality of the prediction is affected by the number of neurons in the neural network, but the relationship is highly non-linear. To determine the best neuron number (Figure 5.14), we compared the mean absolute error on learning with the number of neurons in the first layer (also known as the first hidden layers), while keeping in mind that the first two hidden layers have the same size and the third is half the size of the previous one.

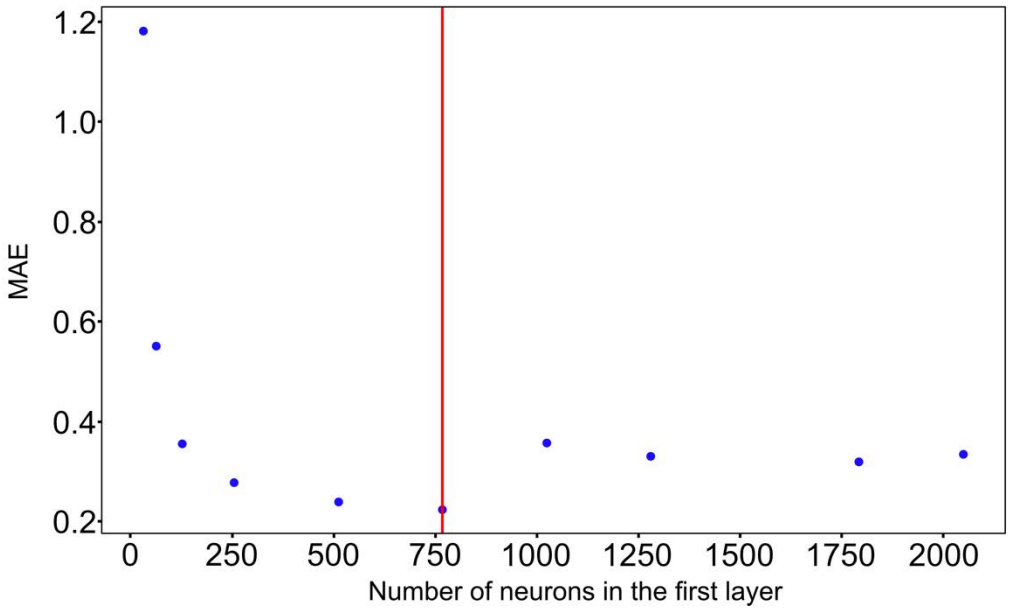

Figure 5.14 : The mean absolute error in relation to the number of neurons in the third layers of the neural network.

We can see that initially the mean absolute error decreases rapidly as the number of neurons increases. However, when there are too many neurons, the error rate of the neural network increases. On the one hand, we want the smallest neural network possible, and on the other, the smallest errors; ultimately, we select 768 neurons for the first two hidden layers and half that number for the third.

After training the neural network using the test database, we evaluated its efficiency using the remaining 20% of data. For the representation, we plot the predicted value, which is the value predicted by the neural network, against a true value, which is the corresponding parameter that came directly from the test database (Figure 5.15).

With this representation, if the predicted value versus the True Value shows a perfect linear relation that means the predicted value corresponds to the true value; otherwise any deviation or spread is a defect of prediction. The predicted parameters range from - 10 V to 10 V, the dielectric length ranges from 10 nm to 140 nm, and the width of the space charge regions ranges from 1 nm to 10 nm.

It quickly became clear that the prediction of density does not work; we believe this is due to a scale factor within the neural network preventing proper learning. Due to time constraints, we attempt to learn at the neural network without detecting charge density, with the understanding that we will be able to integrate it later if we can demonstrate that the network works.

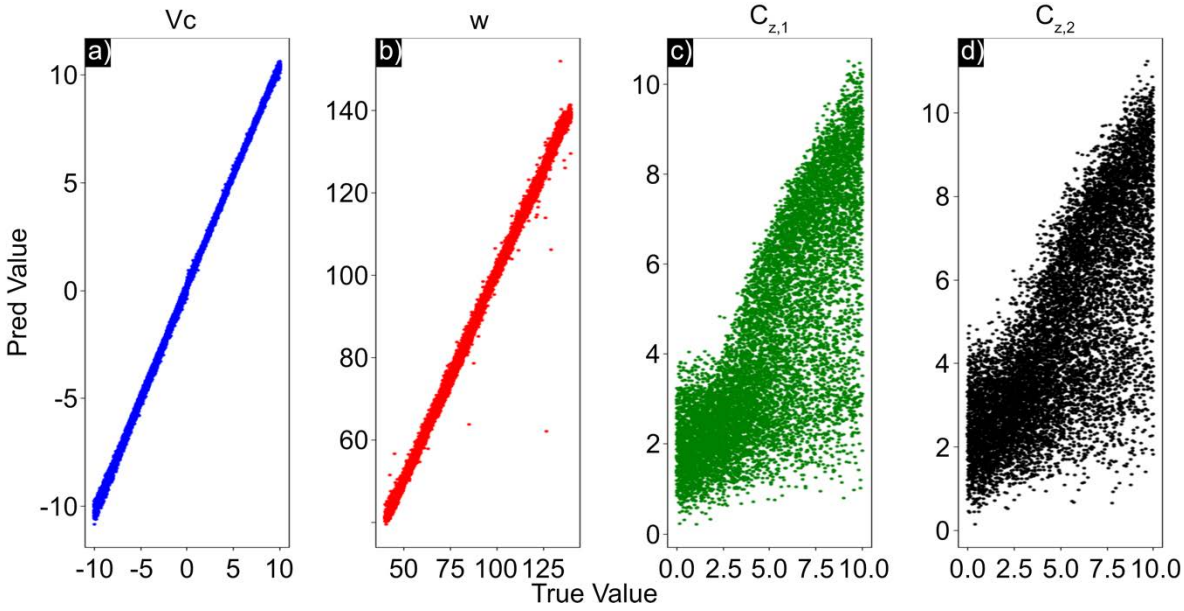

Figure 5.15 : Plot of the predicted value versus the true value for the bias parameter, dielectric length, and charged density length.

Figure 5.15 shows that the potential V_c is very well predicted and does not appear to be distribution dependent, as is the prediction of the dielectric width. At first, the value of the length of the charged layers then appears to be skewed, with a distribution that increases with the length of the charged layers. There are several factors that can explain this behaviour.

The first is that we do not have an adequate training data set, and the second is that we draw the charge density randomly regardless of the applied potential, so for the

same potential, we can have some nonphysical behaviour within the data set, such as a sign of density impossible with the sign of the potential.

To address these prediction flaws, we constrained the dataset to be more physical. For this, we used the measured charged density in the experimental SIO_2 capacitor, as detailed in the modelling experimental data chapter (4).

The charged density ranges know from $-4 \times 10^6 C/m^3$ to $5 \times 10^6 C/m^3$ on the left while on the right $-3.6 \times 10^6 C/m^3$ to $4 \times 10^6 C/m^3$ while there are consistent with the bias applied. The results are shown in Figure 5.16.

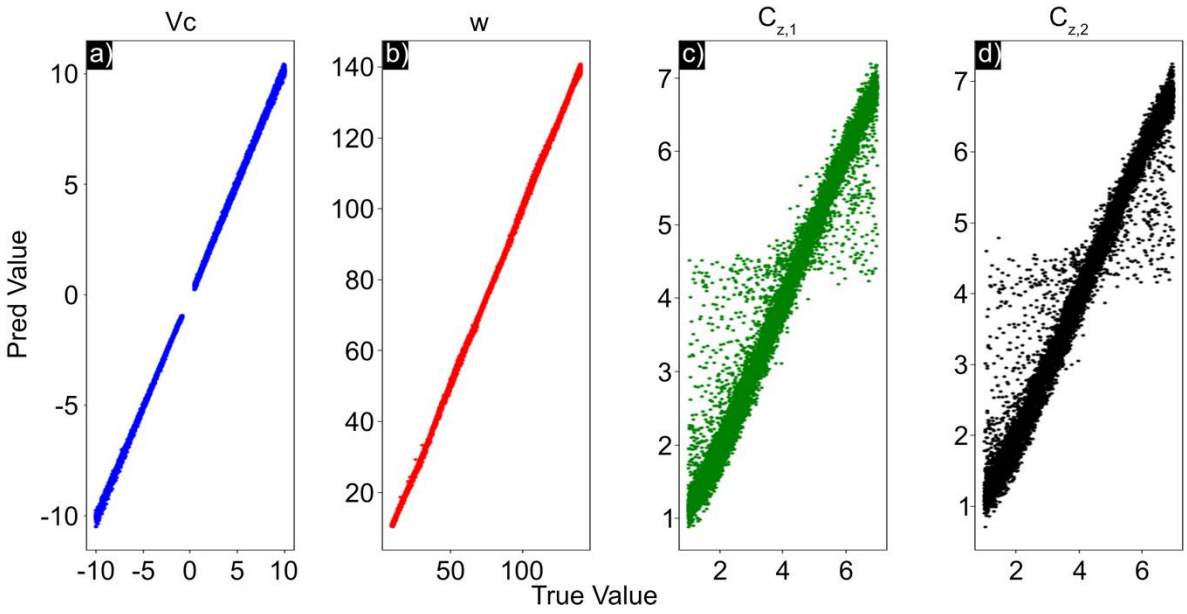

Figure 5.16 : Plot of the predicted value versus the true value for the bias parameter, the length of the dielectric and the length of the charged density.

Because the effect of charging on the profile potential is extremely small, we helped the neural network by avoiding bias around zero on a window ranging from - 0.5 V to 0.5 V, as shown in Figure 5.16.

As hoped, the new training data set shows a better distribution of predicted dielectric length. The prediction on the size of the charged density is then much better, and we can also see that the dispersion of bad values is centred around the centre length of the charged density, implying that the value predicted less than half the length does not go wrong more than half the length, and the values of uppers behave similarly.

To do so, we examined the error distribution minus the true value for each predicted value, which should reveal more about the behaviour of the neural network and how we can improve its performance; in order to do so, we'll create a bar chart to visualise the error dispersion (Figure 5.17).

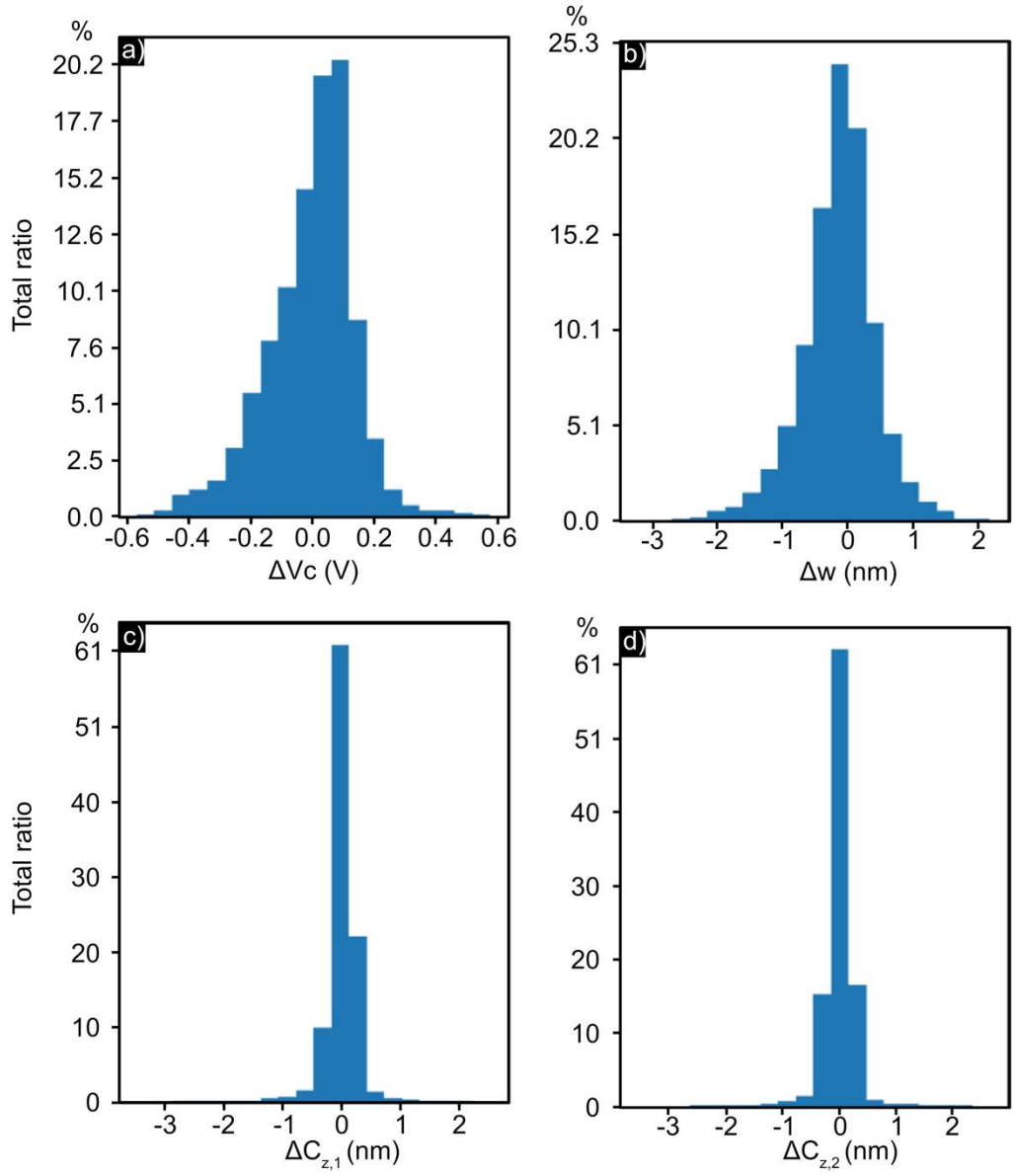

Figure 5.17 : Parameter histograms of the bias dispersion a) along the predicted length of the dielectric length b), and the width of the two charged area c),d).

By studying the histogram, we can see that the mean absolute error (MAE) on the bias is around V = 0.10 V, which is very close to the solution; however, the histogram appears to be non-symmetrical and has a leaning towards the negative side, indicating

that the neural network frequently predicts values that are below the actual value. Although the MAE on the measurement value of the dielectric length seems to be higher, it should be remembered that the measurement is made on a length much shorter than the length of the load zones that is respectively $\Delta w = 0.42$ nm, $\Delta C_{z,1/2} = 0.18$ nm meaning that the spread around the length of the dielectric is as good as that of the charged zones, if not better (if we think in terms of absolute error).

And with these data we touch the sensitive part of the neural engineering, meaning that we can have excellent predictions most of the time but sometimes extreme failure can occur. These are named outliers, while 99% of values are inside the nanometre interval.

To go further, we must continue the integration of the charged density measured and the training of the neural networks on phase profiles. Despite the fact that the predictions were extremely convincing, we should also investigate the confidence of the measure and find a way of identifying outliers. Another possibility is to use a neural network adapted to phase images to find the starting parameters for the Trust Region algorithm, allowing statistically to accelerate convergence and obtain the above-mentioned uncertainty calculation.

3.II. Ellipse Detection

The student project also included research on the development of an automatic alignment system for the microscope in order to improve hologram precision. Though this part is not directly related to modelling, it gave results worth describing.

Obtaining holograms with an optimal signal-to-noise ratio requires a precise alignment of the microscope. This alignment includes the adjustment of the beam shape (Figure 5.18) and its spatial stabilisation with respect to the sample.

Indeed, by combining the ellipse detection and electron beam trajectory simulation (developed during the thesis of Julien Dupuy (Dupuy, 2021)), it might be possible to obtain faster and more accurate values for the different parameters controlling the microscope. The very first step is to see if a neural network can parameterize the shape of the beam, which we will assume to be elliptic for simplicity.

The goal here is to train a network to extract the values that characterise an ellipse from a 128*128 pix image. In the following, I will explain how an ellipse is theoretically defined, then the importance of selecting a random generator that allows the calculation of a variety of ellipses.

An ellipse can be defined by the intersection of an infinite plane with an infinite cone, provided that this plane also cuts the axis of revolution of the cone. More precisely, an ellipse can be defined by 5 parameters. These are *u*, *v* the offset of the centre of the ellipse from the origin, *a*, *b* which are respectively called semi-major and semi-small axes, and finally, θ its inclination to the axes (Figure 5.18).

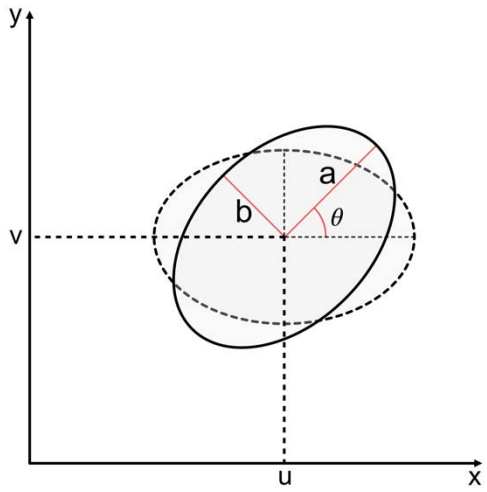

Figure 5.18 : Scheme of the ellipse we want to measure, the semi-minor axe, semi-major axe, the position u and v of the ellipse and the angle.

The equation that was used to calculate the ellipses in the database code is (5.3):

$$\frac{[(x-u)\cos\theta+(y-v)\sin\theta]^2}{a^2}+\frac{[(x-u)\sin\theta-(y-v)\cos\theta]^2}{b^2}=1 \qquad (5.3)$$

In order to generate an unbiased database, I used a generator using the permuted congruential generator (PCG) algorithm (O'Neill, 2014). That is, it is constituted with ellipses having different parameters distributed in a uniform way. Indeed, a good random generator avoids that a range of parameter values are overrepresented

compared to its total range, which avoids learning bias. Moreover, the objective being to create a database in a minimal time, the PCG algorithm is very fast because of its storage format which is binary compared to its quality (period = 2^{64}) which is of a cryptographic level (O'Neill, 2014).

The code generates a database in the file format hdf5 (this format allows extremely fast data access and is not limited in size). In the code we can choose the number of ellipses constituting the database, the size of the image (all sizes are expressed in pixels) and the range over which the parameters of the ellipse vary. There is also a function to add Gaussian noise to the images from the PCG generator (Figure 5.19).

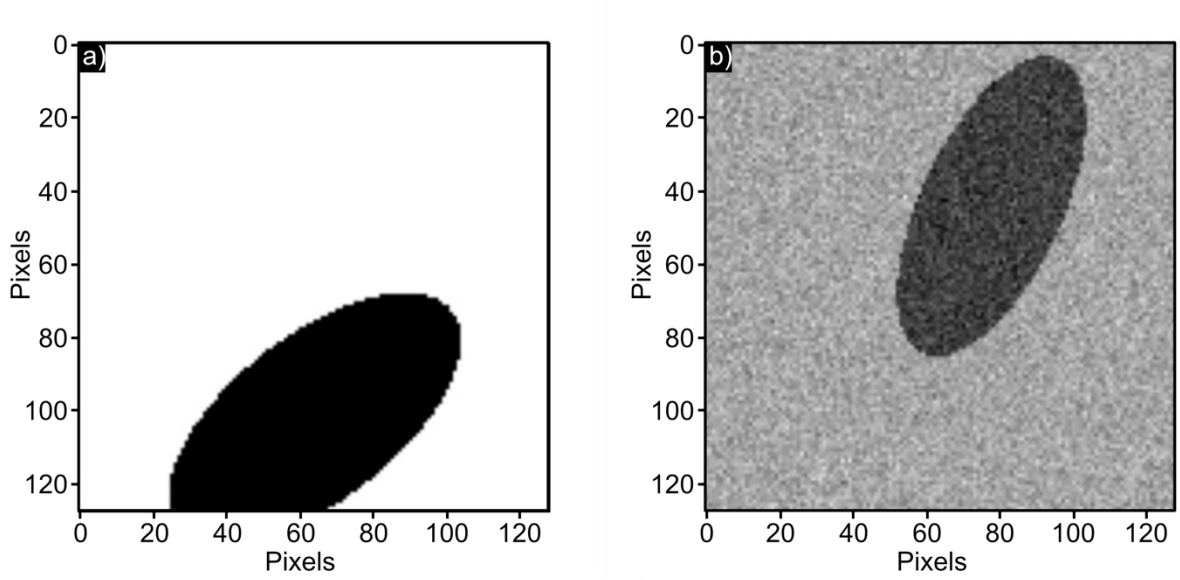

Figure 5.19 : Sample of the ellipse created for training the neural network, on the left without noise, on the right Gaussian noise added.

The neural network was also tested on noisy images, with a standard deviation of the noise of 20% of the mean intensity. There are 3 hidden layers with one ELU activation function framed by Two RELU activation function like the preceding neural network. As before, we first try to optimise the number of neurons in the first two hidden layer knowing that the third is half the first two layers (Figure 5.20).

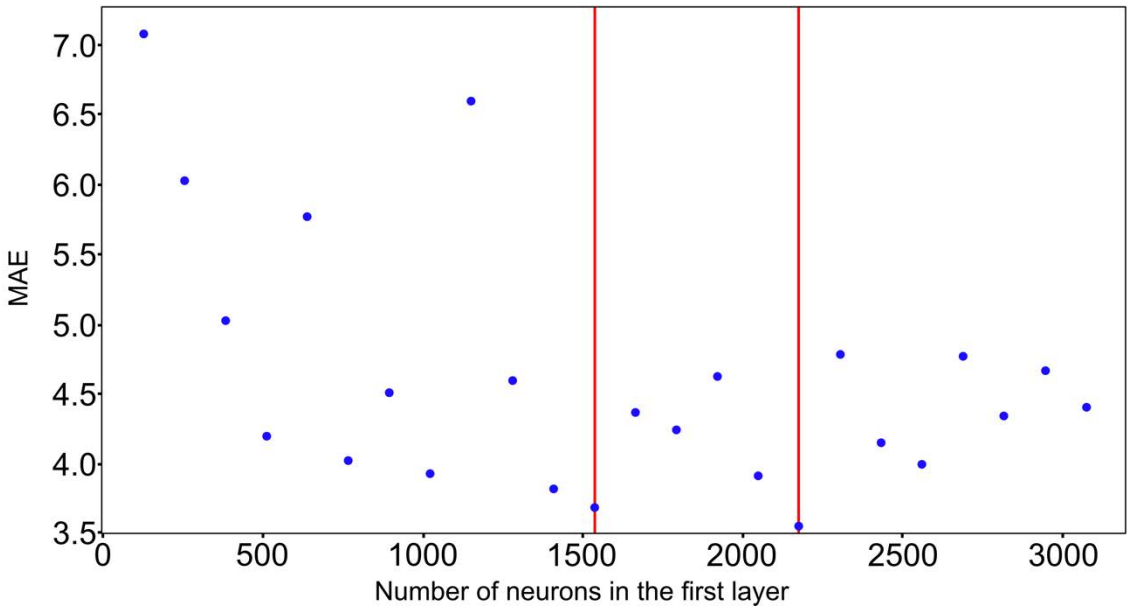

Figure 5.20 : Measure of the mean absolute error in respect to the number of neurons inside the first layers of the neural network.

From the curves, we chose 1536 as the best number of neurons.

Numerous examples of the prediction of our neural network are shown in Figure 5.21.

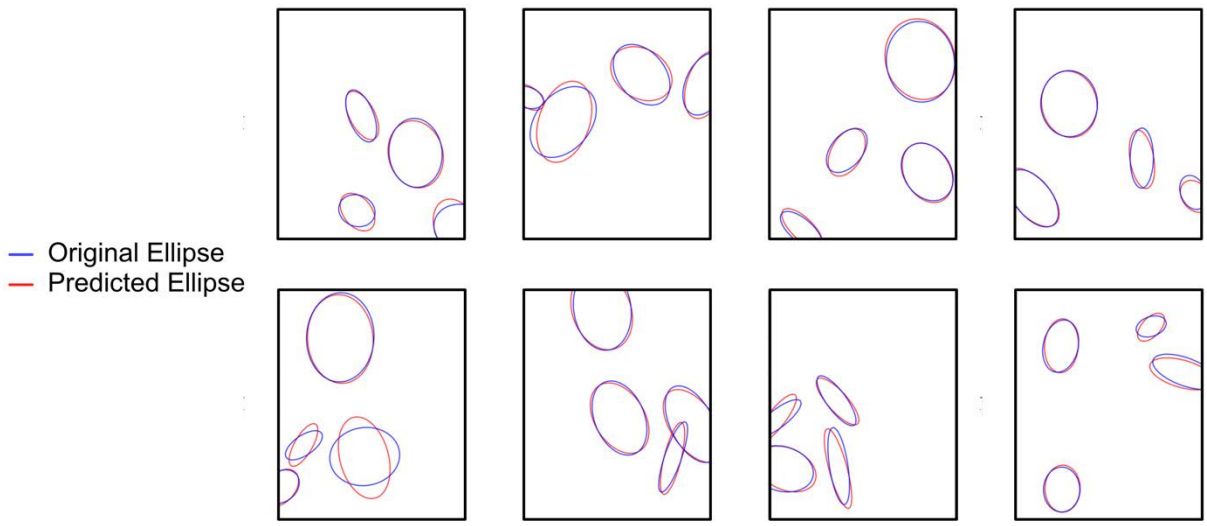

Figure 5.21 : Example of the predicted ellipse in red with the ellipse true ellipse in blue.

We can see that the neural network guesses the size and position fairly well, whereas some ellipses are not well aligned.

To continue the characterisation of the neural network, we plot the predicted value versus the true value to see the error within the distribution (Figure 5.22).

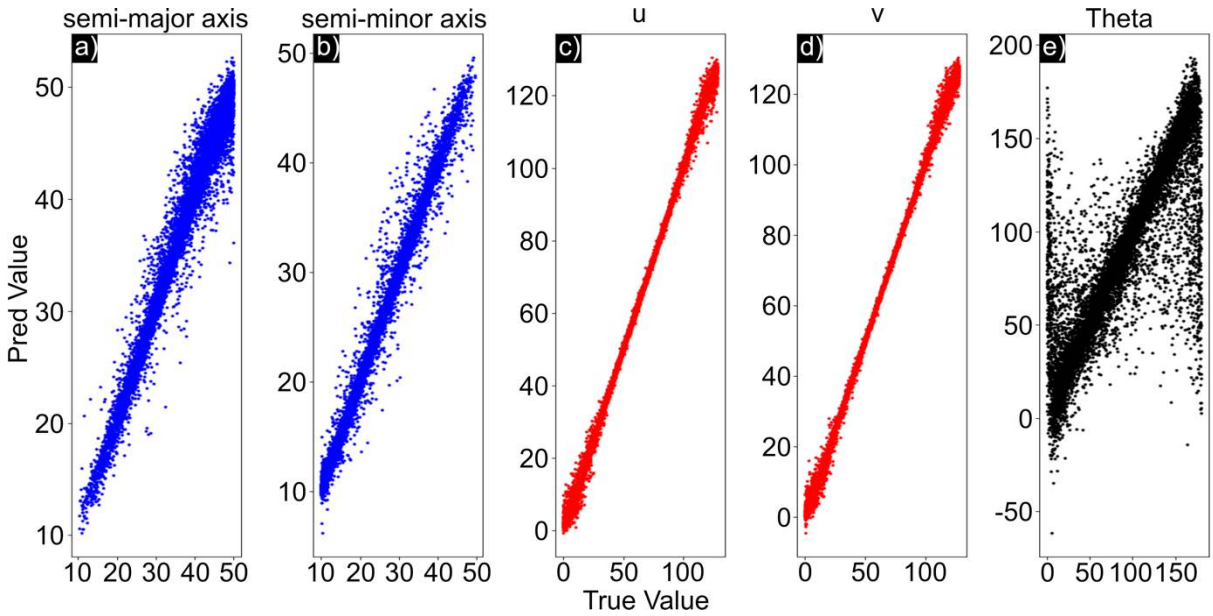

Figure 5.22 : Plot of the predicted value versus the true value for the bias parameter, semi-major length, semi-minor axe length, ellipse position following x and y, and angle.

For the semi-major axis, the error increases with measured length. This is partly due to the fact that the absolute error naturally increases with the length of the measured quantity, but also because larger ellipses have a higher chance of not being wholly inside the image. The error in the semi-minor axis appears more uniform. This is probably due to the fact that large semi-minor axes are less likely (by definition, it is the smaller axis). Nonetheless, despite its low visibility, we can assume that the dispersion would increase within the higher value. For the ellipse position (u and v), on the other hand, the error increases towards both extremes of the ellipse position (u and v). This is again probably caused by the increased likelihood of partial ellipses in the image field of view.

Interestingly, for the orientation of the ellipse, the neural network sometimes predicts value less than 0 and greater than 180, beyond the boundary values in the training techniques exist for constraining a neural network that we did not have time to investigate.

Another point to note is that there is a significant dispersion around the zero and 180 values. Because of its symmetry, an ellipse with an angle of 0 is indistinguishable from an ellipse with an angle of 180.

As previously described, we will examine the error distribution minus the true value for each predicted value and create a bar chart to visualise the error dispersion (Figure 5.23).

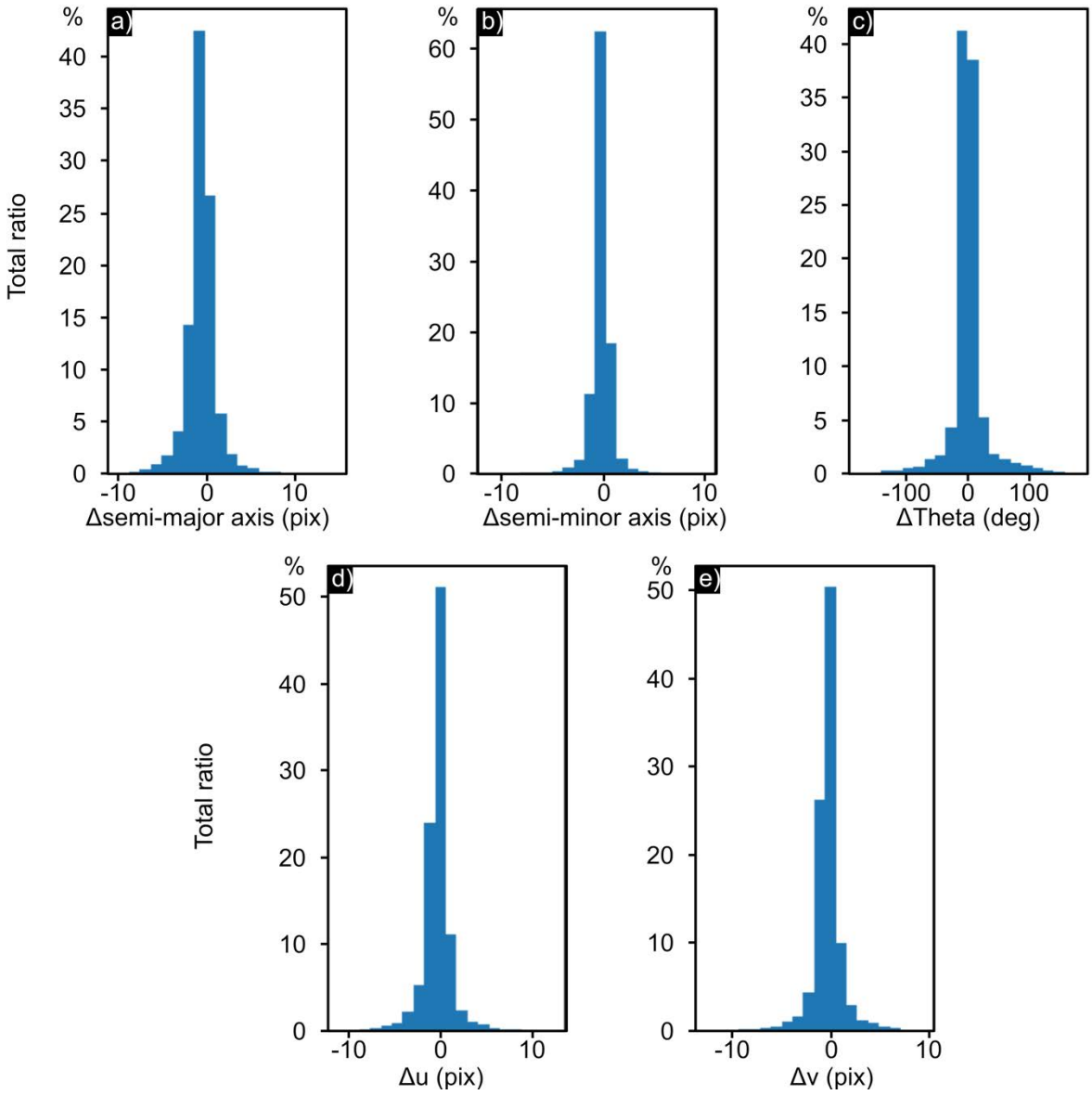

Figure 5.23 : Histogram of the parameters predicted.

The histogram shows that the error is relatively contained, we have the mean absolute error of Δsemi-major axis = 0.76, Δsemi-minor axis = 0.47, Δu = 0.70, Δv =0.64,

ΔTheta = 11.05. Despite the larger angular error, the mean absolute error of the other parameters is very good, being less than one pixel. The measured length has a relative error of about 0.5%, and the angle has a relative error of about 6%. This is good but some outliers in the data can be extremely inaccurate.
The performance of the neural network looks highly promising, surprising even, and should be pursued further

4. Conclusion

Starting with the observation of the complexity to extract quantitative data from our numerical simulations, I showed how we can study the uncertainty of each parameter. The uncertainties can then be propagated using a correlation matrix to be able to determine the overall uncertainty in the desired parameter.
Moving from manual to automatic fitting, I demonstrated that the Trust region reflective method works as long as we give the thickness of the sample to the self-consistency algorithm. Despite the fact that the work was incomplete, I demonstrated that the algorithm can be used on experimental data with the uncertainty calculated on one example.
We began developing an IA-based method to speed up the fit because auto-fitting on 3D models can take hours. I demonstrated that a neural network can be used for fitting and investigated the limitations of the neural network.
To take it a step further, combining this simulation with the electron beam simulation inside the microscope may allow us to better simulate the interaction between the electron beam and the sample. The use of AI to speed up calculation should be pushed a little further by testing the neural network on phase images. Furthermore, I believe that understanding the interaction between the field of the capacitor and the reference area is a challenge that we must overcome in order to study more complex fields for other models with different but complex shapes.

Chapter 6 — Microelectronics Industry Sample

1. Introduction

Nano-electronic devices are important in many fields, and their development continues to receive considerable attention in fundamental and applied research. In fact, the microelectronics industry excels in innovation and the further miniaturisation of products in response to a constantly rising demand for high performance and low-cost devices, as well as being driven by competitiveness. However, device shrinkage and increasing device architecture complexity necessitate local quantitative studies. Access to local electric fields and electric charge distribution mapped at the nanometre scale across a single operating device would provide critical information for future developments or design improvements and optimisation. The resulting data can also help with failure analysis, as very precise high-resolution local observations of nanodevices in operation is being used to detect isolated defects or abnormalities in a single region.

In this chapter, I present the study of a set of metal-insulator-metal (MIM) nanocapacitors that were selected and extracted from production lines of STMicroelectronics to be biased for *in situ* electrical experiments within the TEM. I show how device functioning in real working conditions studied with *operando* electron holography and combined to finite element modelling (FEM) simulations I developed can be used to map electric fields. To that end, we will investigate the operation of two single real devices as well as the interaction of multiple devices belonging to the same type. The main results have been published in two articles (Brodovoi et al., 2021, 2022).

In order to be applicable to real devices, we use and expand the methodology developed on previous analysis. Changes needed to be made to the experimental

procedure, notably the sample preparation by FIB, and to the modelling, which had to be more complex now including a 3D model.

2. Sample Preparation

Experiments were carried out on a matrix of STMicroelectronics devices manufactured using their 28 nm FD-SOI (Fully Depleted Silicon-on-Insulator) process. A thin 11.5 nm tantalum pentoxide (Ta_2O_5) high-k insulator sandwiched between two TiN electrodes connected to a Cu pillar (above) or an Al layer (below) is used in backend upper layers for high frequency circuit applications (Figure 6.1). The upper electrode of TiN is 950 nm wide (in the image plane) and 1.7 µm deep.

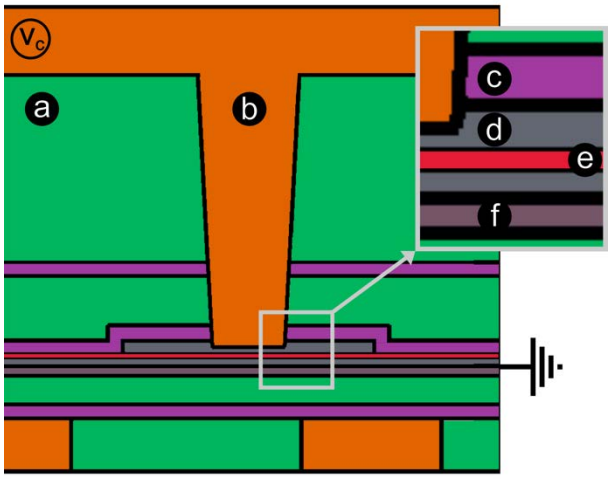

Figure 6.1 : MIM nanocapacitor architecture: active region of Ta_2O_5 e) dielectric sandwiched by two TiN metallic electrodes d), interconnected with Cu b) and Al f) lines, and protected from leakage current with SiO_2 insulating layers a) and Si_3N_4 lines c).

To bring electrical stimuli to the device while ensuring its electrical functionality and compatibility with TEM observations, a specific sample preparation combining a TEM lamella preparation flow and a FIB-Edit capability has been developed in the framework of the thesis of Maria Brodovoi in collaboration with STMicroelectronics. This step was tricky because the approach and methods for circuit modification and electrical connections must be scaled down to the sub-µ scale. Using a ThermoFisher Scientific™ Helios NanoLab 1200AT DualBeam TM with a gallium liquid-metal ion

source, samples were milled and lifted from a fully processed wafer, before being prepared for electron transparency and *in situ* biasing at STMicroelectronics (Crolles, France). A multiple line gas injection delivery system (MultiChem) and a gas injection system (GIS) were included, both of which enable ions and electron beam-induced deposition and selective etching for effective and high-rate circuit modification.

Here now the main steps of this delicate sample preparation. To avoid charging areas thus possible deviation of the ion beam, a thin conductive layer (gold-palladium alloy) was deposited on the surface of the specimen before any further steps. The sample was then grounded by opening the pad (Figure 6.2(a)) and filling it with Pt to connect the top surface to the grounded Si substrate: during sample preparation, the charge of the scanning electron beam (SEM) was drained off to the ground.

Because capacitors are susceptible to electrostatic discharge (ESD) damage, it is critical to keep the structure from floating during FIB-Edit. This can be accomplished by connecting both the top and bottom electrodes ahead of time, by milling a line and filling it with Pt on the top surface (Figure 6.2(a)). This protective layer serves several functions: it acts as a shield to protect the structure during FIB milling, it prevents charge accumulation, and it temporarily brings both electrodes to an equipotential state. The sample was then deprocessed top-down with FIB until the layer of interest is reached. The Cu lines that connect the nanocapacitors are now exposed (Figure 6.2(b)), and top and bottom electrodes are brought back to the same potential by depositing a Pt layer (Figure 6.2(c)).

An Omniprobe (micromanipulator) was used to directly weld the extracted sample onto an electron-transparent Si_3N_4 grid with Au prepatterned tracks (Figure 6.2(e, f)). Tungsten (W) depositions ensured that the sample and grid were electrically connected. The region of interest (here, Ta_2O_5 oxide) must be no more than 500 nm from the vacuum region (Figure 6.2(g)) where the reference wave is placed to meet electron holography criteria. The top electrode was separated from the bottom electrode in order to create two distinct electrical connections for *in situ* biasing. Figure 6.2(h) shows two separation cuts (bottom left and top right).

A final thinning of the lamella with a low energy ion beam (8 or 16 kV) was performed to minimise surface damage and achieve a uniform thickness of less than 100 nm for electron transparency.

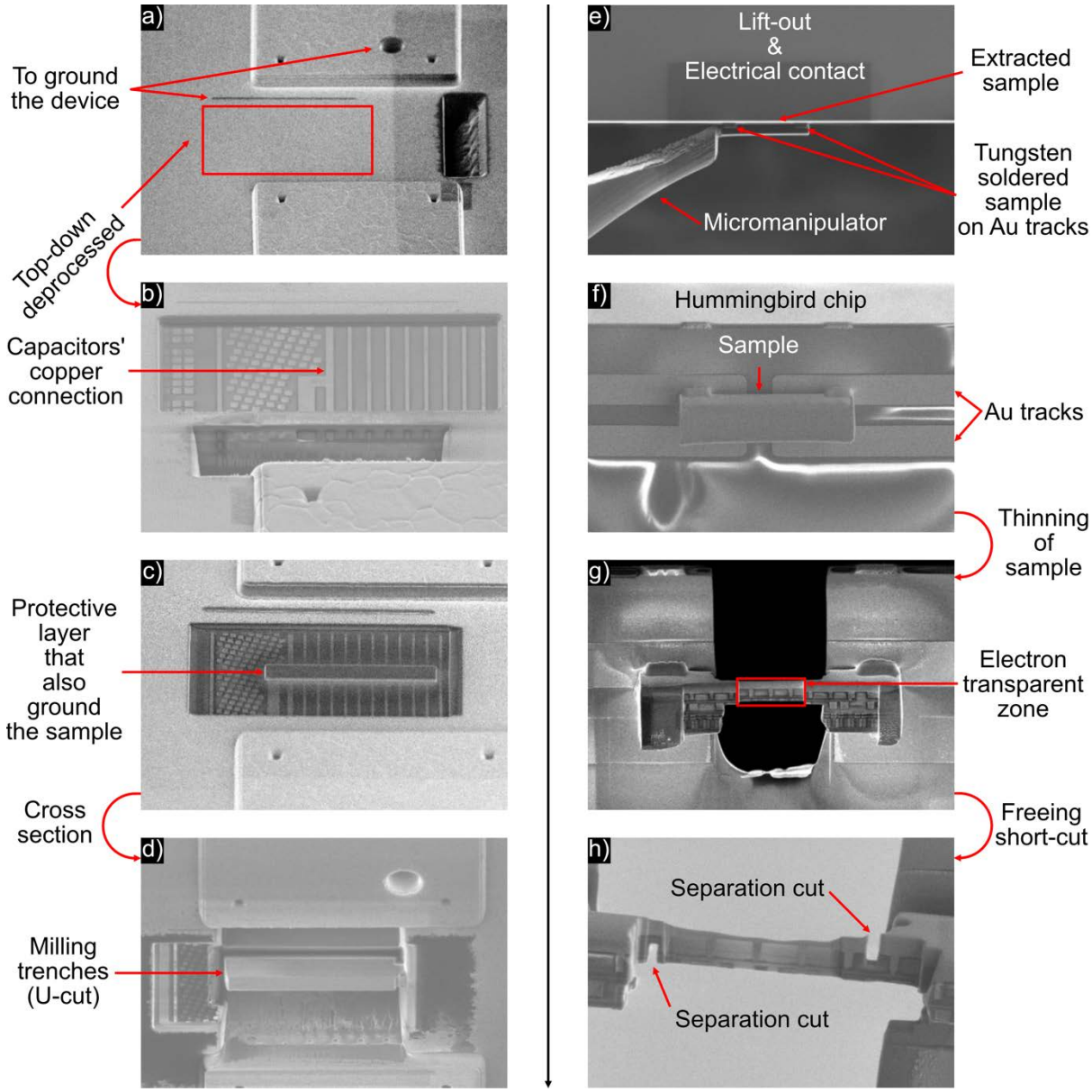

Figure 6.2 : Sample grounding & electrode connections a). Visible Cu lines after FIB deprocessing b). Protective Pt layer c). Sample before lift-out d). Sample welding to the dedicated TEM grid e). Chunk welded on the TEM grid f). TEM grid membrane milling & free area for EH reference wave g). Final thinning & electrodes separation h).

The connected device to a dedicated chip was placed in a Hummingbird holder designed specifically for biasing experiments. Prior to the experiments, the devices were electrically characterised by a nanoprobe (nProber III from ThermoFisher). The capacitance of the array of individual MIM was measured to be 352fF at 1 MHz. Such specimen devices are extremely fragile because their capacitances are estimated to

be only 2.1 fF, highlighting that the cross-sectional area of the dielectric in the thin lamella is 17 times smaller than the original device.

Assuming the parallel plate capacitor formula with a surface corresponding to the top TiN electrode yields a relative electric permittivity of thin-layer Ta_2O_5 of 25, which is within the range (22 to 28) of values found in the literature (Chaneliere et al., 1998). Notwithstanding the protective barrier, the electrical resistance of the final specimen devices was measured prior to TEM experiments to ensure that the nanocapacitors were not electrically shorted. For the electron holography experiments, the bottom electrode was grounded while positive, negative, or zero biases were applied to the top electrode (except for the second sample show in this chapter).

As a reminder of the chapter 2, the *Operando* electron holography experiments were carried out with a 300 kV operating voltage, we used the Lorentz stage, elliptical illumination, two post-specimen biprisms, dynamic automation and the π-shift method were used to acquire holograms over a 120-second exposure time. We achieve 1.1 nm (7 pixels) fringe spacing for these experiments.

Offline data processing was performed with a 5th order Butterworth Fourier-space filter centred on the sideband, using Fourier analysis home-made routines. The numerical mask size was chosen to produce final phase images with a spatial resolution of 2 nm. Because the vacuum region was not visible in the holograms field of view, the internal reference area within the bottom substrate was used: the mean phase and linear phase ramp measured in this region were subtracted from the total phase image.

I didn't go into detail about the three-dimensional (3D) finite element method (FEM) modelling because this is an adaptation of the model thoroughly discussed in the previous chapter. But I can say that the electrical potential is calculated in three dimensions and then integrated along the electron path using the phase equation (see chapter 2 (Eq. 1.42)) to produce the two-dimensional phase map. To get as close to the reality of the experiments as possible, the model geometry and dimensions were based on TEM images of the observed devices. One advantage of TEM experiments is that accurate digital twins can be created relatively easily, leaving the main source of uncertainty on other parameters that cannot be measured in TEM images, such as the lamella thickness as estimate by electron energy-loss spectroscopy (EELS).

Holography experiment was performed on multiple capacitors, at first, we will study two isolated capacitors with a completely different purpose and a final example of two parallel capacitors.

3. A Single Capacitor

Operando electron holography experiments were performed on specimen devices prepared with the FIB preparation described above. Three different holograms were recorded in order to reconstruct the entire field of view, which I purposefully show in Figure 6.3 by cropping the image and cutting it wider to show the assembly of the three images. Figure 6.3(a) and Figure 6.3(b) show the amplitude image and phase image at 1 V extracted from the holograms after subtracting the reference phase image at 0 V, respectively, while Figure 6.3(c) shows the simulated phase image.
The roughness of the sample on the amplitude image shows that the capacitor is from industrial processes. Moreover, the change in the contrast indicates some diffraction. The phase shift appears relatively uniform inside the electrodes, as expected, with a stray field visible at the edges of the upper electrode due to its finite lateral dimension. Comparing the experimental phase image (Figure 6.3(b)) with the simulated one of FEM simulations (Figure 6.3(c)), we can observe a very nice correspondence.

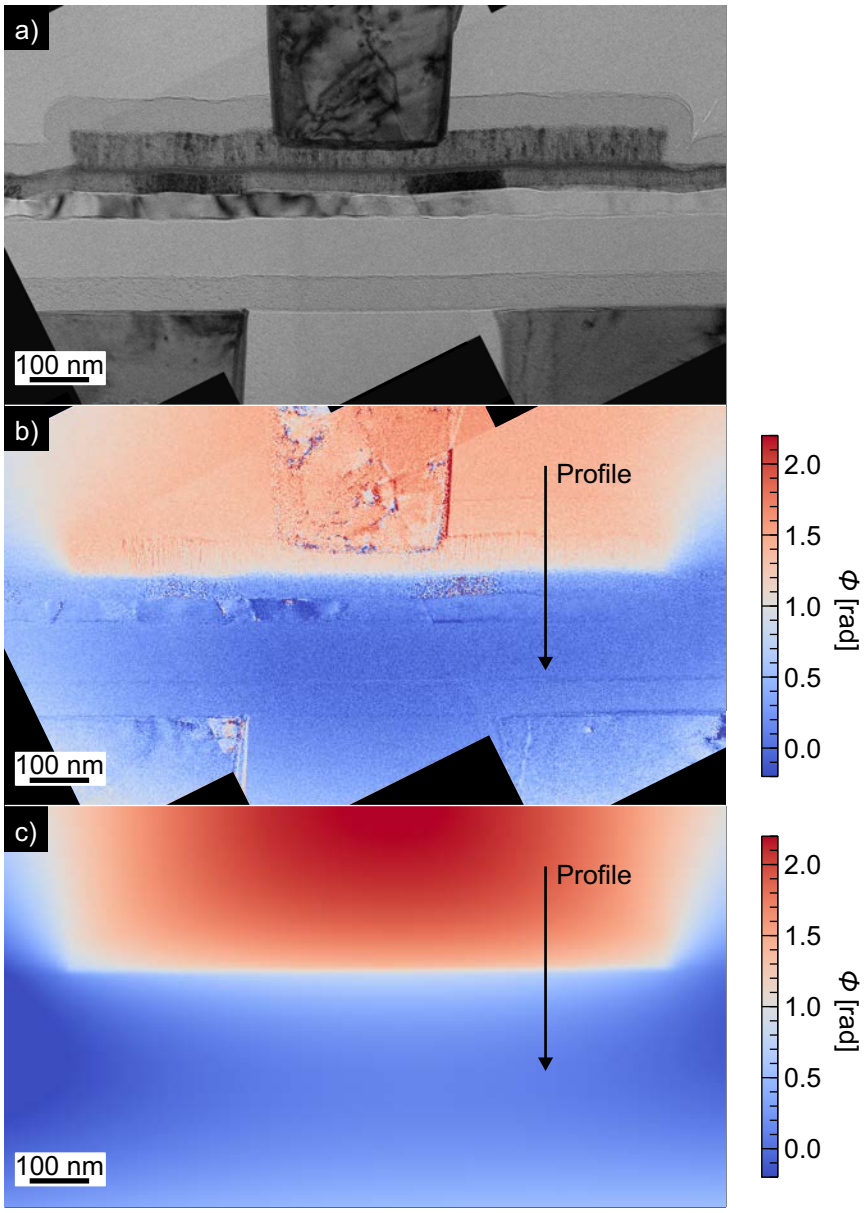

Figure 6.3 : The amplitude image of the capacitor studied a) shows the geometry of the device, followed by a comparison of the experimental phase image b) and the simulated phase image c) biased under 1 V.

This quantitative agreement between the experimental and simulated phase images is also highlighted with the phase profiles extracted through the electrodes and the insulating Ta_2O_5 layer (Figure 6.4). Parameters such as thickness and surface layer conductivity were adjusted to produce the best fit with the experimentally measured phase shift (Figure 6.4). The simulation results confirm the significant linear variation of the phase shift that occurs in the oxide layer, while the curvature of the phase in the electrodes area caused by the stray field around the sample is well reproduced.

However, this agreement was reached for a lower potential drop between the electrodes, and some differences between experimental and simulated data remain.

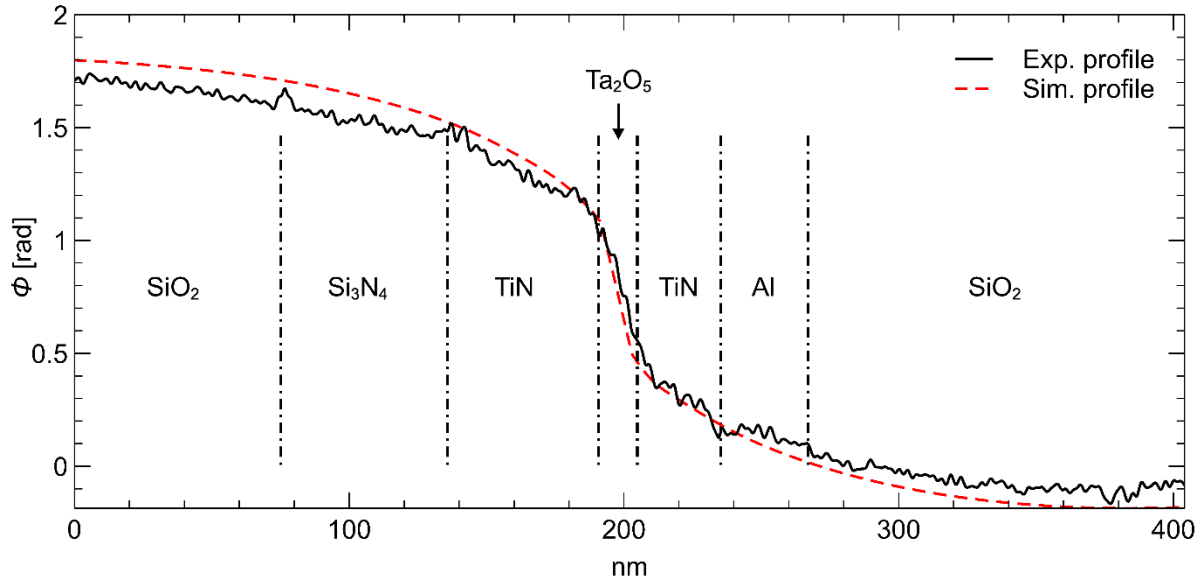

Figure 6.4 : Extracted profiles of experimental and simulated phase images along the black arrows on the phase images Figure 6.3b, c.

Indeed, the potential drop across the dielectric with respect to the applied voltage (1 V), leading in a local bias of 0.65V, is reduced by approximately 0.35 V due to current leakage in the conductive layers. The potential drop could be to the conductive layers approaching the conductivity of the electrodes, as described in the theoretical chapter (3). Parameters such as thickness and surface layer conductivity were adjusted to produce the best fit with the experimentally measured phase shift (Figure 6.4). To summarise, we fit excellently despite the fact that the model used in comparison to the experimental sample is simple. While the capacitor has a much higher complexity and is much rougher than the devices studied in Chapter 4, the simulation works very well. As discussed in Chapter 5, the total phase image is less sensitive to thickness variation than the effect of the stray field potential, which explains how we can fit an experimental sample with roughness to a perfect simulated model.

Experimental and theoretical curves may differ, in particular significant curvature inside the dielectric due to the evolution of accumulated charge in the oxide requires further adjustments by introducing different conditions into the finite element model. Despite the fact that all of the studies in this thesis were successful, all of the samples we wanted to study were not fully understood, which is the subject of the following section.

4. The « Mushroom »

I want to show now an example of a less successful experiment on a different nanocapacitor (same system but prepared in a different time) while using the same preparation technique. This experiment is carried out in the same manner as the previous one, but instead of biasing the pillar, we biased the line. The phase image was processed from a hologram of the device biased to 0.4 V (Figure 6.5).

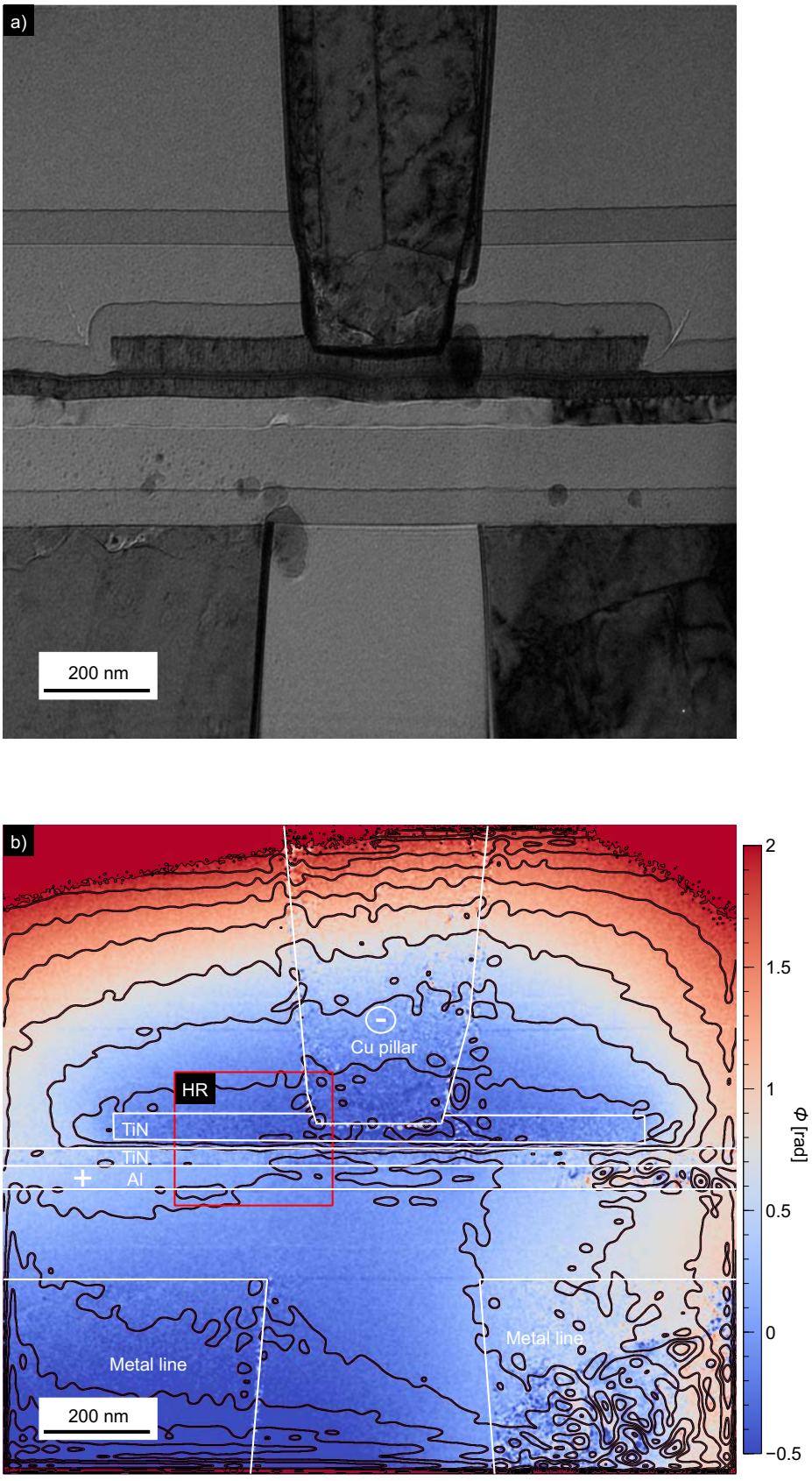

Figure 6.5 : Amplitude Image a) and phase image b) of the capacitor biased under 0.4 V with the area where the “High resolution (HR)” were performed.

The pillar is clearly grounded, while the line above the Ta_2O_5 indicates positive potential. But we can see that the behaviour of the phase does not look like the previous example. In contrast to the previous sample, which had an open shape, the first thing we notice due to the stray field is this close shape named as mushroom shape all around the pillar, which is denoted by a dotted isophase Figure 6.5. This shape was unexpected given the previous study of the same type of sample. I tried several models to explain the experimental data, without completely succeeding. Nevertheless, I will try to explain the significance of this unusual shape, which could be caused by a number of factors that I believe I have identified.

The first, and most obvious, could be caused by a short circuit between the biased line and the bottom line; in this case, the mushroom shape could be due to a strong influence of the stray field from the metal line at the bottom right. However, despite several attempts to change the potential of the bottom metal lines, whether positive or negative with multiple values, none of the combinations I tried worked.

Secondly, the biasing is applied to the bottom electron while on the previous studied capacitor it was on the upper electrode. For one reason or another and from the standpoint of electron holography, because the potential is applied to the bottom electrode, the field thus produced can produce a strong field in the reference zone and interact with the metal lines, disrupting the reference wave. And thus disturbed the final phase image calculation. Unfortunately, we couldn't implement these effects.

For all of these reasons, despite numerous attempts, I have been unable to develop a model to explain this experimental data. But, while I am sure it can be explained, it should not be done at any cost, for example, by inventing some uncorroborated or unrealistic component to make the model fit the data.

Despite the problems with a large field of view, high resolution holograms were taken of only the active part of the sample (HR) (see Figure 6.6). Because of the symmetry, I was able to use a two-dimensional model, as seen in the previous chapter on laboratory samples.

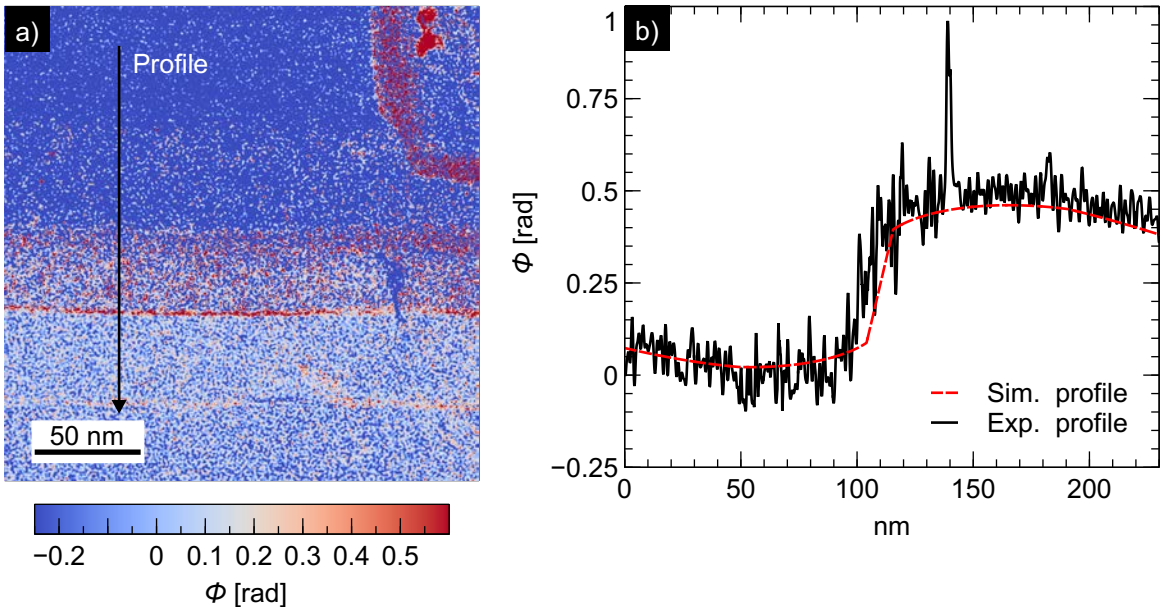

Figure 6.6 : HR phase image of a capacitor biased under 0.4 V a) with the experimental and simulated profiles on the right b).

The model fits the experimental data extremely well, despite the fact that we are unable to simulate the wider field of view. To conclude the capacitor was working, but since we cannot simulate the all-experimental data, it is difficult to extract quantitative data. Therefore, with this example we see that there is a many experimental unknown and we have to take a special care on the biasing, the sample preparation, and the reference wave to avoid any interference on the data analysis.

5. Interaction Between Two Capacitors

In the following example, we study the interaction between two neighbouring MIM nanocapacitors in parallel. Figure 6.7(a) and Figure 6.7(b) show the experimental amplitude and phase images acquired with 0.6 V of bias applied by the power supply. Three different holograms were recorded in order to reconstruct the entire field of view. When biased, the phase varies sharply across the Ta_2O_5 layer due to the strong local electrical field into the dielectric layer, but remains relatively uniform within the electrodes, as expected. Because of the very long exposure times of our automated holography experiments, there is also an in-plane stray field between the nanocapacitors (Figure 6.7(b), arrow).

To keep the model small, the array of parallel devices was limited to four and surrounded by vacuum. The mesh size dynamically adapts to the local dimensions from the external boundaries to the active region of the nanocapacitor, with a minimum mesh size of about 2 nm. The simulated phase corresponding to the experimental case is shown in Figure 6.7(c) for a lamella thickness of 100 nm.

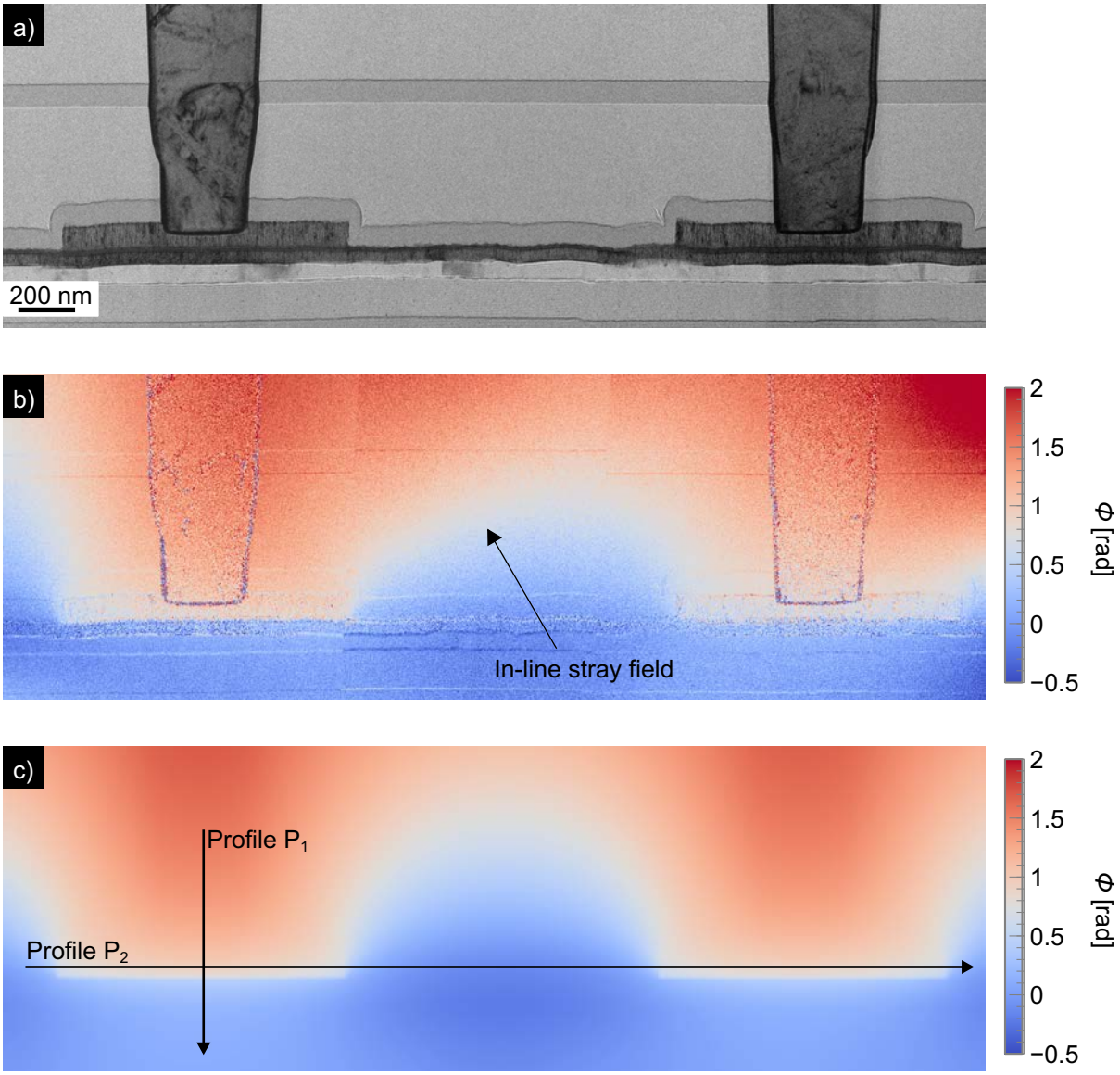

Figure 6.7 : Image of the amplitude of both MIM nanocapacitors in parallel a). The experimental phase image of the induced electrostatic potential for 0.6 V bias applied by the power supply b) is shown below, as is the simulation of the experimental phase image c).

Profiles were plotted from the phase images along the black arrow and averaged over a width of 50 nm parallel to the interfaces to quantify the potential distribution across the thin oxide layer (Figure 6.8(P_1)) while another profile took the phase along all the phase images inside and parallel to the fine oxide (Figure 6.8(P_2)).

The overall phase shift across the dielectric increases linearly with applied bias, as expected from (see chapter 2 (Eq. 1.42)). On the other hand, the phase of the electrodes on either side is not completely flat, despite the fact that we would expect them to be at a uniform potential.

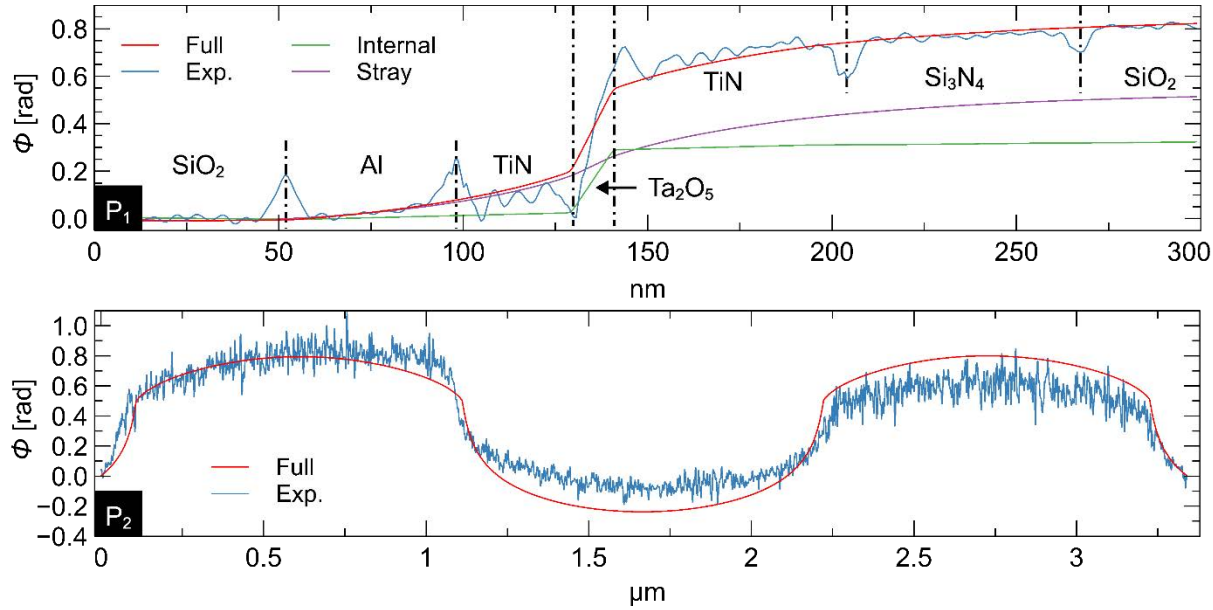

Figure 6.8 : Experimental and FEM simulated phase comparison of Figure 6.7. P_1) and P_2) extracted profiles of the experimental and simulated phase images along the black arrows P_1 and P_2 on Figure 6.7. The inset on P_1) shows the various contributions due to internal and external fields.

The overall phase distribution and phase profiles across the active area are excellently fit. The in-plane stray field is also well reproduced (Figure 6.8(P_1)), and simulations of the out-of-plane stray field confirm that it is the cause of the non-uniform phase in the electrode region.

To achieve this agreement, the local bias was determined at 0.40 V in our EM model, with a possible variation of 40mV when including the uncertainty in lamella thickness. This is much lower than the 0.6 V indicated by the external power supply during the experiment. Again, the difference in bias applied locally and globally is most likely caused by leakage currents and impedances in the connections. Because simulations

and experiments agree, we can be confident in the local electrical parameters extracted from the model, such as electrostatic potential inside the dielectric layer, capacitance, and surface charge density. The electric field inside the dielectric layer of the specimen device was $0.35 \pm 0.04\, MV.cm^{-1}$. Even with the DC bias of the EH experiments, there is reason to believe that the corresponding capacitance is indeed 2.1 fF, as previously estimated (see section sample preparation). The density of surface charge is then established at 0.12 elementary charges per nm^2 and per volt. The energy associated with the induced electrical field between the two electrode plates is $3.9 \times 10^{-16} J.V^{-1}$, whereas the energy associated with the stray field between the two neighbouring devices is $1.24 \times 10^{-18}\, J.V^{-1}$, or 0.3% of the total energy. This study shows that we can study two capacitors from fab with a nanometric resolution on a micrometres length.

6. Conclusion

In fact, capacitors are one of the most important components in all electronic devices. They are widely used in analogue and RF circuit applications for energy storage and delivery in memory devices such as flash memories and random-access memory (DRAM, SDRAM, etc.) chips, as well as processors, the performance of which is dependent on miniaturisation and operation.

We demonstrated that devices extracted from production lines can be prepared for TEM studies whilst preserving their electrical connectivity and functionality. *Operando* electron holography can then be used to quantitatively map the electric potential distribution as a function of bias. The experimental results were compared to numerical simulations using finite element modelling (FEM). Furthermore, the measured electric field can be modelled with almost no fitting parameters, indicating that the device is indeed functioning normally within the microscope. Furthermore, measurements can be correlated to complementary TEM techniques to gain a complete understanding of the structural, chemical, and electrical properties of individual nanometre-scale devices

I also showed an inexplicable sample. Despite the defeat, this experiment teaches us that we must be careful with sample preparation or risk not being able to extract

quantitative information. This experiment also demonstrated the importance of biasing, as the stray field may interfere with the reference wave.

There is no reason why the same methodology cannot be applied to more complex electronic devices like MOS transistors or spintronic devices by modifying the sample preparation workflow to achieve successful circuit modification and electrical stimulation of the device. These studies represent a complete *in situ* electrical investigation of multiple devices under fixed bias and further interpretation of these results will help to enhance sample preparation and minimise its impact on physical parameters modification. Finally, I hope that the ability to study local electric fields quantitatively in newly proposed and existing devices will aid efforts to investigate fundamental physical processes as well as develop and improve existing devices.

To take it a step further, these findings pave the way for future microelectronics research, not only in transistors, but also in other devices such as the ferroelectric capacitor, which has a much higher dielectric constant and can also open the door for negative capacitance and phase-change memory, among other exciting devices.

Chapter 7 — Conclusions

Through dedicated sample preparation, *in situ* biasing, computer-controlled microscopy, electron holography and data processing, remarkably sensitive phase and electrical potential measurements can be obtained for nanocapacitors and devices in working conditions. I have demonstrated, however, that the data cannot be fully exploited without numerical simulations. For example, modelling is required to account for the specific specimen geometry, stray fields and preparation artefacts. The methodology I have developed during my PhD thesis enables the recovery of the potential map within the specimen as well as the local charge density to high spatial resolution and surprising sensitivity.

Despite the fact that the stray field was regarded as a stumbling block (*i.e.* barrier) in the phase analysis of biased samples, it appears that after our research it has become a stepping stone (*i.e.* a force). In this regard, analysing the curvature of the stray field caused by the charging of the oxide layer in grounded samples provides critical information on the presence of surface conducting layers induced by the FIB preparation. Furthermore, in a simple system like a capacitor, the stray field acts as a signal multiplier. In fact, depending on the geometry, the contribution of the stray field to the total signal ranges from 40% to 60%. As a result, the signal that can be recovered from the internal potential applied by the electrodes is multiplied, improving the signal-to-noise ratio.

The grounded sample shows a symmetrical phase distribution. However, biasing the sample creates a non-symmetrical phase distribution (symmetry break) and the phase drop is proportional to the bias. As a result, the applied bias produces the stray field, and the contribution of the stray field to the internal field is determined by the thickness-to-length ratio of the insulator.

While the stray field can be a valuable source of information, the sample thickness (*e.g.* active area, FIB damages layers and irradiated area) is the most difficult parameter to assess. Furthermore, it also appears that the thickness is a critical parameter for extracting quantitative data from numerical simulations based on *in situ* holography. Electron energy-loss spectroscopy (EELS) can provide an estimation of the thickness. When combined with the uncertainty directly measured on the phase image for the other model parameters, this measurement is nevertheless sufficient to extract the uncertainty in important parameters such as bias or charged density.

During this thesis, I have also explored the possibilities of automated data analysis. In comparison to analysis "by hand", that is adjusting the parameters and seeking the best fit to the experimental data manually, automation or automatic data translator has numerous advantages. To begin, I believe that this type of development enables us to minimise human bias, reducing systematic errors. Second, such automation does not only save time, but also allows us to study more parameters in much larger dimensions than previously possible. Finally, and perhaps most importantly, the methods allow a more reliable determination of experimental uncertainties in the fitted parameters.

Automation also gives us the opportunity to create huge databases from our model. If we want to accelerate the algorithm convergence of the gradient descent, which is the Trust region reflective method (TRR) in this case, we can feed an AI algorithm to improve fitting performance by building a data set using an exploration loop. In contrast, with the automatic fitting algorithm, we might save a lot of time by using a neural network that can make a prediction in less than 1 second and thus calculate the uncertainty with the TRR algorithm.

These fundamental developments can be applied to the analysis of microelectronic devices in production. Despite being far more complex than a laboratory sample, an industrial device can be measured on a micrometre scale with a resolution of less than a nanometre. Some samples cannot be explained regardless of our best efforts, but we can always extract useful information, demonstrating that even when we make mistakes, the end result is always interesting.

I would like to emphasise that it was unclear at the beginning of the thesis whether we would be able to use numerical simulations to interpret electron holography data

resulting from unexpected physical phenomena. It should be remembered that we had chosen a capacitor as the device of study precisely because it was supposed to be very well known and understood. Despite this, we were nevertheless able to incorporate unexpected features, such as the charging of the dielectric interfaces, into the modelling. Indeed, numerical modelling was essential to demonstrate that such phenomena were necessary to explain the experimental data. I never expected the analysis of the capacitor to go so far.

Prior to my thesis, it was difficult to characterise industrial electronic components because nanoscopic electrical characterisation does not provide good spatial resolution. The same holds true for purely theoretical research. The use of *operando* electron holography on electronic components was very useful in studying and understanding device operation, but it lacked quantitative data and precise uncertainty measurements. During my thesis, I developed a methodology for simulating electron holography experiments on electrical nanodevices, allowing us to characterise and detect unexpected charging areas on models that we thought we understood well. Therefore, I wanted to not only measure parameters but also create an uncertainty methodology. On this basis, and because we were able to work on real capacitors from the STMicroelectronics production line, I show that we can analyse these devices at the expense of a little more complexity.

Perspectives

At the beginning of this study, my initial focus was on the extrinsic parameters that perturbed the measure, such as the effect of the measurement instrument (*i.e.* electron microscope) and the sample preparation artefacts. More research should be done on FIB preparation. During these studies, we prepare our samples with gallium-source FIB, resulting in conductive layers. Comparable samples could be milled with different sources, such as non-reactive gases. Milling with this kind of source should not form conducting layers on the surface. I also believe that understanding the interaction between the field generated by a biased sample and the reference wave is a challenge that must be overcome in order to study more complex fields for more complex sample geometries.

We can imagine the development of software that is installed as close to the microscope as possible, allowing the study of electrical samples directly during the

experiment. To accomplish this, we could create a user-configurable interface that analyses the hologram directly or we could continue the development of AI technique. Starting from the study developed during my thesis, we could directly use the neural network developed on phase images, helping this type of analysis to become more widespread. Moreover, because capacitors are frequently used in high-frequency applications, it would be an exciting possibility to be able to characterise them, both macroscopically and with *operando* electron holography, as a function of frequency and compare them to our static analysis.

I am convinced that this research paves the way for the study of more complex electronic components, such as transistors, phase-change memory devices and ferroelectric capacitors. For instance, such approaches would promote a better understanding of the negative capacitance to enable devices that consume less energy.

Today, we worked on samples that we thought we knew everything about, but why not envision a systematic application to aid in the development of future microelectronic components? For example, quantum technology could be investigated in the future. Whereas the tunnelling effect makes the miniaturisation of transistor technology difficult, it allows the development of new devices such as the single-electron transistor. We could study these new devices with I2TEM microscope since it is now equipped with a new direct electron detection camera, which gives an increased sensitivity and improved spatial resolution.

References:

Aharonov, Y., Bohm, D., 1961. Further Considerations on Electromagnetic Potentials in the Quantum Theory. Phys. Rev. 123, 1511–1524. https://doi.org/10.1103/PhysRev.123.1511

Aharonov, Y., Bohm, D., 1959. Significance of Electromagnetic Potentials in the Quantum Theory. Phys. Rev. 115, 485–491. https://doi.org/10.1103/PhysRev.115.485

Aizawa, Y., Yamamoto, K., Sato, T., Murata, H., Yoshida, R., Fisher, C.A.J., Kato, T., Iriyama, Y., Hirayama, T., 2017. In situ electron holography of electric potentials inside a solid-state electrolyte: Effect of electric-field leakage. Ultramicroscopy, FEMMS 2015 178, 20–26. https://doi.org/10.1016/j.ultramic.2016.07.015

Beleggia, M., Fazzini, P.F., Merli, P.G., Pozzi, G., 2003. Influence of charged oxide layers on TEM imaging of reverse-biased p – n junctions. Phys. Rev. B 67, 045328. https://doi.org/10.1103/PhysRevB.67.045328

Beleggia, M., Gontard, L.C., Dunin-Borkowski, R.E., 2016. Local charge measurement using off-axis electron holography. J. Phys. D: Appl. Phys. 49, 294003. https://doi.org/10.1088/0022-3727/49/29/294003

Beleggia, M., Kasama, T., Dunin-Borkowski, R.E., Hofmann, S., Pozzi, G., 2011. Direct measurement of the charge distribution along a biased carbon nanotube bundle using electron holography. Appl. Phys. Lett. 98, 243101. https://doi.org/10.1063/1.3598468

Beleggia, M., Kasama, T., Larson, D.J., Kelly, T.F., Dunin-Borkowski, R.E., Pozzi, G., 2014. Towards quantitative off-axis electron holographic mapping of the electric field around the tip of a sharp biased metallic needle. Journal of Applied Physics 116, 024305. https://doi.org/10.1063/1.4887448

Bonnaud, O., 2006. Composants à semiconducteurs: de la physique du solide aux transistors. Ellipses.

Boureau, V., McLeod, R., Mayall, B., Cooper, D., 2018. Off-axis electron holography combining summation of hologram series with double-exposure phase-shifting: Theory and application. Ultramicroscopy 193, 52–63. https://doi.org/10.1016/j.ultramic.2018.06.004

Branch, M.A., Coleman, T.F., Li, Y., 1999. A Subspace, Interior, and Conjugate Gradient Method for Large-Scale Bound-Constrained Minimization Problems 23.

Brodovoi, M., Gruel, K., Chapuis, L., Masseboeuf, A., Marcelot, C., Hÿtch, M., Lorut, F., Gatel, C., 2021. In-Situ Electrical Biasing of Electrically Connected TEM Lamellae with Embedded Nanodevices. Presented at the ISTFA 2021, Phoenix, Arizona, USA, pp. 190–195. https://doi.org/10.31399/asm.cp.istfa2021p0190

Brodovoi, M., Gruel, K., Masseboeuf, A., 2022. Mapping electric fields in real nanodevices byoperando electron holography. Applied Physics Letters 7.

Burr, G.W., Breitwisch, M.J., Franceschini, M., Garetto, D., Gopalakrishnan, K., Jackson, B., Kurdi, B., Lam, C., Lastras, L.A., Padilla, A., Rajendran, B., Raoux, S., Shenoy, R.S., 2010. Phase change memory technology. Journal of Vacuum Science & Technology B, Nanotechnology and Microelectronics: Materials, Processing, Measurement, and Phenomena 28, 223–262. https://doi.org/10.1116/1.3301579

Cazaux, J., 1995. Correlations between ionization radiation damage and charging effects

in transmission electron microscopy. Ultramicroscopy 60, 411–425. https://doi.org/10.1016/0304-3991(95)00077-1
Chaneliere, C., Autran, J., Devine, R., Balland, B., 1998. Tantalum pentoxide (Ta2O5) thin films for advanced dielectric applications. Materials Science and Engineering: R: Reports 22, 269–322.
Checkelsky, J., 2022. A Holographic View Inside a MOS Capacitor. Journal Club for Condensed Matter Physics. https://doi.org/10.36471/JCCM_November_2022_01
Chua, L., 1971. Memristor-the missing circuit element. IEEE Transactions on circuit theory 18, 507–519.
Cooper, D., Ailliot, C., Barnes, J.-P., Hartmann, J.-M., Salles, P., Benassayag, G., Dunin-Borkowski, R.E., 2010. Dopant profiling of focused ion beam milled semiconductors using off-axis electron holography; reducing artefacts, extending detection limits and reducing the effects of gallium implantation 7.
Cowley, J.M., 1992. Twenty forms of electron holography. Ultramicroscopy 41, 335–348. https://doi.org/10.1016/0304-3991(92)90213-4
Cumings, J., Zettl, A., McCartney, M.R., Spence, J.C.H., 2002. Electron Holography of Field-Emitting Carbon Nanotubes. Phys. Rev. Lett. 88, 056804. https://doi.org/10.1103/PhysRevLett.88.056804
de Knoop, L., Gatel, C., Houdellier, F., Monthioux, M., Masseboeuf, A., Snoeck, E., Hÿtch, M.J., 2015. Low-noise cold-field emission current obtained between two opposed carbon cone nanotips during *in situ* transmission electron microscope biasing. Appl. Phys. Lett. 106, 263101. https://doi.org/10.1063/1.4923245
de Knoop, L., Houdellier, F., Gatel, C., Masseboeuf, A., Monthioux, M., Hÿtch, M., 2014. Determining the work function of a carbon-cone cold-field emitter by in situ electron holography. Micron 63, 2–8. https://doi.org/10.1016/j.micron.2014.03.005
de Ruijter, W.J., Weiss, J.K., 1993. Detection limits in quantitative off-axis electron holography. Ultramicroscopy 50, 269–283. https://doi.org/10.1016/0304-3991(93)90196-5
Deal, B.E., 1980. Standardized Terminology for Oxide Charges Associated with Thermally Oxidized Silicon. J. Electrochem. Soc. 127, 979. https://doi.org/10.1149/1.2129800
Deal, B.E., Sklar, M., Grove, A.S., Snow, E.H., 1967. Characteristics of the Surface-State Charge (Qss) of Thermally Oxidized Silicon. J. Electrochem. Soc. 114, 266. https://doi.org/10.1149/1.2426565
den Hertog, M., Songmuang, R., Monroy, E., 2013. Polarization fields in GaN/AlN nanowire heterostructures studied by off-axis holography. J. Phys.: Conf. Ser. 471, 012019. https://doi.org/10.1088/1742-6596/471/1/012019
den Hertog, M.I., Schmid, H., Cooper, D., Rouviere, J.-L., Björk, M.T., Riel, H., Rivallin, P., Karg, S., Riess, W., 2009. Mapping Active Dopants in Single Silicon Nanowires Using Off-Axis Electron Holography. Nano Lett. 9, 3837–3843. https://doi.org/10.1021/nl902024h
Di Ventra, M., Pershin, Y.V., 2013. On the physical properties of memristive, memcapacitive and meminductive systems. Nanotechnology 24, 255201. https://doi.org/10.1088/0957-4484/24/25/255201
Diebold, A.C., 1996. Characterization of two-dimensional dopant profiles: Status and review. J. Vac. Sci. Technol. B 14, 196. https://doi.org/10.1116/1.589028
DiMaria, D.J., Cartier, E., Arnold, D., 1993. Impact ionization, trap creation, degradation, and breakdown in silicon dioxide films on silicon. Journal of Applied Physics 73, 3367–

3384. https://doi.org/10.1063/1.352936
Dunin-Borkowski, R.E., Kovács, A., Kasama, T., McCartney, M.R., Smith, D.J., 2019. Electron Holography, in: Hawkes, P.W., Spence, J.C.H. (Eds.), Springer Handbook of Microscopy, Springer Handbooks. Springer International Publishing, Cham, pp. 767–818. https://doi.org/10.1007/978-3-030-00069-1_16
Dupuy, J., 2021. Contrôle dynamique et optimisation des observations en microscopie électronique en transmission.
Ehrenberg, W., Siday, R.E., 1949. The Refractive Index in Electron Optics and the Principles of Dynamics. Proc. Phys. Soc. B 62, 8–21. https://doi.org/10.1088/0370-1301/62/1/303
Einsle, J.F., Gatel, C., Masseboeuf, A., Cours, R., Bashir, M.A., Gubbins, M., Bowman, R.M., Snoeck, E., 2015. In situ electron holography of the dynamic magnetic field emanating from a hard-disk drive writer. Nano Res. 8, 1241–1249. https://doi.org/10.1007/s12274-014-0610-0
Engelmann, H., Saage, H., Zschech, E., 2000. Application of analytical TEM for failure analysis of semiconductor device structures. Microelectronics Reliability 40, 1747–1751.
Engström, O., 2014. The MOS System, Cambridge University Press. ed.
Fleetwood, D.M., 2018. Border traps and bias-temperature instabilities in MOS devices. Microelectronics Reliability 80, 266–277. https://doi.org/10.1016/j.microrel.2017.11.007
Fleetwood, D.M., 1992. "Border traps" in MOS devices. IEEE Transactions on Nuclear Science 39, 269–271. https://doi.org/10.1109/23.277495
Frabboni, S., Matteucci, G., Pozzi, G., Vanzi, M., 1985. Electron Holographic Observations of the Electrostatic Field Associated with Thin Reverse-Biased p − n Junctions. Phys. Rev. Lett. 55, 2196–2199. https://doi.org/10.1103/PhysRevLett.55.2196
Fumeaux, C., Sankaran, K., Vahldieck, Rü., 2007. Spherical Perfectly Matched Absorber for Finite-Volume 3-D Domain Truncation. IEEE Trans. Microwave Theory Techn. 55, 2773–2781. https://doi.org/10.1109/TMTT.2007.909619
Gabor, D., 1948. A New Microscopic Principle. Nature 161, 777–778. https://doi.org/10.1038/161777a0
Gatel, C., A. Lubk, G. Pozzi, E. Snoeck, M. Hÿtch, 2013. Counting Elementary Charges on Nanoparticles by Electron Holography. Phys. Rev. Lett. 111, 025501. https://doi.org/10.1103/PhysRevLett.111.025501
Gatel, C., Bonilla, F.J., Meffre, A., Snoeck, E., Warot-Fonrose, B., Chaudret, B., Lacroix, L.-M., Blon, T., 2015. Size-Specific Spin Configurations in Single Iron Nanomagnet: From Flower to Exotic Vortices. Nano Lett. 15, 6952–6957. https://doi.org/10.1021/acs.nanolett.5b02892
Gatel, C., Dupuy, J., Houdellier, F., Hÿtch, M.J., 2018. Unlimited acquisition time in electron holography by automated feedback control of transmission electron microscope. Appl. Phys. Lett. 113, 133102. https://doi.org/10.1063/1.5050906
Gatel, C., Serra, R., Gruel, K., Masseboeuf, A., Chapuis, L., Cours, R., Zhang, L., Warot-Fonrose, B., Hÿtch, M.J., 2022. Extended Charge Layers in Metal-Oxide-Semiconductor Nanocapacitors Revealed by *Operando* Electron Holography. Phys. Rev. Lett. 129, 137701. https://doi.org/10.1103/PhysRevLett.129.137701
Giannuzzi, L.A., Geurts, R., Ringnalda, J., 2005. 2 keV Ga+ FIB Milling for Reducing Amorphous Damage in Silicon. MAM 11. https://doi.org/10.1017/S1431927605507797

Goto, T., Jeong, J.S., Xia, W., Akase, Z., Shindo, D., Hirata, K., 2013. Electron holography of magnetic field generated by a magnetic recording head. Microscopy (Tokyo) 62, 383–389. https://doi.org/10.1093/jmicro/dfs090

Grasser, T., Kaczer, B., Goes, W., Reisinger, H., Aichinger, T., Hehenberger, P., Wagner, P.-J., Schanovsky, F., Franco, J., Toledano Luque, M.T., Nelhiebel, M., 2011. The Paradigm Shift in Understanding the Bias Temperature Instability: From Reaction–Diffusion to Switching Oxide Traps. IEEE Transactions on Electron Devices 58, 3652–3666. https://doi.org/10.1109/TED.2011.2164543

Han, M.-G., Smith, D.J., McCartney, M.R., 2008. *In situ* electron holographic analysis of biased Si n+-p junctions. Appl. Phys. Lett. 92, 143502. https://doi.org/10.1063/1.2908045

Harada, K., 2005. Optical system for double-biprism electron holography. Journal of Electron Microscopy 54, 19–27. https://doi.org/10.1093/jmicro/dfh098

Harada, K., Endo, J., Osakabe, N., Tonomura, A., 2008. Direction-Free Magnetic Field Application System. e-J. Surf. Sci. Nanotechnol. 6, 29–34. https://doi.org/10.1380/ejssnt.2008.29

Harada, K., Tonomura, A., Togawa, Y., Akashi, T., Matsuda, T., 2004. Double-biprism electron interferometry. Appl. Phys. Lett. 84, 3229–3231. https://doi.org/10.1063/1.1715155

He, K., Cho, J.-H., Jung, Y., Tom Picraux, S., Cumings, J., 2013. Silicon nanowires: electron holography studies of doped p–n junctions and biased Schottky barriers. Nanotechnology 24, 115703. https://doi.org/10.1088/0957-4484/24/11/115703

He, K., Cumings, J., 2013. Diagnosing Nanoelectronic Components Using Coherent Electrons. Nano Lett. 13, 4815–4819. https://doi.org/10.1021/nl402509c

Hirohata, A., Sukegawa, H., Yanagihara, H., Zutic, I., Seki, T., Mizukami, S., Swaminathan, R., 2015. Roadmap for Emerging Materials for Spintronic Device Applications. IEEE Trans. Magn. 51, 1–11. https://doi.org/10.1109/TMAG.2015.2457393

Hoffmann, M., Fengler, F.P.G., Herzig, M., Mittmann, T., Max, B., Schroeder, U., Negrea, R., Lucian, P., Slesazeck, S., Mikolajick, T., 2019. Unveiling the double-well energy landscape in a ferroelectric layer. Nature 565, 464–467. https://doi.org/10.1038/s41586-018-0854-z

Huang, J., Loeffler, M., Muehle, U., Moeller, W., Mulders, J.J.L., Kwakman, L.F.Tz., Van Dorp, W.F., Zschech, E., 2018. Si amorphisation by focused ion beam milling: Point defect model with dynamic BCA simulation and experimental validation. Ultramicroscopy 184, 52–56. https://doi.org/10.1016/j.ultramic.2017.10.011

Hÿtch, M., Houdellier, F., Hüe, F., Snoeck, E., 2008. Nanoscale holographic interferometry for strain measurements in electronic devices. Nature 453, 1086–1089. https://doi.org/10.1038/nature07049

Ikarashi, N., Takeda, H., Yako, K., Hane, M., 2012. *In-situ* electron holography of surface potential response to gate voltage application in a sub-30-nm gate-length metal-oxide-semiconductor field-effect transistor. Appl. Phys. Lett. 100, 143508. https://doi.org/10.1063/1.3700723

Íñiguez, J., Zubko, P., Luk'yanchuk, I., Cano, A., 2019. Ferroelectric negative capacitance. Nat Rev Mater 4, 243–256. https://doi.org/10.1038/s41578-019-0089-0

International Bureau of Weights and Measures, International Organization for Standardization (Eds.), 2008. Guide to the expression of uncertainty in measurement, 1st ed. 1993. ed. International Organization for Standardization, Genève, Switzerland.

Jarausch, K., Thomas, P., Leonard, D.N., Twesten, R., Booth, C.R., 2009. Four-dimensional STEM-EELS: Enabling nano-scale chemical tomography. Ultramicroscopy 109, 326–337. https://doi.org/10.1016/j.ultramic.2008.12.012

Jiang, Y., Chen, Z., Han, Y., Deb, P., Gao, H., Xie, S., Purohit, P., Tate, M.W., Park, J., Gruner, S.M., Elser, V., Muller, D.A., 2018. Electron ptychography of 2D materials to deep sub-ångström resolution. Nature 559, 343–349. https://doi.org/10.1038/s41586-018-0298-5

Jung, Y., Nam, S.-W., Agarwal, R., 2011. High-Resolution Transmission Electron Microscopy Study of Electrically-Driven Reversible Phase Change in $Ge_2Sb_2Te_5$ Nanowires. Nano Lett. 11, 1364–1368. https://doi.org/10.1021/nl104537c

Khan, A.I., Chatterjee, K., Wang, B., Drapcho, S., You, L., Serrao, C., Bakaul, S.R., Ramesh, R., Salahuddin, S., 2015. Negative capacitance in a ferroelectric capacitor. Nature Mater 14, 182–186. https://doi.org/10.1038/nmat4148

Krebs, D., Raoux, S., Rettner, C.T., Burr, G.W., Salinga, M., Wuttig, M., 2009. Threshold field of phase change memory materials measured using phase change bridge devices. Appl. Phys. Lett. 95, 082101. https://doi.org/10.1063/1.3210792

Latychevskaia, T., Formanek, P., Koch, C.T., Lubk, A., 2010. Off-axis and inline electron holography: Experimental comparison. Ultramicroscopy 110, 472–482. https://doi.org/10.1016/j.ultramic.2009.12.007

Lehmann, M., Lichte, H., 2005. Electron holographic material analysis at atomic dimensions. Cryst. Res. Technol. 40, 149–160. https://doi.org/10.1002/crat.200410318

Li, G., Chen, X., 2012. Modified Fowler–Nordheim tunnelling for modelling charge injection into Si3N4 in an Al/Si3N4/Si structure. Appl. Phys. A 109, 539–545. https://doi.org/10.1007/s00339-012-7065-5

Lichte, H., Lehmann, M., 2008. Electron holography—basics and applications. Rep. Prog. Phys. 71, 016102. https://doi.org/10.1088/0034-4885/71/1/016102

Liu, L.Z. -Y., McAleese, C., Sridhara Rao, D.V., Kappers, M.J., Humphreys, C.J., 2012. Electron holography of an in-situ biased GaN-based LED. Phys. Status Solidi C 9, 704–707. https://doi.org/10.1002/pssc.201100486

Ma, Z., Li, L., 2022. Recent Progress in Exploring the Magnetic Solids with Room-Temperature Skyrmionic Spin Configurations. physica status solidi (a) 219, 2100333.

McCartney, M.R., Agarwal, N., Chung, S., Cullen, D.A., Han, M.-G., He, K., Li, L., Wang, H., Zhou, L., Smith, D.J., 2010. Quantitative phase imaging of nanoscale electrostatic and magnetic fields using off-axis electron holography. Ultramicroscopy 110, 375–382. https://doi.org/10.1016/j.ultramic.2010.01.001

McCartney, M.R., Dunin-Borkowski, R.E., Smith, D.J., 2019. Quantitative measurement of nanoscale electrostatic potentials and charges using off-axis electron holography: Developments and opportunities. Ultramicroscopy 203, 105–118. https://doi.org/10.1016/j.ultramic.2019.01.008

Midgley, P.A., Dunin-Borkowski, R.E., 2009. Electron tomography and holography in materials science. Nature Mater 8, 271–280. https://doi.org/10.1038/nmat2406

Migunov, V., Dwyer, C., Boothroyd, C.B., Pozzi, G., Dunin-Borkowski, R.E., 2017. Prospects for quantitative and time-resolved double and continuous exposure off-axis electron holography. Ultramicroscopy 178, 48–61. https://doi.org/10.1016/j.ultramic.2016.08.010

Moodera, J.S., Kinder, L.R., Wong, T.M., Meservey, R., 1995. Large Magnetoresistance at

Room Temperature in Ferromagnetic Thin Film Tunnel Junctions. Phys. Rev. Lett. 74, 3273–3276. https://doi.org/10.1103/PhysRevLett.74.3273
O'Keeffe, M., Spence, J.C.H., 1994. On the average Coulomb potential (Σ0) and constraints on the electron density in crystals. Acta Crystallogr A Found Crystallogr 50, 33–45. https://doi.org/10.1107/S010876739300474X
O'Neill, M., 2014. PCG: A Family of Simple Fast Space-Efficient Statistically Good Algorithms for Random Number Generation 58.
Ophus, C., 2019. Four-Dimensional Scanning Transmission Electron Microscopy (4D-STEM): From Scanning Nanodiffraction to Ptychography and Beyond. Microsc Microanal 25, 563–582. https://doi.org/10.1017/S1431927619000497
Park, J.B., Niermann, T., Berger, D., Knauer, A., Koslow, I., Weyers, M., Kneissl, M., Lehmann, M., 2014. Impact of electron irradiation on electron holographic potentiometry. Appl. Phys. Lett. 105, 094102. https://doi.org/10.1063/1.4894718
Pozzi, G., Beleggia, M., Kasama, T., Dunin-Borkowski, R.E., 2014. Interferometric methods for mapping static electric and magnetic fields. Comptes Rendus Physique 15, 126–139. https://doi.org/10.1016/j.crhy.2014.01.005
Raoux, S., Burr, G.W., Breitwisch, M.J., Rettner, C.T., Chen, Y.-C., Shelby, R.M., Salinga, M., Krebs, D., Chen, S.-H., Lung, H.-L., Lam, C.H., 2008. Phase-change random access memory: A scalable technology. IBM J. Res. & Dev. 52, 465–479. https://doi.org/10.1147/rd.524.0465
Raoux, Simone, Rettner, C.T., Chen, Y.-C., Burr, G.W., 2008. Electron-Beam Lithographic Studies of the Scaling of Phase-Change Memory. MRS Bull. 33, 847–853. https://doi.org/10.1557/mrs2008.180
Rau, W.D., Schwander, P., Baumann, F.H., Höppner, W., Ourmazd, A., 1999. Two-Dimensional Mapping of the Electrostatic Potential in Transistors by Electron Holography. PHYSICAL REVIEW LETTERS 82, 4.
Robertson, J., 2004. High dielectric constant oxides. Eur. Phys. J. Appl. Phys. 28, 265–291. https://doi.org/10.1051/epjap:2004206
Robertson, J., Wallace, R.M., 2015. High-K materials and metal gates for CMOS applications. Materials Science and Engineering: R: Reports 88, 1–41. https://doi.org/10.1016/j.mser.2014.11.001
Sbiaa, R., Meng, H., Piramanayagam, S.N., 2011. Materials with perpendicular magnetic anisotropy for magnetic random access memory. Phys. Status Solidi RRL 5, 413–419. https://doi.org/10.1002/pssr.201105420
Shimaoka, K., Kinoshita, M., Fujii, K., Tosaka, T., 2008. Evaluation of measurement data-supplement 1 to the guide to expression of uncertainty in measurement-propagation of distributions using a monte carlo method. JCGM 101.
Slonczewski, J.C., 1996. Current-driven excitation of magnetic multilayers. Journal of Magnetism and Magnetic Materials 159, L1–L7. https://doi.org/10.1016/0304-8853(96)00062-5
Snoeck, E., Houdellier, F., Taniguch, Y., Masseboeuf, A., Gatel, C., Nicolai, J., Hytch, M., 2014a. Off-Axial Aberration Correction using a B-COR for Lorentz and HREM Modes. Microsc Microanal 20, 932–933. https://doi.org/10.1017/S1431927614006382
Snoeck, E., Houdellier, F., Taniguch, Y., Masseboeuf, A., Gatel, C., Nicolai, J., Hytch, M., 2014b. Off-Axial Aberration Correction using a B-COR for Lorentz and HREM Modes. Microscopy and Microanalysis 20, 932–933. https://doi.org/10.1017/S1431927614006382

Storn, R., 1997. Differential Evolution – A Simple and Efficient Heuristic for Global Optimization over Continuous Spaces. DIFFERENTIAL EVOLUTION 19.
Strukov, D.B., Snider, G.S., Stewart, D.R., Williams, R.S., 2008. The missing memristor found. Nature 453, 80–83. https://doi.org/10.1038/nature06932
Theis, T.N., Solomon, P.M., 2010. It's Time to Reinvent the Transistor! Science 327, 1600–1601. https://doi.org/10.1126/science.1187597
Toh, S.L., Mai, Z.H., Tan, P.K., Hendarto, E., Tan, H., Wang, Q.F., Cai, J.L., Deng, Q., Ng, T.H., Goh, Y.W., Lam, J., Hsia, L.C., 2007. Use of Nanoprobing as the Diagnostic Tool for Nanoscaled Devices, in: 2007 14th International Symposium on the Physical and Failure Analysis of Integrated Circuits. Presented at the 2007 14th International Symposium on the Physical and Failure Analysis of Integrated Circuits, IEEE, Bangalore, India, pp. 53–58. https://doi.org/10.1109/IPFA.2007.4378057
Toh, S.L., Tan, P.K., Goh, Y.W., Hendarto, E., Cai, J.L., Tan, H., Wang, Q.F., Deng, Q., Lam, J., Hsia, L.C., Mai, Z.H., 2008. In-Depth Electrical Analysis to Reveal the Failure Mechanisms With Nanoprobing. IEEE Trans. Device Mater. Relib. 8, 387–393. https://doi.org/10.1109/TDMR.2008.920300
Tonomura, A., 1987. Applications of electron holography. Rev. Mod. Phys. 59, 639–669. https://doi.org/10.1103/RevModPhys.59.639
Twitchett, A.C., Dunin-Borkowski, R.E., Midgley, P.A., 2002. Quantitative Electron Holography of Biased Semiconductor Devices. PHYSICAL REVIEW LETTERS 88, 4.
Twitchett-Harrison, A.C., Dunin-Borkowski, R.E., Midgley, P.A., 2008. Mapping the electrical properties of semiconductor junctions-the electron holographic approach. Scanning 30, 299–309. https://doi.org/10.1002/sca.20125
Virtanen, P., Gommers, R., Oliphant, T.E., Haberland, M., Reddy, T., Cournapeau, D., Burovski, E., Peterson, P., Weckesser, W., Bright, J., van der Walt, S.J., Brett, M., Wilson, J., Millman, K.J., Mayorov, N., Nelson, A.R.J., Jones, E., Kern, R., Larson, E., Carey, C.J., Polat, İ., Feng, Y., Moore, E.W., VanderPlas, J., Laxalde, D., Perktold, J., Cimrman, R., Henriksen, I., Quintero, E.A., Harris, C.R., Archibald, A.M., Ribeiro, A.H., Pedregosa, F., van Mulbregt, P., SciPy 1.0 Contributors, Vijaykumar, A., Bardelli, A.P., Rothberg, A., Hilboll, A., Kloeckner, A., Scopatz, A., Lee, A., Rokem, A., Woods, C.N., Fulton, C., Masson, C., Häggström, C., Fitzgerald, C., Nicholson, D.A., Hagen, D.R., Pasechnik, D.V., Olivetti, E., Martin, E., Wieser, E., Silva, F., Lenders, F., Wilhelm, F., Young, G., Price, G.A., Ingold, G.-L., Allen, G.E., Lee, G.R., Audren, H., Probst, I., Dietrich, J.P., Silterra, J., Webber, J.T., Slavič, J., Nothman, J., Buchner, J., Kulick, J., Schönberger, J.L., de Miranda Cardoso, J.V., Reimer, J., Harrington, J., Rodríguez, J.L.C., Nunez-Iglesias, J., Kuczynski, J., Tritz, K., Thoma, M., Newville, M., Kümmerer, M., Bolingbroke, M., Tartre, M., Pak, M., Smith, N.J., Nowaczyk, N., Shebanov, N., Pavlyk, O., Brodtkorb, P.A., Lee, P., McGibbon, R.T., Feldbauer, R., Lewis, S., Tygier, S., Sievert, S., Vigna, S., Peterson, S., More, S., Pudlik, T., Oshima, T., Pingel, T.J., Robitaille, T.P., Spura, T., Jones, T.R., Cera, T., Leslie, T., Zito, T., Krauss, T., Upadhyay, U., Halchenko, Y.O., Vázquez-Baeza, Y., 2020. SciPy 1.0: fundamental algorithms for scientific computing in Python. Nat Methods 17, 261–272. https://doi.org/10.1038/s41592-019-0686-2
Voelkl, E., Tang, D., 2010. Approaching routine phase resolution for off-axis type holography. Ultramicroscopy 110, 447–459. https://doi.org/10.1016/j.ultramic.2009.11.017
Volkov, V.V., Han, M.G., Zhu, Y., 2013a. Double-resolution electron holography with

simple Fourier transform of fringe-shifted holograms. Ultramicroscopy 134, 175–184. https://doi.org/10.1016/j.ultramic.2013.06.018
Volkov, V.V., Han, M.G., Zhu, Y., 2013b. Double-resolution electron holography with simple Fourier transform of fringe-shifted holograms. Ultramicroscopy 134, 175–184. https://doi.org/10.1016/j.ultramic.2013.06.018
Wang, T., Nijhuis, C.A., 2016. Molecular electronic plasmonics. Applied Materials Today 3, 73–86. https://doi.org/10.1016/j.apmt.2016.03.001
Wolf, D., Lubk, A., Lenk, A., Sturm, S., Lichte, H., 2013. Tomographic investigation of fermi level pinning at focused ion beam milled semiconductor surfaces. Appl. Phys. Lett. 103, 264104. https://doi.org/10.1063/1.4858957
Yang, H., Rutte, R.N., Jones, L., Simson, M., Sagawa, R., Ryll, H., Huth, M., Pennycook, T.J., Green, M.L.H., Soltau, H., Kondo, Y., Davis, B.G., Nellist, P.D., 2016. Simultaneous atomic-resolution electron ptychography and Z-contrast imaging of light and heavy elements in complex nanostructures. Nat Commun 7, 12532. https://doi.org/10.1038/ncomms12532
Yao, Y., Li, C., Huo, Z.L., Liu, M., Zhu, C.X., Gu, C.Z., Duan, X.F., Wang, Y.G., Gu, L., Yu, R.C., 2013. In situ electron holography study of charge distribution in high-κ charge-trapping memory. Nat Commun 4, 2764. https://doi.org/10.1038/ncomms3764
Yazdi, S., Kasama, T., Beleggia, M., Samaie Yekta, M., McComb, D.W., Twitchett-Harrison, A.C., Dunin-Borkowski, R.E., 2015. Towards quantitative electrostatic potential mapping of working semiconductor devices using off-axis electron holography. Ultramicroscopy 152, 10–20. https://doi.org/10.1016/j.ultramic.2014.12.012
Yu, X., Marks, T.J., Facchetti, A., 2016. Metal oxides for optoelectronic applications. Nature Mater 15, 383–396. https://doi.org/10.1038/nmat4599
Zangwill, A., 2012. Modern Electrodynamics:, 1st ed. Cambridge University Press. https://doi.org/10.1017/CBO9781139034777
Zhirnov, V.V., Cavin, R.K., 2008. Negative capacitance to the rescue? Nature Nanotech 3, 77–78. https://doi.org/10.1038/nnano.2008.18

Annexe :

I initially compute the Debye length (0.1), for subsequent calculations, and subsequently, I calculate surface charges as a function of surface voltage (depletion or accumulation).

$$L_d = \sqrt{\frac{2\varepsilon_r \varepsilon_0 kT}{q^2 N}} = 5{,}8 \text{ nm} \quad (0.1)$$

Calculation of Surface Charge in the Accumulation Regime (0.2) (the sign of the charges depends on the doping "on top sign" if P "lower sign" otherwise):

$$Q_s = \pm \frac{2\varepsilon_r \varepsilon_0 kT}{qL_d} \exp\left(\mp \frac{q\psi_s}{2kT}\right) \quad (0.2)$$

In contrast to the adjacent depletion mode (0.3), this region exhibits a significantly shorter space charge extent, measuring only a few nanometers.

$$Q_s = \mp \frac{2\varepsilon_r \varepsilon_0 kT}{qL_d} \sqrt{\pm\left(\frac{q\psi_s}{kT} - 1\right)} = -qNL_{dep} \quad (0.3)$$

$$L_{dep} = \sqrt{\frac{2\varepsilon_r \varepsilon_0}{qN} \times \pm\left(\psi_s - \frac{kT}{q}\right)} \quad (0.4)$$

Type n	Qs C/m²	Ldep (nm)	Q depletion charge
1V (accumulation)	$-2{,}47 * 10^{-3}$	*	*
5V (accumulation)	$-4{,}26 * 10^{-2}$	*	*
-1V (depletion)	$1{,}35 * 10^{-3}$	8,52	Doping charge ($e*N*L_{dep}$)
-5V (depletion)	$2{,}7* 10^{-3}$	17,2	Doping charge

Type p	Qs C/m^2	Ldep (nm)	Q depletion charge
1V (depletion)	$-1{,}96 * 10^{-3}$	12	Doping charge
5V (depletion)	$-3 * 10^{-3}$	19	Doping charge
-1V (déplétion)	*(inf E thermal)	Sub-nanometre	Doping charge
-5V (accumulation)	$1{,}5* 10^{-2}$	*	*

After computing the charged area, it becomes evident that the charge density within the silicon is notably lower than that within the dielectric. Consequently, it is deemed negligible for the studied system.

Résumé en français des principaux thèmes de la thèse :

Chapter 1 — Introduction et motivation

Contexte général : l'industrie de la microélectronique

La microélectronique est devenue un élément indispensable de notre vie quotidienne et de l'économie mondiale. J'en veux pour preuve la pénurie de puces survenue pendant mon doctorat, qui a eu un impact énorme sur de nombreux secteurs de production. Non seulement l'internet des objets (IoT), par exemple pour les maisons intelligentes et les villes connectées, mais aussi les applications d'intelligence artificielle (IA), pour les voitures autonomes et les robots intelligents, ont pris de l'importance ces dernières années, créant une forte demande de microélectronique à base de silicium. Ces deux types d'applications n'ayant pas les mêmes exigences en matière de puissance de calcul et de consommation d'énergie, elles reposent sur des technologies et des techniques de fabrication différentes.

La puissance de calcul étant moins importante que l'autonomie pour les applications de l'internet des objets, l'échelle de longueur des composants (appelés "nœuds" dans l'industrie microélectronique) peut être moins agressive et les machines à ultraviolet profond (DUV) déjà en place sont suffisantes. En effet, ce type de lithographie représente actuellement 80 % de la demande, ce qui signifie que nous pouvons produire davantage de machines du même type pour répondre à la demande.

Cependant, pour alimenter la prochaine génération de véhicules autonomes ainsi que la microélectronique de demain, nous avons besoin de puces dotées d'une capacité de calcul extrême et d'une faible consommation d'énergie. Pour ce faire, chaque composant électronique doit être réduit en taille, de nouveaux concepts et matériaux doivent être développés, et de nouvelles machines doivent être conçues pour les fabriquer.

Ces machines, bien que très coûteuses à développer et à construire, créent des composants toujours plus fins. Seules quelques entreprises, telles que TSMC, Intel et Samsung, peuvent se les offrir. À cela s'ajoute une demande accrue de la part de sociétés sans usine, telles qu'Apple, Qualcomm, Nvidia et d'autres. En conséquence, notre chaîne d'approvisionnement pour la prochaine révolution de l'information reposera uniquement sur quelques entreprises disposant d'usines localisées dans le monde, ce qui rendra le système vulnérable aux catastrophes naturelles telles que les tremblements de terre et les pandémies... De nombreuses réactions politiques sont en cours pour diversifier et étendre la production, avec le « EU chips act », le « US chips act », le « Japanese chips act », et ainsi de suite... L'investissement dans les nouvelles technologies pour construire et caractériser les composants de demain est considérable.

Les enjeux actuels

Le maintien de la croissance dans le secteur de la microélectronique se heurte à de nombreux défis, le premier d'entre eux étant le développement des technologies actuelles et futures telles que les Magnetic Random Access Memories (MRAM) (Moodera et al., 1995; Sbiaa et al., 2011; Slonczewski, 1996), memristance (Chua, 1971; Di Ventra and Pershin, 2013; Strukov et al., 2008), mémoire à changement de phase (Burr et al., 2010; Jung et al., 2011; Krebs et al., 2009; Simone Raoux et al., 2008; S. Raoux et al., 2008), spintronique (Hirohata et al., 2015), ou, dans un avenir lointain, skyrmionique (Ma and Li, 2022), optoélectronique (Yu et al., 2016), ou moléculaire (Wang and Nijhuis, 2016). Par exemple, les matériaux ferroélectriques, qui présentent une polarisation spontanée même en l'absence d'un champ appliqué, ont suscité un intérêt considérable pour la production de dispositifs exploitant la capacité négative (Khan et al., 2015; Robertson and Wallace, 2015; Hoffmann et al., 2019; Íñiguez et al., 2019) et pourraient offrir une solution à la dissipation de puissance et à la surchauffe qui se produisent lors de la miniaturisation des transistors (Theis and Solomon, 2010). L'amplification d'une faible tension de grille à l'aide de la capacité négative permettrait un fonctionnement à faible consommation d'énergie (Zhirnov and Cavin, 2008). Tous ces dispositifs sont alimentés par des courants électriques et dépendent de la manipulation et du contrôle des champs électriques ou magnétiques à de très petites échelles de longueur. La possibilité de mesurer localement les signaux électriques et les distributions de charge électrique de la puce en fonctionnement est essentielle pour soutenir ces développements et améliorer les technologies existantes, ainsi que pour développer une nouvelle génération de dispositifs. La corrélation entre les champs électriques locaux, cartographiés à travers un dispositif choisi pendant qu'il fonctionne, et ses propriétés structurelles et chimiques aideraient grandement les laboratoires de recherche et l'industrie de la microélectronique. En outre, les études locales des champs électriques pourraient également fournir des méthodes permettant de déterminer les causes profondes des défaillances électriques (Engelmann et al., 2000) pour améliorer les appareils en termes de fiabilité, de vitesse et de consommation d'énergie. La caractérisation électrique peut désormais être effectuée directement sur des nanodispositifs uniques par contact avec des nanotips, actuellement appelés "nanoprobing" (Toh et al., 2007, 2008). Cette technologie présente l'avantage de permettre l'étude des puces électroniques dans leur environnement naturel et à l'échelle microscopique en mesurant leur réponse globale à une excitation. Cependant, en raison du rétrécissement des puces, les blocs élémentaires qui composent le composant doivent être étudiés à une résolution plus élevée, c'est-à-dire à l'échelle nanométrique, pour pouvoir progresser. Plus important peut-être, ces techniques de caractérisation électrique mesurent la réponse globale d'un système ou d'un dispositif : elles ne peuvent pas fournir d'informations sur la localisation des champs électriques ou des distributions de charges à l'intérieur d'un dispositif.

La microscopie électronique à transmission (MET) est une technique puissante qui permet d'étudier les propriétés des nanosystèmes individuels avec une résolution spatiale très élevée. Les tentatives de cartographie des champs électriques locaux à l'aide de la microscopie électronique à transmission à balayage quadridimensionnelle (4D-STEM) suscitent actuellement beaucoup d'enthousiasme (Ophus, 2019). Ces techniques basent leurs mesures sur la déviation du faisceau d'électrons causée par la force de Lorentz d'un champ électrique local. En principe, le champ local à l'intérieur

d'un composant pourrait être déterminé de cette manière, contrairement aux micropointes qui mesurent la réponse globale.
Les techniques 4D-STEM peuvent même avoir une résolution atomique (Jiang et al., 2018) et sont capables de reconstituer des informations tridimensionnelles (Jarausch et al., 2009). Cependant, ils ne mesurent pas le potentiel électrique. En outre, comme elles sont basées sur le balayage, elles sont extrêmement difficiles à mettre en œuvre pour les expériences *in situ*. Par exemple, les techniques basées sur le balayage peuvent être très sensibles à la dérive de l'échantillon (Yang et al., 2016). Elles sont également très exigeantes en termes de collecte et de stockage des données. Par exemple, chaque image est d'environ quatre mégapixels, ce qui donne un ensemble de données d'une taille totale de 420 Go avec une moyenne de 49 images de sondes adjacentes (dans une grille de 7×7) (Ophus, 2019). Une technique plus ancienne, mais moins répandue est l'holographie électronique hors axe (EH), une méthode interférométrique qui permet de cartographier quantitativement les distributions électriques. La réponse d'un composant après une stimulation électrique (Rau et al., 1999; Twitchett et al., 2002), magnétique (Gatel et al., 2015; Dunin-Borkowski et al., 2019), ou de contrainte (Hÿtch et al., 2008) maintenant peut être mesuré. La mesure des distributions de charges a également été rapportée (Midgley and Dunin-Borkowski, 2009; McCartney et al., 2010; Beleggia et al., 2011, 2014; McCartney et al., 2019), cette mesure peut même atteindre une précision jusqu'au niveau de la charge élémentaire (Gatel et al., 2013). L'holographie électronique permet de retrouver ces interactions grâce à la cartographie de la différence de phase entre la partie de l'onde électronique traversant la zone active de l'échantillon et une onde de référence dans le vide. Le déphasage est directement lié aux potentiels électromagnétiques rencontrés le long de la trajectoire du faisceau d'électrons, à la fois dans l'échantillon et dans le champ de fuite environnant.
Cependant, malgré ces perspectives encourageantes, l'holographie électronique a rarement été utilisée pour étudier les propriétés électriques locales des nano systèmes. Quelques systèmes modèles, dont les nanopointes (Cumings et al., 2002; de Knoop et al., 2015, 2014; He and Cumings, 2013; Migunov et al., 2017), puits quantiques (Liu et al., 2012), nanofils (den Hertog et al., 2013, 2009), jonction *p-n* (Beleggia et al., 2003; He et al., 2013; Twitchett et al., 2002; Twitchett-Harrison et al., 2008; Yazdi et al., 2015), couches d'oxydes (Yao et al., 2013), transistor (Rau et al., 1999), ont été étudié. Cependant, l'interprétation des données expérimentales peut être influencée par de nombreux facteurs, tels que la préparation de l'échantillon, les surfaces endommagées, le champ de fuite et le rayonnement électronique (Park et al., 2014; Wolf et al., 2013; Yazdi et al., 2015). En outre, l'étude des dispositifs magnétiques réels (Einsle et al., 2015; Goto et al., 2013) ainsi qu'électriques (Ikarashi et al., 2012) a été rapportée, mais des recherches plus approfondies sont encore nécessaires.
Une demande importante émanant de l'industrie a été de développer des méthodes d'analyse de la distribution des dopants à l'intérieur des composants (Diebold, 1996). De nombreuses recherches ont donc été consacrées à la caractérisation des jonctions *p-n*, en grande partie à l'aide de MET et, entre autres, d'une étude *in situ* pionnière en holographie électronique (Frabboni et al., 1985). Cependant, l'holographie électronique des jonctions *p-n* s'est heurtée à plusieurs difficultés, notamment la préparation de l'échantillon, qui a modifié le dopage à l'intérieur de la jonction. L'implantation d'atomes de Ga à la surface de l'échantillon pendant le fraisage par

faisceau d'ions focalisés (FIB) entraîne la formation de couches dites mortes (« dead layer ») (Cooper et al., 2010; Twitchett et al., 2002) et des couches conductrices amorphes (Han et al., 2008). De plus, il est difficile de générer des données quantitatives, car le déphasage mesuré correspond à l'intégration des potentiels électriques le long du trajet du faisceau d'électrons.
Dans le cadre de mon doctorat, j'ai tenté de résoudre certains de ces problèmes en combinant les dernières données expérimentales issues d'expériences d'holographie électronique *operando* avec une modélisation réalisée à l'aide de la méthode des éléments finis (MEF). Ce travail a été soutenu par les récents développements dans le groupe sur la méthodologie expérimentale, en termes de préparation des échantillons, de polarisation *in situ*, de contrôle du microscope, et d'acquisition et de traitement des données.
Nous avons délibérément choisi d'étudier un composant microélectronique fondamental différent de la jonction *p-n* : le nanocondensateur. Ce composant est à la fois largement utilisé dans l'industrie microélectronique et présente des phénomènes physiques riches et variés.
Plus spécifiquement, j'ai développé une méthodologie basée sur la méthode des éléments finis (MEF) pour modéliser le potentiel électrostatique à l'intérieur et autour de nanodispositifs polarisés électriquement en utilisant un logiciel commercial (COMSOL Multiphysics). Je montrerai comment les problèmes liés aux champs de fuite générés par le nanocondensateur polarisé peuvent être résolus par la simulation numérique, et de la même manière pour d'autres artefacts tels que les dommages de surface introduits pendant la préparation de l'échantillon par FIB ou encore la charge induite par le faisceau (charge induite par le faisceau et artefacts de préparation de l'échantillon). Plus important encore, la modélisation numérique permettra d'interpréter les données expérimentales de manière satisfaisante, ce qui conduira à une meilleure compréhension de la physique sous-jacente, à la découverte de phénomènes inattendus et à la mesure des caractéristiques électriques des dispositifs étudiés.

Description des chapitres

La structure du reste du manuscrit est présentée comme suit.
Le chapitre 2 présente les méthodes développées et utilisées dans ma thèse ainsi que le contexte théorique. Je commence par une définition d'une particule chargée et je présente la théorie du condensateur à l'aide des équations de Maxwell. Le condensateur sera ainsi entièrement décrit, de la dimension nanoscopique à la dimension macroscopique.
Je présenterai la technique de l'holographie, la théorie et la méthodologie de l'analyse des données. La méthode des éléments finis (MEF) sera introduite, ainsi que son formalisme et certains aspects pratiques. Enfin, je présenterai quelques outils numériques que j'ai développés au cours de ma thèse concernant l'ajustement des données expérimentales, des procédés qui permettent d'éliminer un maximum de biais humains tout en accélérant l'étude, telles que les algorithmes d'ajustement et l'IA.

Le chapitre 3 examine les théories qui relient le modèle MEF et les images de phase extraites des hologrammes. Nous commençons par évaluer les artefacts numériques en examinant les paramètres non physiques tels que la taille de la simulation finie et la géométrie du maillage MEF. Après avoir déterminé les conditions pour lesquelles le modèle est exempt de paramètres non physiques, j'examinerai ce que nous pouvons

apprendre des simulations. À cet égard, je démontrerai que nous pouvons mieux comprendre l'effet de certains phénomènes en étudiant la relation entre le modèle physique et l'image de phase à la suite de l'ajustement des paramètres du modèle.

Le chapitre 4 présente la première analyse des données expérimentales. Compte tenu de l'immense complexité et de la diversité de l'étude, nous avons commencé par un modèle de condensateur créé en laboratoire spécifiquement pour l'expérience, ce qui nous a permis de tester plusieurs techniques développées pour l'occasion. Nous voulions avant tout vérifier si nos attentes concernant le comportement du condensateur à cette échelle étaient satisfaites. Si certaines attentes ont été confirmées, l'analyse a également donné lieu à des résultats surprenants. Par exemple, nous mettons en évidence la présence de régions chargées en volume qui altèrent les caractéristiques électriques attendues des nanocondensateur métal-oxyde-semiconducteur (MOS) modèles, alors que ce type de nanodispositif était considéré comme parfaitement compris. Enfin, même si nous pouvons analyser l'échantillon *in operando*, l'échantillon est aminci pour obtenir la transparence électronique, de sorte qu'il peut y avoir une certaine disparité entre la mesure de l'échantillon et son véritable macro-comportement.

Le chapitre 5 présente une étude des incertitudes des paramètres étudiés et des méthodes visant à minimiser le biais humain dans le processus d'ajustement. Je présenterai la méthode acceptée en métrologie pour quantifier l'incertitude et les liens entre les paramètres. Nous avons découvert que certains paramètres de mesure sont corrélés au cours de l'étude théorique, de sorte que la principale question est de savoir si nous pouvons les mesurer s'ils sont corrélés. Par conséquent, nous utilisons des outils statistiques pour résoudre ce problème, en particulier la matrice de corrélation, qui nous permet de calculer la propagation de l'incertitude à travers l'écart-type mesuré.
De plus, le développement de simulations numériques a l'avantage de nous permettre de construire une analyse de données complexe tout en développant des outils d'analyse de données expérimentales tels que le script, l'autoajustement ou le développement d'une IA.

Le chapitre 6 présente l'application de ces techniques à des dispositifs réels qui présentent des géométries plus complexes. Les résultats sur les nanodispositifs provenant des lignes de production de STMicroelectronics sont présentées et analysées, et les incertitudes sont étudiées. Avant de conclure sur l’étude de deux condensateurs fonctionnant ensemble, je montre une étude d'un condensateur en fonctionnement ainsi qu'une étude que nous n’avons pas réussie à résoudre, démontrant que même lorsque nous faisons des erreurs, le résultat final est toujours intéressant.

Chapter 2 — Méthode

Le travail effectué dans le cadre de cette thèse a nécessité la combinaison de plusieurs techniques existantes ainsi que le développement de nouvelles techniques. Cependant, avant d'aborder ces techniques, je commencerai ce chapitre en discutant de quelques aspects théoriques de base.

Comme nous voulons mesurer les charges à l'intérieur de nanodispositifs en fonctionnement, il semble pertinent de commencer par la définition des charges en physique et par la description théorique d'un condensateur. Je discuterai ensuite du comportement des condensateurs dans les circuits électriques. Ainsi, le condensateur sera entièrement décrit, de la dimension nanoscopique à la dimension macroscopique. Enfin, je développerai également certains aspects des équations de Maxwell et des conditions de continuité aux interfaces (équation de passage), ce qui nous donnera une bonne idée de ce que l'on peut attendre du comportement du système considéré.

La première technique que je décrirai est l'holographie électronique et la façon dont nous pouvons tenter de cartographier un potentiel électromagnétique à une échelle nanométrique avec l'interaction entre le faisceau d'électrons et les différents potentiels électromagnétiques rencontrés au cours de leur voyage à travers le microscope. En commençant par une description des électrons rapides à l'aide de la relativité restreinte et de la mécanique quantique, je présenterai les principales équations nécessaires à la compréhension du contexte théorique et de l'interaction entre l'électron et le potentiel électrostatique.

Un problème fondamental de l'holographie électronique est que l'interaction provient de l'intégrale du potentiel le long de la trajectoire de l'électron, ce qui signifie que l'information parallèle à la dimension le long de la trajectoire de l'électron est très difficile à interpréter : c'est le problème bien connu de la projection. Il s'agit là d'une justification majeure de l'utilisation de simulations numériques. Nous pouvons utiliser la méthode des éléments finis pour extraire des données quantitatives et reconstruire l'histoire de la trajectoire du faisceau pour répondre à cette dimension perdue. À l'aide d'un exemple, j'expliquerai la théorie de base et montrerai comment la méthode fonctionne en pratique.

La dernière partie du chapitre est consacrée à une routine d'ajustement automatisée que j'ai développée pour éliminer autant que possible la polarisation humaine dans l'analyse des données. Je passerai en revue les deux méthodes que j'ai utilisées pour automatiser le calcul, ainsi qu'une méthode basée sur l'intelligence artificielle qui, bien que beaucoup plus rapide que les éléments finis, soulève de nouvelles questions sur la définition des incertitudes associées à ces méthodes.

1. Condensateur

En réalité, un condensateur n'est pas infini, surtout lorsqu'il est étudié à l'aide de techniques TEM, car l'échantillon doit être extrêmement fin pour permettre le passage de l'électron. En réalité, les champs électriques deviennent courbes lorsqu'ils sont proches des interfaces entre le diélectrique et le vide (Figure 2.1). En outre, des champs de fuite apparaissent autour du condensateur dans cette configuration, ce qui, comme nous le verrons plus tard, doit être pris en compte dans les simulations. En quelque sorte, chaque plan du condensateur est chargé d'électrons de signe opposé. Chaque charge génère un champ qui, combiné aux champs des autres charges, produit le champ électrique final entre les plaques selon le principe de superposition.

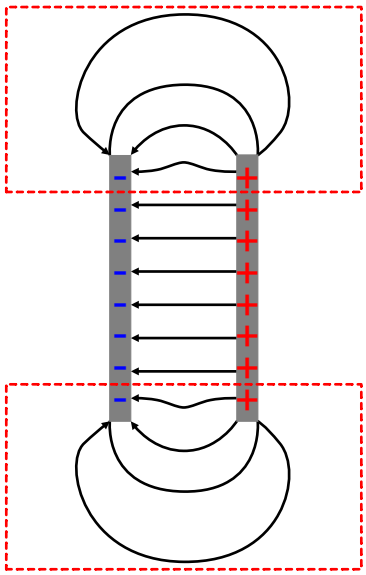

infinite capacitor limit of approximation

Figure 2.1 : Schéma d'un condensateur réel avec le champ de fuite qui l'entoure. (infinite capacitor limit of approximation : limite d'approximation du condensateur infini)

Compte tenu du rapport d'aspect entre la longueur du diélectrique et l'épaisseur de l'échantillon, l'échantillon étudié ici est beaucoup plus proche d'un condensateur réel que d'un condensateur infini. Nous devons tenir compte de ce paramètre pour comprendre son effet. L'importance du champ de fuite sera examinée en détail dans les sections et le chapitre suivants. Mais d'abord, je voudrais parler d'une modification du condensateur qui augmente son énergie sans changer sa géométrie : la physique des diélectriques.

2. Condensateurs diélectriques

Parce qu'un diélectrique permet de stocker plus de charges sur la plaque du condensateur que le vide, plusieurs efforts ont été faits ces dernières années pour incorporer des diélectriques à permittivité relative croissante à l'intérieur des nanocondensateurs : à géométrie et polarisation égales, ces matériaux permettent au condensateur de stocker beaucoup plus de charges et donc beaucoup plus d'énergie.

En effet, la première réaction d'un diélectrique à un champ électrique externe est de contrer le champ en réarrangeant ses charges internes jusqu'à ce qu'il atteigne une limite définie par sa permittivité (Figure 2.2). Le condensateur sera maintenant connecté à un générateur pour mieux décrire le condensateur utilisé dans la vie réelle. Dans un premier temps, on pourrait dire que le potentiel va baisser, mais c'est sans compter sur le fait que le condensateur est connecté à un générateur. Celui-ci a pour principal effet d'imposer une polarisation au dispositif, ce qui augmente le nombre de charges nécessaires pour maintenir la polarisation initiale, augmentant ainsi son énergie.

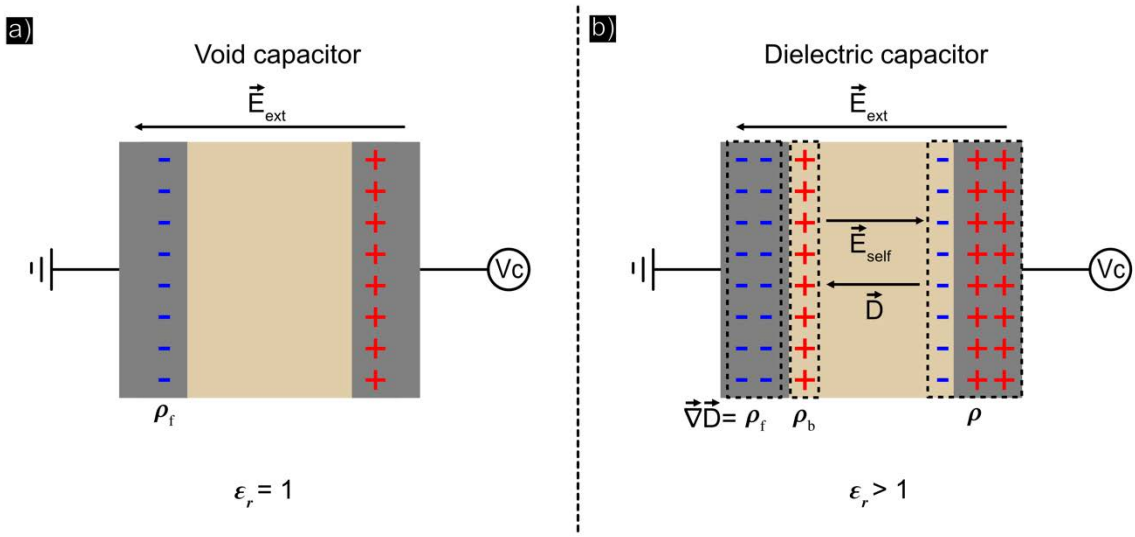

Figure 2.2 : Schéma d'un condensateur de polarisation avec un espaceur vide a) et l'induction de nouvelles charges par l'insertion d'un ferroélectrique ou d'un diélectrique. (void capacitor : condensateur vide ; Dielectric capacitor : condensateur avec un diélectrique)

En d'autres termes, le diélectrique génère des charges liées en réponse au champ de l'électrode. En conséquence, les charges liées feront écran à l'électron sur la plaque du condensateur, et le générateur réagira en injectant davantage de charges à l'intérieur des électrodes pour conserver la chute de potentiel.
Nous pouvons tenir compte de ce phénomène en remplaçant ε_0 par $\varepsilon = \varepsilon_0 \varepsilon_r$ avec ε_r la permittivité relative du diélectrique:

$$E = \frac{\rho_{s,f}}{\varepsilon} \qquad (2.1)$$

Les équations du condensateur:

$$V_c = \frac{\rho_{s,f} w}{\varepsilon} = \frac{Q}{C} \; ; \; C = \frac{\varepsilon S}{w} \qquad (2.2)$$

Ces équations décrivent le comportement d'un condensateur avec un diélectrique. Pour illustrer, lorsque nous ajoutons un élément de permittivité ε entre les deux plaques, la capacité augmente alors que la polarisation devrait diminuer. Mais avec la polarisation fixe apportée par le générateur, les charges sur la plaque vont croître. Globalement, la chute de potentiel aux bornes du condensateur sera la même avec ou

sans diélectrique, mais avec un diélectrique, beaucoup plus de charges seront stockées.

3. Holographie électronique

La microscopie électronique à transmission, plutôt que la microscopie optique, est désormais nécessaire pour étudier les composants microélectroniques en raison de leur miniaturisation. L'holographie électronique est l'une des rares techniques permettant de mesurer les champs électriques, magnétiques et de déformation à l'échelle nanométrique. Par conséquent, lorsqu'elle est combinée à des expériences de polarisation *in situ*, l'holographie électronique devient une technique puissante pour mesurer les potentiels et les champs électriques dans les dispositifs microélectroniques en fonctionnement.
Contrairement à la technique TEM conventionnelle, qui n'enregistre que la distribution spatiale de l'intensité, nous pouvons enregistrer la phase entre une partie du faisceau qui traverse le vide, appelée "onde de référence", qui n'a en principe subi aucune interaction avec un quelconque champ, et une partie qui traverse l'échantillon, appelée "onde objet", et qui acquiert un déphasage dû à son interaction avec un champ magnétique, électrique ou de déformation (Gabor, 1948; Tonomura, 1987; Hÿtch et al., 2008; Pozzi et al., 2014) (Figure 2.3). Nous pouvons étudier la variation locale de ces champs, car cette interaction peut être enregistrée sous la forme d'une figure d'interférence. La figure d'interférence résultante (c'est-à-dire l'hologramme) contient toutes les informations sur le déphasage de l'onde électronique subie lors de l'interaction avec les champs électromagnétiques locaux. (Tonomura, 1987; Midgley and Dunin-Borkowski, 2009). De multiples techniques, telles que la technique hors axe utilisée ici, ont été mises au point pour obtenir cette phase. Par conséquent, jusqu'à 20 autres techniques, telles que l'holographie en ligne, peuvent également être utilisées. (Cowley, 1992), que je ne détaillerai pas.

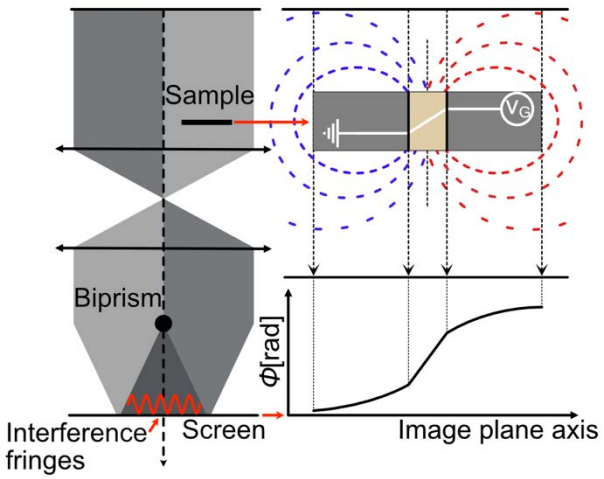

Figure 2.3 : Schéma de la technique d'holographie sur l'image de phase résultante d'un condensateur modèle. (Sample : échantillon ; Screen : écran ; Interference fringes : frange d'interférence ; Image plane axis : axe plan de l'image)

Lorsqu'une onde électronique interagit avec un objet ou un champ électromagnétique, sa phase change. L'effet Aharonov-Bohm (Aharonov and Bohm, 1961, 1959; Ehrenberg and Siday, 1949):

$$\Phi(x,y) = \frac{\pi\gamma}{\lambda_B V_r}\oint V(\vec{r})dz - \frac{e}{\hbar}\oint A_z(\vec{r})dz \qquad (2.3)$$

Avec λ_B représentant la longueur d'onde relativiste de l'électron et A_z le potentiel vecteur magnétique le long de la direction du faisceau. nous pouvons réécrire l'équation ci-dessus sans introduire explicitement la longueur d'onde :

$$\mathrm{C}_e = \frac{e}{\hbar}\frac{\sqrt{m_0}}{\sqrt{E_k E_0}}\frac{E_k + E_0}{\sqrt{E_k + 2E_0}} \qquad (2.4)$$

Lorsque les électrons sont accélérés, la constante C_e diminue, ce qui implique que le déphasage diminue. Cette théorie permet d'étudier des échantillons chargés ou polarisés. Par exemple, je peux illustrer l'effet sur la phase d'un électron qui traverse un potentiel électrostatique (Figure 2.3) et on peut observer le résultat en 2D ou en 3D (Figure 2.4).

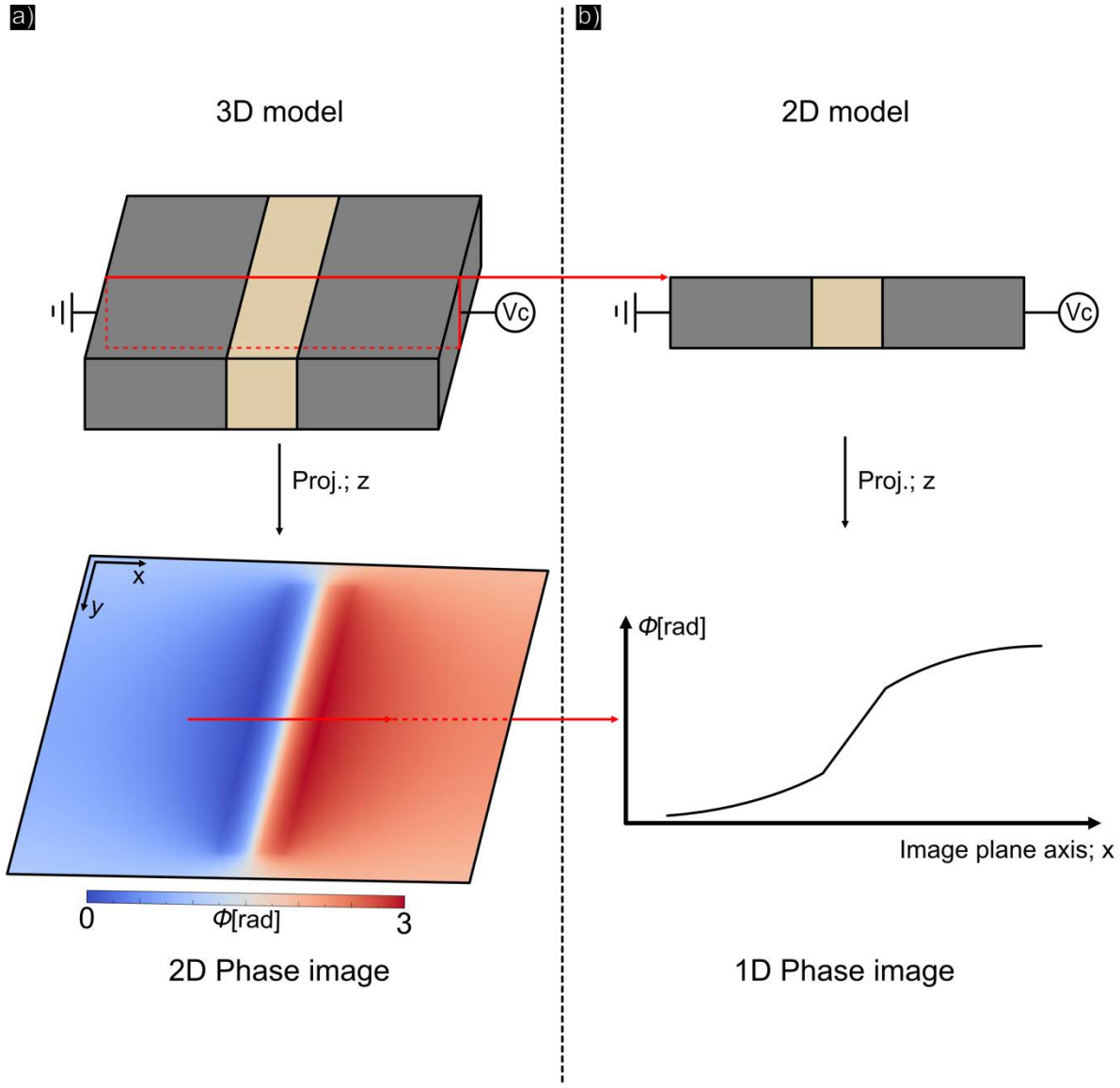

Figure 2.4 : Les résultats de la projection de phase utilisant le modèle 3D (a) et son équivalent en 2D (b) sont tous deux polarisés à 1V. (Phase image : image de phase)

Toutes les observations expérimentales ont été réalisées à l'aide du microscope I2TEM (In-situ Interferometry TEM), un Hitachi 3300-C fonctionnant à 300 kV équipé d'un canon d'émission à champ froid pour une très grande cohérence et d'un correcteur d'aberration BCOR de CEOS avec une résolution spatiale de 0,5 nm en mode Lorentz et de 0,08 nm en mode haute résolution (Snoeck et al., 2014). Une caméra CMOS 4k x 4k présentant une fréquence d'images élevée (caméra One View de Gatan) pour enregistrer les hologrammes complète le dispositif. Mais pour pouvoir mesurer la phase avec une sensibilité croissante tout en gardant une bonne résolution et en améliorant le rapport signal/bruit, des techniques spécifiques ont été développées comme le contrôle dynamique du microscope (Gatel et al., 2018) et des routines d'acquisition intelligentes (Volkov et al., 2013a).

3.I. Conditions limites et boîte de simulation.

Pour résoudre le potentiel, la variable partagée V est calculée à partir d'un modèle divisé en deux parties principales : le condensateur et le milieu extérieur. La première partie utilise deux solveurs distincts pour simuler les zones conductrices et isolantes, respectivement la loi d'Ohm (2.5) pour l'induction (c'est-à-dire les zones conductrices) et la loi de Gauss (2.6) pour l'électrostatique, tandis que la seconde partie (le milieu extérieur) n'utilise que l'électrostatique.

$$-\nabla \cdot d\left(\sigma \nabla V - \overrightarrow{J_e}\right) = dQ_j \qquad (2.5)$$

σ : conductivité S/m ; $\overrightarrow{J_e}$: densité de courant externe (injecté) A/m^2 ; Q_j : source de courant.

$$-\nabla \cdot d\left(\varepsilon_0 \nabla V - \vec{P}\right) = \rho \qquad (2.6)$$

ε_0 : la permittivité du vide F/m ; $\vec{P}$: vecteur de polarisation électrique; ρ : la densité de charge de l'espace C/m^2 ; d : l'épaisseur du plan.

Pour optimiser et limiter les effets de boîte sur les calculs FEM, les conditions sur les bords du domaine ont été fixées à l'infini (Figure 2.5, domaine bleu). Le domaine infini est créé en imposant virtuellement une très grande distance entre les nœuds qui composent le maillage du domaine, ce qui donne une taille de système presque infinie. Plus précisément, le domaine sera agrandi d'une taille caractéristique déterminée en multipliant par 100 la diagonale d'une boîte imaginaire contenant l'ensemble de la géométrie du modèle.
L'utilisation de telles distances dans le modèle réduit les erreurs numériques en limitant les effets de bord tout en préservant les résultats en termes de temps de simulation en limitant la taille de la boîte de simulation, ce qui permet d'obtenir une meilleure solution globale. La "couche infinie" est calculée sur un maillage carré, spécifique et optimisé pour ce type de calcul infini.
Comme l'échantillon sera étudié *in situ* en le polarisant, nous devons expliquer comment nous allons incorporer cet effet dans la simulation FEM. Les conditions électriques sont imposées aux extrémités de l'électrode à l'aide de conditions aux limites, la partie mise à la terre étant égale à $V = 0$ et le potentiel appliqué égal à $V_c = V$, de sorte que le potentiel soit réparti à l'intérieur des électrodes jusqu'au diélectrique et à travers le vide autour par la variable V partagée entre les deux solveurs.

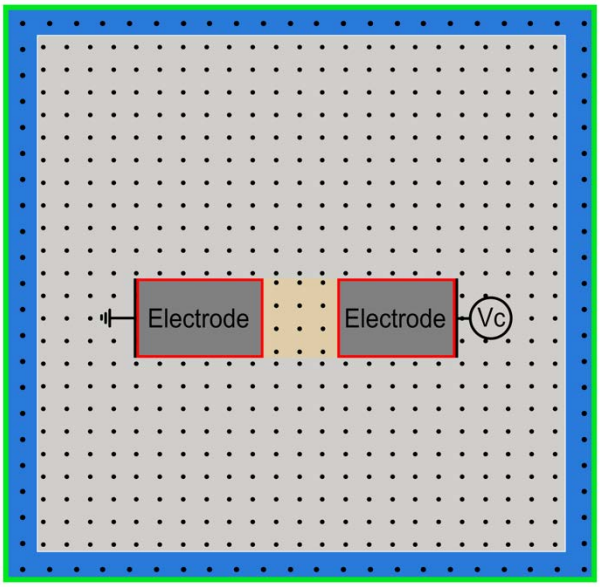

Figure 2.5 : Les conditions aux limites externes sont indiquées en vert, et le domaine de l'infini est indiqué en bleu; la partie métallique est résolue par l'induction tandis que le reste est résolu par la loi d'Ohm (zones en pointillés).

Les deux électrodes étant considérées comme métalliques, elles constituent des zones pertinentes pour la physique de l'induction, et la zone restante est calculée à l'aide de la loi d'Ohm, ce qui implique la coexistence de deux solveurs pour résoudre deux types de physique distincts. Ceci est important, car nous voulons pouvoir étudier les zones conductrices avec les zones isolantes qui peuvent continuer à se charger même si nous résolvons avec le solveur stationnaire.

4. Routine d'ajustement automatique

4.I. Logiciel de contrôle "Batch"

Je voulais nous donner plus de flexibilité et de contrôle sur la façon dont nous analysons les données d'holographie électronique avec les simulations FEM de COMSOL. La flexibilité dans la façon dont nous pouvons explorer les paramètres de l'espace d'une manière plus personnalisée et le contrôle de la partie ajustement nous permettent d'explorer les paramètres de l'espace d'une manière dirigée "sur le flot" en analysant le résultat du calcul en temps réel à chaque boucle, ce qui permet de trouver les prochains paramètres (les mieux ajustés).

4.II. Méthode a région de confiance réflective.

L'automatisation du problème d'ajustement répond à deux problèmes majeurs : d'une part, nous voulons un ajustement plus rapide, et d'autre part, nous voulons être en mesure d'analyser les incertitudes. Pour ce faire, je combine les développements précédents sur le contrôle COMSOL avec la méthode région de confiance réflective (Trust Region Reflective) implémentée dans SciPy (Virtanen et al., 2020). L'algorithme est un processus itératif qui aboutit à des améliorations successives. L'algorithme effectue actuellement un déplacement obtenu en minimisant un modèle simple de la fonction (par exemple, quadratique) sur une région de confiance, généralement une

boule dont le rayon est appelé rayon de confiance du modèle. Le rayon de confiance est ajusté de manière à ce que la fonction diminue suffisamment à chaque itération tout en restant suffisamment petit pour que le modèle simple reste valide. La méthode proposée est une méthode efficace pour résoudre de grands problèmes de minimisation sous contrainte (Branch et al., 1999).

4.III. Évolution différentielle

L'évolution différentielle est de nature stochastique (Storn, 1997), cela signifie qu'il n'utilise pas de méthodes de gradient pour trouver le minimum, et bien qu'il puisse rechercher de grandes zones de l'espace candidat, il nécessite souvent plus d'évaluations de fonctions que les techniques traditionnelles basées sur le gradient.
L'idée sous-jacente à cet algorithme est de commencer avec une population de paramètres choisis au hasard, puis de choisir au hasard deux membres de cette population, et leur différence est utilisée pour faire muter le meilleur membre qui est le plus proche de la solution. Ce calcul est répété à chaque période du calcul nommée période, et si la solution est meilleure avec le membre muté, il remplace le membre original, et ainsi de suite jusqu'à ce que la solution se trouve dans la fourchette définie. Cette méthode permet d'explorer beaucoup plus de paramètres que la méthode de la région de confiance réflective, qui est une méthode basée sur le gradient, et permet donc une meilleure exploration des paramètres, ce qui est utile pour augmenter le nombre de paramètres utilisés pour ajuster le modèle au détriment du temps de convergence.

5. Intelligence artificielle (Tensorflow)

5.I.A. Introduction

Il existe de nombreuses façons de résoudre un problème physique avec l'holographie électronique, comme l'analyse ou la simulation pour la quantification du potentiel ou de la charge, mais la première ne permet pas de résoudre les géométries complexes et la seconde prend beaucoup de temps. Une autre solution consiste à utiliser l'IA pour résoudre ce problème, car elle est très rapide et peut avoir un très bon sens de l'approximation.
Il existe plusieurs approches de l'IA, notamment l'apprentissage automatique, qui tente d'extraire la règle d'un problème à l'aide d'un algorithme, et l'apprentissage profond, qui est en réalité un ajustement complexe de données avec un grand nombre de paramètres. Nous avons choisi de développer la seconde méthode en raison des bons résultats obtenus dans le traitement des images et du fait qu'à la fin, nous avons besoin d'un ajustement des données.
Pour réaliser l'apprentissage profond, nous employons un réseau neuronal, qui est un réseau de neurones artificiels interconnectés permettant de résoudre des problèmes complexes en ajustant les coefficients de pondération pendant la phase d'apprentissage. Les réseaux neuronaux ont été inspirés à l'origine par le système nerveux humain dans le cerveau. Le réseau neuronal peut se modifier lui-même en fonction des résultats de ses actions, ce qui permet d'apprendre et de résoudre des problèmes sans utiliser de règles algorithmiques et donc sans programmation traditionnelle. Notre cerveau peut traiter efficacement les problèmes de vision, de

parole et de reconnaissance des formes. Toutes ces tâches apparemment simples pour l'esprit humain sont en fait extrêmement complexes pour un ordinateur.

6. Conclusion

De la définition d'un simple à un assemblage de particules chargées en utilisant les équations de Maxwell, j'ai discuté du modèle physique d'un condensateur.
J'ai décrit le développement de la stabilisation continue pour l'holographie, sans laquelle nous ne pourrions pas obtenir les résultats de cette thèse.
Ensuite, nous avons noté non seulement pourquoi nous devons tenir compte de la relativité restreinte pour décrire l'électron rapide, mais aussi que l'interaction entre l'électron et différents potentiels peut être décrite par la mécanique quantique. Grâce à cette description, nous pouvons créer une méthodologie pour simuler des données expérimentales. Ainsi, nous pouvons rapidement constater que l'électron sera influencé non seulement par le potentiel à l'intérieur de l'échantillon, mais aussi par le potentiel autour de l'échantillon étudié (c.-à-d. le champ de fuite).
Par conséquent, nous avons dû simuler le champ de fuite autour du condensateur et la géométrie complexe de l'échantillon étudié, nous avons dû employer la méthode FEM pour calculer le potentiel interne et externe du dispositif.
J'ai créé un code Python qui permet un meilleur ajustement avec moins de polarisation due à l'intervention humaine. Je décris deux techniques : d'une part, j'utilise la méthode de réflexion de la région de confiance, qui est relativement rapide, mais peut rester bloquée dans le minimum local ; d'autre part, j'essaie de résoudre ce problème avec l'évolution différentielle, qui explore un espace de paramètres beaucoup plus grand, mais qui est beaucoup plus exigeante en termes de ressources et de temps de calcul. Enfin, j'ai essayé une méthode non traditionnelle (I.A.) pour trouver le meilleur paramètre du modèle.
En résumé, l'objectif de ce développement est de mener des recherches fondamentales sur les nanodispositifs tout en développant un interpréteur automatique d'images holographiques à travers ses défauts.
Pour aller plus loin, même si ce n'est pas l'objet de ma thèse, nous aurions pu effectuer des mesures macroscopiques pour caractériser complètement les nanodispositifs considérés. Deuxièmement, nous aurions pu mesurer les dispositifs en termes de fréquence, mais notre équipe y travaille encore, alors restez à l'écoute.

Chapter 3 — Développement théorique

La compréhension des données expérimentales nécessite un développement théorique qui permet d'extraire de la simulation des paramètres qui ne sont pas accessibles expérimentalement. Nous pouvons également aller au-delà de la réalité expérimentale en incluant une géométrie et des paramètres qui ne sont pas observables lors d'une expérience. On peut ainsi déterminer l'ensemble des lois physiques qui régissent le comportement du système étudié.
Avant tout cela, il est nécessaire de développer les outils FEM nécessaires à la simulation d'une image de phase en holographie électronique et de les tester. Dans ce chapitre, nous étudierons un condensateur modèle, d'abord avec les deux électrodes à la masse, puis avec l'une des électrodes polarisées à différentes tensions. Grâce à la modélisation, j'expliquerai comment l'image de phase est affectée par la géométrie du système, les paramètres du modèle, l'interaction avec le faisceau d'électrons et les artefacts provenant de la préparation de l'échantillon (amorphisation, implantation ionique). À cette fin, nous pouvons établir certaines connexions entre le modèle et le profil de phase, ce qui nous permet d'extraire des informations du profil de phase qui ne seraient pas possibles sans l'étude de simulation (Yazdi et al., 2015). L'une des sources d'erreur systématique, causée par l'interaction entre l'échantillon polarisé et le porte-échantillon, sera également intéressante dans la suite de ce chapitre. Le champ de fuite qui en résulte peut influencer l'onde de référence.

1. Condensateurs mis à la terre avec une densité de charge uniforme dans l'isolant/diélectrique

La physique d'un nanocondensateur mis à la terre est déjà riche à bien des égards. Deux aspects principaux doivent être distingués : l'interaction entre le faisceau d'électrons et l'échantillon, qui crée des charges positives dans l'isolant (Cazaux, 1995), et l'existence du potentiel intérieur moyen (PIM), spécifique à chaque matériau (Beleggia et al., 2016). De plus, du point de vue du protocole expérimental, l'observation du condensateur mis à la terre est la première étape pour comprendre l'effet de la polarisation, pour de nombreuses raisons qui seront développées tout au long de ce manuscrit.
Les modèles sont composés de deux électrodes séparées par une couche diélectrique. Le déphasage produit est une courbe comme indiqué Figure 3.1(b) et le déphasage résultant de l'effet du MIP et des charges statiques est illustré Figure 3.1(c).

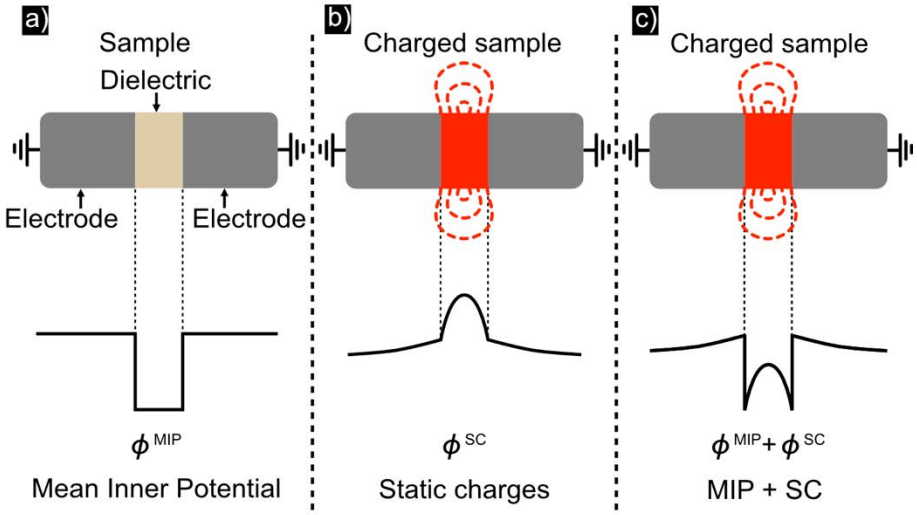

Figure 3.1 : Chaque modèle représente un type d'interaction spécifique et les données recueillies par les électrons qui le traversent. Le premier modèle inclut l'effet MIP a), tandis que le second modèle ne représente que le potentiel chargé b), et le dernier modèle est une combinaison des deux premiers modèles qui se rapproche le plus de la réalité expérimentale c). (Static charges : charge statique ; Charged sample : échantillon chargé)

Les autres contributions aux images de phase seront étudiées dans les sections suivantes à l'aide de plusieurs modèles dont les paramètres varient.

1.I. Étude de l'image de phase produite par une densité de charge

En raison de l'interaction entre le faisceau d'électrons et le condensateur, la couche diélectrique peut se charger positivement en raison de l'émission d'électrons secondaires. Même si le diélectrique fait partiellement écran à ces charges, la densité des charges donne lieu à un champ. En effet, en l'absence de couches conductrices à la surface, il y aura un champ de fuite important dans le vide. Par conséquent, pour obtenir le profil de phase, il faut considérer les champs de fuite ainsi que le champ interne produit par la densité de charge.
À l'exception des paramètres spécifiquement modifiés au cours de l'étude, les paramètres seront toujours les mêmes, comme indiqué dans le tableau suivant Figure 3.2.

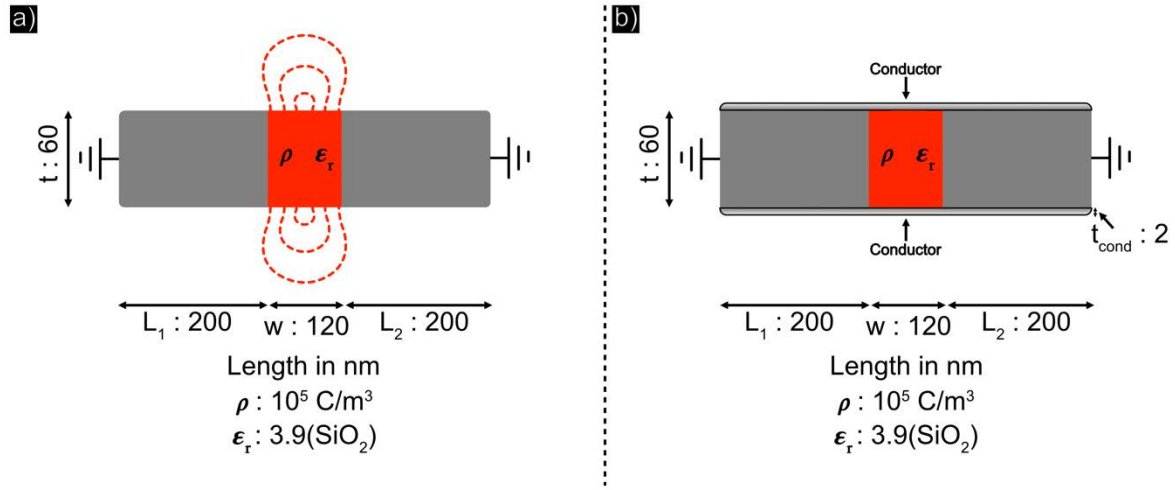

Figure 3.2 : Modèles de base sans surfaces conductrices a) et avec surfaces conductrices b). (Length in : mesure en ; Conductor : conducteur)

Tout au long des études, nous modifierons certains paramètres, parfois plusieurs en même temps, afin de mieux comprendre leur impact sur le profil de phase.
L'effet du MIP étant simplement un décalage constant vers le haut dans notre cas, il ne sera pas étudié ici, alors que la densité chargée étudiée sera comprise entre 10^5 et 3×10^5 C/m^3, correspondant à une fourchette proche des valeurs maximales mesurées expérimentalement (Latychevskaia et al., 2010; Gatel et al., 2013; Beleggia et al., 2016).

1.I.A. Variation de la densité de charge et de la permittivité

La densité de charge et la permittivité ont un effet direct sur l'intensité du champ électrique à l'intérieur et à l'extérieur du condensateur. En effet, leurs effets sont opposés : plus la densité de charges augmente, plus l'intensité du champ augmente, tandis que plus la permittivité du matériau augmente, plus le champ diminue par effet d'écran.
Figure 3.3(a, b) représente les potentiels simulés (Figure 3.2), ainsi que leurs profils de phase respectifs calculés à partir du potentiel déterminé par la méthode des éléments finis et de la projection le long du trajet du faisceau Figure 3.3(c, d) (voir chapitre 2).

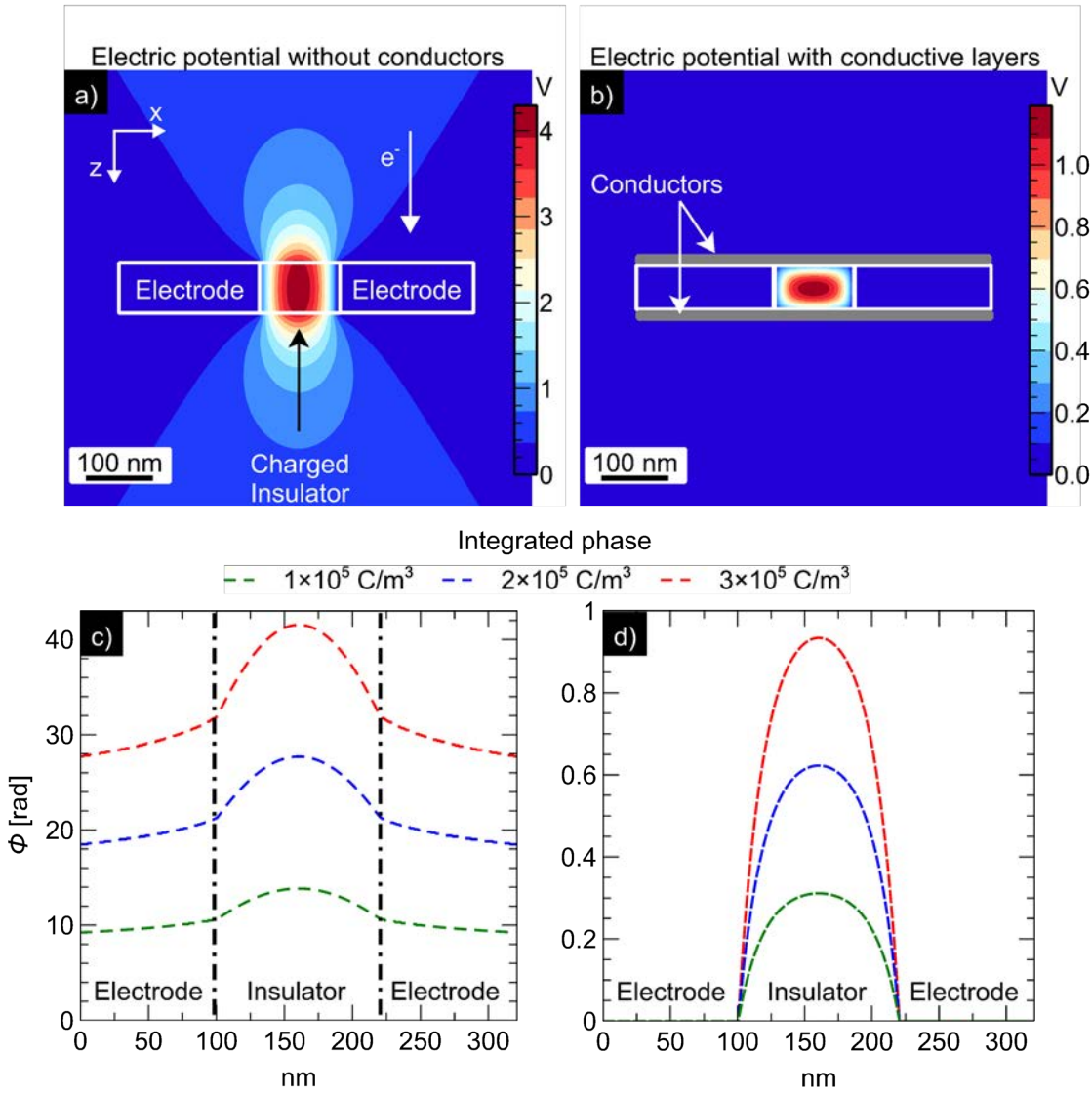

Figure 3.3 : Calcul FEM du potentiel produit par les modèles de la Figure 3.2 pour trois densités de charges différentes a), b) et leur déphasage correspondant c), d). (Insulator : isolant)

Comme prévu, le potentiel calculé sur le condensateur est symétrique et la variation de phase est plus prononcée avec l'augmentation de la densité de charge, comme on peut le voir dans le graphique suivant Figure 3.3 (a, b). Plus intéressant encore, le premier modèle comporte un champ de fuite (Figure 3.3(a)), tandis que le second ne le fait pas (Figure 3.3(b)). Ceci se manifeste par une courbure de la phase dans la région correspondant aux électrodes pour le modèle sans couche conductrice (Figure 3.3(c)); alors que dans le modèle avec une couche conductrice, la phase est uniforme et en fait nulle dans notre cas (Figure 3.3(d)). En effet, la couche conductrice forme une cage de Faraday autour de l'ensemble de l'échantillon qui protège complètement le vide du champ interne.
L'équation de Poisson nous dit qu'une charge positive entraîne une courbure négative du potentiel et qu'en l'absence de charge, le potentiel est uniforme. Étant donné la relation linéaire entre le potentiel électrique et la phase, le profil de phase présente la même propriété.

Comme le profil de phase est affecté à la fois par la densité de charge et par la permittivité diélectrique, je trace une figure 3D de ϕ_{max} versus (ε_r, ρ) pour mieux comprendre ce mécanisme complexe Figure 3.4.

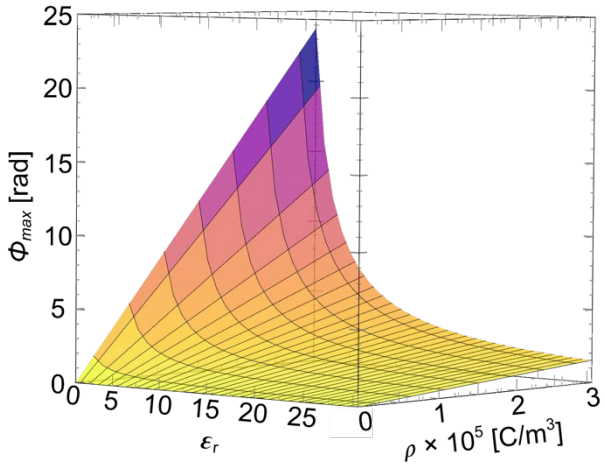

Figure 3.4 : Tracé de $\boldsymbol{\phi_{max}}$ par rapport à ($\boldsymbol{\varepsilon_r}$, $\boldsymbol{\rho}$) pour un modèle de condensateur sans conducteurs.

L'évolution de la ϕ_{max} suit un comportement linéaire en termes de densité chargée pour chaque permittivité tout en étant proche d'une loi inverse en termes de permittivité du milieu.
Pour étudier plus en profondeur les propriétés diélectriques de la charge, la même expérience a été réalisée avec le modèle à couches conductrices ϕ_{max} en fonction des deux paramètres ε_r et ρ est présenté Figure 3.5.

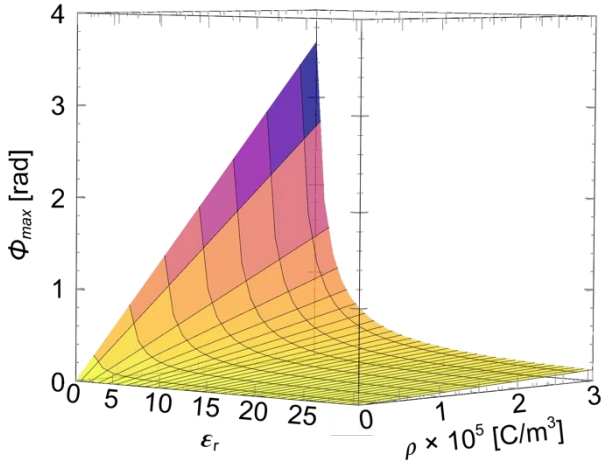

Figure 3.5 : Tracé de $\boldsymbol{\phi_{max}}$ par rapport à ($\boldsymbol{\varepsilon_r}$, $\boldsymbol{\rho}$) pour un condensateur modèle avec des conducteurs.

Ce système est analogue à un diélectrique encastré dans une cage métallique mise à la terre. Étant donné que les conducteurs entourant le condensateur agissent comme une cage de Faraday, il n'y a pas de champ de fuite autour du condensateur.

1.I.A. Évolution de la contribution du champ de fuite en fonction de la géométrie du diélectrique (rapport d'aspect)

Le but de l'étude suivante est de quantifier l'effet du champ de fuite sur le profil de phase en fonction de la géométrie du diélectrique. Pour ce faire, j'étudie la contribution du champ de fuite au champ interne en pourcentage en fonction du rapport entre la longueur du diélectrique et l'épaisseur de l'échantillon *w/t*. Afin d'évaluer la contribution du champ de fuite dans l'image de phase finale, nous calculons séparément la contribution interne (dans le condensateur) et la contribution externe (dans le vide) comme suit Figure 3.6. La contribution interne au potentiel total est ensuite calculée en pourcentage *p* en prenant le maximum de chaque courbe et en le divisant par la contribution totale, puisque l'image de phase totale est la somme des deux projections.

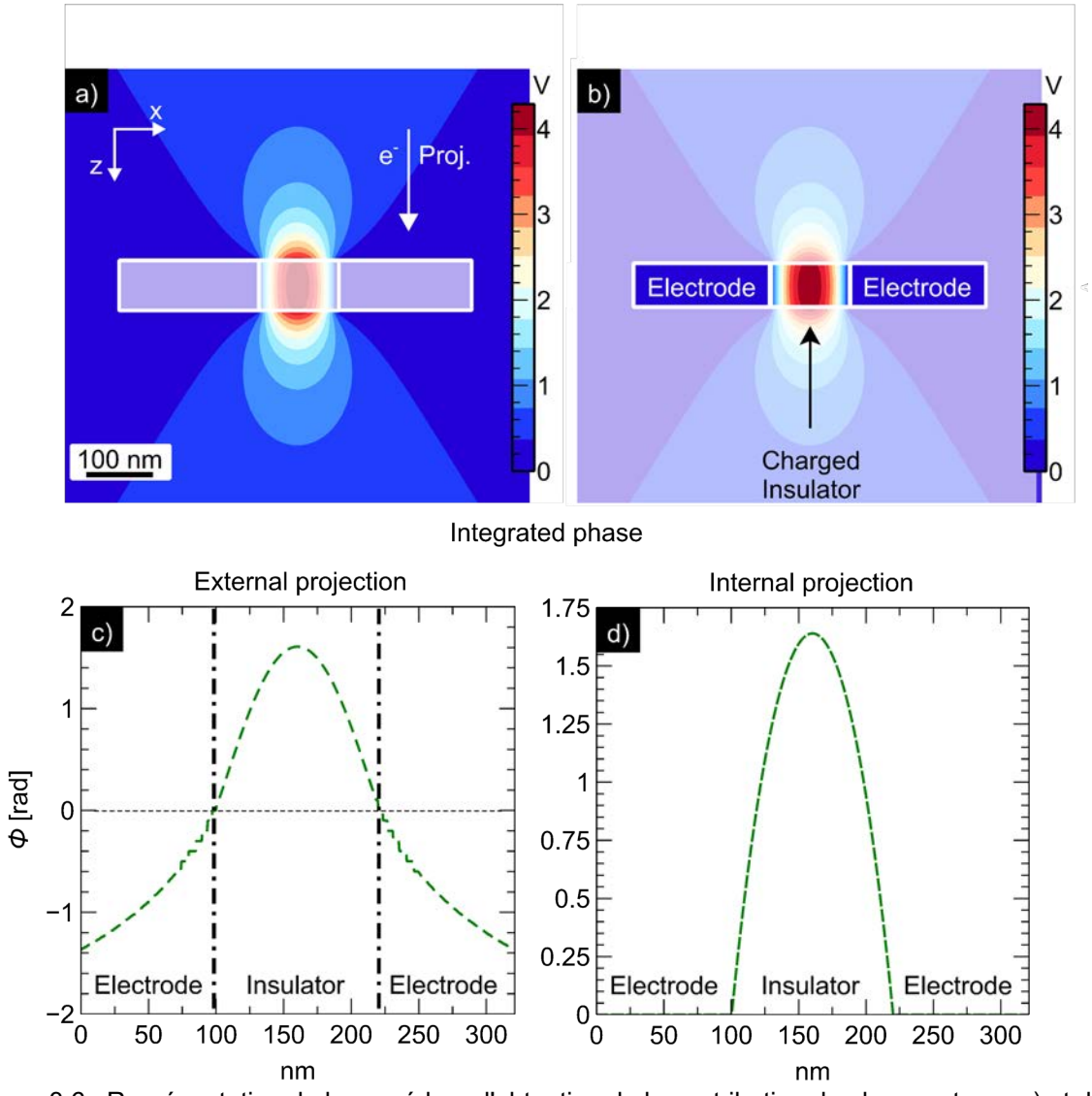

Figure 3.6 : Représentation de la procédure d'obtention de la contribution de phase externe a) et de la contribution de phase interne b) avec le profil de phase externe c) et le profil de phase interne d) juste en dessous. (Charged insulator : isolant chargé)

Il convient de noter que le potentiel interne (Figure 3.6(d)) ressemble au profil de phase d'un condensateur avec des surfaces conductrices, mais l'ampleur est

légèrement plus grande : un conducteur mis à la terre ne fait pas seulement écran au champ de fuite, mais aussi aux charges internes à l'aide de charges libres.
Le modèle a été calculé sans les couches conductrices en surface afin de déterminer la contribution du potentiel interne à la phase totale, désigné par le pourcentage *p*. Ce pourcentage a été calculé pour chaque paire de valeurs *w* et *t* (*w* allant de 2 à 200 nm avec un pas de 10 nm, *t* allant de 20 à 200 nm avec le même pas). Ces plages de valeurs sont définies en termes de taille attendue d'un échantillon expérimental de microscopie électronique. Le résultat de *p* en fonction de *w/t* est indiqué Figure 3.7.

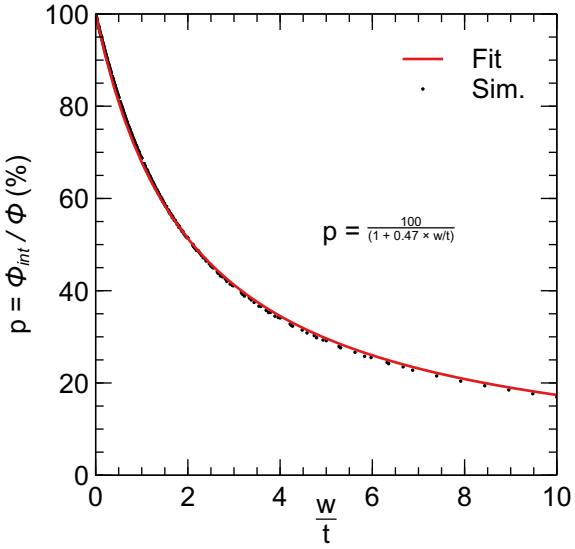

Figure 3.7 : Pourcentage du potentiel interne en fonction du rapport d'aspect w/t.

La distribution des points calculés à partir des simulations met clairement en évidence que le rapport d'aspect *w/t* contrôle la contribution du potentiel interne à la phase totale : *w* et *t* ne sont pas des variables libres, car de multiples combinaisons ne produisent les mêmes résultats. Cette distribution peut être ajustée avec la loi (3.1).

$$p = \frac{100}{(1 + 0.47 \times w/t)} \qquad (3.1)$$

Lorsque *w/t* tend vers 0, le système correspond à un condensateur parfait (à faces infinies) où aucun champ de fuite n'est présent : seule la phase interne contribue à la phase totale avec *p* égal à 100%. Le profil de phase est donc plus facile à interpréter. À l'autre extrême, *p* est fortement réduit lorsque le rapport d'aspect diminue : le profil de phase de ce condensateur aminci présente une forte contribution du champ de fuite.

1. Modèle de condensateur polarisé

1.I. Introduction

Le but de ce travail est d'étudier le potentiel à l'intérieur d'un nanocondensateur lorsqu'une polarisation est appliquée entre ses électrodes. Du point de vue expérimental, deux hologrammes sont enregistrés : avec polarisation et avec les deux électrodes à la masse ("hologramme à 0V"). La soustraction des deux permet

d'éliminer le PIM et les effets de charge dus au faisceau d'électrons, ne laissant subsister que le changement de phase dû à la polarisation.
Pour les études suivantes, les modèles ont été construits de manière identique aux cas précédents, à l'exception du fait que l'électrode de droite est maintenant polarisée (Figure 3.8). Le rapport d'aspect *w/t* a été initialement fixé à 2. Une tension appliquée à une électrode polarise donc le condensateur, ce qui entraîne une dissymétrie de l'image de phase.

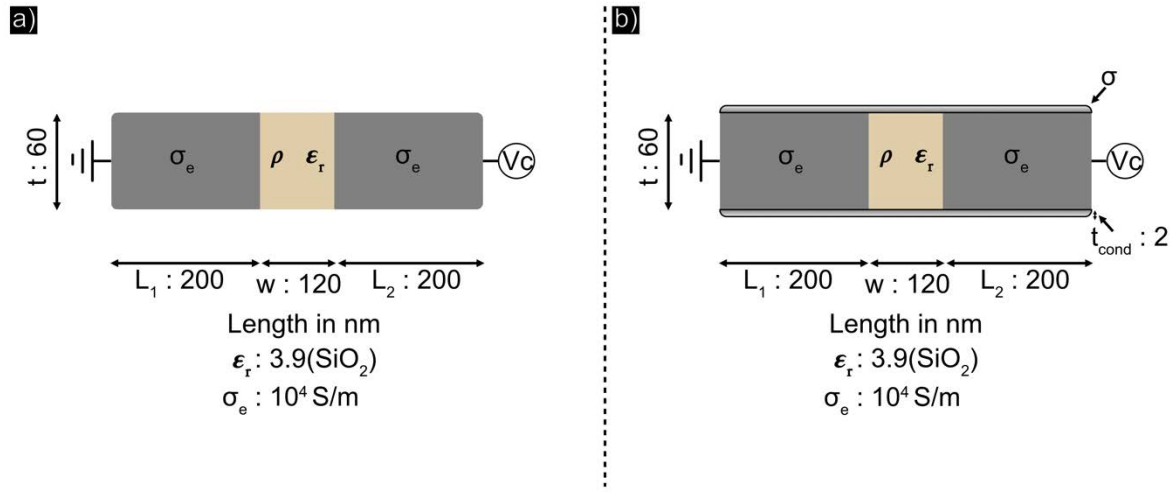

Figure 3.8 : Modèle de base avec ses paramètres de valeur sans conducteurs (a) et avec conducteurs (b)

La conductivité de ces différents éléments, tels que les électrodes et les conducteurs, avait été volontairement omise auparavant parce qu'elle ne jouait pas de rôle et ne faisait qu'ajouter de la complexité. Au contraire, la conductivité des électrodes σ_e et des surfaces conductrices σ est désormais plus importante pour comprendre ce qui se passe dans le modèle de polarisation. Plusieurs paramètres ont été étudiés, notamment la polarisation *Vc*, l'épaisseur de l'échantillon et la présence d'une couche conductrice en surface.

1.II. Étude de l'image de phase

1.II.A. Analyse de la polarisation

En accumulant des charges sur les plaques d'électrodes, un condensateur polarisé stocke de l'énergie. Ces charges et cette énergie augmentent avec la polarisation et la permittivité du diélectrique entre les électrodes.
Figure 3.9 montre une comparaison entre des condensateurs polarisés sans (a) et avec (b) couches conductrices de surface. La polarisation des deux condensateurs modèles à 1V donne lieu à deux distributions de potentiel. La carte des couleurs en escalier représente l'isopotentiel et son intensité locale, qui diminuent à mesure qu'elle s'éloigne des électrodes. Cela met en évidence la relation entre le champ de fuite et la courbure à l'intérieur des électrodes.

Un autre point à considérer est que la symétrie des modèles implique une symétrie dans le potentiel, ce qui n'est pas toujours le cas, comme nous le démontrerons expérimentalement dans le chapitre suivant.
Contrairement aux condensateurs à conducteur mis à la terre, nous observons que le

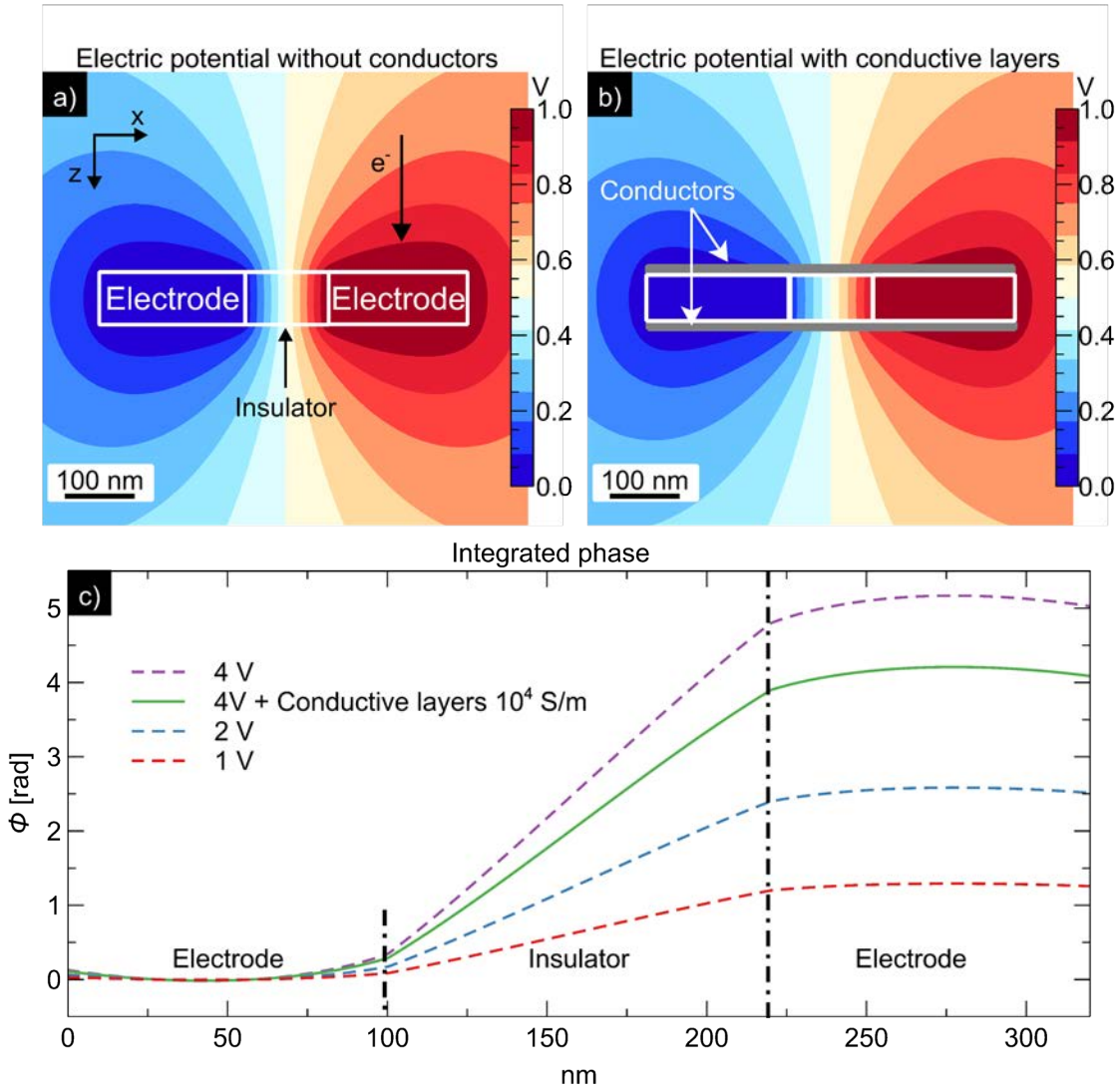

Figure 3.9 : Carte de potentiel d'un condensateur polarisé a) sans et b) avec des couches conductrices à la surface lors de l'application d'une polarisation de 1V. La conductivité de ces couches est de $10^4\ S/m$. c) Profils de phase calculés à partir de a) et b) pour différentes polarisations appliquées. (conductors : conducteurs ; Conductive layers : couches conductrices ; Insulator : isolant)

champ de fuite est généré pour chaque cas et contribue au profil de phase (Figure 3.9(c)). car le champ de fuite est imposé par les conducteurs. Contrairement aux condensateurs mis à la terre dont les conducteurs agissent comme une cage de Faraday, les condensateurs polarisés ont une différence de potentiel imposée entre les deux électrodes.
L'effet principal des surfaces conductrices est de réduire la polarisation locale dans le diélectrique, ce qui est visible sur la carte de potentiel par un léger décalage de l'isopotentiel. Cet effet apparaît plus clairement sur le profil de phase avec une diminution du déphasage total Figure 3.9(c).

Dans les deux cas, cependant, le déphasage reste linéaire par rapport au potentiel appliqué, comme le montre le graphique suivant Figure 3.10 en traçant et en mesurant le déphasage à l'intérieur de la zone diélectrique en fonction de différentes polarisations.

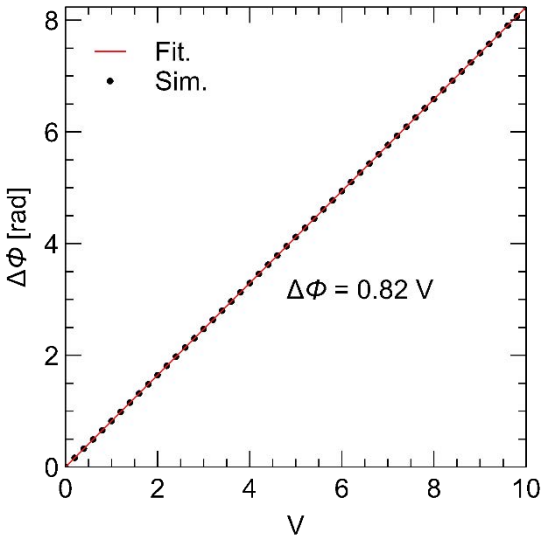

Figure 3.10 : Déphasage dans le diélectrique $\Delta\phi$ versus the applied bias for the model capacitor.

Le déphasage $\Delta\phi$ augmente linéairement avec la polarisation appliquée dans le cas du modèle sans couches conductrices avec une pente d'environ 0,8 liée à la géométrie utilisée ici (rapport d'aspect de 2), comme nous le verrons dans la section suivante.

2. Condensateurs polarisés avec densité de charge aux interfaces

2.I. Introduction

Jusqu'à présent, nous avons étudié le condensateur parfait avec des charges uniquement sur les interfaces, et nous avons découvert (voir chapitre 4) que des charges peuvent être injectées à l'intérieur du milieu diélectrique. Comme nous travaillons avec du silicium, le type de charge que nous injectons peut être des électrons et des trous, ce qui signifie que différentes zones de charge peuvent se former à l'interface en profondeur du diélectrique, c'est-à-dire dans le volume. Je n'entrerai pas dans le détail de ce sujet, car nous verrons cet aspect sur un échantillon expérimental dans le chapitre suivant.
Cela a nécessité la création de deux zones de charge de signe opposé à l'intérieur du diélectrique. Et elles sont prévues aux interfaces entre l'isolant et les électrodes (Figure 3.11).

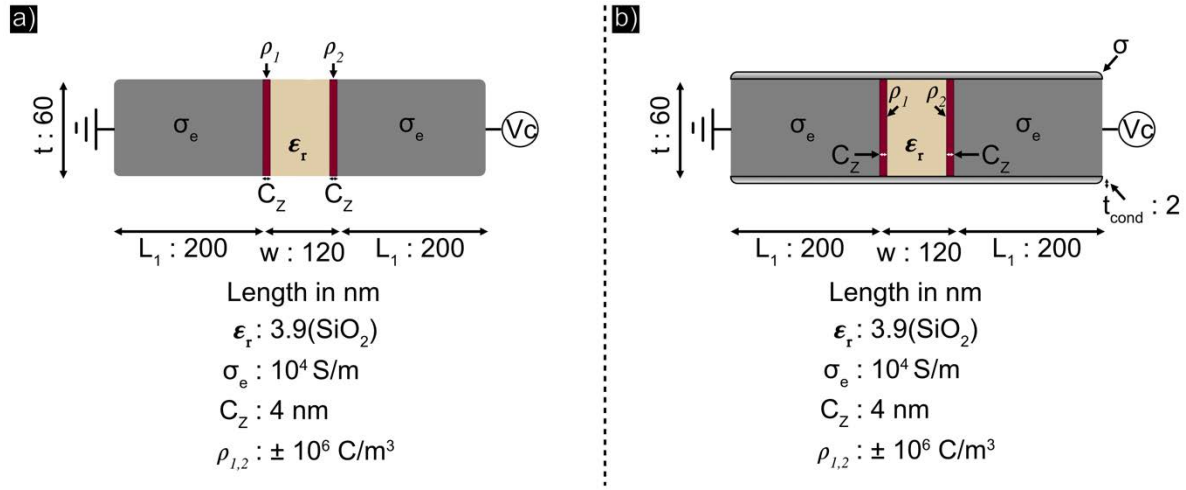

Figure 3.11 : Condensateurs polarisés avec une densité de charges dans le diélectrique à ces interfaces d'électrodes sans a) et avec des couches conductrices b).

Pour simuler la charge de l'espace, nous avons composé la densité de charge uniforme sur la gauche ρ_1 et droite ρ_2 de l'isolant de longueur C_Z. Afin d'être exhaustifs, nous envisagerons également le chargement d'un seul côté et d'autres configurations.

2.II. Étude des profils de phase produits par la densité de charge spatiale

2.II.A. Effet de la couche conductrice

Les profils de phase seront similaires à ceux d'un condensateur polarisé, mais avec de nombreux changements causés par la charge d'espace aux interfaces. Nous commençons par comparer le modèle sans et avec conducteurs (Figure 3.12).

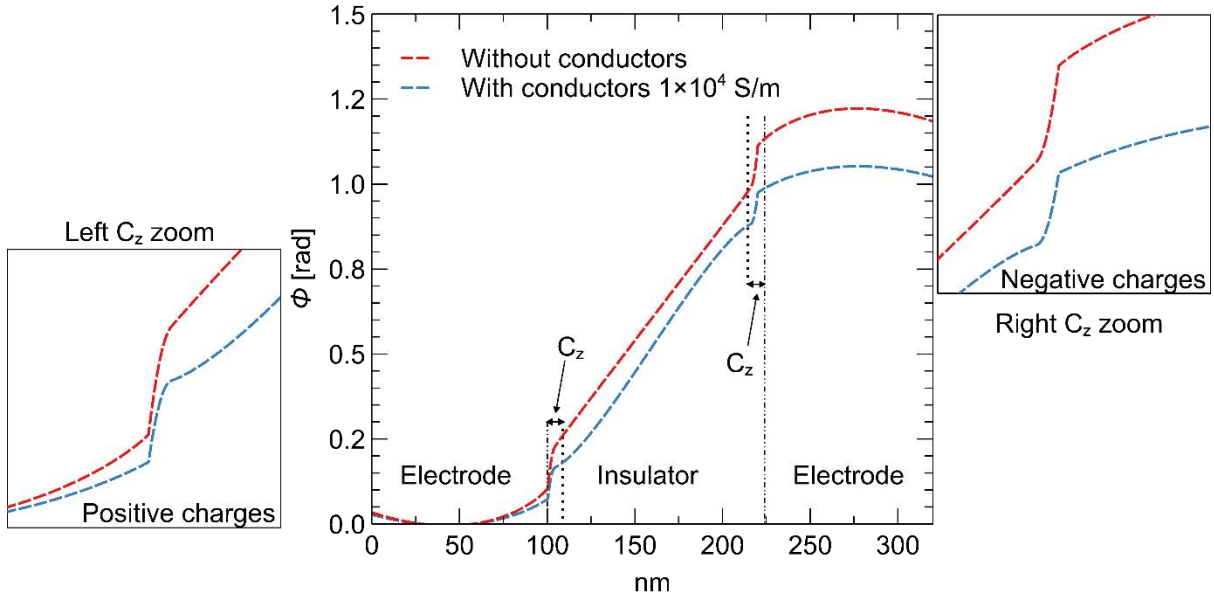

Figure 3.12 : Effet de charge de deux zones chargées opposées à l'intérieur du diélectrique près des interfaces des électrodes. (Without conductors : sans conducteurs ; With conductors : avec conducteurs ; Positive charges : charges positives ; Negative charges : charges négatives ; Left : gauche ; Right : droite)

L'ajout de zones chargées de signe opposé de part et d'autre du diélectrique crée une courbure négative et positive dans l'image de phase.
Pour le modèle avec couches conductrices, on observe une réduction du déphasage total et du déphasage qui se produit dans les zones chargées. Et comme les couches conductrices imposent le champ de fuite, nous pouvons observer une légère courbure entre les zones chargées par rapport au modèle sans conducteur.

3. Conclusion

Tout d'abord, nous nous sommes assurés que les paramètres non physiques n'influençaient pas la solution au cours de notre analyse MEF. Pour ce faire, j'ai réalisé plusieurs études sur la taille de la boîte de simulation et la taille du maillage afin de m'assurer que ces paramètres n'avaient pas d'effet sur la solution. Nous réduisons également le temps de calcul en utilisant différents types et tailles de maillage sur différentes parties du modèle. En outre, une "zone infinie" a été ajoutée tout autour de la boîte de simulation, ce qui permet une plus grande flexibilité en ce qui concerne la taille de la boîte. Cela nous permet de modifier le modèle sans avoir à recommencer l'étude de la taille de la boîte pour chaque géométrie qui diffère de l'originale.
En raison de la charge diélectrique provoquée par le faisceau d'électrons, l'analyse de phase peut être effectuée en particulier lorsque l'échantillon est connecté à la masse (0V). Si l'on considère un échantillon TEM, le champ de fuite produit par la charge représente environ 40 à 60 % de la phase totale mesurée, le reste étant dû au potentiel interne. Cette observation contribue au fait que nous ne pouvons pas extraire de données quantitatives des données expérimentales sans une simulation de champ de fuite.

La présence d'une couche conductrice autour du condensateur affecte considérablement le déphasage. Étant donné qu'une couche conductrice autour de l'échantillon agit comme une cage de Faraday, éliminant le champ de fuite à l'extérieur de l'échantillon, le déphasage mesuré est uniquement dû à une combinaison des charges stockées dans le diélectrique et de la permittivité du milieu.
L'étude du condensateur mis à la terre permet d'étudier les défauts et les perturbations extrinsèques produites par l'instrument, tout en ouvrant la voie à l'étude du condensateur polarisé.
Tout d'abord, la polarisation provoque un déphasage à l'intérieur de l'isolant qui est proportionnel à la polarisation.
Les champs de fuite ainsi générés créent une courbe de déphasage à l'intérieur de la zone des électrodes, et sa contribution à la phase totale est du même ordre que celle du condensateur mit à la terre. Cependant, contrairement au condensateur mis à la terre, il existe un champ de fuite en présence d'une couche conductrice, car il est imposé par celle-ci. De plus, les couches conductrices produisent une chute de potentiel, ce qui réduit la polarisation locale et peut être modélisé à l'aide d'un circuit de résistance qui reproduit le phénomène d'asymptote parfaite.
J'introduis ensuite une densité chargée à l'intérieur du modèle polarisé, qui agit comme une perturbation du déphasage. Ces résultats démontrent que non seulement une courbure de déphasage est induite dans chaque région de charge qui est conforme à la loi de Poisson, mais aussi qu'elle peut réduire la polarisation locale et diminuer la capacité.
Nous avons vu que l'onde de référence pour l'hologramme peut être perturbée par le champ de fuite autour de l'échantillon polarisé. J'ai montré que cette perturbation est faible par rapport au déphasage causé par la polarisation et qu'elle peut être ignorée dans notre cas.

Pour aller plus loin, la recherche théorique sur les condensateurs ferroélectriques, qui ont le potentiel de concurrencer la technologie SiO_2, sera très intéressante. Bien que je n'aie créé que des condensateurs modèles pour extraire le comportement général du système, je suis conscient qu'il existe de nombreuses géométries dans les dispositifs microélectroniques qui peuvent être étudiées, ce que je commencerai à démontrer dans les chapitres suivants.

Chapter 4 — Modélisation des données expérimentales

Les condensateurs métal-oxyde-semiconducteur (MOS) sont l'un des composants électriques fondamentaux utilisés dans les circuits intégrés. Bien que de nombreux efforts soient actuellement déployés pour intégrer de nouveaux matériaux diélectriques ou ferroélectriques, les condensateurs au dioxyde de silicium sur silicium restent les plus répandus. Il est donc surprenant que le champ électrique à l'intérieur d'un tel condensateur n'ait jamais été mesuré ou cartographié à l'échelle nanométrique.
Avant d'étudier des dispositifs microélectroniques réels à l'échelle nanométrique à l'aide de l'holographie électronique *operando*, nous avons donc choisi de commencer par étudier des modèles de condensateurs au dioxyde de silicium avec des matériaux connus et contrôlés. Cela nous permet de tester notre méthodologie combinant l'holographie électronique et la modélisation par la méthode des éléments finis (FEM) et de comparer les résultats expérimentaux aux simulations qui prennent en compte la géométrie exacte de l'échantillon, les dommages éventuels causés par le FIB, les champs de fuite et les effets de charge. Une fois qu'une bonne adéquation aux données expérimentales a été établie, les paramètres physiques seront extraits du modèle concernant le condensateur observé. Ce chapitre présente les résultats obtenus sur des modèles de nanocondensateurs au dioxyde de silicium, y compris des condensateurs à base de nitrure de silicium, et révèle certains phénomènes physiques inattendus (Gatel et al., 2022). L'analyse des erreurs de cette méthode sera détaillée dans un prochain chapitre.

1. Préparation de l'échantillon et expérience TEM

Plusieurs condensateurs fabriqués avec différents diélectriques, oxyde et nitrure, ainsi que différents empilements ont été spécialement conçus pour les expériences *operando* basées sur des films minces et représentés schématiquement Figure 4.1. Ils sont tous composés d'une fine couche diélectrique prise en sandwich entre une électrode métallique supérieure et une électrode inférieure de substrat semi-conducteur. Les substrats en silicium étaient tous fortement dopés, soit N^{++} or P^{++} (N, P $>10^{18}$ atoms/cm^3), pour servir d'électrode inférieure quasi métallique. Pour assurer la cohérence entre les différentes expériences, c'est cette électrode qui sera toujours maintenue à la masse. La couche diélectrique au-dessus de l'électrode inférieure sera soit du dioxyde de silicium (SiO_2), déposé sur le substrat par oxydation thermique à sec ou par voie humide, avec une permittivité relative de $\varepsilon_r = 3.9$, ou nitrure de silicium (Si_3N_4 ; $\varepsilon_r = 7.5$). L'électrode supérieure sera en titane ($\sigma = 2.6 \times 10^6\ S/m$) ou parfois du silicium fortement dopé ($\sigma = 2 \times 10^4\ S/m$).

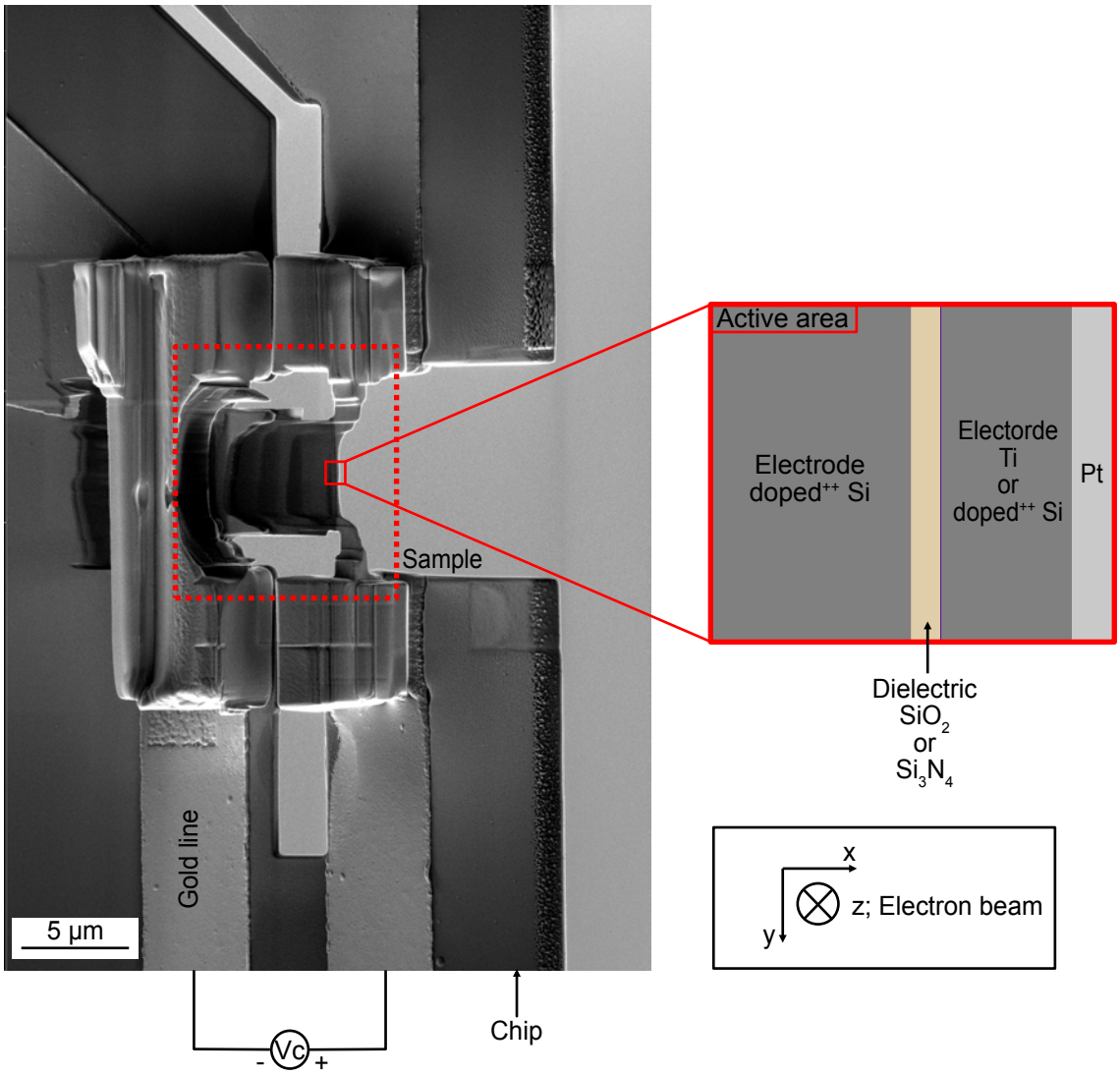

Figure 4.1 : Image MEB d'un exemple de préparation d'un condensateur modèle. Les pistes d'or sur la puce fournissent le potentiel de polarisation de l'échantillon. (Gold line : ligne d'or ; Electron beam : faisceaux d'électrons ; active area : zone active)

Une installation dédiée a été développée en interne à l'aide d'un boîtier de commutation adaptée, de câbles, d'un sourcemètre (Keithley 2635b) et d'un logiciel pour réaliser des connexions de polarisation et des expériences en toute sécurité tout en évitant toute décharge électrostatique (ESD) susceptible de détruire les nanocondensateurs.

2. Nanocondensateur mis à la terre

Lorsque l'échantillon est exposé à un faisceau d'électrons, les matériaux réagissent en émettant des électrons secondaires (ES) et des électrons Auger (EA). Les électrons émis laissent une charge positive dans l'échantillon.
Pour étudier ce phénomène, ainsi que d'autres qui ne sont pas liés à la polarisation, nous avons étudié notre premier modèle de condensateur : un condensateur à couche mince Si-SiO_2-Si mis à la terre.

Figure 4.2 montre les résultats de l'expérience d'holographie électronique près du bord de l'échantillon. En particulier, nous analysons un profil de l'image de phase prise perpendiculairement aux interfaces, le long de la direction de croissance (axe x) représentée par la flèche noire.

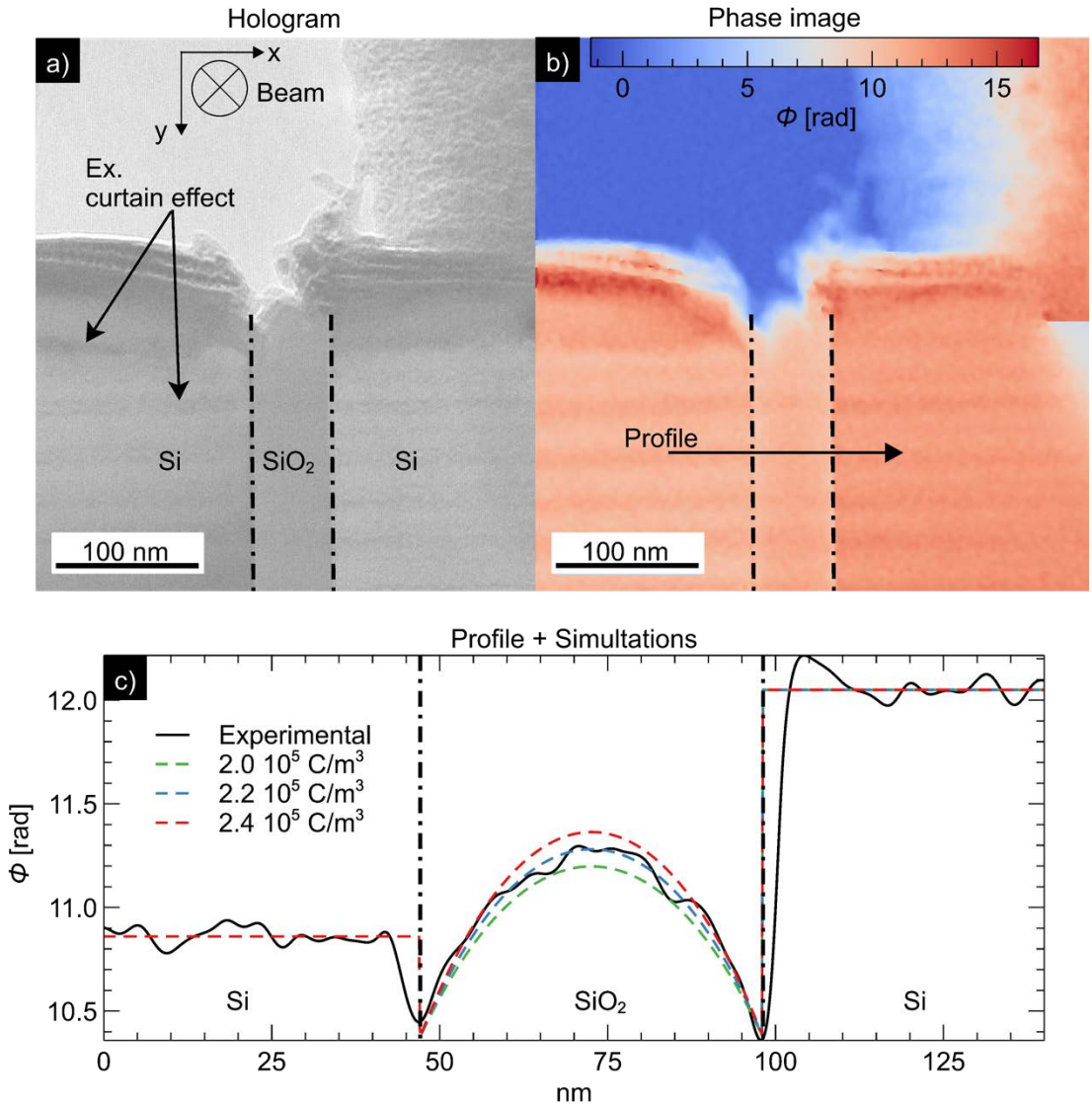

Figure 4.2 : Couche isolante de SiO_2 entourée de deux électrodes de Si. L'hologramme correspondant a) de l'échantillon mis à la terre, qui contient des informations sur l'amplitude et la phase, permet d'extraire une image de phase b), qui sera analysée plus loin à l'aide du modèle simulé c). Nous concluons que le condensateur est entouré de conducteurs et que la densité de charge est de $(2.2 \pm 0.08) \times 10^5 C/m^3$ qui correspond très bien aux données expérimentales. (curtain effect : effet de rideau)

Les différentes couches sont directement visibles dans l'hologramme ainsi que l'effet de rideau dû au processus de préparation par FIB. L'effet de rideau correspond à de légères variations d'épaisseur ayant la forme d'une vague (lignes horizontales dans l'hologramme Figure 4.2 a et b). L'image de phase montre les effets du MIP et de la charge dans le diélectrique résultant de l'interaction avec le faisceau d'électrons.
Il est important de noter que sur la Figure 4.2(c) que la valeur du déphasage est constante dans les électrodes. Les études théoriques du chapitre précédent (3) ont

démontré que la phase devrait être courbée dans les électrodes, en raison du champ de fuite, à moins qu'il n'y ait des couches conductrices à la surface de l'échantillon. Le profil de phase résultant de la simulation FEM présente un très bon accord avec le profil expérimental (Figure 4.2(c)). Des données quantitatives peuvent ensuite être extraites du modèle et utilisées pour estimer la densité de charge d'environ $2.2 \pm (0.08) \times 10^5\ C/m^3$.

3. Condensateur polarisé

Pour la polarisation, nous avons étudié des nanocondensateurs modèles constitués d'une seule couche de diélectrique, Si_3N_4 ou SiO_2, et d'une combinaison des deux. Ces deux matériaux isolants, avec des constantes diélectriques différentes (ε_r = 8 pour Si_3N_4 et (ε_r = 3.9 for SiO_2), sont largement utilisés dans l'industrie microélectronique. L'électrode inférieure était en silicium fortement dopé et l'électrode supérieure en titane.

3.I. Condensateur modèle

Ce nanocondensateur présente un substrat de silicium fortement dopé sur lequel a été déposé une couche de Si_3N_4 de 36 nm d'épaisseur suivie d'une électrode supérieure en Ti. Les différentes couches sont directement visibles sur l'image d'amplitude (Figure 4.3(a)) tandis que le déphasage provenant de la polarisation appliquée de -4 V apparaît sur l'image de phase (Figure 4.3(b)).

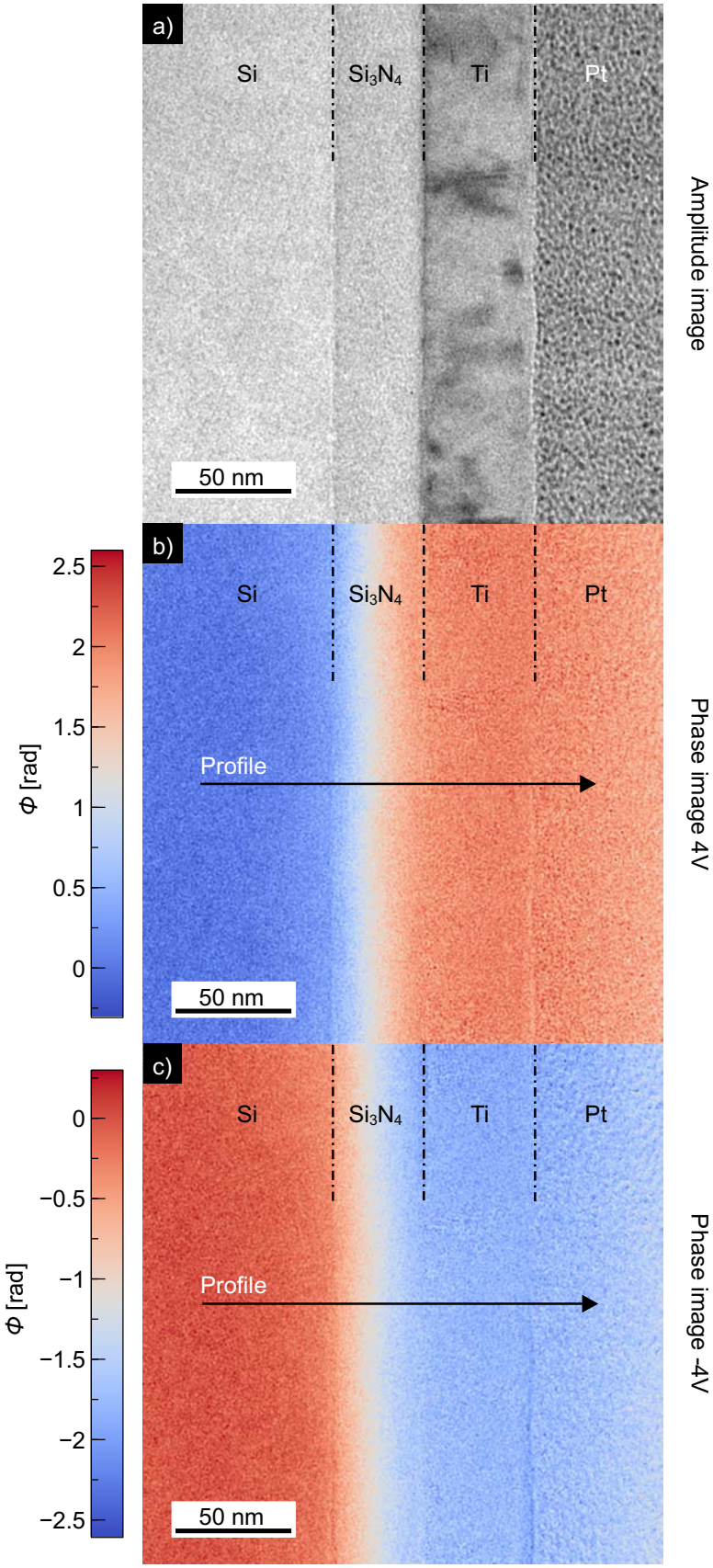

Figure 4.3 : a) Image d'amplitude, image de phase pour une polarisation appliquée de 4V b) et -4V c) après suppression de l'image de phase à 0 V.

Figure 4.3(b, c) montre une chute de phase à l'intérieur du diélectrique Si_3N_4, ce qui signifie que le condensateur est bien connecté et fonctionne. Pour poursuivre l'analyse, nous avons extrait un profil de l'image de phase pour des polarisations d'échantillon de 4V et -4V, comme indiqué Figure 4.4.

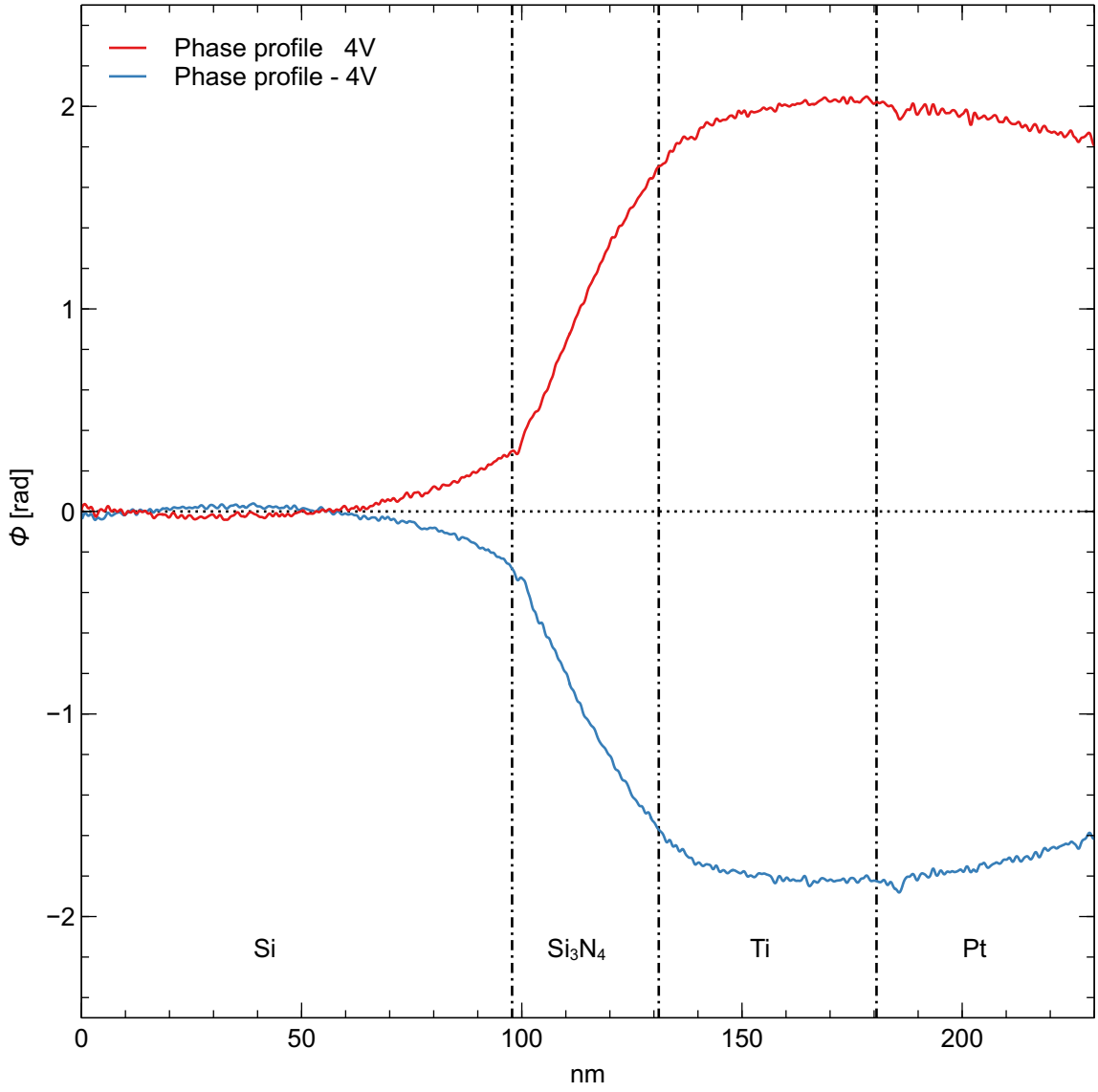

Figure 4.4 : Profil de phase polarisé mesuré à 4V et -4V.

Les profils de phase présentent une courbure notable dans les électrodes (Figure 4.4). D'après le chapitre précédent, nous pouvons attribuer ce phénomène au champ de fuite au-dessus et au-dessous de l'échantillon. Un changement de phase à travers le diélectrique est significatif et change de signe avec la polarisation (comme espéré).
La comparaison des profils de phase simulés et expérimentaux est illustrée. (Figure 4.5(c)).

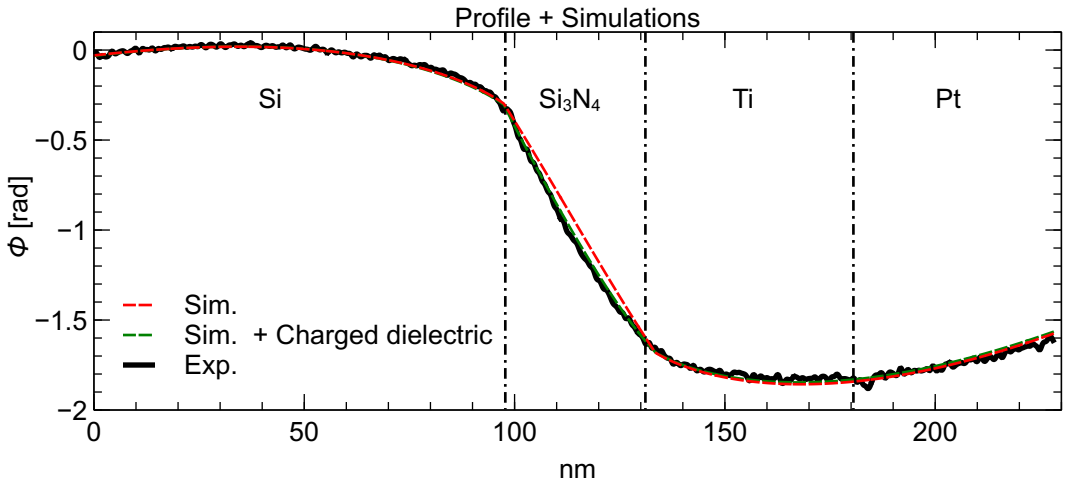

Figure 4.5 : Image de phase pour une polarisation appliquée de -4V après suppression de l'image de phase à 0 V, comparaison entre les profils simulés (ligne rouge en pointillés) et simulés (ligne verte en pointillés).

À l'exception de la zone diélectrique, le profil simulé est en parfait accord avec le profil expérimental. Le léger écart entre les profils simulés et expérimentaux à l'intérieur de la zone diélectrique est intrigant et pourrait être dû à une injection d'électrons et de trous à partir de l'électrode par le modèle d'injection de charge à effet tunnel de Fowler-Nordheim (Li and Chen, 2012). La densité de charges à l'intérieur du diélectrique doit être introduite pour obtenir un ajustement parfait ($2 \times 10^5 C/m^3$), qui est représentée par la ligne verte en pointillés. Cette étude démontre que la polarisation macroscopique appliquée n'atteint pas nécessairement le diélectrique dans son intégralité. En fait, la chute de potentiel à travers le diélectrique est approximativement de (-2.2 ± 0.2) V alors que la polarisation appliquée était d'environ -4 V dans ce cas. Cette chute de potentiel entre la polarisation appliquée et la polarisation locale peut être attribuée aux couches conductrices entourant l'échantillon, et la simulation permet d'estimer la conductivité à environ 660 S/m avec des couches conductrices de 2 nm d'épaisseur, alors que l'épaisseur de l'échantillon est estimée avec la simulation à environ 46 nm. Ce premier résultat suggère qu'un soin extrême doit être apporté au polissage final dans le FIB pour rendre les données de phase plus facilement interprétables.

3.II. Condensateur modèle avec charges

L'exemple suivant est un échantillon fabriqué à partir d'un film mince de dioxyde de silicium de 120 nm d'épaisseur obtenus par croissance thermique sur une plaquette de silicium fortement dopée p et surmontée d'une électrode en titane. L'épaisseur de la lamelle a été mesurée à 55±5 nm par EELS. Après avoir connecté l'électrode supérieure à la puce avec du platine déposé localement et l'avoir insérée dans un support de polarisation TEM dédié, des polarisations positives, négatives ou nulles ont été appliquées *in situ* à l'électrode supérieure. Cet échantillon fait l'objet de l'étude présentée dans le document (Gatel et al., 2022).

3.II.A. Comparaison entre les données expérimentales et la simulation

Des hologrammes ont été prélevés dans la région décrite dans l'encadré ci-dessous Figure 4.6(a) et l'image de phase correspondante pour une polarisation positive de 5 V est montrée en Figure 4.6(b), où l'on peut voir le changement de phase à travers le diélectrique SiO_2. L'échantillon a également été soumis à des tensions allant de -5V à 5 V part pas de 1 V. Le bruit de phase est inférieur à 10 mrad pour une résolution spatiale de 0,8 nm. La phase a été corrigée à l'aide de l'hologramme de l'échantillon mis à la terre, et une région de référence interne au substrat de silicium a été utilisée. Les profils ont été pris dans la même zone de chaque image de phase et la moyenne a été calculée sur 100 nm parallèlement aux interfaces afin d'améliorer le rapport signal/bruit des images de phase. La simulation la mieux adaptée aux données expérimentales à 5 V est présentée Figure 4.6(c).

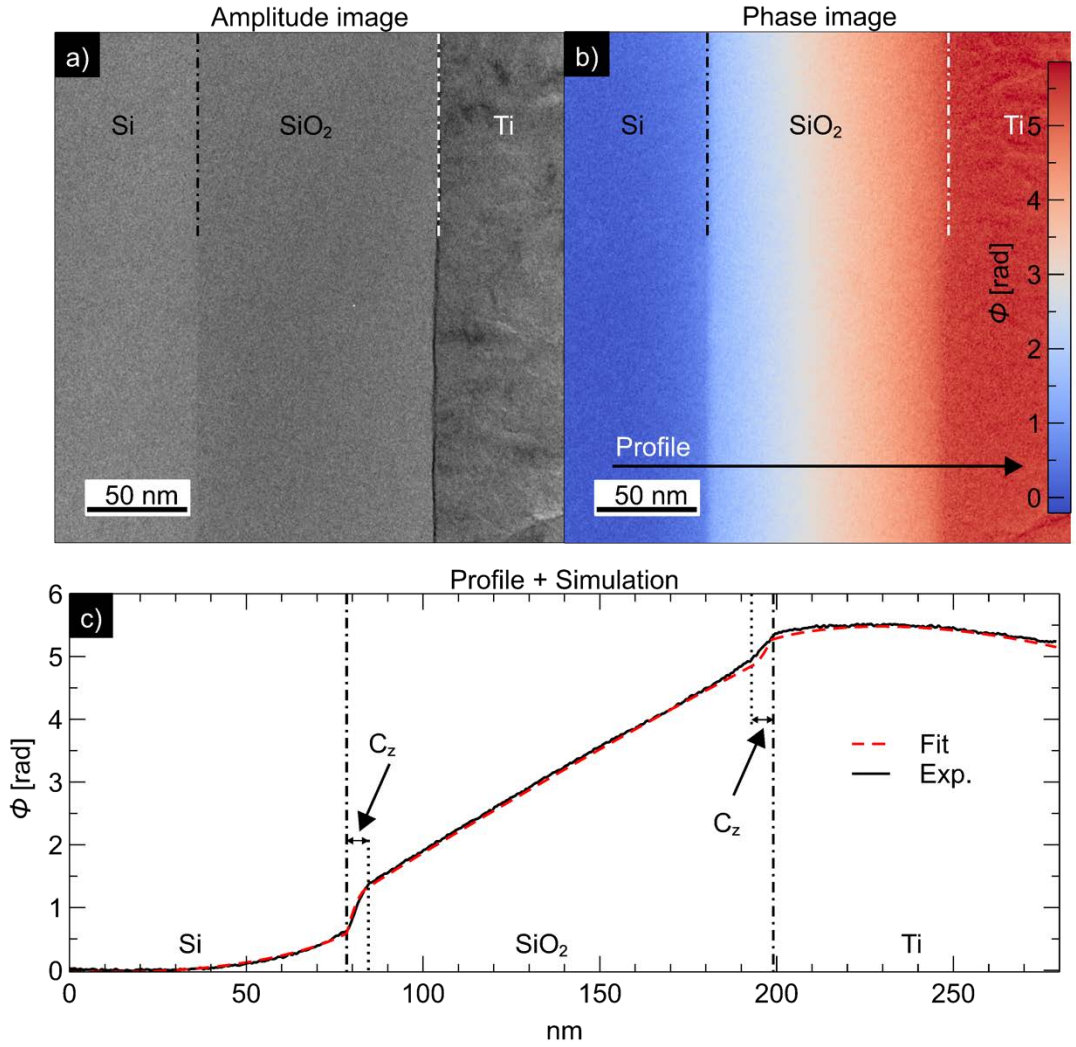

Figure 4.6 : Image d'amplitude a) correspondant à la zone de l'image de phase b) où un profil a été pris et peut être vu sur le tracé c). La polarisation appliquée entre les deux électrodes est égale à 5 V.

Le changement de phase à travers le condensateur est clairement visible et augmente linéairement avec la polarisation appliquée (Figure 4.7), comme prévu (voir chapitre 2 (eq. déphasage). Cependant, la phase n'est pas constante dans les régions

correspondant aux électrodes, alors que nous nous attendrions à ce que les électrodes soient à un potentiel uniforme. Ceci est dû au fait que la phase est également sensible au champ de fuite au-dessus et en dessous de l'échantillon (Aizawa et al., 2017).

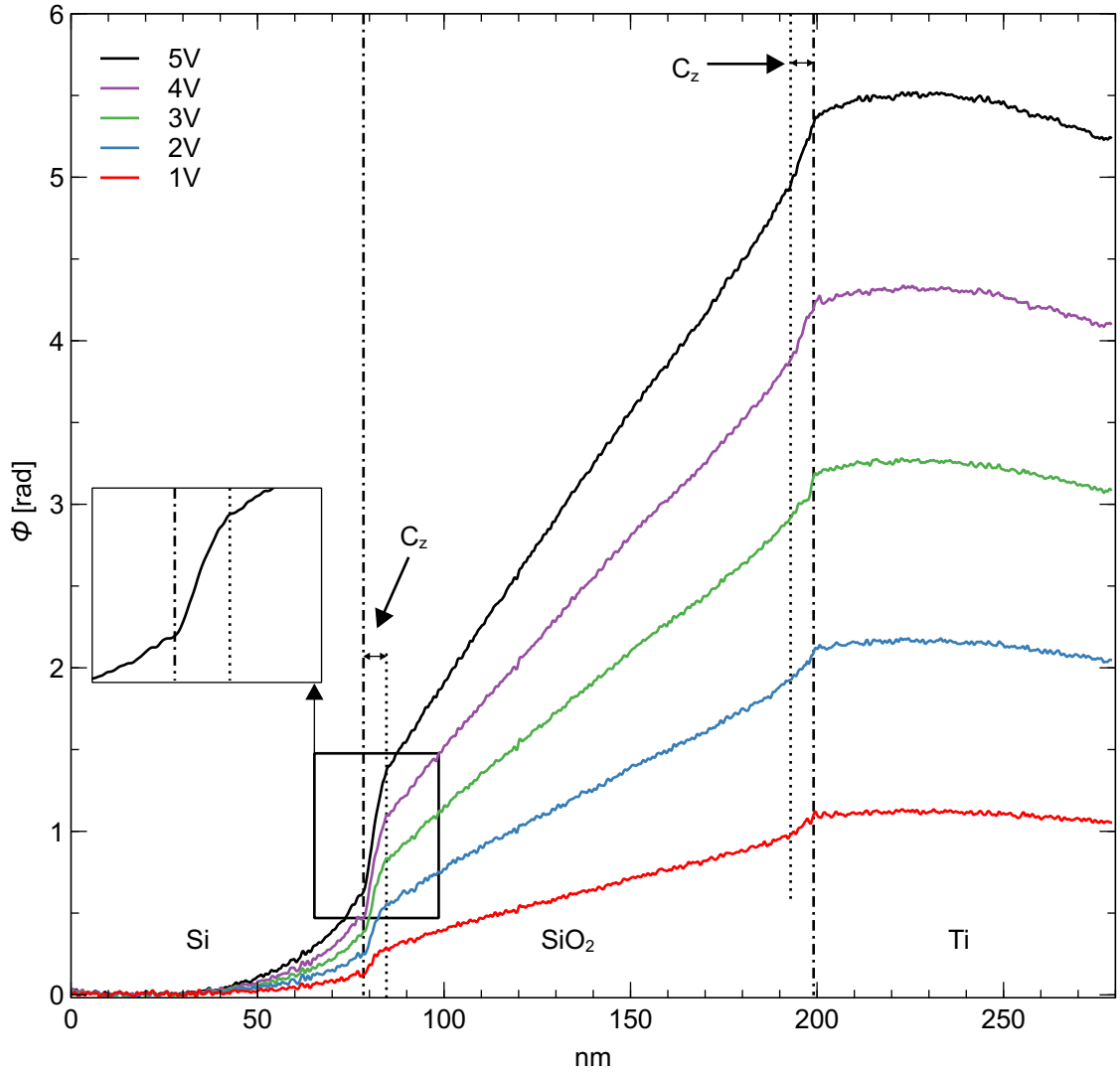

Figure 4.7: Profils de phase en fonction de la polarisation appliquée (1-5 V). Notez la courbure de la phase à l'intérieur des électrodes (Si et Ti fortement dopés) et les sauts de phase aux interfaces électrode-diélectrique s'étendant sur plus de 5 nm à l'intérieur de la couche de SiO_2 (voir l'agrandissement pour une polarisation de 5 V).

L'étape prononcée de la phase qui se produit aux deux interfaces est particulièrement intéressante pour l'analyse et n'était pas présente dans l'exemple précédent. L'élargissement de la phase Figure 4.7(c) montre qu'il existe deux points d'inflexion, l'un au niveau de l'interface et l'autre à une profondeur d'au moins 5 nm dans la couche diélectrique. Cette caractéristique était inattendue et il a fallu beaucoup de conjectures et de modélisation pour en comprendre l'origine.
Contrairement à l'exemple précédent, les simulations montrent que le changement de phase global (5,5 radians) entre les deux électrodes correspond exactement à une tension appliquée de 5 V mesurée sur l'alimentation (en supposant que l'épaisseur mesurée de l'échantillon est correcte). Ceci est très encourageant d'un point de vue

méthodologique et il est donc possible de limiter la couche de dommages de surface pendant le fraisage FIB. Cela indique également que les impédances des connexions sont minimales. En outre, la sensibilité de phase de 10 mrad correspond à seulement 9 mV de polarisation appliquée. Nous ne voyons aucune trace d'une couche de déplétion en silicium, ce qui peut s'expliquer par le niveau élevé de dopage. La seule façon de modéliser avec succès le déphasage à l'interface était d'inclure une couche de charge à l'intérieur de la couche diélectrique, comme les doubles couches de charge observées dans les batteries à l'état solide (Aizawa et al., 2017).
J'ai modélisé cela comme une couche de charge volumique uniforme sur 5,5 nm pour les deux interfaces. En utilisant ce modèle, et en changeant uniquement la densité de charge volumique, j'ai pu reproduire de manière satisfaisante les profils expérimentaux pour l'ensemble de l'expérience de polarisation.

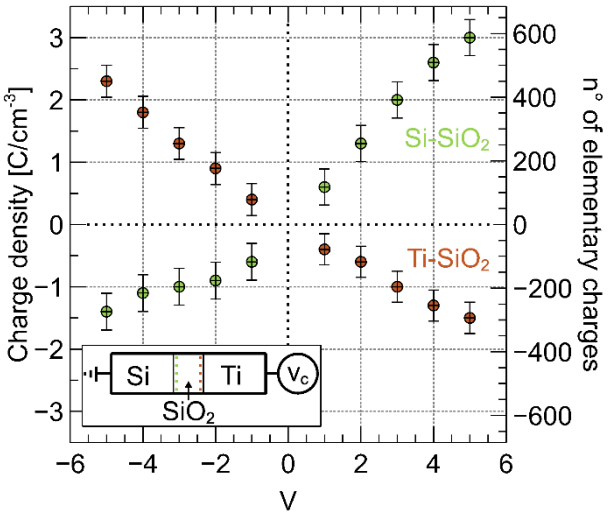

DC Bias (V_c)	ρ_1 (C/cm^3)	ρ_2 (C/cm^3)
-5	$-1.4 \pm 21,1\%$	$2.3 \pm 11,9\%$
-4	$-1.1 \pm 26,9\%$	$1.8 \pm 15,2\%$
-3	$-1.0 \pm 29,5\%$	$1.3 \pm 21,0\%$
-2	$-0.9 \pm 32,8\%$	$0.9 \pm 30,3\%$
-1	$-0.6 \pm 49,2\%$	$0.4 \pm 68,2\%$
1	$0.6 \pm 48,8\%$	$-0.4 \pm 66,7\%$
2	$1.3 \pm 22,3\%$	$-0.6 \pm 44,4\%$
3	$2.0 \pm 14,5\%$	$-1.0 \pm 26,7\%$
4	$2.6 \pm 11,1\%$	$-1.3 \pm 20,5\%$
5	$3.0 \pm 09,7\%$	$-1.5 \pm 17,8\%$

Figure 4.8 : Charge diélectrique aux interfaces Si-SiO_2 (ρ_1) et SiO_2-Ti (ρ_2) en fonction de la polarisation appliquée. Les charges par unité de volume sont représentées sur l'axe gauche. Le nombre de charges élémentaires contenues dans la région analysée du dispositif expérimental est représenté par les axes de droite. Le tableau des données est présenté avec l'incertitude sur la droite.

Chaque profil de phase expérimentale a été simulé de la même manière que le profil présenté dans le document Figure 4.6(c). Par conséquent, nous avons enregistré chaque densité de charge qui s'est accumulée sur chaque interface et l'avons tracée en fonction de la polarisation (Figure 4.8). Les densités de charge volumique nécessaires pour s'adapter aux données expérimentales sont affichées dans le tableau suivant Figure 4.8, y compris les résultats de polarisation négative. Pour souligner la sensibilité des mesures, nous avons également indiqué (échelle de droite) le nombre de charges élémentaires dans la zone analysée.
Lorsqu'une polarisation négative est appliquée à l'électrode de Ti, la densité de charge sur l'interface SiO_2/Ti est positive et lorsque le signe de la polarisation change pour devenir positif, la densité de charge est négative. À l'interface Si/SiO_2, cette tendance est inversée. Je tiens à souligner que ce n'est pas le seul échantillon que nous avons mesuré présentant des couches de densité de charge. L'expérience a été répétée sur des échantillons avec des substrats dopés p et n, ainsi qu'avec différents processus

de fabrication (humide et sec) et des échantillons d'épaisseurs multiples, où la charge s'est toujours produite avec des zones de charge régulières d'une largeur allant jusqu'à 8 nm.

3.III. Condensateur bicouche SiO_2-Si_3N_4

Les composants électroniques étant de plus en plus petits, il est possible d'utiliser des empilements diélectriques de différents matériaux pour limiter les courants de fuite. Nous avons étudié ici la distribution du potentiel électrique dans un modèle de condensateur bicouche composé de SiO_2 ($\varepsilon_r = 3.9$) et de Si_3N_4 de 40 nm de longueur ($\varepsilon_r = 7.2$) en série, tous deux déposé sur un substrat de Si fortement dopé p et surmontés d'une électrode de Ti. La feuille TEM après préparation par FIB avait une épaisseur de 70 nm.
L'échantillon a été polarisé *in situ* de -10 à 10 V part pas de 1 V. J'ai néanmoins décidé de concentrer mon analyse et ma discussion sur l'image de phase de polarisation de 10 V, car ces conditions présentent le meilleur rapport signal/bruit. L'image d'amplitude montrant la géométrie de l'échantillon avec l'image de phase ainsi que le profil expérimental et la simulation correspondante sont représentés (Figure 4.9).

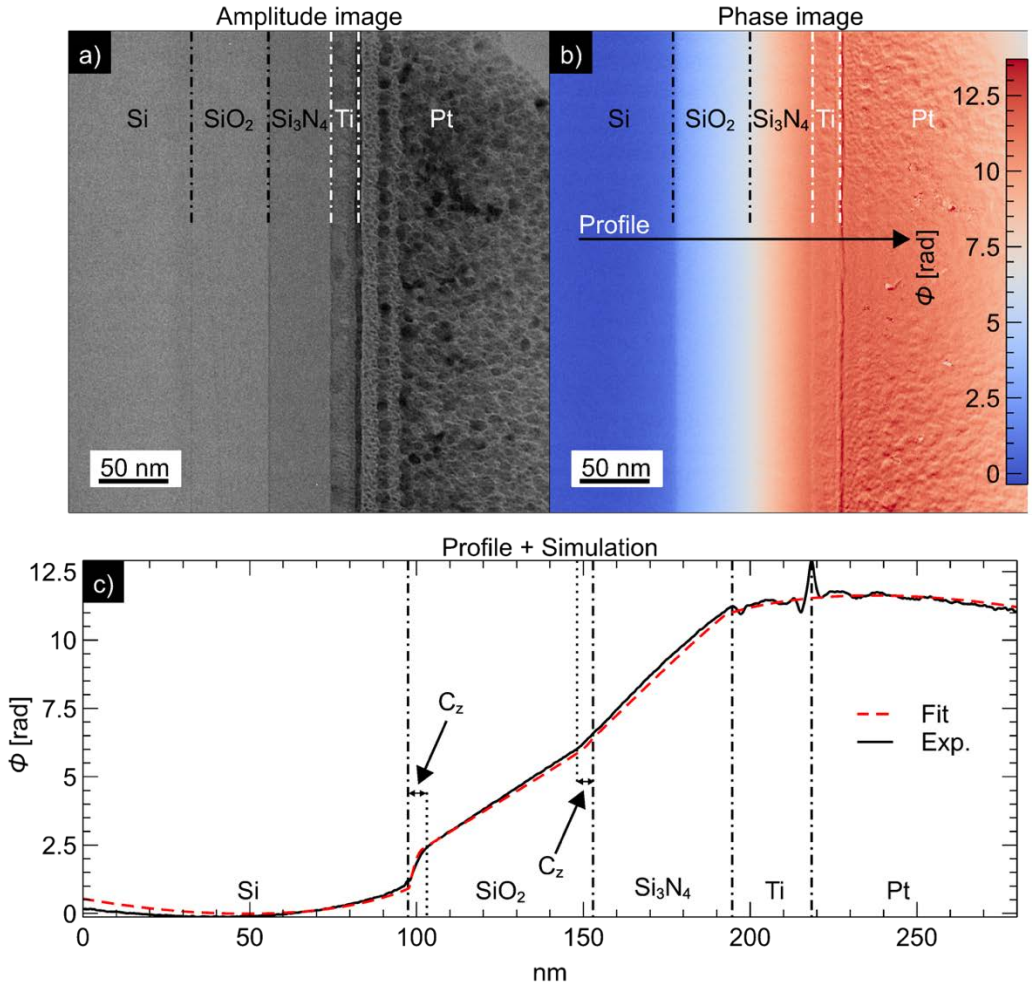

Figure 4.9 : L'image d'amplitude représente la structure de l'échantillon Si-SiO_2-Si_3N_4-Ti a), tandis que le profil de phase dans la même zone représente la phase acquise par les électrons traversant la polarisation du condensateur sous 10 V b). Un profil sur l'image de phase permet ensuite une analyse plus approfondie de la phase c).

Nous pouvons clairement voir un point d'inflexion de la phase à l'interface entre les deux diélectriques. Ce phénomène est attendu, car la condition d'interface indique qu'il doit y avoir une discontinuité dans le champ électrique entre deux diélectriques, même en l'absence de charges libres à l'interface (4.1).

$$\hat{n} \cdot \left[\overrightarrow{D_2} - \overrightarrow{D_1}\right] = 0 \qquad (4.1)$$

Ainsi, lorsque nous appliquons cette analyse au profil expérimental Figure 4.9, nous constatons qu'elle échoue de manière spectaculaire. Le champ électrique aurait dû être plus faible dans le matériau diélectrique ayant une permittivité plus élevée, c'est-à-dire Si_3N_4, mais nous observons le contraire. Il est clair que la courbure semble être l'exact opposé de ce que l'on attendrait d'une combinaison d'un diélectrique SiO_2 ($\varepsilon_r = 3.9$) et un diélectrique Si_3N_4 ($\varepsilon_r = 7.2$), la courbure de la phase étant positive plutôt que négative.

Nous avons vu pour le modèle de condensateur SiO_2 que ce type d'échantillon peut accumuler une charge d'espace, alors que le modèle de condensateur Si_3N_4 ne le fait pas. J'ai donc tenté d'intégrer deux zones de charge à l'intérieur du SiO_2, dans ce condensateur bicouche.

En inversant la courbure à l'intérieur du diélectrique, cette intégration permet un très bon ajustement. Par exemple, ces zones mesurées sur les données expérimentales ont une longueur d'environ 4 nm, et nous avons pu extraire la densité de charge des données de simulation, qui était d'environ $10 \times 10^6\ \mathrm{C/m^3}$ et $-1.5 \times 10^6\ \mathrm{C/m^3}$ à gauche et à droite de la couche de SiO_2, respectivement. Il semble que le SiO_2 soit enclin à créer des pièges frontaliers même aux interfaces avec un autre diélectrique, et qu'il modifie profondément la distribution de potentiel attendue d'un tel système.

4. Conclusion

Nous avons démontré dans ce chapitre que nous avons réussi à simuler des données expérimentales avec les outils développés dans le chapitre précédent. Nous pouvons tenir compte d'une variété d'anomalies expérimentales telles que les dommages causés par le FIB, le champ de fuite et l'effet de charge. La généralité de la préparation du FIB et de la configuration expérimentale est discutée, ce qui nous permet de nous concentrer directement sur la charge de l'échantillon diélectrique SiO_2 mis à la terre.

L'interaction du faisceau d'électrons avec les matériaux diélectriques produit des électrons secondaires, qui à leur tour produisent une émission d'électrons Auger, entraînant une charge positive. Nous avons détecté la présence de couches conductrices tout autour du condensateur qui font écran au champ de fuite en comparant les données expérimentales et simulées. En utilisant le modèle MEF approprié, nous pouvons extraire des informations quantitatives telles que la densité de charge réelle à l'intérieur du diélectrique.

En étudiant le condensateur mis à la terre, nous pouvons détecter les phénomènes extrinsèques causés par nos mesures et donc les éliminer de nos données expérimentales, ce qui nous permet d'ouvrir l'étude sur les condensateurs polarisés.

Nous avons commencé avec le condensateur Si_3N_4 que nous pensions être un modèle parfait. Cependant, nous avons découvert des dommages causés par le FIB qui ont formé une couche conductrice autour de l'échantillon, ainsi qu'une densité chargée qui a été injectée à l'intérieur du diélectrique lors de la polarisation. Nous avons également remarqué que, comme prévu lors de l'étude théorique, le champ de fuite

courbe la phase à l'intérieur des électrodes. Je montre également comment et pourquoi nous pouvons obtenir une bonne adéquation entre la simulation et les données expérimentales, étape par étape.
Ensuite, nous testons un condensateur SiO_2 couramment utilisé avec un diélectrique beaucoup plus utilisé dans l'industrie microélectronique que le condensateur Si_3N_4. Nous avons découvert une charge induite dans le diélectrique qui affecte le fonctionnement normal du dispositif. J'ai pu quantifier ces charges et ainsi comprendre leur impact sur la capacité.
Pour nous assurer que la déplétion à l'intérieur du silicium n'a pas d'effet sur la mesure de la zone de charge, nous avons quantifié la polarisation et la charge générée dans le la zone de déplétion. À cet égard, nous étions curieux de savoir si les charges mesurées à l'intérieur du diélectrique étaient protégées par une zone d'appauvrissement. Même si l'effet de charge n'est pas inclus dans le modèle, la démonstration mathématique montre à quel point cet effet est faible par rapport à la polarisation appliquée.
Enfin, nous étudions un condensateur constitué des deux couches du diélectrique étudié précédemment. Nous remarquons une anomalie intrigante sur le champ à l'intérieur des interfaces entre les diélectriques. Par conséquent, nous avons pu expliquer et créer un bon ajustement des données expérimentales en intégrant les couches de charge dans les diélectriques SiO_2. Ainsi, non seulement nous avons compris l'inversion de la courbure du champ, mais ces résultats soutiennent également la thèse de la zone de charge à l'intérieur du diélectrique SIO_2.
Le potentiel simulé a ensuite été comparé à un profil de potentiel calculé à l'aide d'un script dans un condensateur infini. Cela nous permet de constater que, même si nous ne nous intéressons pas au champ de fuite, les géométries finies du condensateur créent un effet de frontière qui va courber le potentiel interne à l'intérieur de l'isolant. Malgré cette différence de chute de potentiel, nous confirmons que le champ interne d'un échantillon mince correspond étroitement au condensateur infini, ce qui valide à la fois notre modèle et l'utilisation de simulations numériques.
Pour aller plus loin, la préparation du FIB doit être étudiée de manière plus approfondie. Nous devrions essayer de fraiser d'autres échantillons avec d'autres sources, telles que l'hélium ou le xénon, bien que cela puisse nécessiter un temps de préparation beaucoup plus long.
Enfin, ces études ouvrent la voie à d'autres recherches sur d'autres dispositifs microélectroniques tels que les condensateurs ferroélectriques, les transistors...

Chapter 5 — Incertitude des mesures

Je n'ai jamais vraiment expliqué dans les chapitres précédents pourquoi il était si difficile de créer un modèle qui s'adapte suffisamment aux données expérimentales pour en extraire des paramètres quantitatifs. Le problème principal est que tout est lié : chaque paramètre est corrélé d'une manière ou d'une autre. J'ai tenté de créer une figure qui explique la relation entre les paramètres du modèle et leur influence sur l'ajustement en classant qualitativement les paramètres qui ont une forte influence et les paramètres qui ont une faible influence selon mon expérience (Figure 5.1).
La complexité apparente du diagramme peut être frustrante, mais il s'agit d'un choix délibéré de représentation qui montre le problème tel que nous l'avons vu au début de ma thèse. Le cas des couches conductrices a même été laissé de côté pour plus de clarté. Je peux cependant dire quelques mots sur ce dernier problème : la principale différence entre les modèles avec et sans couches conductrices est que la densité de charge locale n'influence plus les autres parties du modèle. Grâce à la couche conductrice, chaque zone chargée ne produit pas de champ de fuite et ne peut donc pas influencer la phase acquise par les électrons dans d'autres zones. Une autre distinction est que les couches conductrice, plutôt que les paramètres de polarisation influenceront directement la chute nette de phase entre les électrodes.

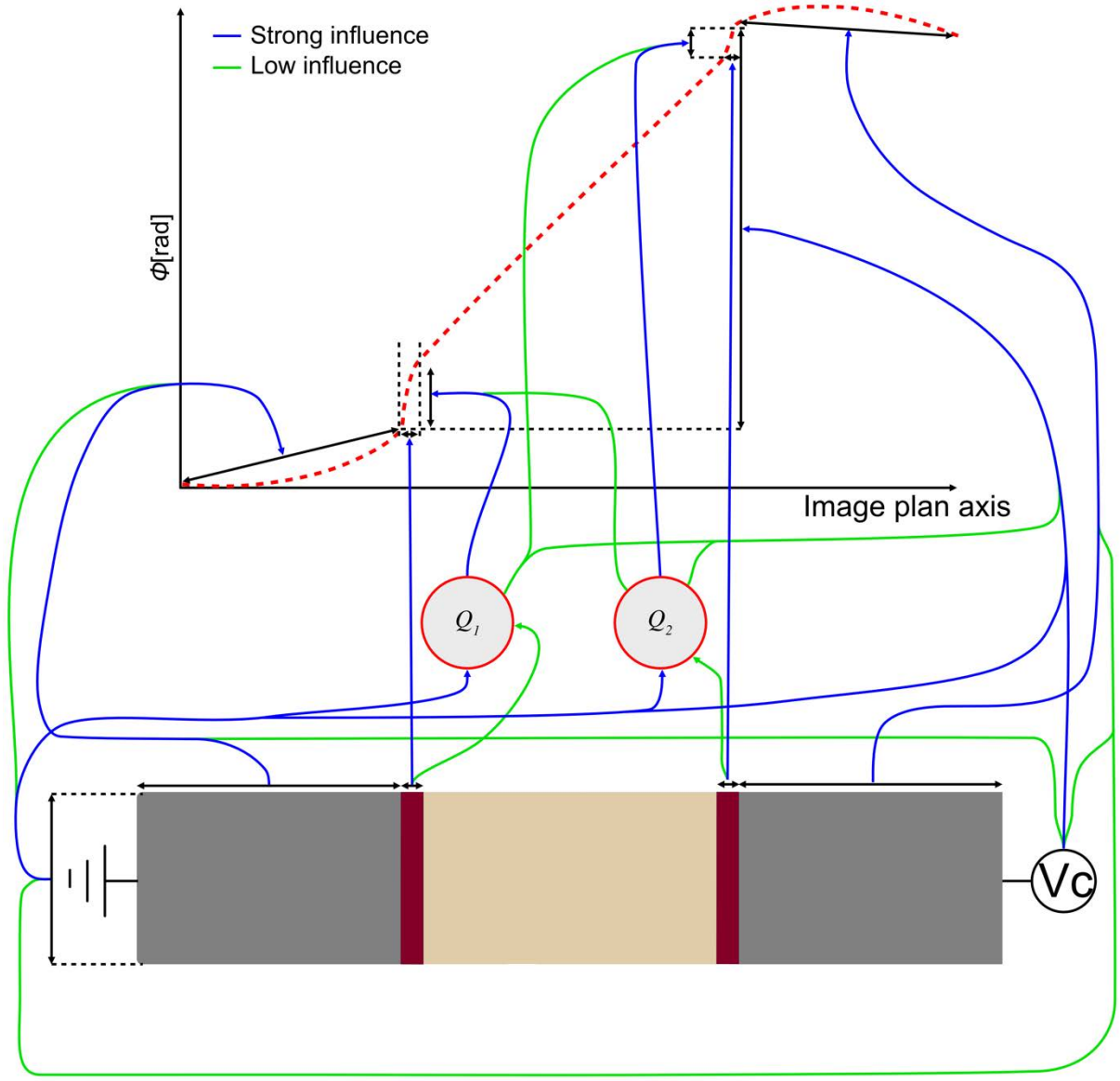

Figure 5.1 : La relation entre la variable du modèle et son effet sur le profil de phase. (Strong influence : forte influence ; Low influence : faible influence)

Ce diagramme illustre les difficultés que j'ai rencontrées lorsque j'ai réfléchi à la manière dont nous pouvons être certains de ce que nous mesurons et si nous mesurons un paramètre, dans quelle fenêtre de confiance pouvons-nous être certains de notre valeur. Tout au long de ce chapitre, je démêlerai cette question. *Méli-mélo* en analysant la mesure de chaque paramètre et en appliquant des méthodes statistiques qui nous permettront d'y voir plus clair. Pour calculer les incertitudes, je suivrai le Guide pour l'expression de l'incertitude de mesure (GUM)(International Bureau of Weights and Measures and International Organization for Standardization, 2008), un guide de métrologie.
Cette étude présente ce que je faisais "à la main" avant de développer récemment un code Python qui nous permettra d'étudier le modèle théorique ainsi que l'étude des algorithmes pour ajuster les données expérimentales. Enfin, je décrirai un premier développement d'un réseau de neurones lors de ma supervision d'un stage INSA. Ce développement aborde deux thèmes : le premier était le développement d'une IA

capable de prédire les paramètres de simulation à partir de données expérimentales, et le second sur la façon d'extraire des paramètres à partir d'images du microscope électronique. Bien qu'incomplet, ce travail est intéressant pour les développements futurs.

1. Incertitude du modèle Si-SiO_2-Ti

1.I. Introduction

L'étude du condensateur Si-SiO_2-Ti dans le chapitre précédent a révélé qu'il existe deux zones chargées de signes opposés à l'intérieur du diélectrique, près des interfaces des électrodes. Ce résultat étant très intéressant, j'ai choisi de montrer comment j'ai tenté de déterminer l'incertitude sur la mesure des densités chargées.
Tout d'abord, le fait que le déphasage obtenu soit lié au mesurande (c'est-à-dire la densité de charge) par la méthode des éléments finis implique qu'il n'y a pas de lien analytique entre ces deux variables. En effet, la densité de charge calculée ne peut être déduite par une simple équation en raison de la complexité du système. Malgré cela, l'équation de rétropropagation de l'incertitude du GUM (Guide to the Expression of Uncertainty in Measurement) reste valable sous l'hypothèse que chaque paramètre a une influence linéaire sur l'image de phase.
Pour propager les incertitudes, nous devons évaluer l'incertitude de chaque paramètre, et comme ils sont de type B, chaque mesure doit être associée à une distribution de probabilité. Comme nous n'avons pas accès à de multiples mesures répétées, nous devons choisir avec soin la distribution de probabilité pour chaque mesurande.
En outre, nous pouvons diviser le mesurande en deux familles : les mesures de longueur (c'est-à-dire sur les axes x et y) et les incertitudes de phase qui sont la variance de phase due au bruit. Les sections suivantes décrivent la manière dont chaque paramètre a été mesuré, ainsi que l'incertitude associée.

1.II. Propagation des incertitudes

Chacune des incertitudes précédentes influence l'incertitude de la densité de charge. Nous devons relier chaque incertitude aux paramètres que nous voulons mesurer (c'est-à-dire la densité de charge) et nous savons que certains paramètres sont interdépendants (corrélés). Pour tenir compte de ces phénomènes et calculer la variance composée u_c^2, nous devons propager la variance de chaque paramètre à travers l'équation (5.1).

$$u_c^2(y) = \sum_{i=1}^{N} c_i^2\, u^2(x_i) + 2\sum_{i=1}^{N-1}\sum_{j=i+1}^{N} c_i c_j u(x_i) u(x_j) r(x_i, x_j) \qquad (5.1)$$

Où:

$$c_i = \frac{\partial f}{\partial x_i}\ ;\ r(x_i, x_j) \approx \frac{u(x_i)\delta_j}{u(x_j)\delta_i} \qquad (5.2)$$

Le facteur 2 est dû au fait que la matrice *r* est symétrique. La fonction "**f**" reliant la densité de charge aux différents paramètres n'existe pas, donc nous ne calculons pas le coefficient C_i directement. Cependant, C_i représente la mesure dans laquelle la sensibilité de chaque paramètre peut affecter la mesure de la densité de charge. Ainsi,

si nous mesurons l'impact de la variation des paramètres x_i sur le paramètre mesuré pour chaque paramètre du modèle, nous pouvons estimer les coefficients C_i. En pratique, cela consiste à remplacer C_i dans l'équation (5.2) par $C_i = \frac{\partial f}{\partial x_i} \approx \frac{\Delta D}{\Delta x_i}$; Δx_i étant une petite variation d'un paramètre du modèle et ΔD la correction apportée à la densité de charge D pour trouver un ajustement correct après une petite variation. Δx_i. En d'autres termes, nous construisons la matrice des coefficients de corrélation (Table 5.1) qui prennent le coefficient de corrélation $r(x_i, x_j)$ calculée à partir de l'ampleur d'une perturbation δ_i à partir du paramètre x_i peut créer un changement δ_j à la mesure de x_j.

correlation matrix	t	L2	Cz	Vc
t	1	0.20	0	0.21
L2	0.20	1	0	0
Cz	0	0	1	0
Vc	0.21	0	0	1

Table 5.1 : Matrice de corrélation prenant en compte les dépendances entre les paramètres.

Les coefficients de la matrice de corrélation représentent l'influence de chaque paramètre les uns par rapport aux autres pour l'ajustement. En outre, chaque zéro représente une corrélation nulle entre les paramètres ; à cette fin, j'indique le paramètre C_z (c'est-à-dire la largeur de la zone de charge) qui n'ont aucune corrélation avec les paramètres. Enfin, l'incertitude relative est présentée ci-dessous (Table 5.2).

DC Bias (V_c)	ρ_1 (C/cm^3)	ρ_2 (C/cm^3)
-5	$-1.4 \pm 21,1\%$	$2.3 \pm 11,9\%$
-4	$-1.1 \pm 26,9\%$	$1.8 \pm 15,2\%$
-3	$-1.0 \pm 29,5\%$	$1.3 \pm 21,0\%$
-2	$-0.9 \pm 32,8\%$	$0.9 \pm 30,3\%$
-1	$-0.6 \pm 49,2\%$	$0.4 \pm 68,2\%$
1	$0.6 \pm 48,8\%$	$-0.4 \pm 66,7\%$
2	$1.3 \pm 22,3\%$	$-0.6 \pm 44,4\%$
3	$2.0 \pm 14,5\%$	$-1.0 \pm 26,7\%$
4	$2.6 \pm 11,1\%$	$-1.3 \pm 20,5\%$
5	$3.0 \pm 09,7\%$	$-1.5 \pm 17,8\%$

Table 5.2: Tableau résumant la densité de charge mesurée en fonction de la tension appliquée au condensateur réel avec les erreurs relatives associées.

L'erreur est la plus élevée pour la polarisation la plus faible alors qu'elle est relativement faible pour la polarisation la plus forte. De même, nous remarquons une asymétrie dans les erreurs dues aux incertitudes de la polarisation, de l'épaisseur et de la taille de l'électrode droite qui ont agi principalement dans la zone de charge à droite.

1.III. Ajustement sur système modèle

Avant d'essayer d'ajuster les données expérimentales, j'ai d'abord voulu tester l'algorithme sur des données simulées avec des paramètres connus. Diverses situations, telles que des condensateurs mis à la terre avec une densité de charge, des condensateurs de polarisation, ont été choisies à cette fin sur la base des modèles déjà présentés au chapitre 3. Je voulais tester deux choses : pouvais-je trouver un ajustement parfait et les paramètres correspondaient-ils à ceux de la simulation ?

Comme une procédure automatisée présente un très faible biais, j'espérais également pouvoir étudier la corrélation entre les paramètres avec une plus grande précision qu'auparavant. Le condensateur polarisé nécessite l'inclusion de paramètres supplémentaires tels que la tension appliquée et la conductivité des couches superficielles. Le premier exemple est un condensateur modèle sans aucune couche de charge dans le diélectrique. Sur les deux Figure 5.2, nous retrouvons la rupture de symétrie causée par la polarisation.

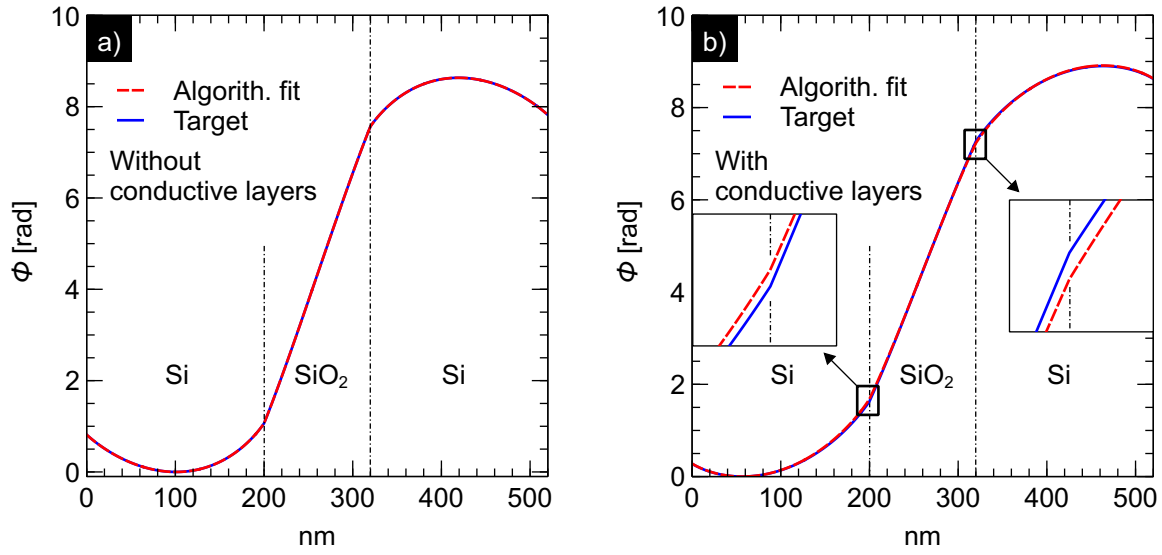

Figure 5.2 : Tracés de l'autofit sur un modèle polarisé sans et avec couches conductrices a) et b). (Target : cible ; without/with : sans/avec ; conductive layers : couche conductrice)

Indépendamment du fait qu'il existe une certaine variation au niveau de l'interface en Figure 5.2(b), les ajustements sur le modèle polarisé sont très bons. La variation sur l'interface est due à un manque d'épaisseur rendant la courbure plus faible, car le champ de fuite est plus important sur la phase totale dans ce cas comme décrit au chapitre 3. J'ai choisi de ne tester que les paramètres difficiles à distinguer sur le modèle, à savoir l'épaisseur en fonction de la polarisation et la conductivité des couches conductrices (Table 5.3).

Fitting	V_c	Thickness (nm)
Initial	a) 5	60
Fitted	5	60
Error	0 %	0 %

Fitting	Thickness (nm)	$\sigma(S/m)$
Initial	b) 60.0	30 000
Fitted	42.6	16 240
Error	29 %	46 %

Table 5.3: Paramètres d'ajustement du modèle sans a) et avec b) couches conductrices pour les paramètres : polarisation V_c, épaisseur et épaisseur, conductivité σ, respectivement. (Thickness : épaisseur)

Dans la plupart des cas, le premier modèle sans couches conductrices Table 5.3(a) récupère de bons paramètres, tandis que le modèle avec des couches conductrices Table 5.3(b) est incohérent. L'utilisation de l'évolution différentielle a donné de meilleurs résultats, mais elle prend beaucoup de temps (plusieurs heures sans optimisation appropriée, c'est-à-dire la parallélisation). Le mieux est, je pense, de

réduire autant que possible la fenêtre de prédiction de l'épaisseur de l'échantillon en utilisant d'autres techniques de mesure indépendantes, telles que la mesure de l'épaisseur par EELS, au risque d'obtenir des prédictions incorrectes pour les autres paramètres utilisés. La matrice de corrélation montre la relation entre les paramètres et peut être utilisée pour propager l'écart-type aux paramètres que nous voulons mesurer. Je tiens à souligner qu'une corrélation entre deux paramètres peut avoir une signification dans certains cas, par exemple la charge totale avec la largeur du diélectrique et l'épaisseur de l'échantillon. La corrélation est définie comme une valeur comprise entre -1 et 1 pour une corrélation maximale et 0 pour une absence de corrélation. Une corrélation positive indique qu'un changement dans l'estimation d'un paramètre implique un changement prévisible des autres paramètres dans la même direction, ce qui signifie que si un paramètre augmente, l'autre augmentera également. En revanche, une corrélation négative indique que l'augmentation d'un paramètre entraîne une diminution de l'autre. Table 5.4 représente la matrice de corrélation de ces paramètres.

a)

correlation matrix	V_c	Thickness
V_c	1	-0.997
Thickness	-0.997	1

b)

correlation matrix	Thickness	σ
Thickness	1	-1
σ	-1	1

Table 5.4 : Matrice de corrélation pour l'autoajustement du modèle sans a) et avec b) couches conductrices pour les paramètres : polarisation V_c, épaisseur et épaisseur, conductivité σ, respectivement. (Correlation matrix : matrice de corrélation)

Un champ de fuite est toujours présent dans le cas du condensateur polarisé, ce qui signifie que la matrice de corrélation entre les modèles avec et sans couches conductrices est très proche, contrairement au modèle mis à la terre. La matrice de corrélation montre que l'épaisseur du condensateur est inversement proportionnelle à la polarisation appliquée Table 5.4(a) et la conductivité de l'élément conducteur Table 5.4(b). En d'autres termes, une augmentation de l'épaisseur entraîne une diminution du potentiel et de la conductivité.

1.III.A. Incertitude sur le modèle Si_3N_4

Le dernier échantillon que j'ai essayé d'ajuster est le condensateur à base de Si_3N_4 présenté au chapitre 4, qui est relativement simple si l'on ignore la courbure de la phase à l'intérieur du diélectrique (voir Figure 5.3).

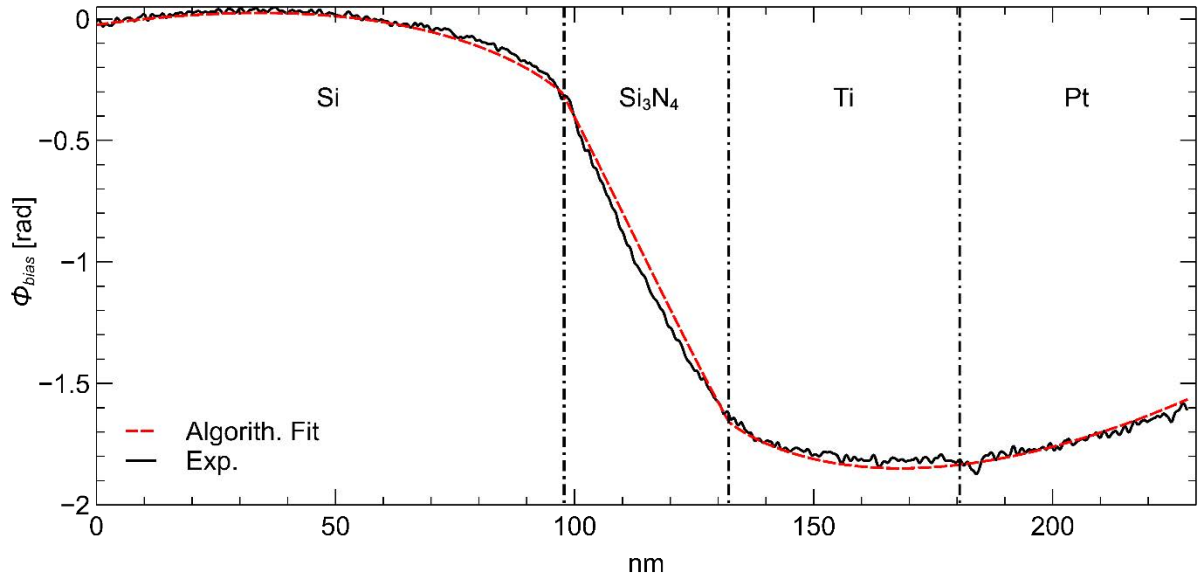

Figure 5.3 : Ajustement sur l'échantillon Si_3N_4 polarisé.

En réduisant la plage d'épaisseur à 40 nm et 50 nm, comme indiqué par les mesures EELS, l'ajustement est très bon, de même que les paramètres prédictifs (Table 5.5), qui sont la conductivité et, indirectement, la polarisation.

Fitting	Thickness (nm)	$\sigma(S/m)$	W (nm)
Manually	46	660	36
Fitted	42.7	566	35
Error	7.2 %	14.2 %	2.8 %

Table 5.5: Paramètres de l'échantillon Si_3N_4 polarisé.

Nous pouvons également calculer la matrice de corrélation à l'aide de ce modèle (Table 5.6).

correlation matrix	Thickness	σ	W
Thickness	1	0.99	0.63
σ	0.99	1	0.68
W	0.63	0.68	1

Table 5.6: Matrice de corrélation de l'échantillon Si_3N_4 polarisé.

En poussant l'analyse un peu plus loin, nous pouvons calculer l'incertitude sur la polarisation appliquée. J'ai calculé le coefficient c_i à partir de l'équation de propagation (5.1) en modifiant une composante de 5% et en déterminant son impact sur le paramètre intéressant (ici la polarisation) en refaisant l'ajustement tout en bloquant les autres paramètres. Nous pouvons utiliser ces coefficients avec la matrice de corrélation et la matrice de covariance pour calculer l'incertitude sur le biais. Avec un biais de - 4V appliqué, l'algorithme prédit une polarisation locale de $-2.2 \pm 0.2V$. Malgré le caractère incomplet de cette étude, je pense que cette technique automatique sera très utile à l'avenir. Le code simplifie ce type d'analyse tout en

éliminant autant que possible les biais humains. Dans le même ordre d'idées, je souhaite présenter un autre développement prometteur dans la section suivante.

2. L'apprentissage automatique

2.I. Prédictions simplifiées du potentiel interne du condensateur

Ces sections ont été réalisées dans le cadre d'un projet de 4e année de Marc Gueissaz (INSA Toulouse) que j'ai supervisé.
Malgré la précision des calculs de la méthode des éléments finis, ils sont lents, en particulier pour le calcul et l'ajustement des modèles 3D, qui peuvent prendre des heures ou des jours à réaliser manuellement ou via des boucles d'algorithmes. Bien que l'entraînement d'un réseau neuronal prenne beaucoup de temps et d'efforts, une fois la phase d'apprentissage passée, l'exécution d'un réseau neuronal est beaucoup plus rapide que les simulations numériques conventionnelles. Il était donc intéressant d'étudier si l'efficacité du processus d'adaptation pouvait être améliorée par l'utilisation de l'apprentissage automatique.
Plutôt que de commencer par des images de phase, j'ai choisi le cas plus simple du profil de potentiel à l'intérieur d'un condensateur, qui est beaucoup plus facile à contrôler parce qu'il y a moins de variables qui peuvent influencer la prédiction. Nous voulions détecter plusieurs paramètres, notamment la longueur diélectrique *w*, la longueur de l'espace chargé de densité C_z et sa norme chargée, ainsi que le biais appliqué (Figure 5.4).

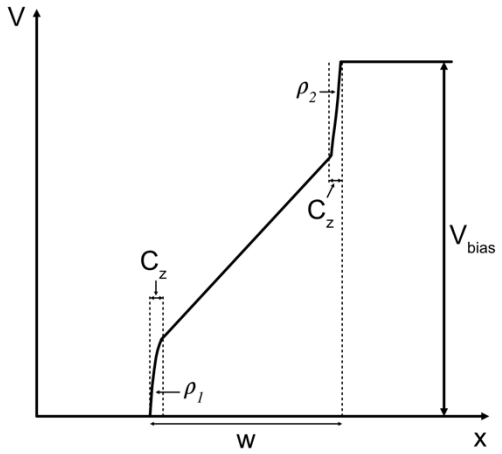

Figure 5.4 : Profil de potentiel à l'intérieur d'un condensateur avec deux zones chargées.

Pour l'apprentissage, j'ai créé une base de données de 100 000 exemples basée sur le modèle analytique développé avec le script GMS que j'ai traduit en code Python. Les paramètres ont été générés aléatoirement par un générateur de nombres pseudoaléatoires PCG-64 (O'Neill, 2014) avec une distribution uniforme, qui a été choisi pour ses très bonnes performances en matière de tests statistiques et son extrême rapidité.
Les plages de densité de charge sont connues de $-4 \times 10^6 C/m^3$ to $5 \times 10^6 C/m^3$ à gauche et à droite $-3.6 \times 10^6 C/m^3$ à $4 \times 10^6 C/m^3$ alors qu'ils sont cohérents avec la polarisation appliquée. Les résultats sont présentés dans Figure 5.5.

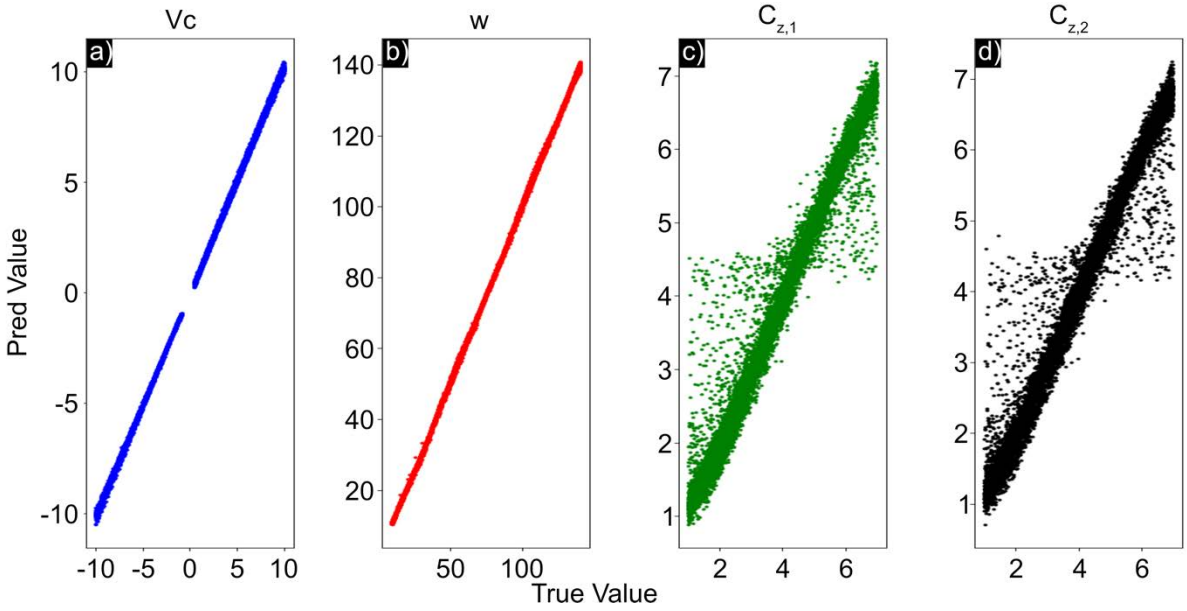

Figure 5.5 : Tracé de la valeur prédite en fonction de la valeur réelle pour le paramètre de polarisation, la longueur du diélectrique et la longueur de la densité chargée. (True value : valeur vraie ; Pred Value : Valeur prédite)

L'effet de la charge sur le potentiel du profil étant extrêmement faible, nous avons aidé le réseau neuronal en évitant les biais autour de zéro sur une fenêtre allant de - 0,5V à 0,5V, comme le montre le graphique suivant Figure 5.5.
Comme nous l'espérions, le nouvel ensemble de données d'entraînement présente une meilleure distribution de la longueur diélectrique prédite. La prédiction de la taille de la densité chargée est alors bien meilleure, et nous pouvons également voir que la dispersion des mauvaises valeurs est centrée autour de la longueur centrale de la densité chargée, ce qui implique que la valeur prédite inférieure à la moitié de la longueur ne se trompe pas plus de la moitié de la longueur, et que la valeur supérieure se comporte de la même manière.
Pour ce faire, nous avons examiné la distribution des erreurs moins la valeur réelle pour chaque valeur prédite, ce qui devrait nous en apprendre davantage sur le comportement du réseau neuronal et sur la manière dont nous pouvons améliorer ses performances ; pour ce faire, nous allons créer un histogramme pour visualiser la dispersion des erreurs (Figure 5.6).

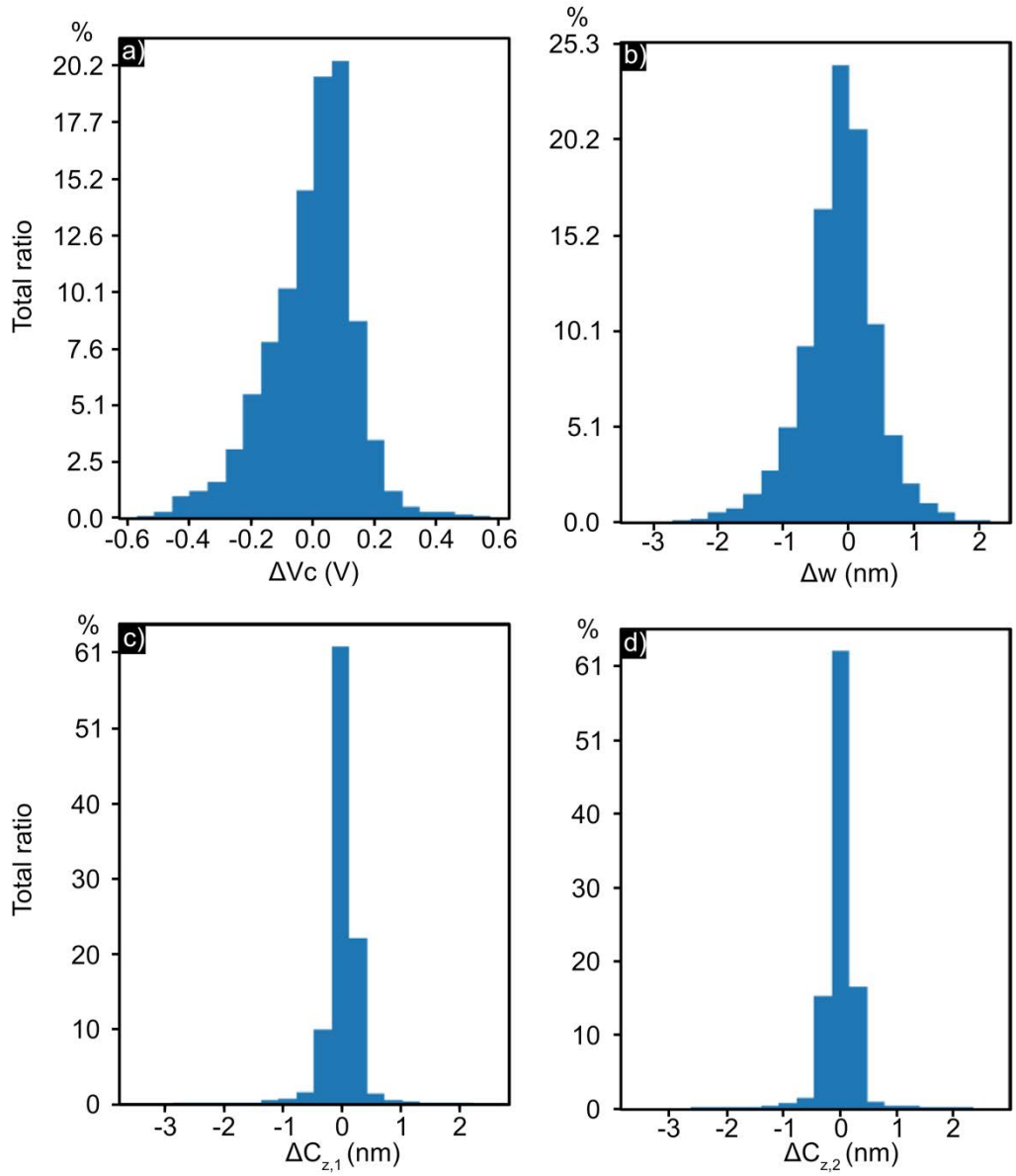

Figure 5.6 : Histogrammes des paramètres de la dispersion de polarisation a) le long de la longueur prédite du diélectrique b), et de la largeur de la zone à deux charges c),d).

En étudiant l'histogramme, on constate que l'erreur absolue moyenne (MAE) sur la polarisation se situe autour de V = 0,10 V, ce qui est très proche de la solution ; cependant, l'histogramme semble être non symétrique et penche vers le côté négatif, ce qui indique que le réseau neuronal prédit fréquemment des valeurs inférieures à la valeur réelle. Bien que la MAE sur la valeur de mesure de la longueur du diélectrique semble plus élevée, il convient de rappeler que la mesure est effectuée sur une longueur beaucoup plus courte que la longueur des zones de charge, soit respectivement Δw = 0,42 nm, $\Delta C_{z,1/2}$ = 0,18 nm, ce qui signifie que la dispersion autour de la longueur du diélectrique est aussi bonne que celle des zones chargées, si ce n'est meilleur (si l'on raisonne en termes d'erreur absolue).
Avec ces données, nous touchons la partie sensible de l'ingénierie neuronale, ce qui signifie que nous pouvons obtenir une excellente prédiction la plupart du temps, mais que des échecs extrêmes peuvent parfois se produire. On parle alors de valeurs

aberrantes, alors que 99 % des valeurs se situent à l'intérieur de l'intervalle nanométrique.

3. Détection d'ellipses

Le projet étudiant comprenait également une recherche sur le développement d'un système d'alignement automatique pour le microscope afin d'améliorer la précision des hologrammes. Bien que cette partie ne soit pas directement liée à la modélisation, elle a donné des résultats qui méritent d'être décrits.
L'obtention d'hologrammes avec un rapport signal/bruit optimal nécessite un alignement précis du microscope. Cet alignement comprend le réglage de la forme du faisceau (Figure 5.7) et sa stabilisation spatiale par rapport à l'échantillon.
En effet, en combinant la détection d'ellipses et la simulation de trajectoires de faisceaux d'électrons (développées lors de la thèse de Julien Dupuy (Dupuy, 2021)), il pourrait être possible d'obtenir plus rapidement des valeurs plus précises pour les différents paramètres contrôlant le microscope. La toute première étape consiste à voir si un réseau neuronal peut paramétrer la forme du faisceau, que nous supposerons elliptique pour des raisons de simplicité.
L'objectif est d'entraîner un réseau à extraire les valeurs qui caractérisent une ellipse à partir d'une image de 128*128 pixels. Dans ce qui suit, j'expliquerai comment une ellipse est théoriquement définie, puis l'importance de choisir un générateur aléatoire qui permette le calcul d'une variété d'ellipses.
Une ellipse peut être définie par l'intersection d'un plan infini avec un cône infini, à condition que ce plan coupe également l'axe de révolution du cône. Plus précisément, une ellipse peut être définie par 5 paramètres. Ce sont u, v le décalage du centre de l'ellipse par rapport à l'origine, a, b qui sont respectivement appelés demi-grand et demi-petit axes, et enfin, θ son inclinaison par rapport aux axes (Figure 5.7).

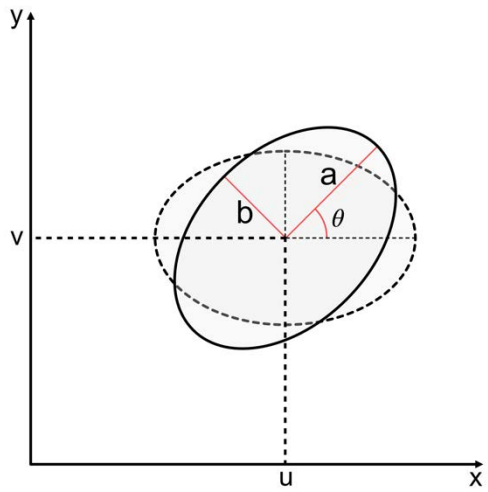

Figure 5.7 : Schéma de l'ellipse à mesurer, le petit axe, le grand axe, la position u et v de l'ellipse et l'angle.

L'équation utilisée pour calculer les ellipses dans le code de la base de données est la suivante (5.3):

$$\frac{[(x-u)\cos\theta+(y-v)\sin\theta]^2}{a^2}+\frac{[(x-u)\sin\theta-(y-v)\cos\theta]^2}{b^2}=1 \qquad (5.3)$$

Afin de générer une base de données non biaisée, j'ai utilisé un générateur utilisant l'algorithme du générateur congruentiel permuté (GCP) (O'Neill, 2014). En d'autres termes, il est constitué d'ellipses dont les différents paramètres sont distribués de manière uniforme. En effet, un bon générateur aléatoire évite qu'une plage de valeurs de paramètres soit surreprésentée par rapport à sa plage totale, ce qui évite les biais d'apprentissage. De plus, l'objectif étant de créer une base de données en un temps minimal, l'algorithme PCG est très rapide du fait de son format de stockage qui est binaire par rapport à sa qualité (période = 2^{64}) qui est d'un niveau cryptographique (O'Neill, 2014).
De nombreux exemples de prédiction de notre réseau neuronal sont présentés dans le tableau ci-dessous Figure 5.8.

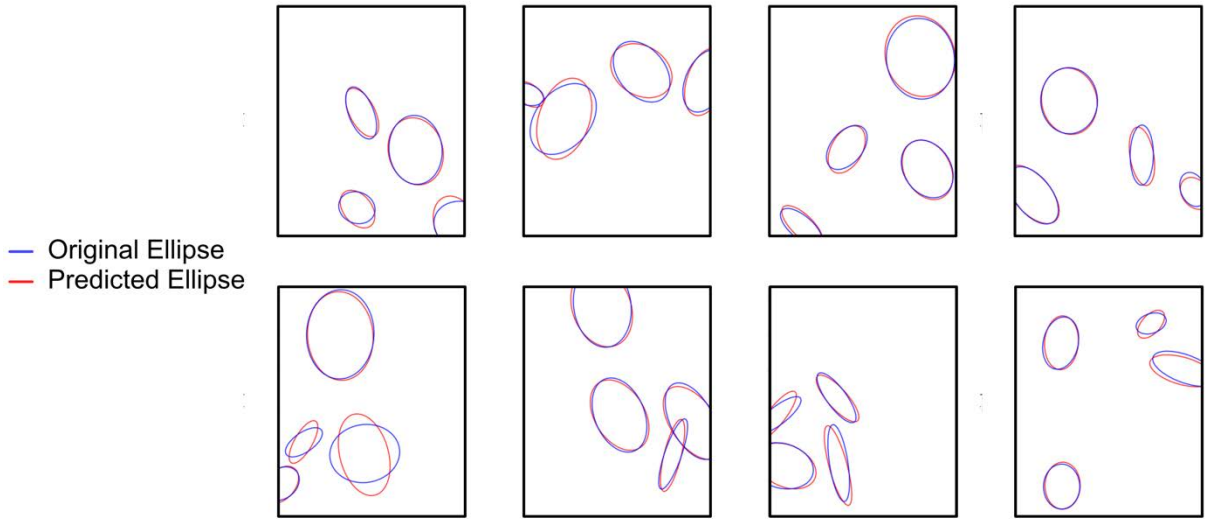

Figure 5.8 : Exemple de l'ellipse prédite en rouge avec l'ellipse réelle en bleu. (Original ellipse : ellipse originale ; predicted ellipse : ellipse prédite)

Nous pouvons constater que le réseau neuronal évalue assez bien la taille et la position, alors que certaines ellipses ne sont pas bien alignées.
Pour poursuivre la caractérisation du réseau neuronal, nous traçons la valeur prédite par rapport à la valeur réelle pour voir l'erreur au sein de la distribution (Figure 5.9).

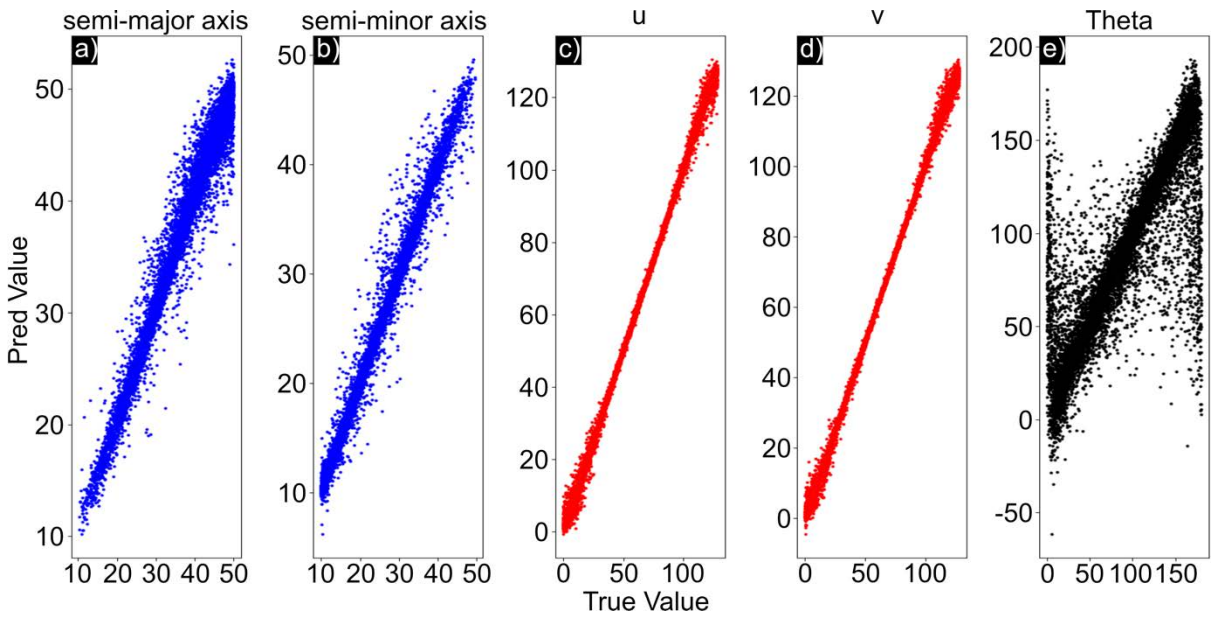

Figure 5.9 : Tracé de la valeur prédite par rapport à la valeur réelle pour le paramètre de polarisation, la longueur du grand axe, la longueur du petit axe, la position de l'ellipse suivant x et y, et l'angle.

Pour le demi-grand axe, l'erreur augmente avec la longueur mesurée. Cela est dû en partie au fait que l'erreur absolue augmente naturellement avec la longueur de la grandeur mesurée, mais aussi au fait que les ellipses plus grandes ont plus de chances de ne pas être entièrement à l'intérieur de l'image. L'erreur sur le demi-grand axe semble plus uniforme. Cela est probablement dû au fait que les grands axes semi-minces sont moins probables (par définition, il s'agit du plus petit axe). Néanmoins, malgré sa faible visibilité, nous pouvons supposer que la dispersion augmenterait dans les limites de la valeur la plus élevée. Pour la position de l'ellipse (u et v), en revanche, l'erreur augmente vers les deux extrêmes de la position de l'ellipse (u et v). Cela est probablement dû à la probabilité accrue d'ellipses partielles dans le champ de vision de l'image.
Il est intéressant de noter que pour l'orientation de l'ellipse, le réseau neuronal prédit parfois des valeurs inférieures à 0 et supérieures à 180, au-delà des valeurs limites dans les techniques d'apprentissage qui existent pour contraindre un réseau neuronal et que nous n'avons pas eu le temps d'étudier.
Un autre point à noter est qu'il existe une dispersion significative autour des valeurs zéro et 180. En raison de sa symétrie, une ellipse avec un angle de 0 est indiscernable d'une ellipse avec un angle de 180.
Comme décrit précédemment, nous examinerons la distribution des erreurs moins la valeur réelle pour chaque valeur prédite et créerons un histogramme pour visualiser la dispersion des erreurs (Figure 5.10).

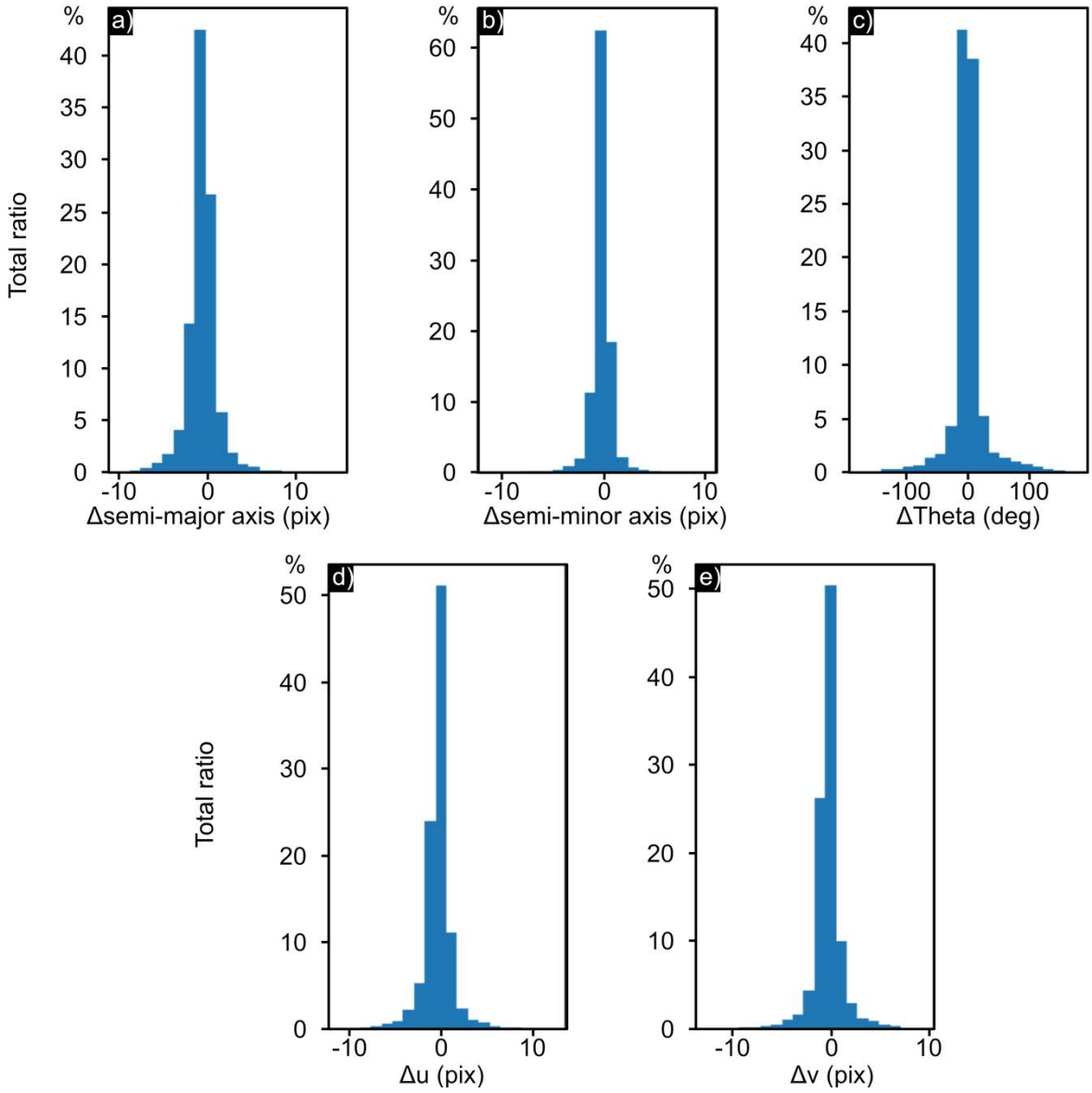

Figure 5.10 : Histogramme des paramètres prédits.

L'histogramme montre que l'erreur est relativement contenue, nous avons l'erreur absolue moyenne de Δsemi-grand axe = 0,76, Δsemi-petit axe = 0,47, Δu = 0,70, Δv =0,64, ΔTheta = 11,05. Malgré l'erreur angulaire plus importante, l'erreur absolue moyenne des autres paramètres est très bonne, puisqu'elle est inférieure à un pixel. La longueur mesurée à une erreur relative d'environ 0,5 % et l'angle a une erreur relative d'environ 6 %. C'est bien, mais certaines valeurs aberrantes dans les données peuvent être extrêmement imprécises.
Les performances du réseau neuronal semblent très prometteuses, voire surprenantes, et devraient être approfondies.

4. Conclusion

Partant du constat de la complexité d'extraire des données quantitatives de nos simulations numériques, j'ai montré comment nous pouvons étudier l'incertitude de

chaque paramètre. Les incertitudes peuvent ensuite être propagées à l'aide d'une matrice de corrélation afin de pouvoir déterminer l'incertitude globale du paramètre souhaité.
Passant de l'ajustement manuel à l'ajustement automatique, je démontre que la méthode de la région de confiance réflective fonctionne tant que nous donnons l'épaisseur de l'échantillon à l'algorithme d'autoconsistance. Bien que le travail soit incomplet, j'ai démontré que l'algorithme peut être utilisé sur des données expérimentales avec l'incertitude calculée sur un exemple.
Nous avons commencé à développer une méthode basée sur l'IA pour accélérer l'ajustement, car l'ajustement automatique sur des modèles 3D peut prendre des heures. Je démontre qu'un réseau neuronal peut être utilisé pour l'ajustement et j'étudie les limites du réseau neuronal.
Pour aller plus loin, la combinaison de cette simulation avec la simulation électronique à l'intérieur du microscope peut nous permettre de mieux simuler l'interaction entre le faisceau d'électrons et l'échantillon. L'utilisation de l'IA pour accélérer les calculs devrait être poussée un peu plus loin en testant le réseau neuronal sur des images de phase. En outre, je pense que la compréhension de l'interaction entre le champ du condensateur et la zone de référence est un défi que nous devons relever afin d'étudier des champs plus complexes pour d'autres modèles ayant des formes différentes, mais complexes.

Chapter 6 — Échantillon de l'industrie microélectronique

1. Introduction

Les dispositifs nanoélectroniques sont importants dans de nombreux domaines, et leur développement continue de faire l'objet d'une attention considérable dans la recherche fondamentale et appliquée. En fait, l'industrie microélectronique excelle dans l'innovation et la miniaturisation des produits en réponse à une demande sans cesse croissante de dispositifs à haute performance et à faible coût, ainsi que pour des raisons de compétitivité. Cependant, le rétrécissement des dispositifs et la complexité croissante de leur architecture nécessitent des études quantitatives locales. L'accès aux champs électriques locaux et à la distribution des charges électriques cartographié à l'échelle du nanomètre sur un seul appareil en fonctionnement fournirait des informations essentielles pour les développements futurs ou l'amélioration et l'optimisation de la conception. Les données obtenues peuvent également contribuer à l'analyse des défaillances, car des observations locales très précises à haute résolution de nanodispositifs en fonctionnement sont utilisées pour détecter des défauts ou des anomalies isolés dans une seule région.
Dans ce chapitre, je présente l'étude d'un ensemble de nanocondensateurs métal-isolant-métal (MIM) qui ont été sélectionnés et extrait des lignes de production de STMicroelectronics afin d'être polarisé pour des expériences électriques *in situ* dans le TEM. Je montre comment le fonctionnement du dispositif dans des conditions de travail réelles, étudié à l'aide de l'holographie électronique *operando* et combiné aux simulations de modélisation par éléments finis (MEF) que j'ai développés, peut être utilisé pour cartographier les champs électriques. À cette fin, nous étudierons le fonctionnement de deux dispositifs réels uniques ainsi que l'interaction de plusieurs dispositifs appartenant au même type. Les principaux résultats ont été publiés dans deux articles (Brodovoi et al., 2021, 2022).
Afin d'être applicables à des dispositifs réels, nous utilisons et développons la méthodologie mise au point lors d'analyses antérieures. Des modifications ont dû être apportées à la procédure expérimentale, notamment à la préparation de l'échantillon par FIB, et à la modélisation, qui a dû être plus complexe et inclure désormais un modèle 3D.

2. Préparation de l'échantillon

Des expériences ont été réalisées sur une matrice de dispositifs STMicroelectronics fabriqués à l'aide de leur procédé FD-SOI (Fully Depleted Silicon-on-Insulator) de 28 nm. Un isolant high-k mince de 11,5 nm en pentoxyde de tantale (Ta_2O_5) pris en

sandwich entre deux électrodes TiN connectées à un pilier Cu ou à une couche Al est utilisé dans les couches supérieures dorsales pour les applications de circuits à haute fréquence (Figure 6.1). L'électrode supérieure de TiN a une largeur de 950 nm (dans le plan de l'image) 1.7 µm profond.

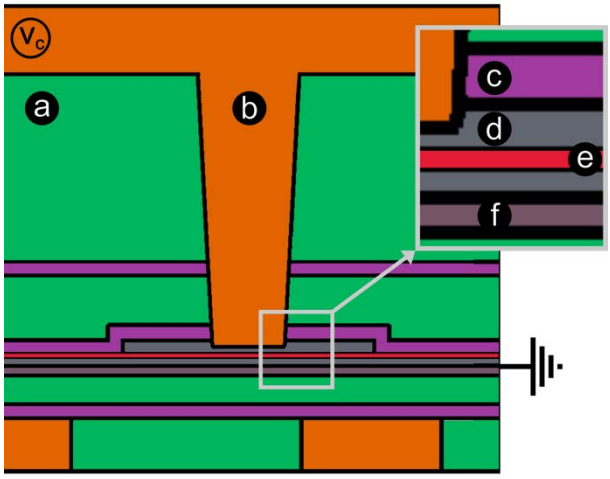

Figure 6.1 : Architecture du nanocondensateur MIM : région active du diélectrique Ta_2O_5 e) prise en sandwich par deux électrodes métalliques TiN d), interconnectée avec des lignes Cu b) et Al f), et protégée du courant de fuite par des couches isolantes SiO_2 a) et des lignes Si_3N_4 c).

Pour apporter des stimuli électriques au dispositif tout en assurant sa fonctionnalité électrique et sa compatibilité avec les observations TEM, une préparation d'échantillon spécifique combinant un flux de préparation de lamelles TEM et une capacité FIB-Edit ont été développées dans le cadre de la thèse de Maria Brodovoi en collaboration avec STMicroelectronics.

3. A Single Capacitor

Des expériences d'holographie électronique *operando* ont été réalisées sur des spécimens préparés à l'aide de la préparation FIB décrite ci-dessus. Trois hologrammes différents ont été enregistrés afin de reconstruire l'ensemble du champ de vision, que je montre à cette fin en Figure 6.2 en recadrant l'image et en la coupant plus largement pour montrer l'assemblage des trois images. Figure 6.2(a) et Figure 6.2(b) montrent l'image d'amplitude et l'image de phase à 1V extraites des hologrammes après soustraction de l'image de phase de référence à 0V, respectivement, tandis que Figure 6.2(c) montre l'image de phase simulée.
La rugosité de l'échantillon sur l'image d'amplitude montre que le condensateur provient d'un processus industriel. En outre, le changement de contraste indique une certaine diffraction. Le déphasage semble relativement uniforme à l'intérieur des électrodes, comme prévu, avec un champ de fuite visible sur les bords de l'électrode supérieure en raison de sa dimension latérale finie. Comparaison de l'image de phase expérimentale (Figure 6.2(b)) avec celle simulée à partir des simulations FEM (Figure 6.2(c)), on observe une très belle correspondance.

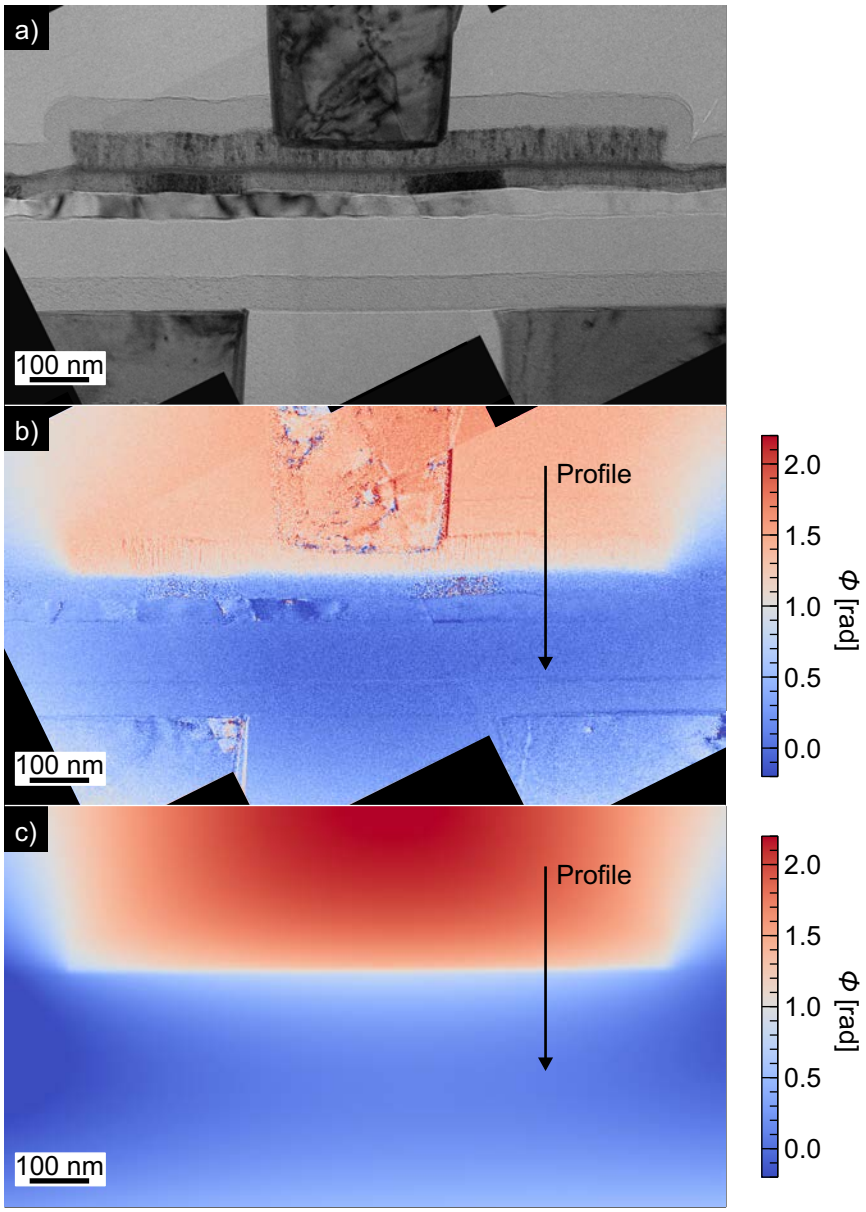

Figure 6.2 : L'image d'amplitude du condensateur étudié a) montre la géométrie du dispositif, suivi d'une comparaison de l'image de phase expérimentale b) et de l'image de phase simulée c) polarisée sous 1V.

Cet accord quantitatif entre les images de phase expérimentales et simulées est également mis en évidence avec les profils de phase extraits à travers les électrodes et la couche isolante de Ta_2O_5 (Figure 6.3). Les paramètres tels que l'épaisseur et la conductivité de la couche superficielle ont été ajustés pour obtenir la meilleure adéquation avec le déphasage mesuré expérimentalement (Figure 6.3). Les résultats de la simulation confirment la variation linéaire significative du déphasage qui se produit dans la couche d'oxyde, tandis que la courbure de la phase dans la zone des électrodes causée par le champ de fuite autour de l'échantillon est bien reproduite. Toutefois, cet accord a été obtenu pour une chute de potentiel plus faible entre les électrodes, et certaines différences entre les données expérimentales et simulées subsistent.

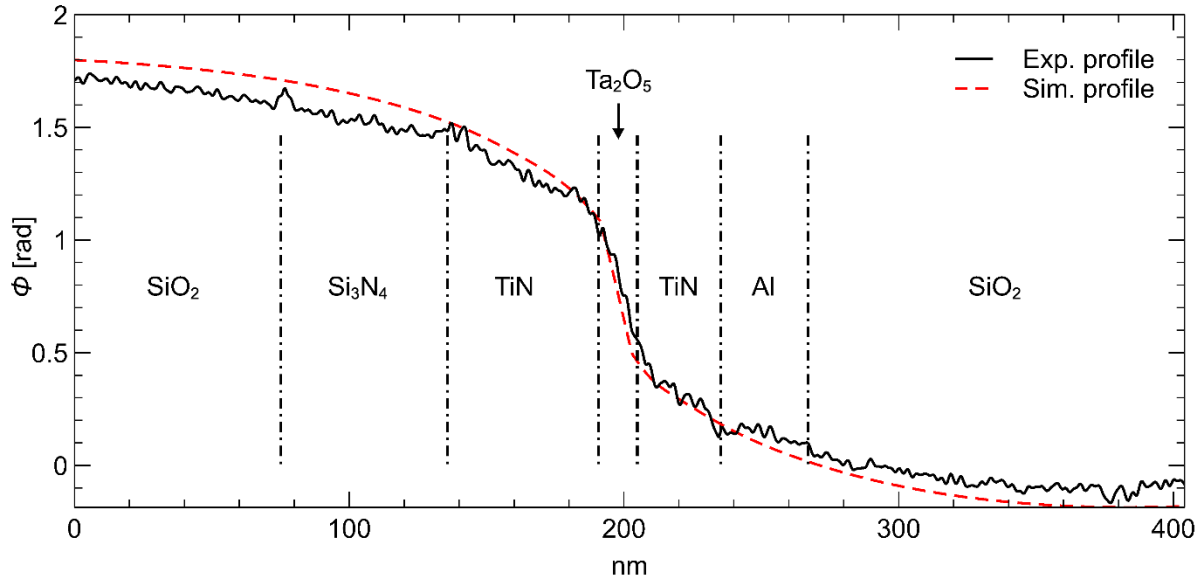

Figure 6.3 : Profils extraits des images de phase expérimentales et simulées le long des flèches noires sur les images de phase Figure 6.2b, c.

En effet, la chute de potentiel à travers le diélectrique par rapport à la tension appliquée (1V), conduisant à une polarisation locale de 0,65V, est réduite d'environ 0,35 V en raison de la fuite de courant dans les couches conductrices. La chute de potentiel pourrait être due aux couches conductrices qui se rapprochent de la conductivité des électrodes, comme décrite dans le chapitre théorique (3).

4. Interaction entre deux condensateurs

Dans l'exemple suivant, nous étudions l'interaction entre deux nanocondensateurs MIM voisins en parallèle. Figure 6.4(a) et Figure 6.4(b) montrent les images expérimentales d'amplitude et de phase acquises avec une polarisation de 0,6 V appliquée par l'alimentation. Trois hologrammes différents ont été enregistrés afin de reconstruire l'ensemble du champ de vision. Lorsqu'elle est polarisée, la phase varie fortement à travers la couche de Ta_2O_5 en raison du fort champ électrique local dans la couche diélectrique, mais reste relativement uniforme à l'intérieur des électrodes, comme prévu. En raison des temps d'exposition très longs de nos expériences d'holographie automatisée, il existe également un champ de fuite dans le plan entre les nanocondensateurs (Figure 6.4(b), flèche).

Pour que le modèle reste petit, le réseau de dispositifs parallèles a été limité à quatre et entouré de vide. La taille des mailles s'adapte dynamiquement aux dimensions locales, depuis les limites externes jusqu'à la région active du nanocondensateur, avec une taille de maille minimale d'environ 2 nm. La phase simulée correspondant au cas expérimental est illustrée en Figure 6.4(c) pour une épaisseur de lamelle de 100 nm.

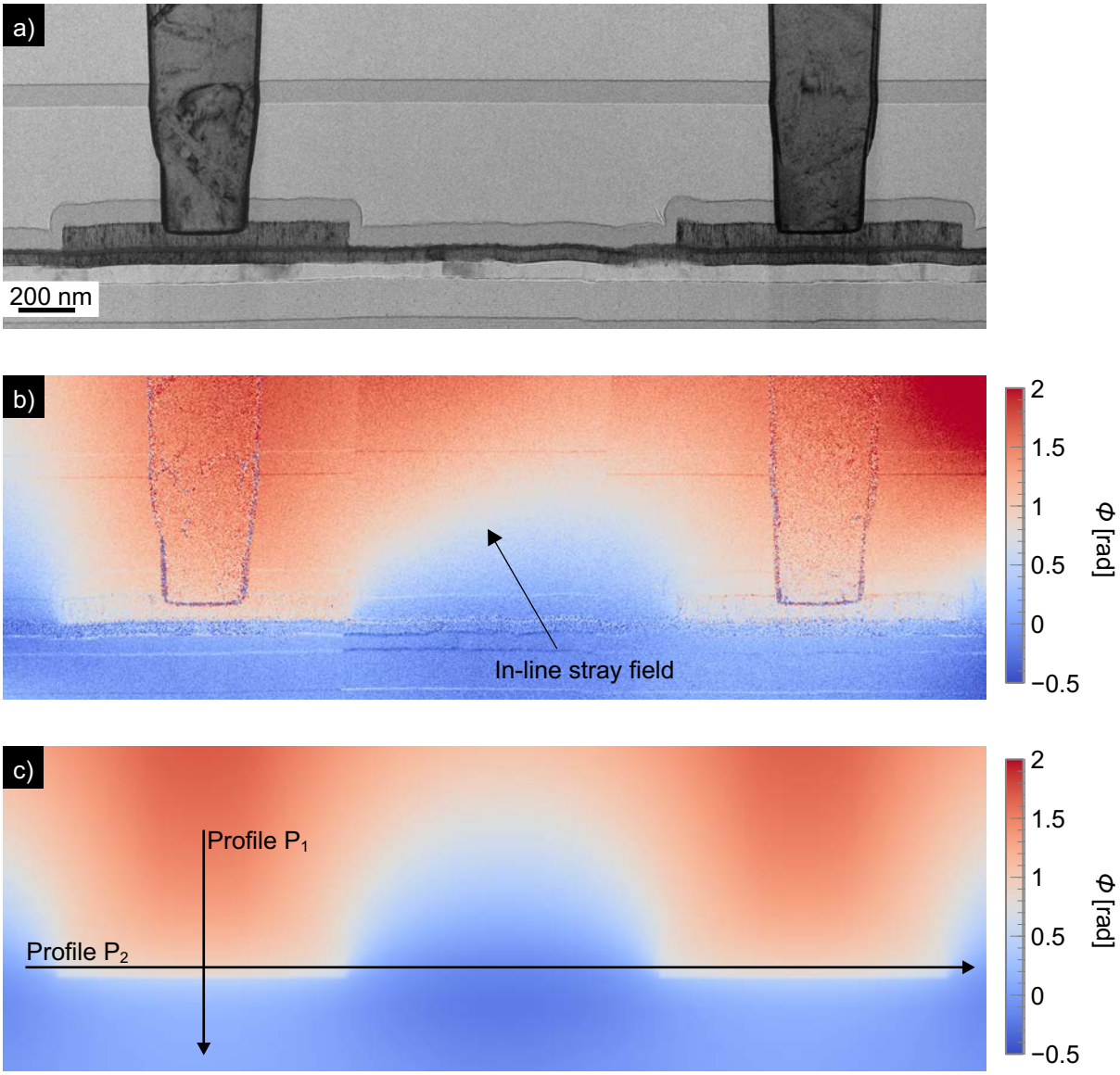

Figure 6.4 : Image de l'amplitude des deux nanocondensateurs MIM en parallèle a). L'image de phase expérimentale du potentiel électrostatique induit pour une polarisation de 0,6 V appliquée par l'alimentation b) est présentée ci-dessous, de même que la simulation de l'image de phase expérimentale c). (In-line stray field : champ de fuite en chaîne)

Les profils ont été tracés à partir des images de phase le long de la flèche noire et moyennés sur une largeur de 50 nm parallèlement aux interfaces afin de quantifier la distribution du potentiel à travers la fine couche d'oxyde (Figure 6.5(P_1)) tandis qu'un autre profil a pris la phase tout au long de l'image de phase à l'intérieur et parallèlement à l'oxyde (Figure 6.5(P_2)).
Le déphasage global à travers le diélectrique augmente linéairement avec la polarisation appliquée, comme prévu (voir chapitre 2 (Eq. 1.42)). D'autre part, la phase des électrodes situées de part et d'autre n'est pas complètement plate, bien que l'on s'attende à ce qu'elles soient à un potentiel uniforme.

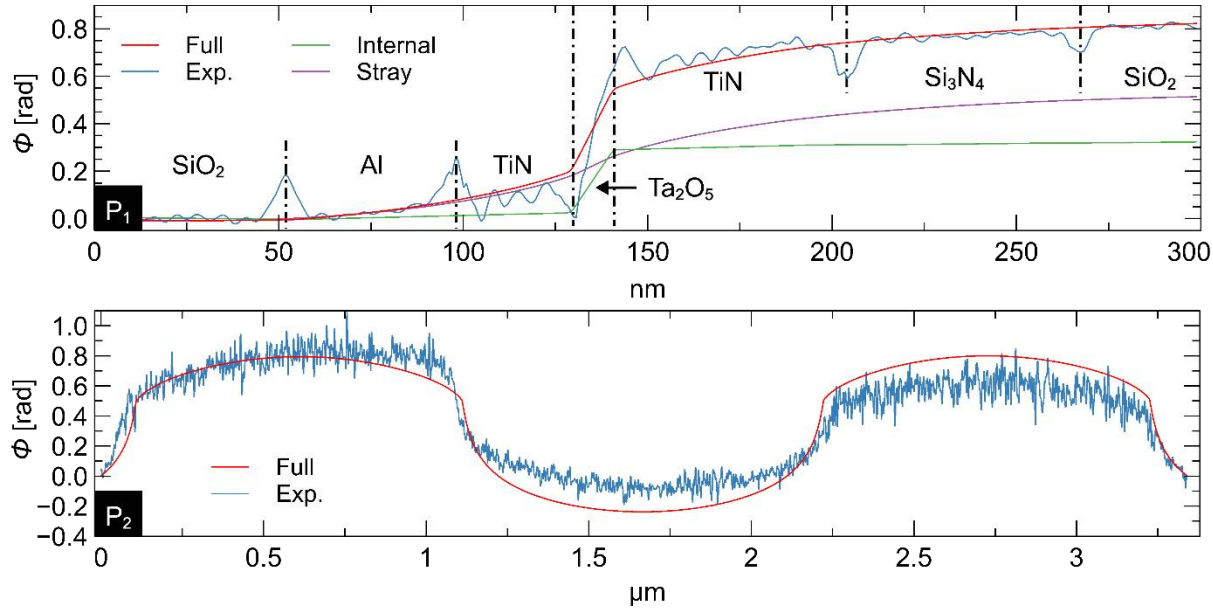

Figure 6.5 : Comparaison de la phase expérimentale et de la phase simulée par FEM Figure 6.4. P_1) and P_2) profils extraits des images de phase expérimentales et simulées le long des flèches noires P_1 et P_2 sur Figure 6.4. L'encadré sur P_1) montre les différentes contributions dues aux champs internes et externes. (Internal : interne ; Full : total ; Stray : champ de fuite)

La distribution globale de la phase et les profils de phase à travers la zone active sont parfaitement adaptés. Le champ de fuite dans le plan est également bien reproduit (Figure 6.5(P_1)), et les simulations du champ de fuite hors plan confirment qu'il est à l'origine de la non-uniformité de la phase dans la région de l'électrode.
Pour parvenir à cet accord, le biais local a été déterminé à 0,40 V dans notre modèle EM, avec une variation possible de 40 mV si l'on tient compte de l'incertitude sur l'épaisseur des lamelles. Cette valeur est bien inférieure au 0,6 V indiqué par l'alimentation externe pendant l'expérience. Une fois encore, la différence de polarisation appliquée localement et globalement est très probablement due aux courants de fuite et aux impédances dans les connexions.

5. Conclusion

En fait, les condensateurs sont l'un des composants les plus importants de tous les appareils électroniques. Ils sont largement utilisés dans les circuits analogiques et RF pour le stockage et la distribution de l'énergie dans les dispositifs de mémoire tels que les mémoires flash et les puces de mémoire vive (DRAM, SDRAM, etc.), ainsi que dans les processeurs, dont les performances dépendent de leurs miniaturisations.
Nous avons démontré que les dispositifs extraits des lignes de production peuvent être préparés pour des études MET tout en préservant leur connectivité électrique et leur fonctionnalité. L'holographie électronique *operando* peut alors être utilisée pour cartographier quantitativement la distribution du potentiel électrique en fonction de la polarisation. Les résultats expérimentaux ont été comparés à des simulations numériques utilisant la modélisation par éléments finis (MEF). En outre, le champ électrique mesuré peut être modélisé avec presque aucun paramètre d'ajustement, ce qui indique que le dispositif fonctionne effectivement normalement dans le microscope. En outre, les mesures peuvent être corrélées à des techniques TEM complémentaires afin d'obtenir une compréhension complète des propriétés

structurelles, chimiques et électriques des dispositifs individuels à l'échelle du nanomètre.
J'ai également montré un échantillon inexplicable. Malgré la défaite, cette expérience nous apprend qu'il faut faire attention à la préparation de l'échantillon sous peine de ne pas pouvoir extraire d'informations quantitatives. Cette expérience a également démontré l'importance de la polarisation, car le champ de fuite peut interférer avec l'onde de référence.
Il n'y a aucune raison pour que la même méthodologie ne puisse pas être appliquée à des dispositifs électroniques plus complexes tels que les transistors MOS ou les dispositifs spintroniques en modifiant le processus de préparation des échantillons afin de réussir à modifier le circuit et à stimuler électriquement le dispositif. Ces études représentent une investigation électrique *in situ* complète de plusieurs dispositifs sous un biais fixe et une interprétation plus poussée de ces résultats aidera à améliorer la préparation des échantillons et à minimiser son impact sur la modification des paramètres physiques. Enfin, j'espère que la possibilité d'étudier quantitativement les champs électriques locaux dans les dispositifs nouvellement proposés et existants contribuera aux efforts d'investigation des processus physiques fondamentaux ainsi qu'au développement et à l'amélioration des dispositifs existants.
Pour aller plus loin, ces résultats ouvrent la voie à de futures recherches en microélectronique, non seulement pour les transistors, mais aussi pour d'autres dispositifs tels que le condensateur ferroélectrique, qui a une constante diélectrique beaucoup plus élevée et peut également ouvrir la voie à la capacité négative, parmi d'autres dispositifs passionnants.

Chapter 7 — Conclusions

Grâce à une préparation spécifique des échantillons, une polarisation *in situ*, une microscopie contrôlée par ordinateur, une holographie électronique et un traitement des données, il est possible d'obtenir des mesures de phase et de potentiel électrique remarquablement sensibles pour des nanocondensateurs et des dispositifs en fonctionnement. J'ai cependant démontré que les données ne peuvent être pleinement exploitées sans simulation numérique. Par exemple, la modélisation est nécessaire pour tenir compte de la géométrie spécifique de l'échantillon, des champs de fuite et des artefacts de préparation. La méthodologie que j'ai développée dans le cadre de ma thèse de doctorat permet de récupérer la carte de potentiel à l'intérieur de l'échantillon ainsi que la densité de charge locale avec une résolution spatiale élevée et une sensibilité surprenante.

Bien que le champ de fuite ait été considéré comme une barrière dans l'analyse de phase des échantillons polarisés, il semble qu'après nos recherches, il soit devenu une force. À cet égard, l'analyse de la courbure du champ de fuite causé par la charge de la couche d'oxyde dans les échantillons mis à la terre fournit des informations essentielles sur la présence de couches conductrices de surface induites par la préparation FIB. En outre, dans un système simple comme un condensateur, le champ de fuite agit comme un multiplicateur de signal. En fait, selon la géométrie, la contribution du champ de fuite au signal total varie de 40 à 60 %. Par conséquent, le signal qui peut être récupéré à partir du potentiel interne appliqué par les électrodes est multiplié, ce qui améliore le rapport signal/bruit.

L'échantillon mis à la terre présente une distribution de phase symétrique. Cependant, la polarisation de l'échantillon crée une distribution de phase non symétrique (rupture de symétrie) et la chute de phase est proportionnelle à la polarisation. Par conséquent, la polarisation appliquée produit le champ de fuite, et la contribution du champ de fuite au champ interne est déterminée par le rapport épaisseur/longueur de l'isolant.

Alors que le champ de fuite peut être une source d'information précieuse, l'épaisseur de l'échantillon (par exemple, la zone active, les couches endommagées par le FIB et la zone irradiée) est le paramètre le plus difficile à évaluer. En outre, il apparaît également que l'épaisseur est un paramètre critique pour l'extraction de données quantitatives à partir de simulations numériques basées sur l'holographie *in situ*. La spectroscopie de perte d'énergie des électrons (EELS) peut fournir une estimation de l'épaisseur. Combinée à l'incertitude directement mesurée sur l'image de phase pour les autres paramètres du modèle, cette mesure est néanmoins suffisante pour extraire l'incertitude sur des paramètres importants tels que la polarisation ou la densité de charge.

Au cours de cette thèse, j'ai également exploré les possibilités d'analyse automatisée des données. Par rapport à l'analyse "à la main", c'est-à-dire l'ajustement des

paramètres et la recherche du meilleur ajustement aux données expérimentales manuellement, l'automatisation ou le traducteur automatique de données présente de nombreux avantages. Pour commencer, je pense que ce type de développement permet de minimiser le biais humain, en réduisant les erreurs systématiques. Ensuite, une telle automatisation ne permet pas seulement de gagner du temps, mais aussi d'étudier plus de paramètres dans des dimensions beaucoup plus grandes que ce qui était possible auparavant. Enfin, et c'est peut-être le plus important, les méthodes permettent une détermination plus fiable des incertitudes expérimentales dans les paramètres ajustés.

L'automatisation nous donne également la possibilité de créer d'énormes bases de données à partir de notre modèle. Si nous voulons accélérer la convergence de l'algorithme de descente du gradient, qui est la méthode de la région de confiance réflective (TRR) dans ce cas, nous pouvons alimenter l'algorithme d'IA pour améliorer les performances d'ajustement en construisant un ensemble de données à l'aide d'une boucle d'exploration. En revanche, avec l'algorithme d'ajustement automatique, nous pourrions gagner beaucoup de temps en utilisant un réseau neuronal capable de faire une prédiction en moins d'une seconde et donc de calculer l'incertitude avec l'algorithme TRR.

Ces développements fondamentaux peuvent être appliqués à l'analyse des dispositifs microélectroniques en production. Bien que beaucoup plus complexe qu'un échantillon de laboratoire, un dispositif industriel peut être mesuré à l'échelle du micromètre avec une résolution inférieure au nanomètre. Certains échantillons ne peuvent être expliqués malgré tous nos efforts, mais nous pouvons toujours en extraire des informations utiles, ce qui prouve que même lorsque nous commettons des erreurs, le résultat final est toujours intéressant.

Je voudrais souligner qu'au début de la thèse, il n'était pas certain que nous puissions utiliser la simulation numérique pour interpréter les données de l'holographie électronique résultant de phénomènes physiques inattendus. Il faut rappeler que nous avions choisi un condensateur comme dispositif d'étude précisément parce qu'il était censé être très bien connu et compris. Malgré cela, nous avons pu intégrer dans la modélisation des caractéristiques inattendues, telles que la charge aux interfaces diélectriques. En effet, la modélisation numérique était essentielle pour démontrer que ces phénomènes étaient nécessaires pour expliquer les données expérimentales. Je ne m'attendais pas à ce que l'analyse du condensateur aille aussi loin.

Avant ma thèse, il était difficile de caractériser les composants électroniques industriels, car la caractérisation électrique nanoscopique n'offre pas une bonne résolution spatiale. Il en va de même pour la recherche purement théorique. L'utilisation de l'holographie électronique *operando* sur les composants électroniques était très utile pour étudier et comprendre le fonctionnement des appareils, mais elle manquait de données quantitatives et de mesures d'incertitude précises. Au cours de ma thèse, j'ai développé une méthodologie pour simuler des expériences d'holographie électronique sur des nanodispositifs électriques, ce qui nous a permis de caractériser et de détecter des zones de charge inattendues sur des modèles que nous pensions bien comprendre. Je voulais donc non seulement mesurer des paramètres, mais aussi créer une méthodologie d'incertitude. Sur cette base, et parce que nous avons pu travailler sur des condensateurs réels provenant de la ligne de production de STMicroelectronics, je montre que nous pouvons analyser ces dispositifs au prix d'un peu plus de complexité.

Perspectives

Au début de cette étude, je me suis concentré sur les paramètres extrinsèques qui perturbaient la mesure, telle que l'effet de l'instrument de mesure (c'est-à-dire le microscope électronique) et les artefacts liés à la préparation de l'échantillon. La préparation du FIB devrait faire l'objet de recherches plus approfondies. Au cours de ces études, nous préparons nos échantillons avec un FIB à source de gallium, ce qui permet d'obtenir des couches conductrices. Des échantillons comparables pourraient être fraisés avec d'autres sources, telles que des gaz non réactifs. Le fraisage avec ce type de source ne devrait pas former de couches conductrices à la surface. Je pense également que la compréhension de l'interaction entre le champ généré par un échantillon polarisé et l'onde de référence est un défi qui doit être relevé afin d'étudier des champs plus complexes pour des géométries d'échantillons plus complexes.

On peut imaginer le développement d'un logiciel installé au plus près du microscope, permettant l'étude d'échantillons électriques directement pendant l'expérience. Pour ce faire, nous pourrions créer une interface configurable par l'utilisateur qui analyse directement l'hologramme ou nous pourrions poursuivre le développement de la technique de l'IA. À partir de l'étude développée dans le cadre de ma thèse, nous pourrions utiliser directement le réseau neuronal développé sur les images de phase, favorisant ainsi la généralisation de ce type d'analyse. De plus, les condensateurs étant fréquemment utilisés dans des applications à haute fréquence, il serait passionnant de pouvoir les caractériser, à la fois macroscopiquement et par holographie électronique *operando*, en fonction de la fréquence et de les comparer à notre analyse statique.

Je suis convaincu que cette recherche ouvre la voie à l'étude de composants électroniques plus complexes, tels que les transistors, les dispositifs de mémoire à changement de phase et les condensateurs ferroélectriques. Par exemple, de telles approches permettraient de mieux comprendre la capacité négative afin de créer des dispositifs moins énergivores.

Aujourd'hui, nous avons travaillé sur des échantillons dont nous pensions tout savoir, mais pourquoi ne pas envisager une application systématique pour aider au développement des futurs composants microélectroniques ? Par exemple, la technologie quantique pourrait être étudiée à l'avenir. Alors que l'effet tunnel rend difficile la miniaturisation de la technologie des transistors, il permet le développement de nouveaux dispositifs tels que le transistor à électron unique. Nous pourrions étudier ces nouveaux dispositifs avec le microscope I^2TEM, car il est désormais équipé d'une nouvelle caméra à détection directe d'électrons, qui offre une sensibilité accrue et une meilleure résolution spatiale.

Electron holography is a powerful transmission electron microscopy (TEM) technique, one of the few capable of quantitatively mapping electric, magnetic, and strain fields at the nanoscale. Holography allows the measurement of the phase shift of the electron beam caused by the interaction with electromagnetic potentials along its trajectory, both within the polarized sample but also in the surrounding stray field.

When combined with *in situ* biasing experiments, electron holography provides unprecedented opportunities to measure electric fields in operating microelectronic devices. However, it is necessary to demonstrate that such *operando* measurements are fully quantitative, and therefore exploitable, by first studying model systems. Experimental results will have to be compared to models that account for variables such as sample geometry, damage caused by the focused ion beam (gallium-source FIB) used for thinning, stray fields, and charging.

The specially prepared samples are placed on a chip that is inserted into a dedicated TEM holder for in situ electrical signal injection. Operando electron holography was carried out on the I2TEM microscope (In-situ Interferometry TEM), a Hitachi 3300-C TEM, specifically designed for such experiments. Extremely long exposure times were used (up to 30 minutes) to improve the signal-to-noise ratio, thanks to recently developed dynamic automation that allows the stabilization of the position of the sample and the hologram fringes during acquisition.

This thesis shows how experimental phase images obtained by electron holography can be quantitatively interpreted for biased model nanocapacitors, as well as devices from production lines, using numerical simulations with the finite element method (FEM). I created a FEM-based methodology for modeling the electrostatic potential in and around electrically polarized nanodevices using commercial software (COMSOL Multiphysics). To account for the effect of surface damage introduced during FIB sample preparation, conductive superficial layers were included in the model. To fit the experimentally measured phase shift, the parameters are manually adjusted and then algorithmically adjusted iteratively using the trust region reflective method. The fitting process estimates the true bias applied to the nanodevices, determines the presence and characteristics of conductive layers on the surface, and measures the charge densities that may occur. The results of model nanocapacitors and nanodevices from STMicroelectronics manufacturing lines are presented and analyzed, and errors are investigated. There is also a detailed theoretical study of the relationship between a model capacitor and the resulting phase image.

This thesis demonstrates the interest of studying the distribution of electric fields and potentials at a nanometric scale. For example, we highlight the presence of volume charged regions that alter the expected electrical characteristics of model metal-oxide-semiconductor (MOS) nanocapacitors, despite the fact that this type of nanodevice was considered to be completely understood. We anticipate that establishing the relationship between local electric fields and the structural and chemical information will greatly assist research laboratories and the microelectronics industry in the development of new nanoelectronic devices.

L'holographie électronique est une méthode dérivée de la microscopie électronique en transmission (MET) et l'une des rares techniques capables de cartographier quantitativement les champs électriques, magnétiques et de déformation à l'échelle nanométrique. L'holographie permet d'accéder au déphasage acquis par le faisceau électronique lorsqu'il interagit avec des potentiels électromagnétiques. Les électrons acquièrent ce déphasage non seulement en traversant l'échantillon polarisé, mais aussi par le champ de fuite rayonné et qui l'entoure inévitablement.

Associée à des expériences de polarisation *in situ*, l'holographie électronique ouvre des perspectives sans égales pour mesurer les champs électriques dans des dispositifs issus de la microélectronique pendant leur fonctionnement. Il est cependant nécessaire dans un premier temps de démontrer que ces mesures sur des nanocomposants en fonctionnement sont parfaitement quantitatives et exploitables, en commençant par des systèmes modèles. Les résultats expérimentaux doivent également être comparés aux modélisations prenant en compte différents facteurs tels que la géométrie de l'échantillon, les dommages causés par le faisceau d'ions focalisés (FIB à source de gallium) utilisés pour l'amincissement, les champs de fuites et les effets de charge.

Les échantillons préparés spécifiquement sont placés sur une puce insérée dans un porte-objet MET dédié à l'injection *in situ* de signaux électriques. Les expériences d'holographie électronique dites *operando* ont été réalisées sur le microscope I2TEM avec des temps d'exposition extrêmement longs pour améliorer le rapport signal/bruit (jusqu'à 30 minutes) grâce à l'automatisation dynamique qui permet la stabilisation des franges d'interférence et de l'échantillon.

Ce travail de thèse démontre comment interpréter quantitativement les images de phase expérimentales obtenues par holographie électronique sur des nanocondensateurs modèles polarisés, ainsi que dans des dispositifs issus de lignes de production, en utilisant des simulations numériques avec la méthode des éléments finis (MEF). J'ai ainsi développé une méthodologie basée sur la MEF à l'aide d'un logiciel commercial (COMSOL Multiphysics) pour modéliser le potentiel électrostatique à l'intérieur et autour de nanodispositifs polarisés électriquement. Des couches conductrices ont été incluses dans le modèle pour prendre en compte l'effet de dommages de surface introduits pendant la préparation de l'échantillon par FIB. Pour s'ajuster au déphasage mesuré expérimentalement, les paramètres sont d'abord ajustés manuellement, puis de manière algorithmique en utilisant la méthode de la région de confiance avec réflexion de manière itérative. Le processus d'ajustement permet d'estimer la véritable polarisation appliquée aux nanodispositifs, de déterminer la présence et les caractéristiques des couches conductrices à la surface, et de mesurer les densités de charge pouvant apparaître. Les résultats obtenus sur des nanocondensateurs modèles et des nanocomposants issus des lignes de production de STMicroelectronics sont présentés et analysés, et les erreurs sont étudiées. Une étude théorique de la relation entre un condensateur modèle et l'image de phase résultante est également détaillée.

Ce travail de thèse démontre l'intérêt d'étudier à une échelle nanométrique la distribution des champs et potentiels électriques. Nous mettons par exemple en évidence la présence de zones chargées en volume qui modifient les caractéristiques électriques attendus dans des nanocondensateurs métal/oxide/semiconducteur (MOS) modèles alors que tout semblait parfaitement compris sur ce type de nanodispositifs. De plus, la corrélation des champs électriques locaux avec les propriétés structurales et chimiques aiderait considérablement les laboratoires de recherche et l'industrie microélectronique dans la recherche fondamentale et le développement de nouveaux dispositifs nanoélectroniques.